

ABSTRACT

Title of Document: FIBER OPTICAL TWEEZERS FOR MICROSCALE AND NANOSCALE PARTICLE MANIPULATION AND FORCE SENSING

Yuxiang Liu, Ph.D., 2011

Directed By: Assistant Professor Miao Yu,
Department of Mechanical Engineering

Optical tweezers have been an important tool in biology and physics for studying single molecules and colloidal systems. Most of current optical tweezers are built with microscope objectives, which are: i) expensive, ii) bulky and hard to integrate, iii) sensitive to environmental fluctuations, iv) limited in terms of working distances from the substrate, and v) rigid with the requirements on the substrate (transparent substrate made with glass and with a fixed thickness). These limitations of objective-based optical tweezers prevent them from being miniaturized. Fiber optical tweezers can provide a solution for cost reduction and miniaturization, and these optical tweezers can be potentially used in microfluidic systems. However, the existing fiber optical tweezers have the following limitations: i) low trapping efficiency due to weakly focused beams, ii) lack of the ability to control the positions of multiple particles simultaneously, and iii) limited functionalities.

The overall objective of this dissertation work is to further the fundamental understanding of fiber optical tweezers through experimental study and modeling, and to develop novel fiber optical tweezers systems to enhance the capability and functionalities of fiber optical tweezers as microscale and nanoscale manipulators/sensors. The contributions of this dissertation work are summarized as follows. *i) An enhanced understanding of the inclined dual-fiber optical*

tweezers (DFOTs) system has been achieved. Stable three dimensional (3D) optical trapping of a single micron-sized particle has been experimentally demonstrated. This is the first time that the trapping efficiency has been calibrated and the stiffness of the trap has been obtained in the experiments, which has been carried out by using two methods: the drag force method and power spectrum analysis. Such calibration enables the system to be used as a picoNewton-level force sensor in addition to a particle manipulator. The influence of system parameters on the trapping performance has been carefully investigated through both experimental and numerical studies. ***ii) Multiple traps have been created and carefully studied with the inclined DFOTs for the first time.*** Three traps, one 3D trap and two 2D traps, have been experimentally created at different vertical levels with adjustable separations and positions. ***iii) Multiple functionalities have been achieved and studied for the first time with the inclined DFOTs.*** Particle separation, grouping, stacking, rod alignment, rod rotation, and optical binding have been experimentally demonstrated. The multiple functionalities allow the inclined DFOTs to find applications in the study of interaction forces in colloidal systems as well as parallel particle manipulation in drug delivery systems. ***iv) Far-field superfocusing effect has been investigated and successfully demonstrated with a fiber-based surface plasmonic (SP) lens for the first time.*** A planar SP lens with a set of concentric nanoscale rings on a fiber endface has been developed. For the first time, a focus size that is comparable to the smallest achievable focus size of high NA objective lenses has been achieved with the fiber-based SP lens. The fiber-based SP lens can bridge the nanoscale particles/systems and the macroscale power sources/detectors, which has been a long standing challenge for nanophotonics. In addition to optical trapping, the fiber-based SP lens will impact many applications including high-resolution lithography, high-resolution fluorescence detection, and sub-wavelength imaging. ***v) Trapping ability enhanced with the fiber-based SP***

lens has been successfully demonstrated. With the help of the fiber-based SP lens, the trapping efficiency of fiber optical tweezers has been significantly enhanced, which is comparable with that of objective-based optical tweezers. A submicron-sized bacterium has been successfully trapped in three dimensions for the first time with optical tweezers based on single fibers.

FIBER OPTICAL TWEEZERS FOR MICROSCALE AND NANOSCALE PARTICLE MANIPULATION AND FORCE SENSING

By

Yuxiang Liu

Dissertation submitted to the Faculty of the Graduate School of the
University of Maryland, College Park, in partial fulfillment
of the requirements for the degree
of Doctor of Philosophy in
Mechanical Engineering
2011

Advisory Committee:

Assistant Professor Miao Yu, Chair/Advisor

Professor Balakumar Balachandran

Associate Professor Elisabeth Smela

Assistant Professor Teng Li

Associate Professor Wolfgang Losert, Dean's Representative

© Copyright 2011, Yuxiang Liu.

All rights reserved.

To Lijuan, and my parents

Acknowledgements

I owe great thanks to many people, whose help and friendship have been instrumental in completing this dissertation. My doctoral study experience is one that I will cherish forever, and I expect to benefit it from in the future.

The deepest gratitude is owed to my Ph.D. advisor Prof. Miao Yu. I would like to thank her for supporting me during the last five years. I have learned so much from her over the last five years, and the learning has not just been limited to fiber optics. Her enthusiasm and constant stream of ideas have provided a great impetus to my work. Her mentoring has made my thinking mature and also made me appreciate aspects such as securing support for your work and publishing the research findings and the difficulty of doing them. The experience of working with Prof. Yu is actually one of the reasons for my reaching a decision to pursue a career in academia in the future.

I would also like to express my sincere gratitude to Prof. Elisabeth Smela. Prof. Smela has been one of the best teachers that I have had thus far. I feel lucky that I took her MEMS courses during my first year here, in which I had a chance of being systematically trained on almost all the aspects of doing research. This experience was like a detailed two-semester “research orientation” to me, which later benefited my research greatly. Two important things I learned from her are academic integrity and precision of expression. I deeply appreciate her generosity in spending so much time in helping me when I was working on my first publication and sharing

with me her opinions of academia. Every time talking to her made me feel being “polished”. She has exerted an influence over my thinking and my work.

I am indebted to Prof. Balakumar Balachandran for all his assistance and advice. He was the first professor I met at UMD other than my advisor, and he was also the first one I would turn to when I encountered difficulties. His encouragement and advice helped me a lot when I taught the Fiber Optics course. He cared about my research and we had extensive discussions about it. I also appreciate his willingness to let me use the computer resources in his laboratory for my FDTD simulations. He set an example to me about being professional and kind to others no matter how busy one might be.

I am very grateful to Prof. Wolfgang Losert and Prof. Teng Li for their advice and suggestions on my proposal. I am also thankful to them for spending time reading and commenting on my dissertation. I would like to show my appreciation to Prof. Losert for providing me the glass rods and micro-beads. I would like to acknowledge Prof. Li for the discussions and his encouragement for my research. I would thank Dr. Hua Xu and Dr. Nikolai Zhetenev at National Institute of Standards and Technology for the collaboration and discussions on the fabrication of the fiber based surface plasmonic lens.

I am also appreciative of the courses that I had with Prof. Edward Ott and Prof. Peter Bernard on Electromagnetic Theory and Fluid Mechanics, respectively. The confidence and the attitude toward a research life that they conveyed to me will have a long-term effect on my future carrier.

I owe my thanks to everyone working and having worked in the Sensors and Actuators Lab. Special thanks go to Felix Stief, who helped me a lot with the experiments to do with the last stage of the dissertation. My gratitude is also extended to Zhong Chen, Silas Nesson, Alexander Lacher, Haijun Liu, Xuming Zhang, Christian Altmeyer, Hyungdae Bae, Cheng Pang, Andrew Lisiewski, and Laithe Sawaqed. They were all like family to me during my graduate study since I spend most of my time with them. I did learn a lot from them and benefited from their help in both my academic and my private life.

Finally, none of this would have been possible without the love and patience of my wife Lijuan Pi, and my parents, Mr. Desheng Liu and Mrs. Guiying Ding. They provided the support and strength that helped me to persist with my studies and research. I cannot thank them enough, and I don't think I can ever repay them enough. This dissertation is dedicated to my family.

TABLE OF CONTENTS

CHAPTER 1. INTRODUCTION AND BACKGROUND	1
1.1. PROBLEM OF INTEREST	1
1.2. REVIEW OF PREVIOUS WORK	4
1.2.1. Basic optics	4
1.2.2. Optical tweezers based on microscope objectives.....	7
1.2.2.1. <i>Basic experimental arrangement</i>	7
1.2.2.2. <i>Current state-of-the-art of optical tweezers based on objective lenses</i>	9
1.2.2.3. <i>Limitations of objective-based optical tweezers</i>	19
1.2.3. Fiber optical tweezers	23
1.2.3.1. <i>Advantages of optical fiber trapping systems</i>	23
1.2.3.2. <i>Single fiber optical tweezers</i>	27
1.2.3.3. <i>Dual fiber optical tweezers</i>	30
1.2.3.4. <i>Other fiber optical tweezers</i>	32
1.2.3.5. <i>Limitations of current fiber optical tweezers</i>	33
1.3. MOTIVATION FOR THIS DOCTORAL RESEARCH	34
1.4. OBJECTIVES AND SCOPE OF DISSERTATION.....	37
CHAPTER 2. INCLINED DUAL-FIBER OPTICAL TWEEZERS: SYSTEM DEVELOPMENT, MODELING, AND EXPERIMENTS	39
2.1. SYSTEM DEVELOPMENT OF INCLINED DFOTs.....	39
2.2. TRAPPING PRINCIPLES OF INCLINED DFOTs	42
2.3. EXPERIMENTAL STUDY OF INCLINED DFOTs FOR MANIPULATION OF SILICA BEADS.....	44

2.3.1.	Three-dimensional trapping ability	44
2.3.2.	Calibration of trapping efficiency with drag force method	45
2.3.2.1.	<i>Basic principles of drag force calibration</i>	45
2.3.2.2.	<i>Evaluation of the fiber tip deflection due to the drag force</i>	46
2.3.2.3.	<i>Drag force calibration results</i>	47
2.3.3.1.	<i>Basic principles of power spectrum analysis</i>	50
2.3.3.2.	<i>Experiments with the PSD</i>	55
2.3.3.3.	<i>Results obtained from power spectrum analysis</i>	59
2.4.	MODELING OF TRAPPING FORCES OF INCLINED DFOTS	62
2.4.1.	Ray optics model.....	63
2.4.2.	Trapping force along the z direction.....	65
2.4.3.	Trapping forces along the x and y directions.....	69
2.4.4.	Robustness of the DFOTs to z-axis misalignment	73
2.5.	OPTICAL TRAPPING OF YEAST CELLS WITH INCLINED DFOTS	77
2.5.1.	3D Cell trapping	77
2.5.2.	Spring constant calibration of yeast cell trapping	78
2.5.3.	Simulation results on ellipsoidal particle trapping.....	81
2.6.	SUMMARY.....	84
CHAPTER 3. MULTIPLE TRAPS CREATED WITH INCLINED DFOTS		85
3.1.	REVIEW OF EXISTING MULTIPLE OPTICAL TRAPPING SYSTEMS	85
3.2.	EXPERIMENTAL SETUP	88
3.3.	PRINCIPLES OF MULTIPLE TRAPS CREATED WITH INCLINED DFOTS	89

3.4. INVESTIGATION OF MULTIPLE TRAPS AND MULTIPLE FUNCTIONALITIES WITH SILICA	
BEADS	90
3.4.1. Experimental demonstration of multiple traps and multiple functionalities with silica beads	90
3.4.1.1. <i>Demonstration of multiple traps and bead separation</i>	90
3.4.1.2. <i>Bead stacking</i>	92
3.4.1.3. <i>Bead grouping</i>	94
3.4.1.4. <i>Multiple beads trapping and stacking in three dimensions</i>	95
3.4.2. Numerical study of multiple traps and multiple functionalities with silica beads	96
3.4.3. Discussion of multiple traps with silica beads	100
3.5. INVESTIGATION OF MULTIPLE TRAPS AND MULTIPLE FUNCTIONALITIES WITH GLASS RODS.	
.....	103
3.5.1. Motivation of optical manipulation of cylindrical particles.....	103
3.5.2. Working principles of multiple traps on glass rods.....	104
3.5.3. Experimental investigation of multiple functionalities with glass rods.....	105
3.5.3.1. <i>Trapping and alignment of glass rods</i>	106
3.5.3.2. <i>Rotation of glass rods</i>	107
3.5.3.3. <i>Stacking of glass rods</i>	109
3.5.3.4. <i>Optical binding of silica beads and glass rods</i>	111
3.5.4. Numerical investigation of multiple functionalities with glass rod.....	113
3.5.4.1. <i>Optical force and torque fields of a single 2D trap applied on a y-oriented rod..</i>	
.....	114

3.5.4.2.	<i>Optical torque field of a single 2D trap applied on an arbitrarily oriented rod...</i>	116
3.5.4.3.	<i>Optical force and torque fields of two 2D traps applied on a y-oriented rod.</i>	117
3.5.4.4.	<i>Explanation of optical trapping, alignment, rotation, and stacking of glass rods</i>	119
3.5.5.	Discussion of multiple traps with glass rods.....	120
3.6.	SUMMARY.....	123

CHAPTER 4. TRAPPING EFFICIENCY ENHANCEMENT FOR FIBER OPTICAL TWEEZERS..... 125

4.1.	SUPERFOCUSING WITH FIBER-BASED SURFACE PLASMONIC LENSES.....	127
4.1.1.	Modeling and design of fiber-based SP lenses.....	130
4.1.2.	Development and experimental study of fiber-based SP lenses	134
4.1.3.	Experimental results of fiber-based SP lenses	136
4.1.3.1.	<i>Experimental results obtained from the 4-slit fiber-based SP lens (SP1).....</i>	136
4.1.3.2.	<i>Experimental results obtained from the 3-slit fiber-based SP lens (SP2).....</i>	139
4.1.3.3.	<i>Discussion of the superfocusing results obtained with the SP lenses.....</i>	141
4.1.4.	Modeling of fiber-based SP lens: FDTD simulations	147
4.1.4.1.	<i>Basic principles of FDTD methods.....</i>	147
4.1.4.2.	<i>FDTD simulations carried out with FDTD Solutions.....</i>	151
4.1.4.3.	<i>FDTD simulation results of SP1.....</i>	153
4.1.4.4.	<i>FDTD simulation results of SP2.....</i>	155
4.1.4.5.	<i>Discussion of the simulation results of the SP lenses</i>	156
4.1.5.	Discussion of the differences between the experimental and simulation results	159

4.1.6.	Significance of the superfocusing achieved with fiber-based SP lenses	160
4.2.	OPTICAL TRAPPING ABILITY ENHANCEMENT WITH FIBER-BASED SP LENSES.....	161
4.2.1.	Experimental demonstration of enhanced trapping ability achieved with fiber-based SP lenses.....	162
4.2.1.1.	<i>Experimental results of bacteria trapping with SP fiber tweezers</i>	<i>162</i>
4.2.1.2.	<i>Discussion of the trapping force enhancement demonstrated by using the SP lensed fiber tweezers</i>	<i>165</i>
4.2.2.	Modeling of enhanced trapping efficiency with fiber-based SP lenses.....	166
4.2.2.1.	<i>Models for obtaining trapping forces on Rayleigh particles</i>	<i>167</i>
4.2.2.2.	<i>Modifications to the CN model following the conventions used in the HA model</i>	<i>175</i>
4.2.2.3.	<i>Summary and comparisons of the HA and CN models</i>	<i>177</i>
4.2.2.4.	<i>Stability of optical trapping versus particle sizes in the Rayleigh regime.....</i>	<i>179</i>
4.2.2.5.	<i>Electric fields of fundamental (TEM₀₀) Gaussian beams.....</i>	<i>180</i>
4.2.2.6.	<i>Parametric study of Rayleigh particle trapping.....</i>	<i>182</i>
4.2.3.	3D Trapping force fields of the SP fiber optical tweezers.....	191
4.2.3.1.	<i>3D force mapping of SP1</i>	<i>192</i>
4.2.3.2.	<i>3D force mapping of SP2</i>	<i>193</i>
4.2.3.3.	<i>Discussion of the calculated trapping force fields</i>	<i>195</i>
4.2.4.	Significance of the enhanced trapping ability with the SP fiber optical tweezers ..	199
4.3.	SUMMARY.....	200
CHAPTER 5. SUMMARY AND FUTURE WORK		202
5.1.	SUMMARY AND CONTRIBUTIONS OF THE DISSERTATION WORK	202

5.2. FUTURE WORK	206
APPENDIX A: MATLAB CODES	210
APPENDIX B: PUBLICATIONS	226
REFERENCES	228

List of Figures

Figure 1.1. Scattering and gradient forces of optical tweezers. [23]	5
Figure 1.2. Basic experimental setup of objective-based optical tweezers. The dimensional sketch of the microscope is reprinted from the CKX41 Brochure [29].	8
Figure 1.3. Evolution of optical trapping. (a) Optical trapping with two counter-propagating beams (1970). Equilibrium between the radiation pressures of the two beams. (b) Optical levitation built with a low NA objective (1971). Equilibrium between the gravity force and the radiation pressure. (c) Stable 3D single beam trapping built from a tightly focused beam with a high NA objective. Equilibrium between the scattering force (radiation pressure) and the gradient force (1986).	10
Figure 1.4. (a) Intensity profile of the focus of a Gaussian beam (w_0 is the beam size) with an optical vortex (w_v is the vortex size) and (b) different trapping location of the particles with high-index and low-index [36].	13
Figure 1.5. (a) Interference of two beams (left) and the interference patten (right) and (b) two hollow spheres trapped by the interference pattern [34].	13
Figure 1.6. (a) Glass cylinders before trapping and (b)-(p) trapped glass cylinders with axis aligned with the optical axis (perpendicular to the paper surface) rotates while being dragged along a larger cylinder. [43].	15
Figure 1.7. A complex-shaped mirrorrotor fabricated and rotated by optical tweezers. [46]	15
Figure 1.8. Rotation of the Plasmodium infected red blood cells [50].	17
Figure 1.9. Large deformation of the stretched RBC. The values shown on the left are the measured optical forces applied to stretch the RBC [53].	18
Figure 1.10. Limited working distance of objective-based optical tweezers.	21
Figure 1.11. The optical fiber (left) is much smaller than the objective (middle) and readily to be integrated.	24
Figure 1.12. Degradation of focus quality in a colloid. (a) Optical fiber tweezers and (b) objective-based optical tweezers. Less degradation due to light travels a smaller distance in the solution.	26
Figure 1.13. Single fiber optical tweezers by using a fiber with (a) tapered spherical end [71], (b) dielectric sphere glued on the cleaved fiber end [73], (c) axicon lens [74], d) annular exposed end [66], (e) sharply tapered end [75], and (f) two cores [76].	28
Figure 1.14. Dual fiber optical tweezers with (a) two cleaved fibers [81], (b) two trapping fibers (one probing fiber to excite and one detection fiber to sense fluorescence) [82], and (c) two inclined fibers [86].	30
Figure 1.15. Reflection-based four-fiber optical tweezers. [90]	33
Figure 2.1. (a) Experimental setup of the inclined DFOTs system. (b) Close-up showing the optical trap built from the two beams emitted from lensed fibers. (c) Microscope image showing two auras due to the beam scattering.	40
Figure 2.2. Illustration of forces applied to a trapped particle in (a) SFOTs and (b) DFOTs. F_s represents the axial net force of the scattering force and the gradient force and F_g denotes the transverse gradient force.	43
Figure 2.3. Silica bead with a diameter of 4.74 μm manipulated in three dimensions by the DFOTs. The arrows indicate the next movement direction of the coverglass. (a) Initial positions of free beads with the coverglass moved along $+y$. (b)-(c) The coverglass moved	

along $+x$ with Bead 1 trapped. (c)-(e) The coverglass moved along $+y$, $-x$, and then $-y$. Bead 2 was moved out of the view field and another free bead, Bead 3, was brought in. (e)-(f) The trap together with Bead 1 moved out of focus along $+z$. (f)-(h) The coverglass moved downwards ($+x$) with Bead 3 moved freely below Bead 1.	44
Figure 2.4. Schematic of the drag force calibration for obtaining the trapping efficiency.	46
Figure 2.5. An example of image correlation that is used to determine the bead displacement. The image to the right shows the correlation of the two left images.	48
Figure 2.6. The bead displacement data obtained from a video clip at a laser power of 15.3 mW from the source. The water movement was initiated at around 2.5 s, and then at around 3.7 s, it reached a constant speed of 25 $\mu\text{m/s}$. The water movement was stopped at around 10.2 s. The triangle and the square data points correspond to the vertical (y -axis) and horizontal (x -axis) displacements, respectively.	48
Figure 2.7. Calibration curves of x -axis trapping efficiencies obtained with different laser powers. The experiments were carried out with silica beads of 4.74 μm in diameter. The optical powers shown are the total powers from both fibers.	49
Figure 2.8. The influence of D and f_c to $P_{vv}(f)$. D determines the height of the plateau, while f_c determines where the “corner” is located.	53
Figure 2.9. Experimental setup for testing the PSD. The fiber guiding a red laser beam was mounted above the sensitive area of the PSD.	56
Figure 2.10. Picture of the PSD holder with the PSD attached.	57
Figure 2.11. Power spectrum shown the resonance peaks of the microscope body at 30~40 Hz. The power spectrum was recorded when the microscope was placed, but not bolted, on the floated optical table. After the microscope was fixed, the above peaks disappeared.	59
Figure 2.12. Lorentzian fitting of experimentally measured power spectrum. Here, the corner frequency f_x is 11.3 Hz, which gives a spring constant k_x of 2.82 pN/ μm	60
Figure 2.13. (a) Geometric sketch for the incident direction calculation at Point Q and (b) incident condition at the interface.	64
Figure 2.14. The simulation results of optical force versus bead displacement along z axis with different θ values. G is the gravity and F_b is the buoyancy of the trapped silica bead. The optical force should be larger than $G-F_b$ in order to trap the bead in the z direction. The total optical power emitted from both fibers is 8.05 mW. The bead size is 4.74 μm in diameter.	66
Figure 2.15. The simulation results of optical force versus bead displacement along z axis with different bead sizes. G is the gravity and F_b is the buoyancy of the trapped silica bead. For each bead sizes, $G-F_b$ is expressed with a horizontal dashed line with the same color as the optical force curve. The total optical power emitted from both fibers is 8.05 mW. The inclination angle θ is 50°.	68
Figure 2.16. The dependence of optical forces on bead displacements along (a) the x axis and (b) the y axis for different fiber inclination angles. The total optical power emitted from both fibers is 15.3 mW. The bead size is 4.74 μm in diameter. The fiber separation along the y axis is 45 μm	70
Figure 2.17. Simulation results of the forces applied on a 4.74- μm bead in the yz plane with a misalignment of 1 μm along the z axis for (a) the inclined DFOTs ($\theta = 50^\circ$) and (b) the counter propagation DFOTs ($\theta = 90^\circ$). The dash-dotted lines indicate the optical axes of the two fibers. It is noted that the forces are the net forces of optical forces, gravity, and buoyancy applied on the beads.	75

Figure 2.18. Images of 3D yeast cell manipulation by using inclined DFOTs, obtained with an Olympus 100*/1.25 oil-immersed objective.....	77
Figure 2.19. (a) Photograph of Cell 1 and (b) experimental results and fitted curve of the relationship between optical forces and cell displacements in the optical tap.	79
Figure 2.20. (a) Photograph of Cell 2 and (b) experimental results and fitted curve of the relationship between optical forces and cell displacements in the optical tap.	79
Figure 2.21. Schematic of round cell and prolate cells in optical traps.....	80
Figure 2.22. Simulation of the optical force versus the displacement for a spheroid particle with the same size as Cell 1 in Figure 2.19. Experimental results are also plotted for comparison.	82
Figure 2.23. Simulation for the optical force versus the displacement for a spheroid particle with the same size as Cell 2 in Figure 2.20. Experimental results are also plotted for comparison.	83
Figure 3.1. Experimental arrangement of the inclined DFOTs for creating multiple traps.....	88
Figure 3.2. Principle of multiple traps created by using the inclined DFOTs.....	89
Figure 3.3. Images of beads manipulated in the multiple traps. (a) Three free beads on the coverglass. (b) Beads 1, 2, and 3 trapped in contact. (b)-(d) The fiber block was moved upward along +z and trapped beads had been separated. (d)-(f) The coverglass was moved along +x and then along -y. The arrows in (d) and (e) indicate the next movement direction of the coverglass. The xy coordinate system is shown at the lower left corner of (a). The bead size is 4.74 μm in diameter.....	91
Figure 3.4. Experimental demonstration of particle stacking. With the fiber block lowered down toward the coverglass, the four beads were (a) first separated, (b) then brought into contact, and (c) finally stacked. (a)-(c): pictures captured from a video clip; (d)-(f): sketches illustrating pictures (a)-(c), respectively. The bead size is 4.74 μm in diameter.....	93
Figure 3.5. Experimental demonstration of particle grouping. (a) Six free beads were initially lying on the substrate. (b) Beads 1 to 5 were trapped and separated into three groups. Bead 6 was free and served as the reference of the coverglass movement. (c) The coverglass was move along -y. (d) The laser was switched off and all beads returned to the coverglass. (e) After the laser was turned on, Beads 1 to 5 were separated into three new groups, while Bead 6 remained free. (f) The coverglass was moved along -x. The bead size is 4.74 μm in diameter.	93
Figure 3.6. Experimental demonstration of multiple particles trapped in three dimensions. (a) Six free beads were lying on the coverglass. (b) Beads 1, 2, and 3 were trapped by the 3D trap, and Bead 4 and 5 were trapped by the 2D traps. Bead 6 was free and served as the reference of the coverglass movement. (c) The coverglass was moved along +x, with the trapped beads staying stable. (d)–(e) The objective lens was moved along +z direction. Bead 2 was first brought into focus before Beads 1 and 3 (see the media). Beads 1 and 3 were in focus in (e). (f) The sketch illustrating the images (d) and (e).....	95
Figure 3.7. Simulation results to explain the principles of particle separation. (a) The yz plane force field of F_n (the net force of the optical force, gravity, and buoyancy, excluding the normal forces between the beads and between the beads and the coverglass); (b) free body diagrams of three beads (Beads 1, 2, and 3) at three different vertical levels shown in (a): Level A, B, and C. F_{ni} stands for F_n of Bead i. N_{si} and N_{ij} stand for the normal forces between the substrate (the coverglass) and Bead i and between Beads i and j, respectively.	97

Figure 3.8. The yz plane force field of F_n (the net force of the optical force, gravity, and buoyancy, excluding the normal forces between the beads) in order to explain the principles of particle stacking in three dimensions. Beads 1, 2, and 3 are stacked in three dimensions.	99
Figure 3.9. Diagram of multiple traps obtained from the inclined DFOTs. Inset is the top view of the rod trapped at Location 3.	105
Figure 3.10. Experimental demonstration of trapping and alignment of glass rods. (a) Two free rods were initially lying on the substrate. (b) The two rods were trapped and aligned along the y axis. A third free rod (on the top left side) was moved into the view field serving as a reference. (c) The coverglass was moved along $+y$. The scale bar is $10\ \mu\text{m}$ in length. The rods are $\sim 3.5\ \mu\text{m}$ in diameter, and $8\sim 15\ \mu\text{m}$ in length.	106
Figure 3.11. Experimental demonstration of rotating glass rods. The arrows at the lower right corner indicate the next movement of the coverglass, and the small arrow beside the rod shows the rod orientation. (a)-(b) The rod escaped from the trap when the water was moved fast in $-x$ direction. (b)-(e) The rod was re-trapped and eventually aligned along the x axis, when the water was moved in $+x$ direction. The rod was rotated clockwise by 180° in the above process. (e)-(h) The process of (a)-(e) was repeated with the opposite direction of water movement. The rod was rotated counter-clockwise by 180° . The scale bar is $10\ \mu\text{m}$ in length. The rods are $\sim 3.5\ \mu\text{m}$ in diameter, and $8\sim 15\ \mu\text{m}$ in length.	108
Figure 3.12. Working principle of rod rotation. The arrows at the top left corner indicate the next movement of the water. The two ovals illustrate the spots of the two beams.	109
Figure 3.13. Experimental demonstration of glass rod stacking. (a)-(c) Images of glass rods stacked in different ways. The scale bar is $10\ \mu\text{m}$ in length. (d)-(f) Sketches of the stacked rods corresponding to (a)-(c), respectively. The rods are $3.5\ \mu\text{m}$ in diameter and $8\sim 15\ \mu\text{m}$ in length.	110
Figure 3.14. Experimental demonstration of optical binding of silica beads. The arrows at the lower right corner indicate the next movement of the coverglass. Bead 1 was trapped in 3D. Bead 2 was optically bound to Bead 1, so it was out of focus and not contacting the substrate. Beads 1 and 2 remained in the trapped and bound positions, respectively, when the water was moved in $+y$ ((a)-(b)) and $+x$ ((b)-(c)) directions. The scale bar is $10\ \mu\text{m}$ in length. (d) A sketch of the three beads on the yz plane. The beads are $4.74\ \mu\text{m}$ in diameter.	111
Figure 3.15. Experimental demonstration of optical binding of glass rods. (a) The three free rods lay on the coverglass, and the silica bead was trapped by the right 2D trap. (b) The bead was trapped by the 3D trap. It can be seen that the light beams were refocused by the bead. (c) Rod 1 and 3 were tilted up by the optical binding, while Rod 2 remained free. The optical binding helped Rods 1 and 3 remain stationary while the water was moved in $+x$ ((c)-(d)) and $-y$ ((d)-(e)) directions. The scale bar is $10\ \mu\text{m}$ in length. (f) Sketch shows the optical bound rods on the yz plane. The rods are $\sim 3.5\ \mu\text{m}$ in diameter, and $8\sim 15\ \mu\text{m}$ in length. The silica bead is $3.5\ \mu\text{m}$ in diameter.	112
Figure 3.16. Simulation results of (a) the optical force field and (b) the z -axis optical torque field of a single 2D trap (Trap 3 in Figure 3.9). Each arrow in (a) stands for the optical force applied on a glass rod when the center of the rod is located at the start point of the arrow. The origin of the coordinate system is located at the intersection of the optical beam axis	

and the horizontal plane passing the rod center. The rod is 3.5 μm in diameter, 10 μm in length, and oriented along the y axis. The optical power is 7.65 mW.	115
Figure 3.17. Simulation results of the dependence of the z -axis optical torque on the orientation of a rod. The torque is applied by a single 2D trap (Trap 3 in Figure 3.9). θ is the angle between the rod axis and the y axis, as shown in Figure 3.9. The rod is 3.5 μm in diameter, 10 μm in length at located on the y axis ($x=0$). The optical power is 7.65 mW.	117
Figure 3.18. Simulation results of (a) the optical force field and (b) the z -axis optical torque field of two 2D traps (Traps 2 and 3 in Figure 3.9). Each arrow in (a) stands for the optical force applied on a glass rod when the center of the rod is located at the start point of the arrow. The origin of the coordinate system is located at the center of the line segment connecting the two traps. The intersections of the optical beams and the xy plane are at (0, -4 μm) and (0, 4 μm). The rod is 3.5 μm in diameter, 10 μm in length, and oriented along the y axis. The optical power is 7.65 mW from each fiber.	118
Figure 4.1. One-dimensional focusing using the SP lens on a fused silica substrate. [134].....	128
Figure 4.2. Two-dimensional focusing using the SP lens on a quartz substrate. [137] (a) Topography of the SP lens measured with atomic force microscopy (AFM). (b) Intensity distribution at the focus. (c) Intensity profile of the SP lens on the xz plane.	129
Figure 4.3. Illustration of SP lens fabricated on the endface of an optical fiber.	130
Figure 4.4. Schematic of the principle of a fiber based SP lens.	131
Figure 4.5. Schematic of the experimental arrangement for SP lens testing.	135
Figure 4.6. SEM image of the sample SP1 on a fiber endface.	137
Figure 4.7. Experimentally measured intensity distribution from SP1 on two orthogonal planes: (a) xz plane and (b) yz plane. The origin of the coordinate system is located at the center of the SP lens surface. The optical beam is propagating downwards.	138
Figure 4.8. Experimentally measured intensity profile of SP1 at the strongest intensity position ($z = 3.2\pm 0.1 \mu\text{m}$) along (a) x axis, (b) y axis, and (c) z axis. (d) The image of the focus at $z = 3.2 \mu\text{m}$. The scale bar at the upper right corner of (d) denotes 600 nm (10 pixels).	139
Figure 4.9. SEM image of the sample SP2 on a fiber endface.	140
Figure 4.10. Experimentally measured intensity distribution from SP1 on two orthogonal planes: (a) xz plane and (b) yz plane. The origin of the coordinate system is located at the center of the SP lens surface. The optical beam is propagating downwards.	141
Figure 4.11. Experimentally measured intensity profile at the strongest intensity position ($z = 1.1\pm 0.1 \mu\text{m}$) along (a) x axis, (b) y axis, and (c) z axis. (d) The image of the focus at $z = 1.1 \mu\text{m}$. The scale bar at the upper right corner of (d) denotes 500 nm (10 pixels).	142
Figure 4.12. Components of the electric and magnetic fields in a cubic cell of the Yee's lattice.	149
Figure 4.13. Procedure of FDTD simulations.	151
Figure 4.14. Intensity distribution obtained from the simulations of SP1 on two orthogonal planes: (a) xz plane and (b) yz plane. The origin of the coordinate system is located at the center of the SP lens surface. The optical beam is propagating downwards.	154
Figure 4.15. Intensity profile at the strongest intensity position ($z = 2.42 \mu\text{m}$) along (a) x axis, (b) y axis, and (c) z axis.	155
Figure 4.16. Intensity distribution of SP2 obtained from the simulations on two orthogonal planes: (a) xz plane and (b) yz plane. The origin of the coordinate system is located at the center of the SP lens surface. The optical beam is propagating downwards.	156

Figure 4.17. Intensity profile at the strongest intensity position ($z = 1.47 \mu\text{m}$) along (a) x axis, (b) y axis, and (c) z axis.	158
Figure 4.18. Images showing 3D trapping of a bacterium with SP2. The white arrows point to the bacterium, and the black arrows show the location of a reference silica bead. (a-c) A free bacterium was trapped by the focus created with SP2. (d-f) The bacterium was lifted up in the vertical direction while the focal plane is on the coverglass. (g) The focal plane was brought to the plane where the bacterium is located. In (g-h), the water is moved in the x direction, and in (h-i), the water is moved in the y direction with the bacterium remaining trapped. The optical power measured outside the SP lens was 0.91 mW.	163
Figure 4.19. An electric dipole.	171
Figure 4.20. Comparison of results obtained with both HA and CN models. (a) The x -axis transverse force versus the x position for the bead coordinates of $y=0$ and $z=0$. (b) The z -axis longitudinal force versus the z position along the optical axis ($x=0$ and $y=0$). The diamond data points are the results provided in ref. [163].	183
Figure 4.21. Dependence of the x -axis escape force on the particle size. The escape force is determined by the maximum x -axis force with the particle coordinates of $y=0$ and $z=0$. The diamond data points are the results provided in ref. [155].	185
Figure 4.22. Dependence of the z -axis restoring force on the particle size. Here the forces indicate the maximum restoring forces (or minimum scattering forces). The optical wave is propagating along $+z$ direction. A 3D trap is possible only when there exists a negative restoring force.	187
Figure 4.23. Dependence of the x -axis escape force on the beam waist. The optical power is 1 W. The particle is a sphere with a refractive index of $n_s=1.38$. The results of three particle sizes are obtained, $a=50$ nm, 100 nm, and 150 nm.	188
Figure 4.24. Dependence of the z -axis restoring force on the beam waist. The negative z -axis force is a restoring force that enables a 3D trap. The optical power is 1 W. The particle is a sphere with a refractive index of $n_s=1.38$ and a radius of $a=50$ nm, 75 nm, or 100 nm.	189
Figure 4.25. Dependence of the x -axis escape force on the refractive index. The optical power is 1 W and the beam waist is $0.44 \mu\text{m}$. The particle is a sphere with a radius of $a=50$, 75, or 100 nm.	190
Figure 4.26. Force mapping in the (a) xz and (b) yz planes of SP1. The optical power is 1 W and the wavelength is $0.808 \mu\text{m}$. The particle is a sphere with a radius of $a=100$ nm and a refractive index of 1.38.	192
Figure 4.27. Optical forces along three orthogonal directions for SP1. (a) x -axis optical force versus the x displacement for $y=0$ and $z=3.2 \mu\text{m}$. (b) y -axis optical force versus the y displacement for $x=0$ and $z=3.2 \mu\text{m}$. (c) z -axis optical force versus the z displacement for $x=0$ and $y=0$. The forces are calculated according to the intensity profile measured in the experiment. The optical power is 1 W and the wavelength is $0.808 \mu\text{m}$. The particle is a sphere with a radius of $a=100$ nm and a refractive index of 1.38.	193
Figure 4.28. Force mapping in the (a) xz and (b) yz planes of the SP 2. The optical power is 1 W and the wavelength is $0.808 \mu\text{m}$. The particle is a sphere with a radius of $a=100$ nm and a refractive index of 1.38.	194
Figure 4.29. Optical forces along three orthogonal directions for SP2. (a) x -axis optical force versus the x displacement for $y=0$ and $z=1.1 \mu\text{m}$. (b) y -axis optical force versus the y displacement for $x=0$ and $z=1.1 \mu\text{m}$. (c) z -axis optical force versus the z displacement for $x=0$ and $y=0$. The forces are calculated according to the intensity profile measured in the	

experiment. The optical power is 1 W and the wavelength is 0.808 μm . The particle is a sphere with a radius of $a=100$ nm and a refractive index of 1.38..... 195

List of Tables

Table 2.1. Spring constants obtained with beads of different sizes.....	61
Table 4.1. Design parameters of 4-slit SP lens.....	134
Table 4.2. Design parameters of 3-slit SP lens.....	134
Table 4.3. Spot sizes (FWHMs) of SP1 and SP2.	158
Table 4.4. Maximum forces of SP1 and SP2.	196
Table 4.5. Comparisons of optical forces obtained using the fiber-based SP lens and the tapered fiber lens.	198

Chapter 1. Introduction and Background

Single-beam optical trapping, also referred to as optical tweezers, is a technique that uses a tightly focused laser beam to trap or rotate micrometer-sized particles. [1] To be precise, any kind of optical forces resulting from inhomogeneous optical fields can be called optical trapping. In this dissertation, a distinction is not made between optical trapping and optical tweezers, and by either one the author refers to the application of optical forces to manipulate or sort particles and to sense forces or displacements.

1.1. Problem of interest

In biology and in physics, there has been a common interest in single molecules and particles with sizes ranging from 1 nm to 1 μm [2]. The forces and strains induced by biological molecular motors are in the range of picoNewtons (pN). To measure these forces and manipulate the particles in these ranges, appropriate tools are needed [3]. The tools currently used for single molecular manipulation include optical tweezers, magnetic tweezers, and atomic force microscopes (AFMs) [2, 3, 4]. Magnetic tweezers can normally apply forces up to 10 pN, while an AFM works better when forces are above tens of pN [3, 4]. Compared to magnetic tweezers and AFMs, the forces of optical tweezers range from 0.1 pN to 100 pN, which covers a broader range of forces [3]. Furthermore, most biomolecules have no magnetic susceptibility [3], and thus a magnetic bead is always necessary when magnetic tweezers are used. Therefore, magnetic tweezers become inapplicable when attaching beads is not possible (e.g., manipulation of

organelles inside a cell). However, optical tweezers are readily applicable to such applications [5, 6]. In addition, the stiffness of optical tweezers can be 1000 times smaller than that exhibited in an AFM [3], and this can help optical tweezers realize better resolution for force measurements and displacement measurements (with nanometer resolution [7] or even Angstrom resolution [8]).

Optical tweezers are routinely applied in studies of molecular motors and mechanoenzymes at the single-molecule level [1], colloidal physics, and mechanical properties of polymers [9]. As a unique tool, optical tweezers have helped to achieve an improved understanding of many problems in physics and biology; for example, the attractive force between like-charged particles [10] and base-pair stepping of the RNA polymerase during transcription [8]. Currently, most of optical tweezers are based on objective lenses due to their technical maturity and diffractive-limit focus quality [1, 7, 11, 12, 13]. In combination with three-dimensional piezoelectric stages, high resolutions of force-displacement measurements and better force control are realized [7]. With the help of holograms and other types of diffractive optics, one can generate up to 400 controllable multiple traps [14, 15].

Despite the abovementioned attractive features, the main problem with objective-based optical tweezers is that compared with the size of a typical MEMS device, there has to be a huge objective lens to achieve a sharp focus. This eliminates the possibility to integrate an optical trapping system into a small system. In addition, many practical issues have to be taken care of relative to the objective lens, such as, thickness and transparency of the substrate, working distance [16, 17], spherical aberrations [18], and so on. Other problems arise from the external free-space optics used before the laser is coupled into the objective. Besides precise alignment

and the large space needed, the free-space optics has to be enclosed and protected in a gas like helium environment [8] to isolate the environmental disturbances, especially, when high precision is needed [7]. These issues may not be so harmful when a large passive air table in a well controlled laboratory environment is available [7], but it is a different story when the space is limited, especially when the system is to be miniaturized. Interest is increasing in scaled down analytical processes, which can be used to perform laboratory operations on a miniature device (lab-on-a-chip) [19]. The chip-based methods can reduce reagent costs, amount of chemical waste, and the time needed to synthesize and analyze a product. Optical tweezers have been proposed to combine with lab-on-a-chip formats for future individual molecule studies, but integrating the optical tweezers into chip-based systems needs a lot of further efforts [20].

Fiber optical tweezers provide a reasonable solution to the problem of integration with a lab-on-a-chip system. An optical fiber is flexible and small in size. With the fiber serving as a good waveguide, free optics and large objectives can be eliminated from the optical trapping system. In addition, an optical fiber is inexpensive, biocompatible, mechanically robust, free of electromagnetic interference [21], and most importantly, compatible with Micro-Electro-Mechanical Systems (MEMS) technology [22]. However, fiber optical tweezers are far from having been extensively investigated as compared with objective-based optical tweezers. Most of current fiber optical tweezers employ two well aligned opposite fibers fixed in the substrate, with which the flexibility of fibers is actually limited. Moreover, this kind of configuration cannot be used to pick up microscale particles lying on the substrate. Other configurations that make use of two inclined fibers can be used to pick up particles lying on the substrate, but no experimental calibrations of these configurations have been carried out. Another issue that deserves attention

is that an optical fiber cannot achieve a sharp focus as objective-based optical tweezers; so, the trapping efficiency is not as strong. Currently, it remains a challenge to achieve a sharp focus, and hence, a large gradient force with fiber optical tweezers.

1.2. Review of previous work

1.2.1. Basic optics

When an optical beam is incident on an interface, typically the surface of the trapped object, the beam is deflected due to reflection and/or refraction. The deflection of the beam induces changes to the photon momentum that the beam carries, and these momentum changes cause optical forces to be applied to the trapped object. It is noted that the momentum of the photons may be increased or decreased, depending on the beam intensity distribution; the optical forces may be either along or opposite to the direction of the incident photons. The optical forces can be classified into two types, the scattering force and the gradient force [1], as shown in Figure 1.1. The scattering force results from the reflection, scattering, and absorption of incident photons, and it is always along the direction of optical beam propagation. The gradient force is along the gradient direction of the optical field, and it pulls the object towards the position of the highest intensity. An optical trap is essentially an optical field that can apply optical forces on the particles located in the field and, therefore, confine the positions of particles, as if the particles are “trapped” by the optical field. A three-dimensional (3D) optical trap has an equilibrium position so that any displacement from this position will result in a restoring force, just like a

spring but in three dimensions. To realize a stable 3D optical trap with a single optical beam, the beam needs to be focused tightly to achieve a large optical field gradient; this gradient allows one to have a strong enough gradient force to prevent the object from being pushed away along the optical beam due to the scattering force. In addition, to enable the trap, the size of the trapped object should be small enough, since the optical force is on the order of picoNewtons (10^{-12} N).

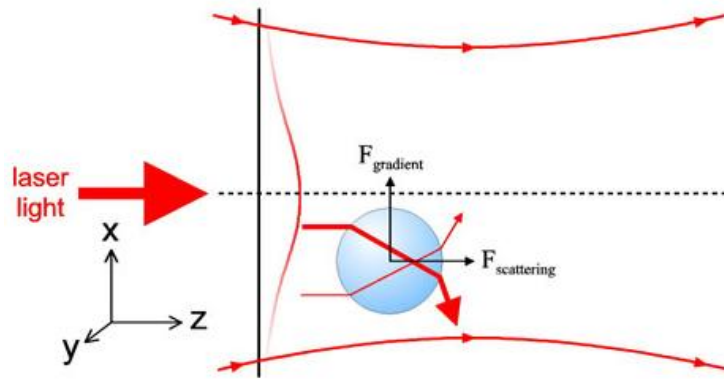


Figure 1.1. Scattering and gradient forces of optical tweezers. [23]

In the ray optics regime (or Mie regime), where the particle size (a) is much larger than the wavelength of light (λ) ($a > 10\lambda$), the scattering force can be viewed as the result of scattering (reflection) and absorption [1, 7]. The light is incident on the particle surface and is randomly scattered (including reflected) in a variety of directions with absorption. Since the absorbed photons and the scattered photons have directions opposite to that of the beam propagation, their momentum along the propagation direction reduces and the net momentum that the particle gains from these photons is along the propagation direction; that is, the particle is pushed down by the optical beam. This is easy to understand if the laser beam is considered as a stream of photons with momentum. The collision of the photons with the particle will transfer photon momentum

to the particle and push it along the beam, which is referred to as “radiation pressure”. For the gradient force, its origin is due to refraction. If a particle has a higher refractive index than the surrounding medium and the beam is incident from the medium, the refraction light leans towards the normal direction of the surface, and hence, the refracted photons gain momentum. Therefore, the particle is always pushed towards the beam by the refraction. As shown in Figure 1.1, if there is a gradient in the optical field, a stronger light beam will induce a larger force on the particle than a weaker beam. The net force due to the refractions of these two beams will attract the particle towards the strongest intensity position; the gradient force generates [11].

In the Rayleigh regime, where the particle size is much smaller than the laser wavelength ($a < 0.1\lambda$), the particle can be treated as a point electric dipole, which is induced by the external optical field [7, 11, 24]. It should be noted that the induced dipole momentum is oscillating because the external optical field is oscillating. In this case, the scattering force is due to the absorption and re-radiation of the optical field by the dipole. Moreover, a dipole in an inhomogeneous electric field experiences another force in the direction of the field gradient; this is the gradient force. The gradient force is proportional to both the beam gradient and the polarizability of the dielectric (i.e., how easily the dipole can be induced). It should be emphasized that although the dipole momentum is oscillating in both magnitude and sign, the induced dipole momentum remains harmonic with respect to the external optical field. This makes the sign of the gradient force invariant with time and results in a time-averaged constant gradient force instead of zero.

When the particle size is comparable with the wavelength ($a \sim \lambda$), neither the ray optics nor Rayleigh approximation is valid [7]. Further development of electromagnetic theory is needed for the optical trapping that falls in this regime. However, most useful or interesting trapping in biological research is within this size range ($0.1\lambda \sim 10\lambda$). For example, bacteria [25], yeast cells [26], and organelles inside cells [5, 6] all lie in this size range. The dielectric microspheres used as handles when studying biological cells and molecules are also in the range of $0.2 \sim 5 \mu\text{m}$ [7]. With these considerations, calibration of optical tweezers is always necessary, and this calibration cannot be replaced by modeling and simulations.

1.2.2. Optical tweezers based on microscope objectives

1.2.2.1. Basic experimental arrangement

A basic objective-based optical tweezers is shown in Figure 1.2. The essential elements include a laser system, steering optics, a dichroic mirror, the sample cell, and a microscope with a high numerical aperture (NA) objective [7].

- a) The laser system contains a laser source and a beam expander. Either free space lasers [5, 24, 25, 26] or fiber-coupled laser diodes [27] can be used to build the optical tweezers. For single-beam optical tweezers, the gradient forces must be large enough to overcome the scattering forces. The gradient force, to a good approximation, is proportional to the spatial intensity gradient [28]. This explains the necessity for two components of the system: i) the high NA objective to achieve a small focus, and hence, a steep gradient and ii) the beam

expander to allow the laser to overfill the back aperture of the objective. The wavelength of the optical tweezers needs to be chosen with considerations of possible optical damage and heating. For optical trapping of biological materials, the relative transparent wavelengths are between 750 nm and 1200 nm [7]. For *Escherichia coli* cells, the optical damage is minimized at 970 nm and 830 nm.

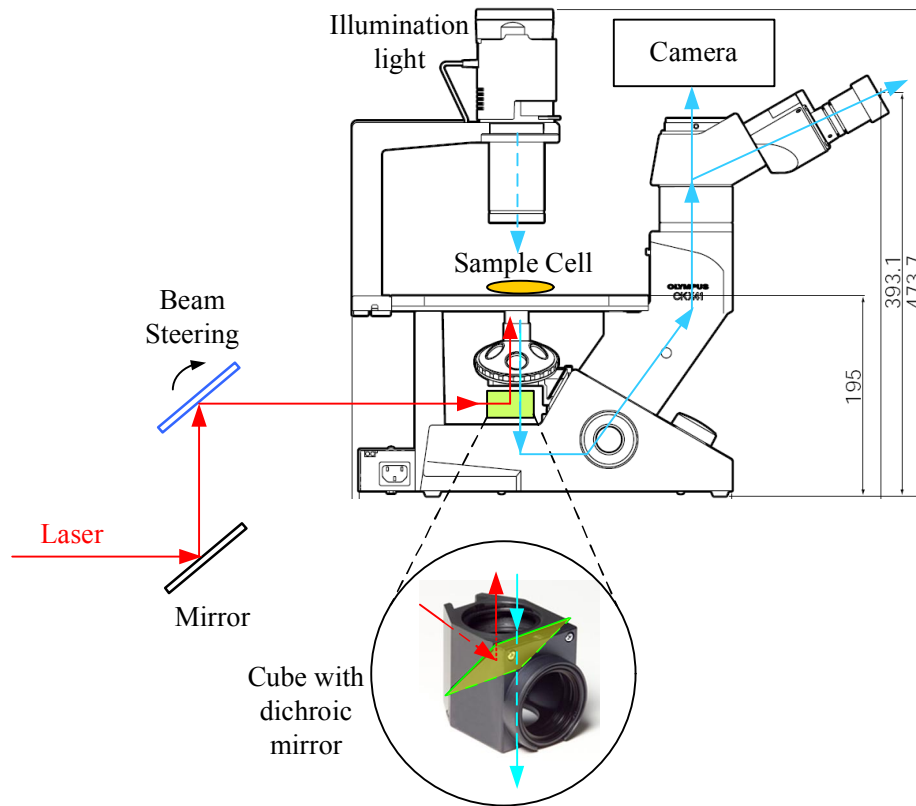


Figure 1.2. Basic experimental setup of objective-based optical tweezers. The dimensional sketch of the microscope is reprinted from the CKX41 Brochure [29].

- b) Steering optical systems are used to move the optical traps relative to the sample chamber. Moreover, a steering optical system allows for a dynamic control of the position and the stiffness of the trap. This control system can enable both force and position clamps for the measurement conditions. Also, a scanning optical trap can generate multiple traps if the

scanning speed is faster than the Brownian relaxation time of the trapped particles. Typical strategies for beam steering include scanning mirrors, acousto-optic deflectors, electro-optic deflectors, and piezoelectric stages [7].

- c) A dichroic mirror is a filter that selectively allows for the transmission of a range of wavelengths while reflecting other wavelengths. The dichroic mirror couples the laser beam upwards into the objective to form an optical trap, and filters out the downward laser beam reflected from the trapped particles and from the surfaces of the objective and coverglass. This helps prevent the reflected laser coupling into the oculars or the CCD camera, which can dazzle the field of view.

If more complex dynamics of the trapped particles are required, other beam controlling components can be added into the beam path, such as wave plates [27], spatial light modulators [26], and diffractive optical elements [15].

1.2.2.2. Current state-of-the-art of optical tweezers based on objective lenses

Evolution of optical tweezers based on objective lenses

Photons carry no mass but they carry momentum. One can intuitively think of the possibility that the momentum carried by photons can be transferred to objects, which is manifested as forces applied to the objects of interest. It was Mr. Arthur Ashkin at AT&T Bell Labs in the US, who pioneered optical tweezers. He found that optical forces were able to significantly affect the dynamics of small particles, and further built the first stable 3D optical trap with two counter-

propagating Gaussian beams (shown in Figure 1.3(a)) in 1970 [1]. The particles dispersed in water were $2.68\ \mu\text{m}$ in diameter, and the laser power was 128 mW [30]. One year later, Ashkin and his co-workers built an optical levitation device (shown in Figure 1.3(b)), in which the radiation pressure from a single vertical beam is employed to balance the gravity of the particle. The experiment was carried out in air. Since the damping coefficient was much smaller in air than in water, a feedback scheme was needed to damp particle oscillations caused by beam fluctuations.

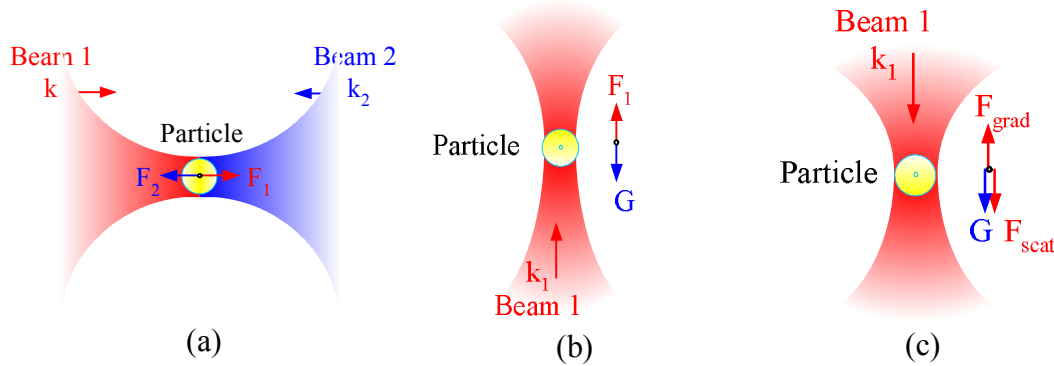


Figure 1.3. Evolution of optical trapping. (a) Optical trapping with two counter-propagating beams (1970). Equilibrium between the radiation pressures of the two beams. (b) Optical levitation built with a low NA objective (1971). Equilibrium between the gravity force and the radiation pressure. (c) Stable 3D single beam trapping built from a tightly focused beam with a high NA objective. Equilibrium between the scattering force (radiation pressure) and the gradient force (1986).

In the two optical traps introduced previously, trapped particles reached equilibrium either by balancing the optical pressures from the counter-propagating beams, or by being pushed upwards against gravity. Neither case is surprising since the existence of radiation pressure has been known for a long time. However, during the experiments, Ashkin and his co-workers found that the particles off the beam axis were dragged into the axis and then accelerated along the axis

under the radiation pressure [1]. This observation means that there exists a transverse optical force component other than the radiation pressure (scattering force) along the beam axis. They came to realize that this transverse optical force rose from the gradient of the optical field. Based on this finding, it was proposed that atoms could be trapped analogously.

The first single-beam optical tweezers for micron-sized particles were built by Ashkin *et al.* in 1986 [31], somewhat accidentally [1]. The single beam optical tweezers were originally intended for atom cooling and trapping, which succeeded in 1985 [32]. Steve Chu, also from AT&T Bell Labs, was awarded the 1997 Nobel Prize in physics for inventing the single beam atom trapping. At a time of temporary difficulty in atom trapping, it was decided to test the single beam trapping on submicron Rayleigh particles instead of atoms, and it turned out to work well. It was demonstrated later that it also worked with micron-sized particles. Single-beam optical tweezers use a tightly focused Gaussian beam to generate a large gradient on-axis, as shown in Figure 1.3(c). It is counter-intuitive at first sight, since the optical beam pulls the particle back when the trapped particle tries to move down the beam axis. Only tightly focused beams can achieve strong enough on-axis gradient forces to overcome scattering forces. Therefore, most existing optical tweezers based on microscope objectives require high numerical aperture (NA) objectives. Researchers have found out that the single-beam optical trapping was not difficult to construct and that it is helpful and efficient to perform manipulation and force/position sensing in micro-scales and nano-scales; and it has become an important and even a routine technique in some physical and biological studies [1, 7, 11, 12, 13].

Ashkin pointed out in 1986 that optical trapping would be used for studies of macromolecules, colloids, small aerosols, and biological particles [31], and this is exactly what researchers were working on in the last two decades [11]. Some of the research conducted on the use of objective-based optical tweezers is reviewed next.

Optical trapping of low-index particles

It is well known that a highly focused optical beam serves as a 3D potential well for particles that have a higher refractive index than that of the surrounding medium [33]. On the other hand, the particles with a low refractive index are always repelled from the focus of a TEM₀₀ laser beam and these particles are thus pushed to the position of lowest intensity [5]. The ability to trap particles with a low refractive index will enable manipulation of bubbles and droplets so that the properties and evolution of the bubbles can be investigated [34]. This is also of great interest to biologists because some organelles in cells, such as vacuoles, are also low-index particles relative to the surrounding medium. Furthermore, the optically trapped aqueous droplets can provide a micrometer-size container for single molecule studies in biology [35]. This container can confine a single molecule inside the detection volume, and yet allow the molecule to freely diffuse for a substantial period of time. In addition, hollow glass spheres can also be used as laser fusion targets [1].

According to the work of Gahagan *et al.* [36], a 3D potential well also exists for the particles with lower refractive index compared to the surrounding medium if the laser beam with an optical vortex is used, as shown in Figure 1.4. In this manner, the low-index particles are actually trapped by an optical bubble, which is the dark region surrounded by the optical field. A similar

optical bubble created by the interference between two plane waves can also produce a two-dimensional trap for low-index particles, as shown in Figure 1.5 [34]. However, if the low-index particles are out of the dark region, there is no way for the optical force to pull it back, unless one uses other effects of the beam such as thermal effects. More recently, Ivanova *et al.* [37] used an absorbing liquid as the surrounding medium, so that the thermocapillary forces, which are dependent on the temperature gradient due to the laser beam heating, can drag a gas bubble outside the laser caustic to the trapping position.

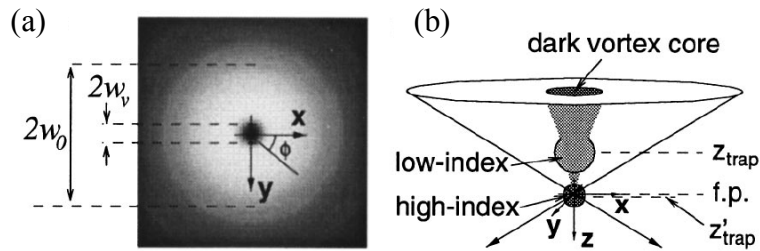


Figure 1.4. (a) Intensity profile of the focus of a Gaussian beam (w_0 is the beam size) with an optical vortex (w_v is the vortex size) and (b) different trapping location of the particles with high-index and low-index [36].

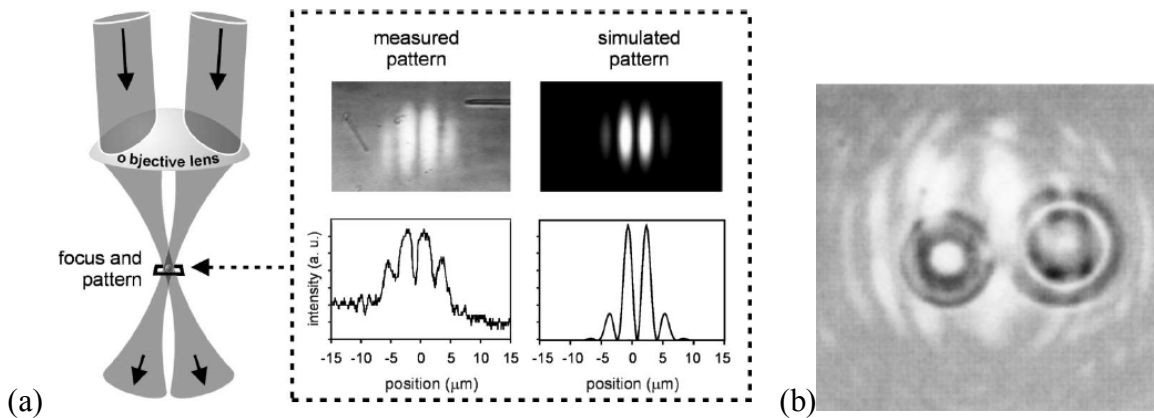


Figure 1.5. (a) Interference of two beams (left) and the interference pattern (right) and (b) two hollow spheres trapped by the interference pattern [34].

Optical trapping with holographic optical fields and special laser beams

Holograms have been used to generate complex, high-order optical trapping systems [7, 14, 15, 38]. Dufresne *et al.* [15] first presented a holographic optical tweezers system in 2001. A diffractive optical element (DOE) was placed in a plane optically conjugated to the back aperture of the objective. Thus, the pattern generated on the DOE will be Fourier transformed to the focal plane. In this case, multiple traps can be generated and controlled independently. 400 traps were generated with these holographic optical tweezers. Holographic optical tweezers have also been used to sort particles and realize complex 3D motion control of multiple particles [14, 38, 101]. These 3D patterns created with the trapped particles are artificial crystalline structures with controllable material properties. [101] In addition to a holographic optical field, Bessel beams can also be used for optical tweezers [39, 40]. As a beam with a tightly confined size, Bessel beams have been used either to stack multiple beads or align rod-shaped particles [40]. Laguerre-Gaussian (LG) beam is a beam with helical wavefront, and this beam has been used to trap and rotate multiple particles. [41, 42]

Optical trapping of nonspherical particles and micromachined particles

Particles with different shapes have been experimentally trapped and rotated with optical tweezers. Gauthier optically trapped glass cylinders with inclined end-surfaces, with the cylinders' axes aligned along the optical axis [43]. Rotation of the trapped glass cylinders was observed, as shown in Figure 1.6.

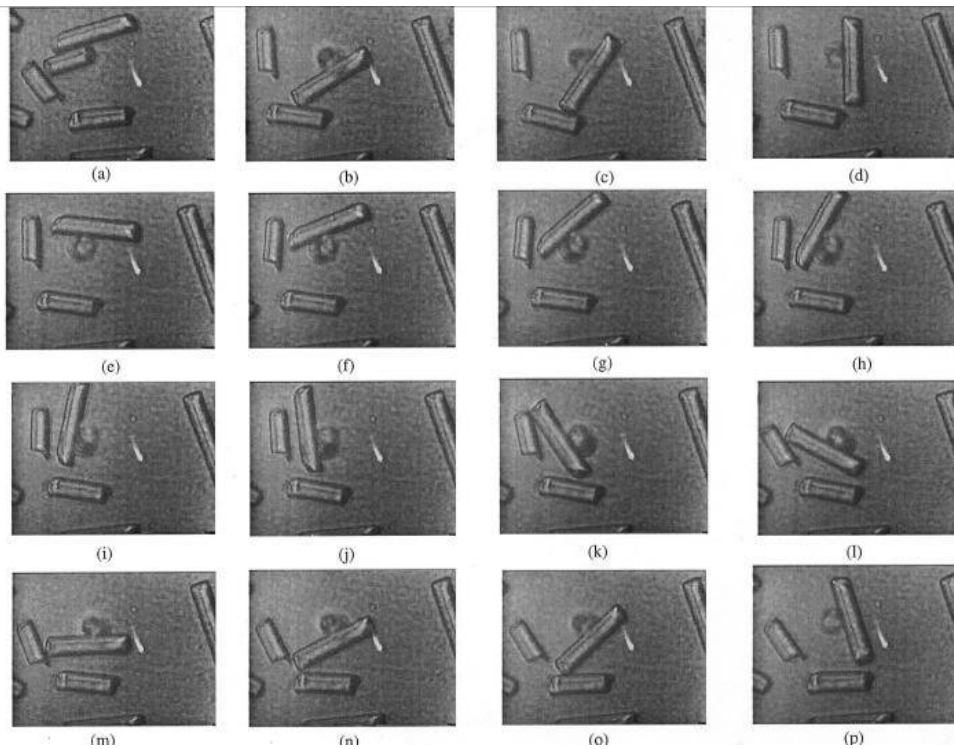


Figure 1.6. (a) Glass cylinders before trapping and (b)-(p) trapped glass cylinders with axis aligned with the optical axis (perpendicular to the paper surface) rotates while being dragged along a larger cylinder. [43].

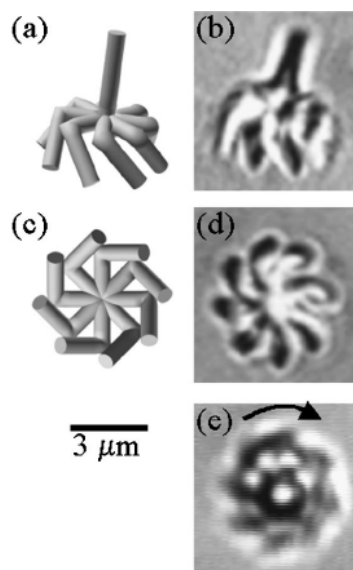


Figure 1.7. A complex-shaped mirror rotor fabricated and rotated by optical tweezers. [46]

Micromachines have also been optically trapped and rotated by optical tweezers [44, 45]. A microrotor with complex shape was fabricated with two-photon excitation in optical tweezers, and then optically trapped and rotated, as shown in Figure 1.7 [46].

Optical trapping of living cells

Optical trapping can be used to apply remotely controlled forces to living cells, internal parts of cells, and large biological molecules without inducing detectable optical damages [12]. This makes it an ideal tool for manipulation and sensing of biological particles in their naturally living conditions.

Right after the single beam optical trap, or a system of optical tweezers, was invented in 1986 [47], it was used to trap biological cells, such as viruses and bacteria that are readily available. The first biological application was demonstrated by Ashkin *et al.* [48], the inventor of the optical tweezers in 1987. The viruses and bacteria were trapped by using a 514.5 nm laser. Because of the absorption and heating of the laser, the death of the bacteria due to the laser posed a problem. Later in 1987, they changed the light source to a 1.06 μm infrared laser in order to decrease the absorption of the laser [49]. In this case, the trapped cells were alive for a long time and the reproduction of the bacteria was even observed within the trap. Currently, the optical tweezers have been used to study cell motions (e.g. [25, 50, 51, 52]) and measure cell properties, such as mechanical properties of cell membranes [50, 53]. Some of the recent work on optical trapped cells is discussed in what follows.

Some illness may cause cells to function differently from normal cells. Dharmadhikari *et al.* showed that Plasmodium malaria infected red blood cells (iRBCs) rotated within the optical trap built with a linearly polarized laser, while normal red blood cells (RBCs) did not [50]. The rotations of the trapped iRBC are shown in Figure 1.8. When trapped, both the normal RBCs and iRBCs were folded to a rod-like cylinder. IRBCs rotated with a speed of 19-300 rpm. The rotation direction of trapped iRBCs changed when the focus of the laser beam moved from under to above the cells, but the rotation speed remained the same if the laser power did not change. The reason why iRBCs rotated was believed to be the gradients of K^+ , Na^+ , and Ca^{2+} around the diseased cell, which were generated due to altered ion transportation caused by the disease. These ion gradients increase the anisotropy of the polarization tensor for iRBCs, which affects the anisotropy of the induced dipole moment and induces a rotational motion.

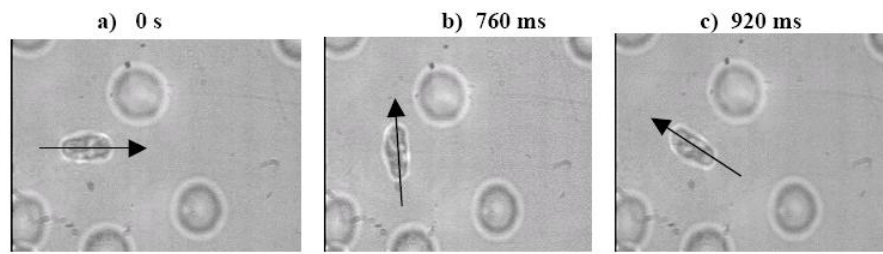


Figure 1.8. Rotation of the Plasmodium infected red blood cells [50].

Another work that was carried out to induce large deformation in human RBCs with optical tweezers is shown in Figure 1.9 [53]. Two silica beads of $4.12 \mu\text{m}$ in diameter were attached diametrically onto the cell surface, to serve as handles. One of the beads was fixed to the glass surface. A 1064 nm laser with a power of 1.5 W was used to trap the free bead and to apply stretching forces to the cell. The mechanical responses of the cell during loading and after release of the optical force were analyzed to obtain the elastic properties of the cell membrane.

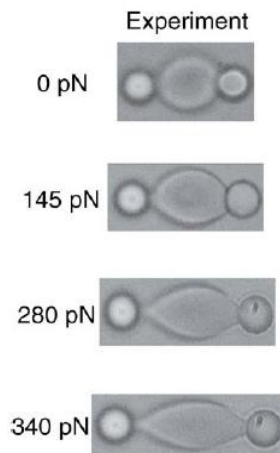


Figure 1.9. Large deformation of the stretched RBC. The values shown on the left are the measured optical forces applied to stretch the RBC [53].

In addition, optical tweezers have also been used in other work related to living cells, including orientation control of cells by controlling polarization of the trapping beam [51], trapping and damage evaluation of cells with a femtosecond laser [52] and study of the influence of confinement on the growth of a yeast cell [26].

Optical trapping of subcellular structures

Optical tweezers have been employed to trap subcellular structures such as cytoskeletons and cell membranes. [54-57] Murdock *et al.* [54] used optical tweezers to find that the drug effect of chlorpromazine on the mechanical properties of a mammalian outer hair cell is the plasma membrane-cytoskeleton interaction. Tolic-Norrelykke *et al.* [55] investigated the viscoelastic properties of the cytoplasm and the contribution of the cytoskeleton to those properties by optically trapping small lipid granules embedded in the cytoskeleton. Balland *et al.* [56] applied oscillating forces to the cytoskeleton of C2 myoblasts, and found that the actomyosin activity appears as an essential mechanism making the cytoskeleton more rigid and more dissipative.

Titushkin *et al.* [57] measured the membrane mechanics of human mesenchymal stem cells (MSCs) and fibroblasts by extracting tethers from the outer cell membrane with optical trapped beads. They found that the fibroblasts use two mechanisms, membrane stiffness and membrane-cytoskeleton interactions, for membrane regulation, while MSCs only use the former mechanism and have weak membrane-cytoskeleton interaction. Nishizaka *et al.* [58] used optically trapped beads to examine the position dependence of binding and release cycle of fibronectin-integrin-cytoskeleton interactions.

Currently objective-based optical tweezers plays a major role in single-particle studies in physics and biology, and they have been thoroughly investigated. [1] Briefly, the most important advantage of optical tweezers that distinguishes them from other nano-manipulation methods, such as atomic force microscopes (AFM), is that they interfere with the trapped particles much less (non-contact manipulation except for the attached bead) while allowing one to perform high-resolution measurements at the same time. One can manipulate a free particle in its natural existing state while performing high-resolution measurements. This is extremely important especially for the study of single molecules in biology (such as DNA and RNA) and colloidal systems in physics. [7] One example is the direct observation of single base pair stepping by RNA polymerase during transcription, facilitated by optical tweezers with Angstrom resolution. [8]

1.2.2.3. Limitations of objective-based optical tweezers

In most of the current research, objective-based optical tweezers are used due to their technical maturity and good focus quality. However, objective-based optical tweezers have some disadvantages, which limit their applications. The limitations of objective-based optical tweezers include the following:

i). High costs make commercial optical tweezers unaffordable.

Some optical tweezers systems are commercially available. In 2000, the price of the basic *Laser Tweezers Workstation* was \$56,000, excluding a microscope, which is necessary for monitoring and imaging. Its motorized stage only has a resolution of approximately 200 nm. A company in Chicago, Arrayx, Inc., manufactures the “BioRyx 200” system that can steer up to 200 optical traps independently. The minimum incremental motion of a trap is approximately 20 nm. However, this system cost \$377,500 in 2004 [59]. Most of the commercial optical trapping systems run between \$100,000 and \$350,000 in 2009. [60] The high cost limits the availability and application of objective-based optical tweezers both in lab and in industry.

ii). Large sizes make objective-based optical tweezers hard to integrate.

Objective-based optical tweezers require a free-space laser to be focused by a high NA objective. The high NA objective measures tens of millimeters, both in diameter and in length. The reason for this large size is that the high NA objective needs a set of carefully designed and positioned lenses to remove optical aberrations [61]. The free-space optical system and the beam steering system require even more space. The steering laser system includes a number of (at least 1 for the very basic setup, see section 1.2.2.1 for details) reflection mirrors and an additional scanning mirror so that the system can steer at least hundreds of millimeters. If one wants to perform more

complex dynamic particle trapping, further beam controlling components are necessary, such as wave plates [27], spatial light modulators [26], and diffractive optical elements [15]; each of them has a size of tens to hundreds of millimeters. The large size makes it difficult to integrate objective-based optical tweezers with the emerging lab-on-a-chip systems. This is a barrier for its wide-scale application, since the objects one needs to deal with are in the micrometer scale or nanometer scale.

iii). *Objective-based optical tweezers are not “robust” to environmental fluctuations.*

Free-space optics needs a well controlled environment to achieve best focus quality. A lot of issues might influence the free-space optics, such as varying temperature and humidity, air flow, particle density in air, and vibration of mirrors or other nominally stationary components [7]. For example, random air currents can introduce air density fluctuations that can perturb the position of a laser beam. These disturbances will increase the aberration of focusing, and degrade the trapping performance. In order to eliminate these influences, objective-based optical tweezers need to be used in a clean and protected environment, which adds another restriction to their working conditions.

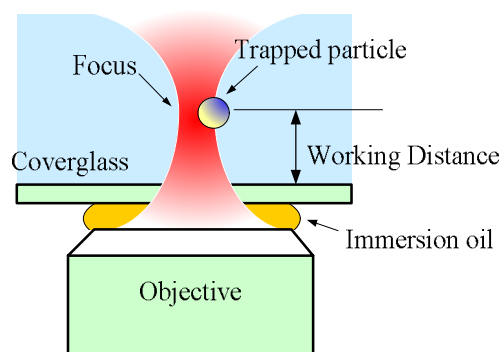


Figure 1.10. Limited working distance of objective-based optical tweezers.

iv). *Objective-based optical tweezers have limited working distances.*

Currently, high NA water immersion lenses are not widely used for optical tweezers. Most optical tweezers still use oil immersion objectives, as shown in Figure 1.10. The mismatch between the refractive indices of oil (~ 1.55) and water (1.33) causes spherical aberration, which becomes even worse as the focal depth increases. This aberration smears out the focus and causes instability and stiffness decrease of the optical trap [18]. As a result, optical tweezers using an oil immersion objective have a working distance limited within a couple of tens micrometers from the cover-glass surface [16]. Even though water immersion objectives are used, the working distance is still limited to several hundreds of micrometers from the cover-glass surface, due to its high NA. To the best of our knowledge, the longest working distance that has been achieved is $220\ \mu\text{m}$ [17]. If one wants to use optical tweezers to assemble a micromachined gear to a position $500\ \mu\text{m}$ away from the coverglass, it is currently impossible with a high NA objective unless one switches to a low NA objective [62] or adds another objective to build up a counter-propagation optical tweezers [33]. However, with a low NA, one cannot achieve a stable 3D trap, while using two objectives makes the system even more complex.

v). *Objective-based optical tweezers require a clean, glass substrate to obtain good focus.*

First, a transparent substrate is needed for the laser to pass through in order to obtain a focus on the other side. Second, the oil-immersion objective is designed to work with oil between the front lens and the coverglass [63]. If a substrate with a refractive index different from that of glass, spherical aberration will be induced, as discussed above in iii). Therefore, only glass (or materials with the same refractive index) can be used in order to get a good-quality trap, although glass may not be the most

preferred substrate for other components. For example, silicon is a commonly used substrate for fabricating microfluidic channels [41]. At the wavelength between 780 nm and 1330 nm, silicon has a refractive index between 3.5 and 3.7 [64], which is different by more than a factor of 2 from the refractive index of glass (~ 1.5). Due to the large refractive index difference between silicon and glass, optical tweezers with a wavelength within this range does not work well in a microfluidic system with a silicon substrate although most optical tweezers use wavelengths in this range due to the minimal optical damage to biological specimens [7]. Moreover, the substrate should be clean enough to allow the laser beam to pass without significant distortion. Apparently the possibility of using objective-based optical tweezers *in vivo* practically diminishes due to the requirement of a clean glass substrate.

1.2.3. Fiber optical tweezers

1.2.3.1. Advantages of optical fiber trapping systems

Despite the above disadvantages, objective-based optical tweezers still play a very important role in today's research. However, fiber optical tweezers can resolve or potentially address the aforementioned problems associated with objective-based optical tweezers. It has been widely accepted that optical fibers are biocompatible, mechanically robust, and free of electromagnetic interference [21]. Some of the advantages of fiber optical tweezers are summarized as follows.

- i). Fiber optical tweezers are inexpensive.*

The use of optical fibers greatly simplifies the optical trapping system. Optical fibers are inexpensive compared to the high quality mirrors and lenses required by objective-based optical tweezers. In an optical fiber tweezers system, the expensive and bulky beam steering system of objective-based optical tweezers can be replaced with micromachined actuators or fiber optic intensity/phase modulators. Fiber optical tweezers are thus much less expensive compared to objective-based optical tweezers.

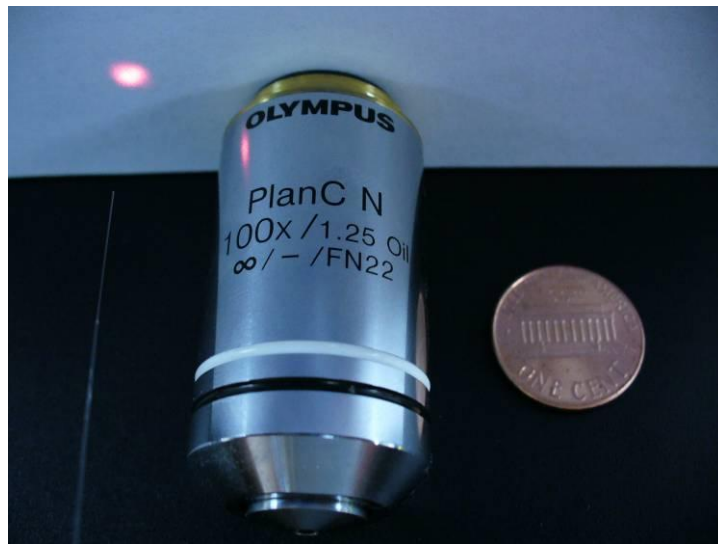


Figure 1.11. The optical fiber (left) is much smaller than the objective (middle) and readily to be integrated.

ii). *Fiber optical tweezers can be readily integrated with MEMS systems.*

Optical fibers are compatible with MEMS devices, since the diameters of optical fibers have similar geometrical scale as MEMS devices [22]. Optical fiber tweezers need only optical fibers with a 125 μm diameter to work with instead of objectives with diameters of tens of millimeters. In Figure 1.11, the comparison of an optical fiber to a microscope objective is shown. In addition, optical fibers serve as additional spatial filters to ensure a good spatial mode (TEM_{00}) quality. In this case, all the free

space optical components including mirrors, lenses, and spatial light filters can be removed from the optical trapping system, which results in much less cost as well as smaller size of the trapping system.

iii). *Fiber optical tweezers are much less sensitive to environmental disturbance.*

An optical fiber serves as a good waveguide protected by a polymer coating. It effectively reduces the noise induced by environmental disturbances such as humidity, temperature variation, and air flow. The mirrors in objective-based optical tweezers however suffer from the noise due to acoustic noise and mechanical vibration of the optical mounts [7]. This feature allows fiber optical tweezers to be more compliant with working conditions. For example, the optical stretcher based on a fiber optical trapping system [65] illuminated by a fiber-coupled laser diode can work independently without attachment to an optical table. By contrast, an objective-based optical tweezers system with similar functions can hardly work properly without an optical table to mount the mirrors [47].

iv). *Fiber optical tweezers have less limitation on working distances.*

Optical fibers are light in weight and small in diameter. They are flexible and can be moved technically anywhere inside the solution, no matter how far it is from the coverglass (if there is one). Therefore, the optical traps can also be moved anywhere in the solution, and they are not limited to a thin layer of 20 μm from the coverglass. This feature is important for micrometer-scale applications that require the trapped particles to be moved far from the coverglass; for example, the assembly of a micromachined gear onto a tall shaft. For the study of biological molecules, a trap far from the substrate can reduce the wall effect [7].

v). *Fiber optical tweezers require no substrate for focusing.*

Fiber tweezers do not need oil or coverglass for focusing. There are no constraints on the substrate. This is an obvious advantage when a substrate is not available or the substrate material cannot be freely chosen, such as experiments *in vivo*.

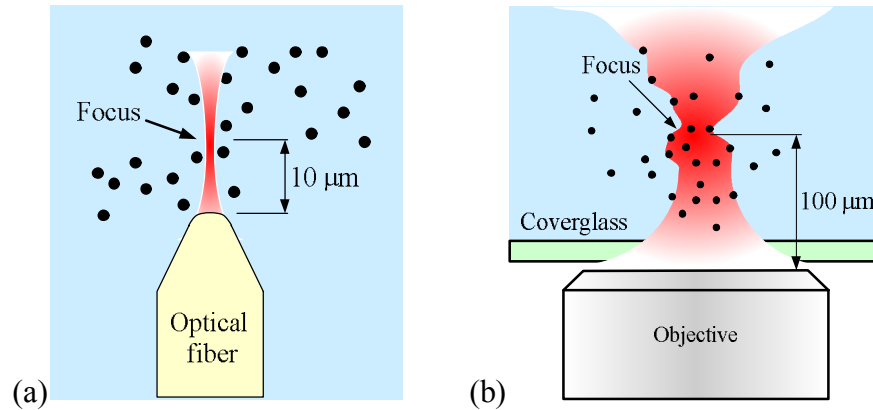


Figure 1.12. Degradation of focus quality in a colloid. (a) Optical fiber tweezers and (b) objective-based optical tweezers. Less degradation due to light travels a smaller distance in the solution.

vi). *Fiber optical tweezers enable good focus quality in a turbid solution.*

The focus quality of fiber optical tweezers is less distorted in a turbid solution, when compared with that of objective-based optical tweezers. In fiber optical tweezers, the focal length, which is referred to as the distance between the focus and the fiber surface, is the length in which disturbance of the beam focus by the colloid occurs. The focal length of a tapered fiber (from OZ Optics Ltd.) is around 10 μm. The disturbance does not get worse no matter how far the fiber is away from the substrate. However, in objective-based optical tweezers, the disturbance gets worse when the optical trap moves away from the coverglass, as illustrated in Figure 1.12. Therefore, in turbid solutions, fiber optical tweezers are expected to have less performance

degradation [66]. This is important because studies of colloidal solutions are one of the major applications of optical tweezers [7, 11]. In physics, optical tweezers are needed to measure miscellaneous colloidal dynamics and interactions, such as diffusion, hydrodynamic interactions and electrostatic interactions [9]. In biology, milk and blood are examples of colloids.

Based on the aforementioned features, fiber optical tweezers have the potential to be integrated to an implantable device and used for *in vivo* applications.

1.2.3.2. *Single fiber optical tweezers*

Taguchi *et al.* [67] proposed and demonstrated fiber optical tweezers by using a single fiber in 1997. An inclined single-mode fiber with a tapered spherical end was inserted into a reservoir, and a two-dimensional (2D) trap was formed near the focus, as shown in Figure 1.13(a). Both dielectric beads and yeast cells were trapped on the reservoir bottom. They also calibrated the escape velocity versus transverse offset in some later work [68, 69]. In 2005, Hu *et al.* [70, 71] used a similar system to demonstrate manipulation and arrangement of yeast cells. The beam diameter at the focus was 3.7 μm . Experimental calibration of the trapping efficiency by using both static and dynamic method was carried out. In 2007, Abedin *et al.* [72] employed a bismuth fiber, instead of a common silica fiber, with a tapered end to manipulate and rotate liquid crystal drops. Because bismuth has a larger refractive index than silica, the beam had a tighter focus, but still the focus size is on the order of micrometers. In 2006, a polystyrene sphere with a diameter of 10 μm was glued to the fiber end as a focusing lens, as shown in Figure 1.13(b) [73]. The

optically cured resin filled the gap between the bead and the fiber end to fix the bead and reduce beam distortion. A focus diameter of $1.8 \mu\text{m}$ was achieved. Gold nanoparticles with diameters of 40 nm, 100 nm, and 200 nm were trapped in two dimensions (2D) under this microsphere lens. An axicon structure was fabricated on the fiber endface using focused ion beam (FIB) milling, as shown in Figure 1.13(c). [74] 2D trapping of 2- μm polystyrene beads was achieved using the Bessel beam created by the axicon structure.

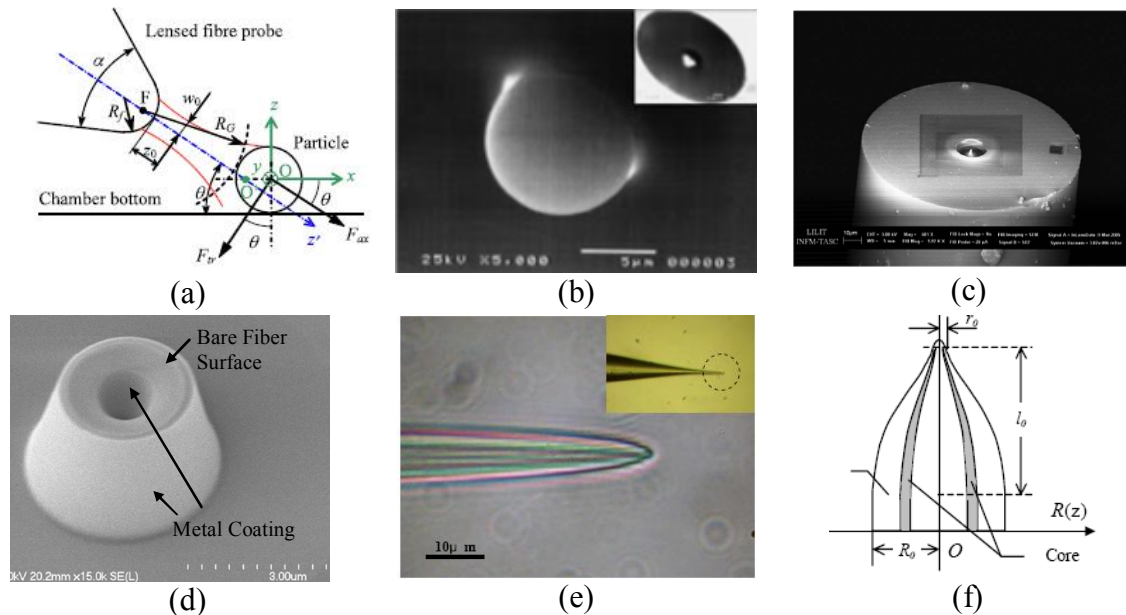


Figure 1.13. Single fiber optical tweezers by using a fiber with (a) tapered spherical end [71], (b) dielectric sphere glued on the cleaved fiber end [73], (c) axicon lens [74], (d) annular exposed end [66], (e) sharply tapered end [75], and (f) two cores [76].

Generally single fiber tweezers cannot achieve a strong focusing due to the limited aperture size of the fiber, such as the systems introduced above. However, different configurations of single fiber optical tweezers have been attempted to overcome such limitations by using fibers with an engineered end face. A partially metalized fiber end face with a hollow tip was fabricated to replace the regular tapered end, as shown in Figure 1.13(d) [66]. An annular rim ($\sim 1 \mu\text{m}$ in

diameter and ~ 750 nm in thickness) of the fiber surface was exposed with all of the other areas on the end face coated with aluminum. Thus, a ring-shaped optical field emitted from the fiber end face and the ring diameter did not increase much within several micrometers of propagation. A $2\ \mu\text{m}$ diameter glass bead was trapped in 3D. Since there was no strong focusing effect, the restoring force that balanced the scattering force was the electrostatic force, rising from the negative-charged bead and the induced positive charge on the metalized fiber end. To be precise, this is a combination of one dimensional (1D) electrostatic trap and a 2D optical trap. This system requires a large charge density on the surface of the trapped bead [66], which is not always allowed especially for biological particles. Another configuration presented by *Liu et al.* [75] in 2006 used a thinned tapered fiber to confine the beam size emitting at the fiber end, as shown in Figure 1.13(c). Heating and drawing method was used to thin the fiber diameter from $125\ \mu\text{m}$ to about $10\ \mu\text{m}$. According to the simulation results, the beam size was decrease to $0.5\ \mu\text{m}$ due to the small core size of the fiber end. A 3D stable trapping of a yeast cell was demonstrated. Although this system can achieve a 3D trap with a single fiber, it has significant power loss due to the greatly tapered fiber tip. A laser with a power of $120\ \text{mW}$ [75] was used, while typical single fiber tweezers only need a couple of milliWatts [71]. Similar approach was carried out for a twin-core fiber by the same group [76], as shown in Figure 1.13(f). The taped twin-core fiber can achieve 3D trapping of $\sim 6\text{-}\mu\text{m}$ cells with an output power of $5\ \text{mW}$. For the systems using such sharply tapered fibers, one can hardly obtain a repeatable, uniform, and controllable size of the fiber end by using the heating and drawing methods [77]. Moreover, the spot size cannot be too small (close to diffraction limit), otherwise the power loss will be significant [78].

As a summary of single fiber tweezers, most current single fiber tweezers can only achieve a 2D trap. 3D trap with a single fiber can be achieved by tapering the fiber tip to a small size, but there are considerations of power loss and controllability.

1.2.3.3. Dual fiber optical tweezers

Dual fiber optical tweezers were demonstrated even before the invention of single fiber optical tweezers, since it is intuitive to use two counter-propagating beams to balance the scattering forces, and hence, to realize a 3D optical trap. Constable *et al.* [79] proposed and demonstrated the first dual fiber optical tweezers built with two opposite cleaved fibers in 1993, as shown in Figure 1.14(a). Polystyrene beads with diameters between 0.1 μm and 10 μm as well as living yeast cells were trapped in 3D with a output power of 7 mW from both fibers. Two years later, Lyons *et al.* [80] replaced the two cleaved fibers with two tapered fibers. Using tapered fibers enables larger divergence angles, and hence, higher transverse trapping efficiency.

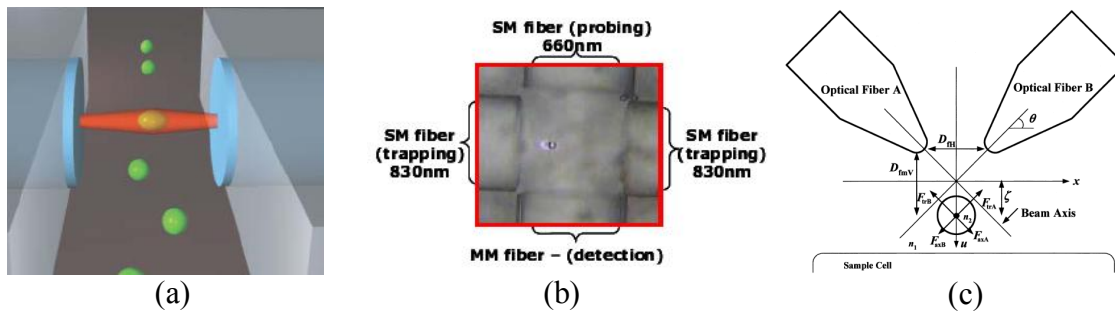


Figure 1.14. Dual fiber optical tweezers with (a) two cleaved fibers [81], (b) two trapping fibers (one probing fiber to excite and one detection fiber to sense fluorescence) [82], and (c) two inclined fibers [86].

Compared with single fiber optical tweezers, stable 3D traps are much easier to obtain with opposite dual fibers. Moreover, due to the illumination from multiple directions which spreads the optical power, the transverse trapping force without inducing photodamage of the trapped samples is larger for dual fiber tweezers. For this reason, dual fiber tweezers have been used in more applications than single fiber optical tweezers [81, 82, 83]. Jensen-McMullin *et al.* [82] introduced another fiber, perpendicular to the two trapping fibers, to sense the position of the trapped beads by collecting the intensity from the scattered light. A fourth fiber was then added to the system for fluorescence excitation, as shown in Figure 1.14(b). An excitation laser with a proper wavelength was guided by the fourth fiber, and the excited fluorescence from the trapped bead was collected by the third sensing fiber. Opposite dual fiber tweezers were also used to increase the coupling efficiency between two fibers [83]. A trapped ball lens can center itself with respect to the fiber axis, and hence so that the coupling efficiency can be increased by a factor of 2. Another important application of dual fiber tweezers is cancer diagnosis, as demonstrated by Guck *et al.* in 2005 [81]. The cancerous cell has a softer membrane compared to that of a normal cell. The cell trapped in opposite dual fibers can be stretched due to the gradient force. Therefore, the large deformation of the cell membrane in the trap can serve as an indicator of a cancerous cell. This method requires no bead attached to the cells and enables a quick and simple disease diagnosis.

Although opposite dual fiber tweezers have better stability and greater accessibility for a large trapping volume compared to single fiber tweezers [80], the alignment of the two fibers are critical [65, 79]. To achieve a precise alignment, the two fibers are always fixed to the substrate, by being pressed along a fixed capillary with a large diameter [65, 79] or by being embedded in a

V-groove or a substrate [81, 82]. This method actually sacrifices the flexibility of the fiber tweezers. The fibers cannot be moved, and more importantly, particles lying on the substrate cannot be trapped due to the size of the fiber. Particles to be trapped need to be previously suspended in the solution and then flushed into the trapping area along microfluidic channels [65, 81, 82]. In the work of Taguchi et al. [84, 85], dual fiber tweezers with two inclined fibers were developed, as shown in Figure 1.14(c); this can help address the limitations of the dual fiber tweezers with counter propagating beams. Levitation and 3D trapping of 6-micrometer microspheres were demonstrated. Later in 2002, the influence of tapered end radius to the trapping efficiency was numerically investigated [86]. More recently in 2006, an actuation method using intensity modulation was presented by the same group [87]. However, the trapped particles were staying on the substrate when being actuated. Currently, this system has not been studied thoroughly. 3D actuation and experimental calibration of the trapping efficiency have not been carried out.

1.2.3.4. Other fiber optical tweezers

In addition to the single fiber tweezers and dual fiber tweezers, other work on fiber optical tweezers has also been reported. Tam *et al.* [88] employed a fiber bundle to form an optical trap array. Each fiber can form a single fiber tweezer if a laser beam is coupled to it. Similar to fiber imaging but in an opposite direction, by selecting some fibers in the bundle to couple the light while blocking other fibers, a desired array of optical traps can be achieved and controlled. In another effort, Collins *et al.* [89] combined two opposite dual fiber tweezers into one system and proposed a set of four fiber tweezers. The system has a similar configuration as that shown in

Figure 1.14(b), but all four fibers emit light. The position control of the trapped particles was demonstrated in two dimensions by using intensity modulation.

Recently a 3D optical trap was realized using a four-fiber configuration. [90] The four fibers are parallelly bounded in a glass tube, with an inclined slit etched into each fiber's endface, as shown in Figure 1.15. The slits serve as mirrors to bend optical beams towards the optical axis. Large inclination angles ($\sim 70^\circ$) of the light beams can be achieved, equivalent to the focusing effect with a high NA objective. 3D trapping of 10- μm polystyrene beads was achieved with a power of 7 mW from each fiber. This fiber trap is strong for trapping microscale particles, but cannot be used to trap submicron-size particles due to the large beam sizes ($> 7 \mu\text{m}$). The alignment of the four slits may be an issue during the fabrication process. The transverse size of the probe is twice larger than the size of a single fiber.

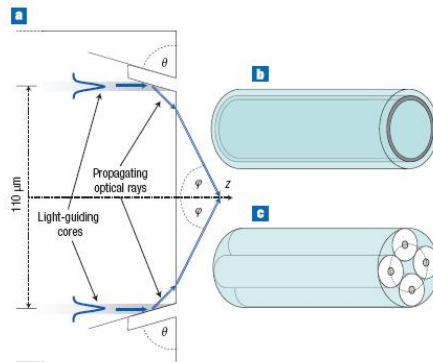


Figure 1.15. Reflection-based four-fiber optical tweezers. [90]

1.2.3.5. Limitations of current fiber optical tweezers

Based on the above review, most of current optical tweezers can be classified into two categories, single fiber tweezers and dual fiber tweezers. With most of single fiber tweezers, one has difficulties in forming a stable a 3D trap due to the large focus size. Single fiber tweezers that can achieve 3D trapping have problems of controllable spot size and power loss. Dual fiber tweezers usually use the configuration of opposite fibers, due to which, one sacrifices the versatility of fiber optical tweezers and cannot levitate particles lying on the substrate. Dual fiber tweezers with inclined fibers can overcome these limitations. However, this system has not been investigated thoroughly and is far from being mature for applications.

1.3. Motivation for this doctoral research

Objective-based optical tweezers has been an important tool for physical and biological studies. [1, 7, 11, 12, 13] Optical tweezers have been proposed to be combined with the emerging lab-on-a-chip technology for future individual molecule studies [20]. Scaling down to chip level devices can have many advantages, such as low cost, better accessibility, little chemical waste, and reduced synthesis time. Based on discussion provided in Section 1.2.2.3, the limitations of objective-based optical tweezers become important when the whole system needs to be scaled down. Objective lens and free-space optics can hardly be integrated due to their large sizes. Free-space optics makes the optical trapping system sensitive to environmental disturbances. The requirement of a clean, glass substrate for the objective imposes many constraints to the working conditions of optical tweezers. The limited working distance (within several hundreds of micrometers) and spherical aberrations for large working distances (over 100 μm) allow for even less flexibility in the use of these optical tweezers.

Fiber optical tweezers can potentially overcome the abovementioned limitations of the objective-based optical tweezers. This is due to the following reasons: i) optical fibers are inexpensive and can be readily integrated; ii) optical fibers serve as a perfect waveguide and spatial light filter so that free-space optics is not needed; iii) optical fibers are biocompatible, mechanically robust, and free of electromagnetic interference [21]; iv) fiber optical tweezers have less limitations in terms of working distance, and they do not have any constraints on the substrate; and v) fiber optical tweezers suffer less from the focus distortion when used in a high-density colloidal solution. Therefore, fiber optical tweezers are very appealing for scaled-down applications.

However, current research on fiber optical tweezers is far from being complete. The focusing of the beam emitted from an optical fiber is weaker than that from an objective. Hence, the trapping efficiencies of fiber optical tweezers are lower. Single fiber optical tweezers are difficult to achieve 3D traps, so most fiber optical tweezers employ opposite (counter-propagating) dual fibers. With this configuration, one sacrifices the flexibility of the optical fibers, since the fibers need to be fixed to the substrate in order to ensure a good alignment. Moreover, counter-propagating dual-fiber tweezers cannot lift particles lying on the substrate due to the physical size of the optical fiber. In addition, because of the cumbersome configurations, the counter-propagating dual-fiber tweezers cannot be used to realize complex functionalities; they are currently only used to move particles along the common optical axis or to apply forces to stretch particles.

The most important limitations of the existing fiber optical tweezers are summarized as follows, which pose great challenges to the development of fiber optical tweezers.

i) Lack of fundamental understanding of some highly potential fiber optical trapping systems. Some highly potential fiber trapping systems have not been investigated thoroughly. The inadequate knowledge prevents these systems from being widely used. As some capabilities offered by these systems cannot be provided by other existing fiber optical tweezers, it is imperative to achieve an enhanced understanding of these systems.

ii) Limited functionalities. Existing fiber optical tweezers cannot be used to realize a complex 3D pattern of multiple particles with adjustable separations, which has been achieved by using objective-based optical tweezers. The abilities of 3D particle stacking and separation have not yet been demonstrated with the existing fiber optical trapping systems. These functionalities are desirable in many applications such as creating artificial crystalline structures with controllable material properties and study of colloidal interactions. Therefore, it is worthwhile to investigate how to create multiple traps and realize versatile functionalities with fiber optical tweezers.

iii) Weak trapping strength. Although existing fiber optical tweezers are much more compact in size compared with objective-based tweezers, due to the weak focusing effect from the fiber based devices, fiber optical tweezers produce much weaker trapping forces. The weak trapping force of fiber optical tweezers has severely hindered their applications in many fronts.

1.4. Objectives and scope of dissertation

The overall goal of this dissertation work is to achieve a fundamental understanding of the inclined dual-fiber optical tweezers system and to develop novel fiber optical trapping systems with enhanced trapping capabilities for micro-/nano-scale manipulation and force sensing.

Specific objectives include the following:

- i) Develop and enhanced understanding of the inclined dual-fiber optical trapping systems.
- ii) Study multiple 3D traps created with the inclined dual-fiber optical tweezers.
- iii) Develop novel techniques to improve the focusing effect of optical fiber devices.
- iv) Improve the performance (such as trapping efficiency, stability, controllability and flexibility) of fiber optical tweezers.
- v) Explore new applications of fiber optical tweezers in emerging research fields.

To achieve these objectives, three major research thrusts are carried out in this dissertation work.

Research Thrust 1: System development, experimental study, and modeling of the 3D trap created with the inclined dual fiber optical tweezers. *This thrust addresses Specific Objectives 1 and 4.*

Research Thrust 2: Experimental study and modeling of multiple traps and multiple functionalities realized with the inclined DFOTs. *This thrust addresses Specific Objectives 1, 2, 4, and 5.*

Research Thrust 3: Development of fiber-based surface plasmonic (SP) lens to achieve far-field superfocusing effect and study of trapping efficiency enhancement with SP lensed fiber tweezers. *This thrust addresses Specific Objectives # 3, 4, and 5.*

The rest of this dissertation is organized as follows. In Chapter 2, inclined dual-fiber optical tweezers system is introduced, followed by thorough experimental and numerical study of the system for 3D manipulation of a single particle. In Chapter 3, multiple traps created with the inclined DFOTs are investigated. Multiple functions enabled by the multiple traps are also studied. In Chapter 4, a surface plasmonic lens on a fiber endface is designed, experimentally demonstrated, and numerically studied. 3D trapping of bacteria is demonstrated with SP lensed fiber optical tweezers. The trapping efficiency enhancement achieved by using SP lensed fiber trapping system is also studied here. In Chapter 5, the dissertation work is summarized and contributions are discussed, followed by suggesting the future work.

Chapter 2. Inclined Dual-fiber Optical Tweezers: System Development, Modeling, and Experiments

In this chapter, the inclined dual-fiber optical tweezers (DFOTs) system is thoroughly investigated. In addition to demonstration of 3D trapping in experiments, a model based on ray optics is developed to help achieve enhanced understanding of the inclined DFOTs system. Based on this model, parametric study of the inclined DFOTs on manipulation of various sized silica beads as well as yeast cells is carried out. The chapter is organized as the following. First, the inclined DFOTs system setup is introduced, followed by the trapping principle of the 3D trap. The trapping efficiency of the inclined DFOTs versus particle displacement was experimentally calibrated, which is the first time for this system, with both the drag force method and the power spectrum analysis method. Second, the influence of the system parameters on the trapping performance is investigated in simulations. Third, robustness to fiber misalignments of the inclined DFOTs is discussed and compared with that of the counter-propagating DFOTs. In addition, 3D trapping of yeast cells is demonstrated and the trapping efficiency depends on the shape of the particle is investigated.

2.1. System development of inclined DFOTs

The experimental setup of the inclined DFOTs is shown in Figure 2.1(a). An 808 nm laser diode (FMXL808-080SA0B, Bluesky Research) with a maximum power of 70 mW was used as the light source. A 1×2 fiber coupler (Gould Fiber Optics) was employed to split the laser beam into

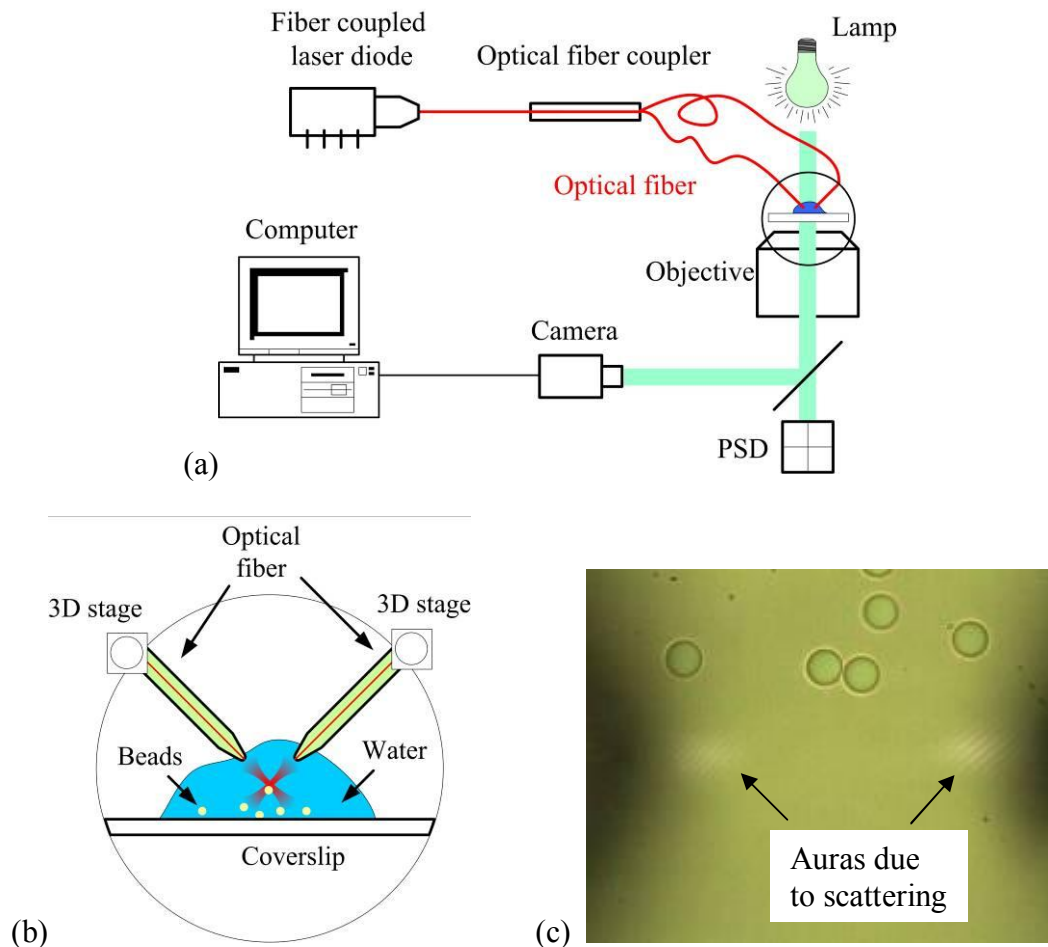


Figure 2.1. (a) Experimental setup of the inclined DFOTs system. (b) Close-up showing the optical trap built from the two beams emitted from lensed fibers. (c) Microscope image showing two auras due to the beam scattering.

two lensed fibers (OZ Optics). The optical beams exiting from the lensed fibers had Gaussian profiles and formed an optical trap. Each lensed fiber was clamped on a fiber holder so that the suspended fiber length is 10 ± 2 mm. The optical power emitted from the lensed fiber end was measured by using a free-space powermeter (PM144, Thorlabs). All the fibers and the coupler are single-mode at the wavelength of 808 nm. Imaging was carried out by using a microscope (CKX41, Olympus Inc.) with an oil-immersion objective (PlanC N 100 \times /1.25, Olympus Inc.).

Since the objective is not required to form the optical trap, it can be adjusted freely to visualize different horizontal planes. A CCD camera (Moticam 1000, Motic) was used to capture the videos. For the purpose of calibration, a position sensitive detector (PSD) (DL 100-7PCBA3, Pacific Silicon Sensor Inc.) was utilized to provide position detection of the trapped beads.

The close-up of the optical trap is shown in Figure 2.1(b). Two lensed fiber were attached to a board via two 3D translation stages (3D Stages 1 and 2) to facilitate fiber alignment, which was achieved by examining the positions of the optical beams at different focal planes. Due to the scattering, the auras of the optical beams can be seen from the microscope images, as shown in Figure 2.1(c). When the objective moves along the z axis, the aura of each beam will move along a line parallel to the y axis. The x -axis fiber alignment was achieved when both auras moved along a common line, while the z -axis alignment was realized when the distances between the auras and the corresponding fiber tips were the same.

After the fiber alignment was achieved, Stages 1 and 2 were fixed so that the board containing the two fibers can be moved as a whole block by adjusting a common stage (3D Stage 3). The optical beam emitted from the lensed fiber has a waist radius of $1.35 \pm 0.25 \mu\text{m}$, which is located $12 \pm 2 \mu\text{m}$ from the end face of the fiber, according to the data provided by the manufacture. The fibers were arranged to have an inclination angle $\theta = 50^\circ$. This inclination angle can be adjusted so that the influence of the inclination angle on the trapping performance can be investigated experimentally. The separation between the two fibers was arranged to be $45 \mu\text{m}$ along the y axis. It is noted that the beam intersection was located around $17 \mu\text{m}$ downstream below the beam focuses, rather than at the focuses where a stronger trap can be achieved. This is due to the

limitation of the fiber tip geometry, which has a cone shape with an opening angle of around 90 degrees, as shown in Figure 2.2(b). If the fibers are arranged so that the beam intersection (where the trap is) is at the two focuses, the fiber tip geometry will prevent the intersection from reaching the substrate, and hence beads lying on the substrate cannot be picked up. A coverglass with a water drop containing silica beads (Bangs Laboratories, Inc.) was placed on a two-dimensional stage, which was attached to a one-dimensional motorized stage (UTM50MVTP, Newport Corp.) to achieve a constant moving speed for calibration purpose.

Silica beads of four different sizes ranging from 3.01 to 4.74 μm in diameter were trapped in the experiment. The silica beads have a density of 2.0 g/cm^3 and a refractive index of 1.45 according to the data provided by the manufacturer. Beads solution was first diluted with distilled water by 600 times. To reverse bead aggregation, a glass beaker containing the diluted bead solution was immersed in ultrasonic bath for 15 minutes. One drop of the bead solution was then added onto the coverglass, where the trapping experiment was carried out. The thickness of the water drop was controlled to be 3~4 mm. To prevent the water on the coverglass from drying up under the illumination light, water was added to the coverglass frequently.

2.2. Trapping principles of inclined DFOTs

For typical single-fiber optical tweezers (SFOTs) built with lensed fiber shown in Figure 2.2(a), the trapped particle reaches equilibrium only when there is a normal force N from the substrate. If there is no substrate, the particle will be pushed away. Therefore, SFOTs can only achieve two dimensional (2D) optical trapping.

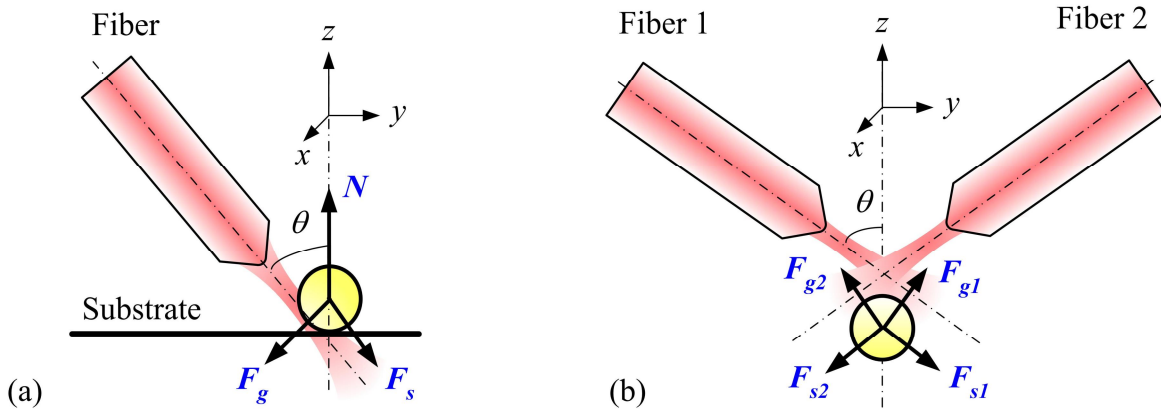


Figure 2.2. Illustration of forces applied to a trapped particle in (a) SFOTs and (b) DFOTs. F_s represents the axial net force of the scattering force and the gradient force and F_g denotes the transverse gradient force.

In the case of the inclined DFOTs as shown in Figure 2.2(b), there are two transverse gradient forces (F_{g1} and F_{g2}) and two net axial forces (F_{s1} and F_{s2}) applied by the two beams, respectively. When the four forces are balanced, the particle is three-dimensionally trapped. The equilibrium position is below the intersection of the two beams, and thus, the distance between the trap and the fibers is large enough to manipulate particles of tens of micrometers without any physical contact. It is noted that the gravity and buoyancy are not considered here, whereas in practice to determine whether a 3D trap can be formed, they are important to consider.

A special case of the inclined DFOTs is when the inclination angle of the fibers (θ in Figure 2.2(b)) is 90° ; i.e., the two fibers are arranged to share the same beam axis, which is known as the counter-propagating DFOTs. In most counter-propagating DFOTs, cleaved fibers are used [65] and the distance between the fiber ends is usually larger than $100 \mu\text{m}$. The particle is drawn

by the gradient forces to the optical axis where the transverse gradient forces disappear, and the scattering forces balance each other to enable a 3D optical trap.

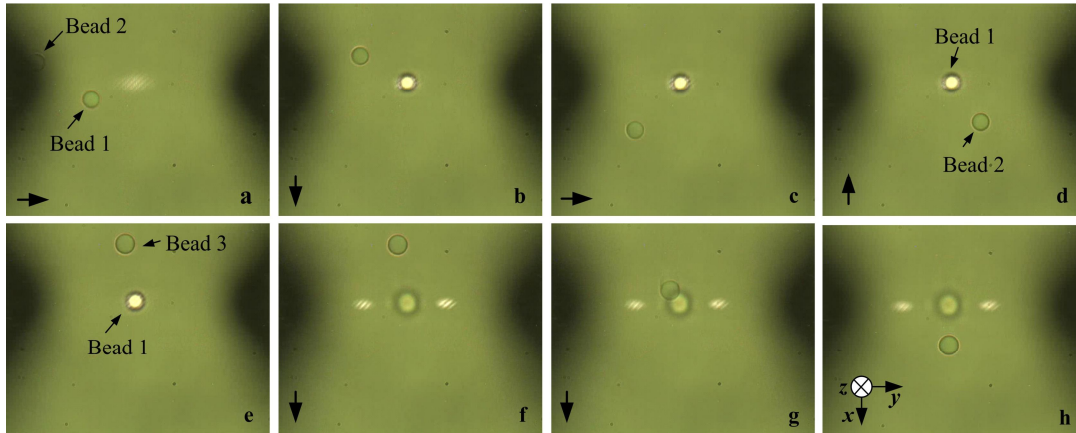


Figure 2.3. Silica bead with a diameter of $4.74 \mu\text{m}$ manipulated in three dimensions by the DFOTs. The arrows indicate the next movement direction of the coverglass. (a) Initial positions of free beads with the coverglass moved along $+y$. (b)-(c) The coverglass moved along $+x$ with Bead 1 trapped. (c)-(e) The coverglass moved along $+y$, $-x$, and then $-y$. Bead 2 was moved out of the view field and another free bead, Bead 3, was brought in. (e)-(f) The trap together with Bead 1 moved out of focus along $+z$. (f)-(h) The coverglass moved downwards ($+x$) with Bead 3 moved freely below Bead 1.

2.3. Experimental study of inclined DFOTs for manipulation of silica Beads

2.3.1. Three-dimensional trapping ability

To demonstrate the 3D trapping ability, a silica bead in water was manipulated in three dimensions using the inclined DFOTs, as shown in Figure 2.3. The two black shadows in the pictures were the fiber tips. The bead (Bead 1) that initially lay on the coverglass was trapped and then lifted by raising the trap. It is noted that the focal plane of the observing objective was fixed and all the pictures in Figure 2.3 were captured on the same vertical plane while the trap or

the water was moved. When Bead 1 was trapped, the coverglass can be moved freely along the x or y direction (Figure 2.3(b)-(f)), and another bead (Bead 3 in Figure 2.3(f)-(h)) can move below Bead 1 without interfering the trap.

2.3.2. Calibration of trapping efficiency with drag force method

2.3.2.1. Basic principles of drag force calibration

In order to use the inclined DFOTs for force sensing, the trapping efficiency and the spring constant must be calibrated. Here, the drag force method [7] was used to obtain the trapping stiffness. After trapped, the bead was lifted to at least 50 μm (about 10 times the bead diameter) above the substrate in order to reduce side wall effects in the drag force calculation. The water was moved with a constant speed by using a motorized stage, so that the bead could be displaced by the drag force, as shown in Figure 2.4. To measure the bead displacement, a video was captured with a CCD video camera from the beginning of the motion. The bead displacement at each frame was obtained by performing image correlation. A mean value of displacements after the bead reached equilibrium was consequently obtained as the equilibrium position, which depends on the water speed. The optical force exerted on the bead was calculated by the drag force, which can be expressed as [91]

$$F_{drag,bead} = 6\pi\mu\nu r, . \quad (2-1)$$

where μ is the dynamic viscosity ($8.9 \times 10^{-4} \text{ Pa} \cdot \text{s}$ for water), ν is the speed of the water (along the x axis), and r is the radius of the bead. By varying the water speed, the dependence of the optical forces on the displacements of the trapped bead was obtained.

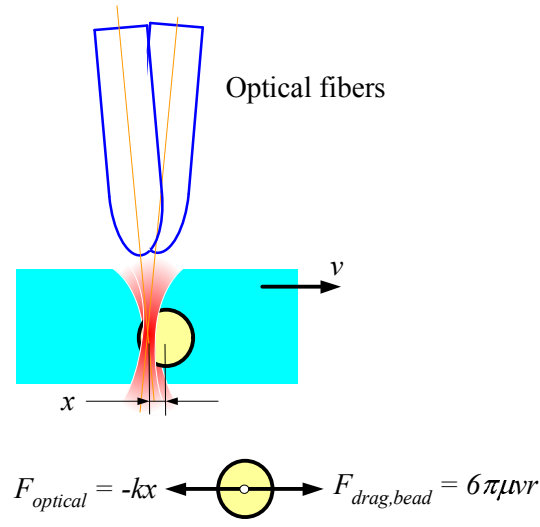


Figure 2.4. Schematic of the drag force calibration for obtaining the trapping efficiency.

2.3.2.2. Evaluation of the fiber tip deflection due to the drag force

In order to ensure that the measurement of the bead displacement was faithful, the fiber tip deflection due to the drag force needs to be estimated. According to the equation derived by Lamb [91], when the Reynolds number is small compared to 1, the drag force exerted on a cylinder that has only translational motion in the water with its axis perpendicular to the flow direction can be expressed as

$$F_{drag,cyl} = \frac{4\pi\mu vl_c}{0.5 - \gamma - \ln\left(\frac{\rho v D}{4\mu}\right)}, \quad (2-2)$$

where l_c is the length of the cylinder, γ is the Euler-Mascheroni constant (~ 0.577), ρ is the density of the water, and D is the diameter of the cylinder. For a stripped optical fiber, $D = 125 \mu\text{m}$, rendering a Reynolds number of 0.073. The maximum flow speed of $80 \mu\text{m/s}$ and the fiber immersion length of 10 mm were used to calculate the fiber tip deflection. Based on Eq. (2-2),

the drag force exerted on the fiber can be obtained ($F_{drag,cyl} = 1540$ pN). If the fiber is considered as a clamped pure silica (Young's modulus of 46 GPa [92]) cylinder with a suspension length of 15 mm, and it is subject to a concentrated load ($F_{drag,cyl}$) at the free tip (where the largest deflection can be induced by the load), a deflection of 0.19 nm at the free tip can be obtained. It is noted that all the parameters have been chosen to ensure a safe estimation. Since this estimated fiber tip deflection is three orders of magnitude smaller than the bead displacement (in sub-micrometers), it is safe to neglect the fiber tip deflection due to the drag of the flow.

2.3.2.3. Drag force calibration results

Image correlation was performed to determine the equilibrium of the displaced particle. The reference image with the trapped bead was taken when the water stayed still. The water was actuated to reach a constant speed and then stopped. During the process, a video clip was captured, and the image at each frame was correlated with the reference image to obtain the displacement of the trapped bead. In Figure 2.5 an example of image correlation is shown, which was used to obtain the data points at 12.5 second in Figure 2.6. The bead displacement as a function of time obtained with the drag force calibration is shown in Figure 2.6. The bead reached the equilibrium at around 1.2 second after the water was actuated (at ~ 2.5 second), and the bead was pulled back to the trap slowly after the water movement was stopped (at ~ 10.2 second). The water was actuated only along the x axis, so that the y displacements were close to 0 during the whole process. It was noticed that the Brownian motion as well as the misalignment of the camera with respect to the motorized stage can cause slight changes to the y displacements, as shown in Figure 2.6. However, within the time period of 4~9 second, the bead

can be considered to be in equilibrium when subjected to both the drag force and optical forces. Averaging over this time period can thus help remove the errors induced by the Brownian motion.

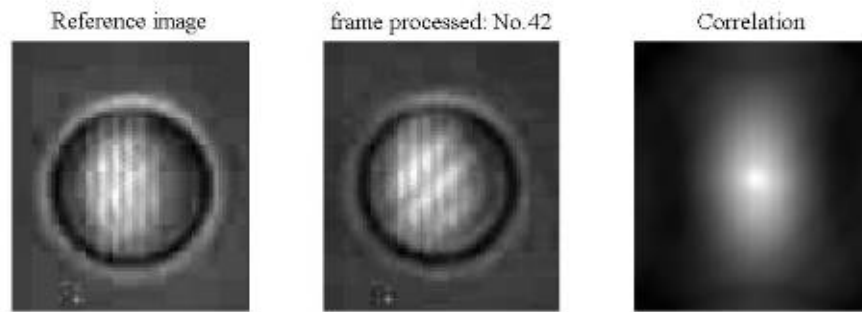


Figure 2.5. An example of image correlation that is used to determine the bead displacement. The image to the right shows the correlation of the two left images.

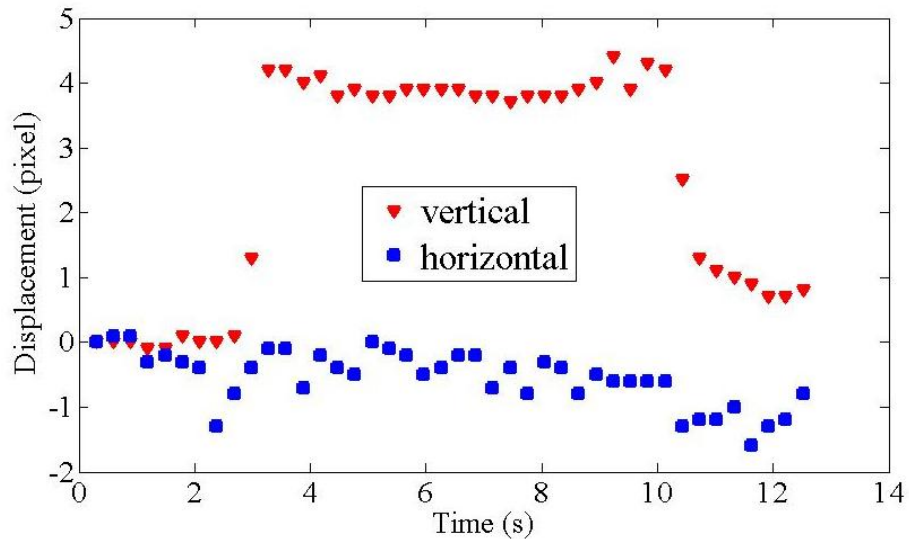


Figure 2.6. The bead displacement data obtained from a video clip at a laser power of 15.3 mW from the source. The water movement was initiated at around 2.5 s, and then at around 3.7 s, it reached a constant speed of 25 $\mu\text{m/s}$. The water movement was stopped at around 10.2 s. The triangle and the square data points correspond to the vertical (y -axis) and horizontal (x -axis) displacements, respectively.

To compare the optical forces obtained with respect to different optical powers, trapping efficiencies were calculated, which describes the efficiency of transferring the momentum from the light to the trapped object. The trapping efficiency is defined as [93]

$$Q = \frac{Fc}{nP}, \quad (2-3)$$

where F is the optical force, c is the speed of light in vacuum, P is the optical power, and n is the refractive index of the medium (here in the water, $n = 1.33$).

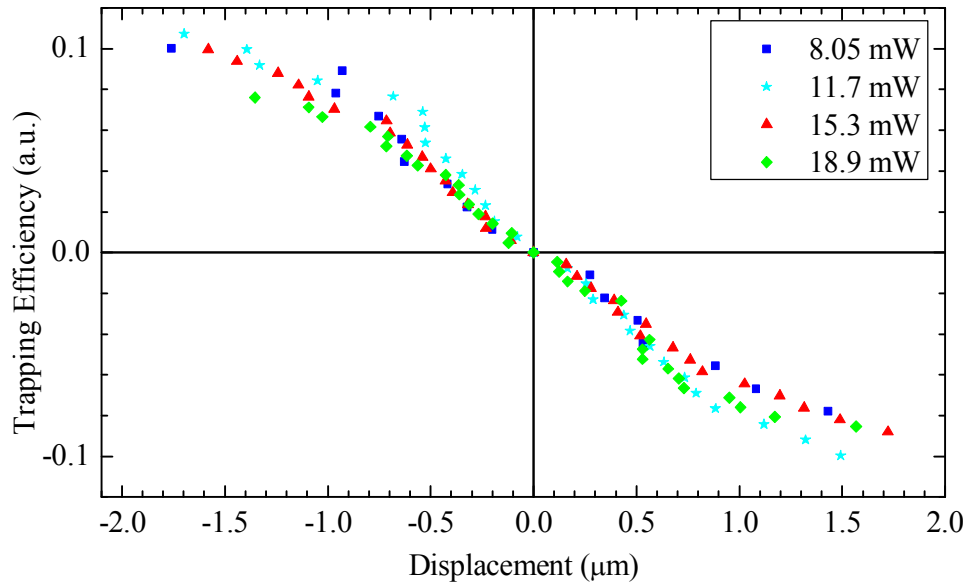


Figure 2.7. Calibration curves of x -axis trapping efficiencies obtained with different laser powers. The experiments were carried out with silica beads of $4.74 \mu\text{m}$ in diameter. The optical powers shown are the total powers from both fibers.

The experimentally obtained trapping efficiencies at different optical powers are shown in Figure 2.7. Every single data point is the mean value of the displacements obtained from video clips with duration of at least 5 seconds.

According to the calibration results shown in Figure 2.7, the trapping efficiency is linearly dependent on the displacement within the range of $-1 \mu\text{m}$ to $+1 \mu\text{m}$, which bestows the DFOTs an ability to carry out force sensing. Moreover, the superposition of the trapping efficiencies at different optical powers implies that the trapping efficiency does not depend on the optical power, which is intuitive and can be explained by its definition.

2.3.3. Calibration of trapping efficiency with power spectrum analysis

In addition to the drag force calibration, the power spectrum analysis method [7, 94] was used to obtain both the x - and y -axis spring constants. This method is chosen because the power spectrum of trapped beads can also be used to diagnose possible problems of the optical tweezers, such as alignment errors and other system noise, which cannot be provided by other calibration techniques such as the equipartition method. [7]

2.3.3.1. Basic principles of power spectrum analysis

The Brownian motion of a bead in a harmonic trapping potential (along the x direction) can be described by the Einstein-Ornstein-Uhlenbeck theory with the form of the Langevin equation: [94]

$$m\ddot{x}(t) + \gamma_0\dot{x}(t) + k_x x(t) = (2k_B T \gamma_0)^{1/2} \eta(t), \quad (2-4)$$

where $x(t)$ is the trajectory of the particle along the x axis, m is the mass, γ_0 is the friction coefficient, k_x is the spring constant of the trap, and the $(2k_B T \gamma_0)^{1/2} \eta(t)$ term represents the

Brownian forces from a random Gaussian process at an absolute temperature T , with k_B denoting the Boltzmann's constant. For any t and t' , $\eta(t)$ satisfies

$$\langle \eta(t) \rangle = 0; \quad \langle \eta(t)\eta(t') \rangle = \delta(t-t'), \quad (2-5)$$

where the angle brackets denote an average over time t . Following Eq. (2-1), the Stokes friction coefficient is expressed as

$$\gamma_0 = 6\pi\mu r. \quad (2-6)$$

After performing Fourier transform of Eq. (2-4) and averaging over time, the expected two-sided power spectrum is obtained as [94]

$$P_{xx}(f) = \frac{|\tilde{x}(f)|^2}{T_{msr}} = \frac{k_B T}{f_c^2 + f^2}, \quad f > 0. \quad (2-7)$$

Here $\tilde{x}(f)$ is the Fourier transform of $x(t)$, T_{msr} is the total recording time, and f is the frequency. f_c in Eq. (2-7) is called the corner frequency [94], or the rolloff frequency [7], which is related to the trapping stiffness by

$$f_c \equiv \frac{k_x}{2\pi\gamma_0} = \frac{k_x}{12\pi^2\mu r}. \quad (2-8)$$

There are a couple of important issues about Eq. (2-7) worth noting here. The first issue, which is the most important one, is that the expected power spectrum has an exponential distribution instead of a more common Gaussian distribution. Data with an exponential distribution cannot be fitted with least-squares fitting, and this brings difficulties into data processing of the experimentally recorded data. [94] The solution to this problem will be discussed later in this section. The second issue is that the power spectrum in Eq. (2-7) is a two-sided power spectrum.

In some literature [7, 95], single-sided power spectra are used, and the corresponding expression of the power spectrum differs from that in Eq. (2-7) by a factor of 2. In the experiment, one should be careful on whether a two-sided or single-sided power spectrum is being recorded, because the latter introduces an additional factor of 0.5 to Eq. (2-7). If Labview is used as an interface to obtain data and calculate power spectra, two-side power spectra will be obtained instead of single-sided ones. The third issue is the power spectrum in Eq. (2-7) cannot be directly obtained from the experimentally measured data. The direct output data of a PSD are voltages (to be discussed in Section 2.3.3.2), but $P_{xx}(f)$ in Eq. (2-7) has a unit of $\mu\text{m}^2/\text{Hz}$. Therefore, another power spectrum $P_{vv}(f)$ needs to be introduced, which can be obtained from the Fourier transform of the output voltages instead of the bead displacements. The two power spectra can be related with each other by the linear sensitivity of the PSD, ρ (in Volt/ μm): [7]

$$P_{xx}(f) = P_{vv}(f) / \rho^2. \quad (2-9)$$

If $P_{vv}(f)$ is used instead of $P_{xx}(f)$ in Eq. (2-7), the expression of the power spectrum directly obtained from the experiment can be written as:

$$P_{vv}(f) = \frac{|\tilde{V}(f)|^2}{T_{msr}} = \frac{D}{f_c^2 + f^2}, \quad f > 0, \quad (2-10)$$

where $\tilde{V}(f)$ is the Fourier transform of the voltage output from the PSD, and D is expressed as

$$D = \frac{k_B T \rho^2}{2\pi^2 \gamma_0}. \quad (2-11)$$

The right-hand side of Eq. (2-10) is a Lorentzian function. To understand how the parameters D and f_c influence the power spectrum $P_{vv}(f)$, $P_{vv}(f)$ with respect to different D and f_c are shown

in Figure 2.8. There are two distinct regions for each curve. The plateau of each curve corresponds to the region where $f \ll f_c$. The height of the plateau, or the amplitude of the signal, is determined by D/f_c^2 . The linear region happens when $f \gg f_c$, and the slope is always -1. f_c determines where the two regions intersect, and that is why it is called the corner frequency. It is noted that both axes are in logarithmic scales. This determines what type of data compression should be used, and will be explained below.

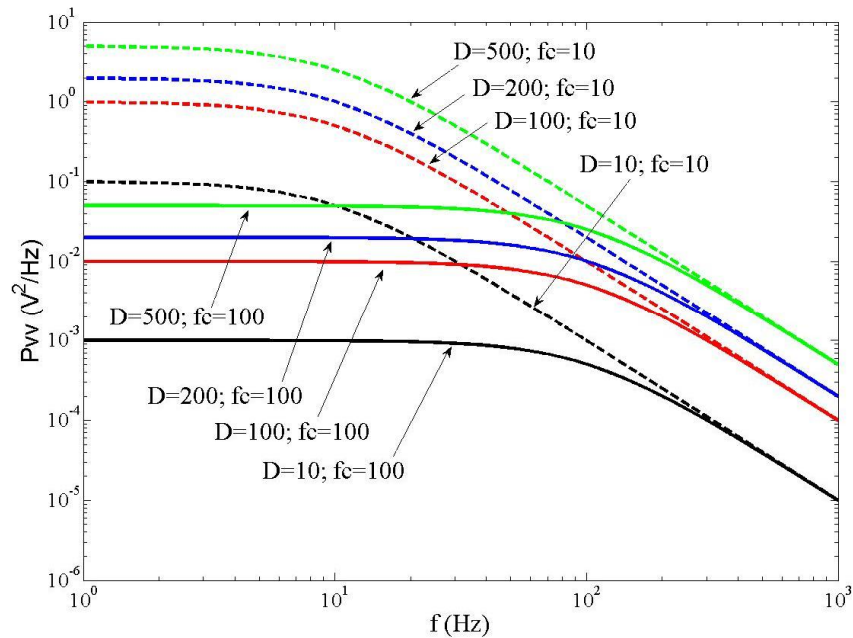


Figure 2.8. The influence of D and f_c to $P_{vv}(f)$. D determines the height of the plateau, while f_c determines where the “corner” is located.

The experimental data are well characterized by the Lorentzian in Eq. (2-10). Two parameters, D and f_c , can be determined with each curve fitted to a set of experimental data. Consequently, both the detector sensitivity and the trapping stiffness (spring constant) can be determined independently. Therefore, the errors in calibrating the detector sensitivity will not be

accumulated into the calibration of the spring constant. This is one of the advantages of the power spectrum analysis over the equipartition method. [7]

As mentioned previously, the power spectrum $P_{xx}(f)$ as well as $P_{vv}(f)$ is exponentially distributed. Least-squares fitting can be applied for a set of data under two conditions: i) the data points are statistically independent, and ii) the distribution of the data is Gaussian. [94] The power spectrum $P_{vv}(f)$ does not satisfy the second condition because it is exponentially distributed, as discussed above. In order to apply least-squares fitting to the data, proper preprocessing, namely data compression, must be performed to convert the data distribution from exponential to Gaussian. [94] There are two methods of data compression that can be used: windowing and blocking. Windowing is to apply window functions to the signal so that the data after windowing will have a Gaussian distribution, provided that the number of windows used is large. However, the compressed data from windowing are always equidistant in the linear scale of the frequency, and thus it is not preferable when the logarithmic scale is used. Blocking is another way to compress the data. In blocking, multiple data points are replaced (blocked) by a single point that is the mean value. Gaussian distributed compressed data can also be generated by blocking if the number of blocked data points is large. Since different numbers of blocked points can be chosen at different regions, the data obtained after the compression can be equidistant in the logarithmic scale.

The above mentioned power spectrum analysis method is expected to have a reasonable error (~10% according to [94]). To further decrease the error, other issues such as anti-aliasing filters and the PSD's frequency-dependent sensitivity [94] need to be considered. In this work, since

other noise sources such as the power fluctuation from the laser source and the fiber movement can result in even larger errors. No further efforts will be undertaken to further decrease the errors in the power spectrum analysis. The x -axis spring constant can be calculated from the fitted values of f_c by

$$k_x = 12\pi^2 \mu r f_c. \quad (2-12)$$

The detector sensitivity can also be calibrated from the fitted values of D , although in this work it is not of interest. The y -axis spring constant follows the same equation as Eq. (2-12).

2.3.3.2. Experiments with the PSD

A PSD is a device that can be used to measure the transverse movement of an optical beam centroid. A PSD has better linearity and a larger linear area compared with a quadrant photodiode. Prior to the calibration experiment, the PSD was first tested in the experimental setup shown in Figure 2.9. The laser beam from a source of 675 nm (S1FC675, Thorlabs) was coupled to one end of an optical fiber. The other end of the fiber was mounted on a two-dimensional stage and the output beam was registered directly on the sensitive area of the PSD. The PSD used in the experiment works under a DC voltage of 20 V and a bias voltage of 0 ~ -10 V. The four voltage outputs (say V_a , V_b , V_c , and V_d) of the PSD are proportional to the intensity sums along the x axis and y axis and the intensity differences along the x axis and y axis, respectively. The x and y positions of the beam centroid can be expressed as $\frac{V_c}{V_a}L$ and $\frac{V_d}{V_b}L$, where L is the dimension of the PSD sensitive area. As discussed in Section 2.3.3.1, the absolute amplitude of the signal is not related to the corner frequency f_c and the trapping efficiency.

Therefore, only $\frac{V_c}{V_a}$ and $\frac{V_d}{V_b}$ were used as the output signals in the experiment, and the spring constant calibration obtained from the power spectrum will not be influenced. The orientations of the x and y axes of the PSD were calibrated by sweeping the fiber across the PSD, and this was important for determining the orientation of the PSD when it was mounted onto the microscope platform.

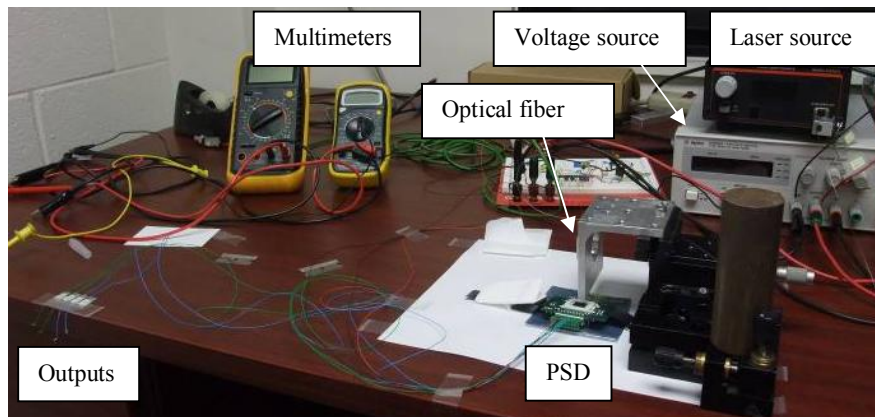


Figure 2.9. Experimental setup for testing the PSD. The fiber guiding a red laser beam was mounted above the sensitive area of the PSD.

The PSD was then mounted on the camera port of the microscope. The vertical position of the PSD should be adjusted so that the sensitive area of the PSD is conjugate to the focal plane of the objective. The PSD position can be determined by the position of the camera chip when the trapped particle is in focus. A home-made adapter, as shown in Figure 2.10, was used to mount the PSD at the required position by adjusting the vertical distance between the PSD sensitive area and the outer surface of the microscope C-mount. The orientation of the PSD should be aligned with respect to the setup of the inclined DFOTs system, so that the PSD outputs can be used for trapping force calibration along the x and y axes shown in Figure 2.2(b). A Labview

program was written to collect both the time-domain and frequency-domain data in the experiment.

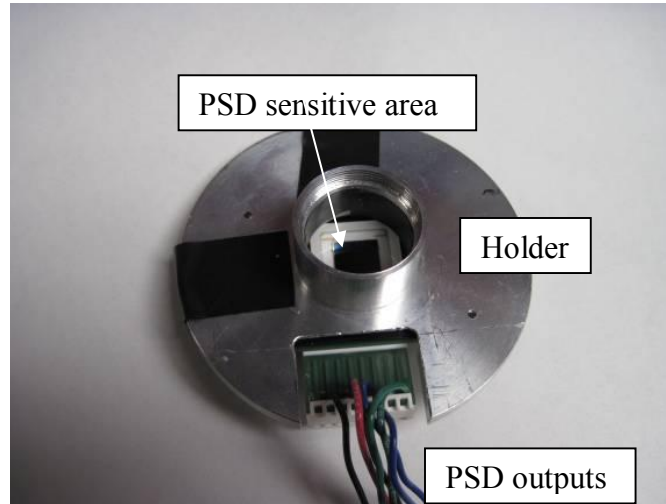


Figure 2.10. Picture of the PSD holder with the PSD attached.

Before recording any data, the errors from the system setup must be identified and removed from the measurements. As mentioned previously, the power spectrum analysis can be used to diagnose possible system errors since the obtained power spectrum should be fitted nicely by a Lorentzian, as shown in Figure 2.8. The common errors are discussed as follows based on the experience gained in the experiments. The common sources of errors include the mechanical vibrations of the systems (both the trapping and the detection systems) at their natural frequencies and electrical noise at particular frequencies introduced by the voltage source. These errors can induce spikes in the power spectrum. To identify the sources for these spikes, the system setup must be carefully examined. The mechanical resonances generally result from long suspending length of the poles/fibers in the experimental setup. More common sources of vibrations including the microscope and the optical table, however, are easier to be ignored. The optical table should be supported on compressed air (also called “air springs”) in order to be able

to isolate the ambient vibrations. The microscope must be bolted down to the optical table to decrease the vibration amplitude and increase the natural frequency of the system. As an example, the power spectrum without bolting down the microscope is shown in Figure 2.11. The high spikes at ~ 30 Hz disappeared after the microscope was bolted down, as shown in Figure 2.12. The voltage as well as the PSD must be grounded. The bias voltage applied to the PSD should be adjusted accordingly based on the real measurement results. Even though using a high absolute value of the bias voltage can help improve the linearity of the PSD, this can result in a higher noise level and a lower sensitivity. Therefore, in the experiment, zero bias voltage was used to increase the sensitivity and reduce the noise level. Even with all the spikes removed, the experimentally obtained power spectrum always deviates from the Lorentzian fitting at the high frequency region. This is clearly visible because the slope of the recorded data changes at high frequencies. This deviation is believed to be due to the anti-aliasing filters used in the PSD. [94] Anti-aliasing filters are needed to remove the aliasing due to the finite sampling rate, and they are typically added to commercial data acquisition electronics. However, since the original signals are multiplied by the characteristic functions of all the anti-aliasing filters, the output signals will be changed. The effects of the anti-aliasing filters are more prominent at the frequencies close to the highest recording frequency, as shown in Figure 2.11. To solve this problem, a sampling frequency of 10 kHz was used and the obtained frequency-domain signals were chopped at 2 kHz. By doing this, the deviation from the Lorentzian is greatly decreased, as shown in Figure 2.12.

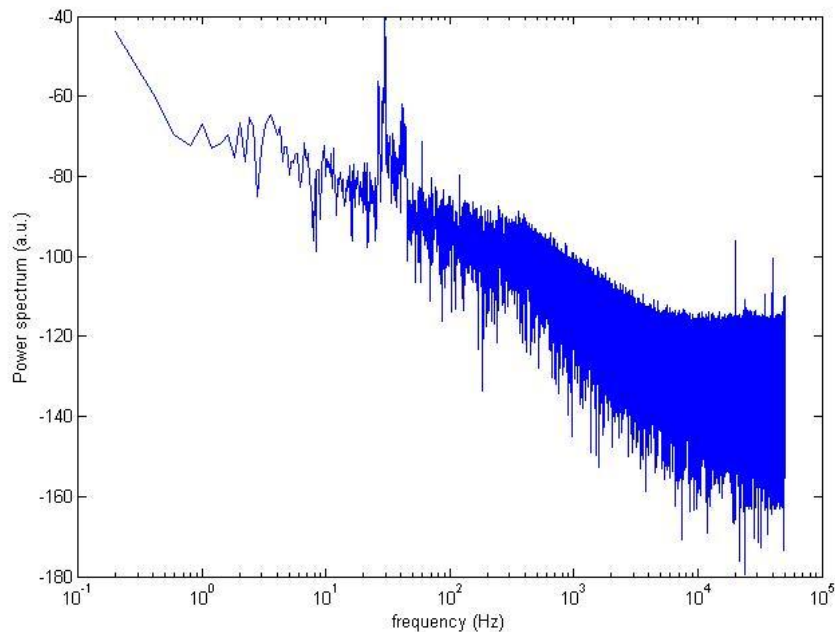


Figure 2.11. Power spectrum shown the resonance peaks of the microscope body at 30~40 Hz. The power spectrum was recorded when the microscope was placed, but not bolted, on the floated optical table. After the microscope was fixed, the above peaks disappeared.

2.3.3.3. Results obtained from power spectrum analysis

In the experiments, the power spectra were obtained by collecting the light scattered by the trapped bead using the PSD. In order to minimize the sidewall effect, a bead was trapped in three dimensions and then lifted up to around 35 μm above the coverglass. The PSD output data were collected within a time period of 5 seconds at a sampling frequency of 10 kHz. This sampling frequency is much larger than the measured corner frequencies (less than 20 Hz) so that faithful results can be obtained. The power spectra were blocked before the curve fitting by replacing 100 consecutive data points with the averaged data point at the corresponding mean frequency. This is necessary because the power spectra obtained from the experiment are exponentially

distributed. After data averaging with a sufficient large number of blocking points, the power spectra approach Gaussian distribution and the least-squares fitting can be used [94]. Curve fitting of the experiment data with Eq. (2-10) was carried out within the frequency range of 1 Hz to 2 kHz. The spring constants were calculated from the fitted corner frequency f_c according to Eq. (2-12). As an example, a fitted x -axis power spectrum obtained with a bead size of $4.74 \mu\text{m}$ and the optical power of 18.9 mW is shown in Figure 2.12. The spring constant obtained from the power spectrum analysis ($2.82 \text{ pN}/\mu\text{m}$) compares well with that obtained from the drag force calibration at the same power ($2.98 \text{ pN}/\mu\text{m}$).

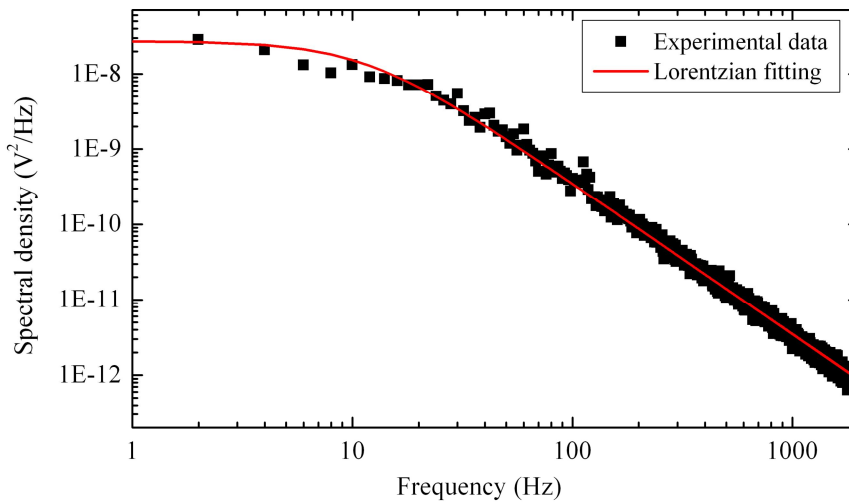


Figure 2.12. Lorentzian fitting of experimentally measured power spectrum. Here, the corner frequency f_x is 11.3 Hz , which gives a spring constant k_x of $2.82 \text{ pN}/\mu\text{m}$.

It is noted that the trapped bead was not imaged onto the PSD plane. Since the trapped bead was close to the intersection of the two laser beams but off-axis, not all the optical power was scattered. If the bead center were conjugate to the PSD plane, the scattered light could be overwhelmed by the unscattered light, and Lorentzian fitting of the experimental data could fail. To solve this problem, the objective was lowered by a proper distance so that the images of the two optical axes were further away from the bead center, resulting in less unscattered light

registered at the PSD. However, the objective could not be lowered too much. Otherwise, the scattered light collected by the PSD was not strong enough and a good fitting could not be achieved, either. In the experiments, proper distances to lower the objective were found to be within 50 μm to 75 μm in order to minimize the influence of the unscattered light. Since the optical axes were located in the yz plane, y -axis power spectra were influenced more than x -axis power spectra.

Table 2.1. Spring constants obtained with beads of different sizes.

Bead diameter (μm)	Experiment		Simulations	
	k_x (pN/ μm)	k_y (pN/ μm)	k_x (pN/ μm)	k_y (pN/ μm)
4.74	2.82	1.86	2.35	1.01
3.93	1.71	1.16	1.64	0.66
3.50	1.38	0.74	1.05	0.43
3.01	1.21	0.34	0.70	0.17

Both x - and y - axis spring constants of four beads of different sizes were calibrated under the power of 18.9 mW. The results are summarized in Table 2.1. The simulation results shown in Table 2.1 will be discussed further in Section 2.4.3. It can be seen that the larger the bead, the higher the spring constants. The x -axis spring constants were always larger than the y -axis spring constants. This is intuitive since no scattering forces appear along the x axis while along the y axis, and the scattering forces prevent the bead from being trapped (see Figure 2.2(b)).

The calibration results along with the experimental results obtained in Section 2.3.2 demonstrate that the inclined DFOTs can serve as both a 3D actuator that is able to pick up particles lying on the substrate and a force sensor. By detecting the displacement of the trapped particle, the external forces applied on the particle can be measured.

2.3.4. Influence of the fiber inclination angle θ

In addition to the influence of the optical power, the trapping performance with respect to different fiber inclination angles θ is also investigated. At a total power of 8.05 mW, θ was decreased with a decrement of 5° while keeping the same fiber distance. The reason for choosing this optical power is that the trap was the weakest amongst the four different power levels that were used in the experiments. When the trap is weaker, it is more sensitive to the influences of the parameters including θ , and thus the consequence of changing parameters becomes easier to observe.

The beads could not be lifted up when $\theta \leq 45^\circ$ in the experiments, but they can still be trapped in two dimensions along the x and y directions. For $\theta \geq 50^\circ$, the bead can be lifted up, and thus trapped in three dimensions. Given the same optical power, the DFOTs exhibit a stronger z -direction trap for a larger θ value. These results imply that the trapping performance along the z direction also depends on the inclination angle. The 3D trapping degrades into a 2D trapping when the inclination angle is below a critical value, which was obtained to be between 45° and 50° in the experiments.

2.4. Modeling of trapping forces of inclined DFOTs

2.4.1. Ray optics model

It is assumed in the model that the optical beam emitted from the lensed fiber has a Gaussian profile (i.e., operating on the fundamental transverse mode (TEM₀₀ mode)) and the beam is unpolarized. When the particle size is larger than the wavelength, the forces exerted on the particle can be derived based on a ray-optics model including the Gaussian beam profile. [96] The incident optical beam can be considered as a stream of photons carrying momentum. The refraction and reflection on the surface can result in the direction change of the photon momentum, which, according to the Newton's second law of motion, implies that the optical beam applies a force to the surface of the particle. The direction and intensity of the incident beam are determined by using Gaussian beam propagation. For a laser beam propagating along the z axis with the beam waist located at $z = 0$, the incident direction at a point $P(x, y, z)$ on the particle surface is perpendicular to the wavefront. In Figure 2.13(a), a geometric sketch for calculation of the incident direction is shown. R is the radius of wavefront curvature at Point P . The distance dz and R can be obtained by solving the following equations:

$$\begin{cases} R = (z + dz) \times \left[1 + \left(\frac{z_0}{z + dz} \right)^2 \right], \\ R^2 = (R - dz)^2 + x^2 + y^2, \end{cases} \quad (2-13)$$

where $z_0 = \frac{\pi \omega_0^2}{\lambda}$, ω_0 is the beam waist, and λ is the wavelength in vacuum. The incident

direction can be expressed as $\vec{in} = \overline{CQ}(x, y, R - dz)$. The incident light intensity at $P(x, y, z)$ is

$$I(x, y, z) = \frac{2P_0}{\pi \omega_z^2} \exp\left[\frac{-2(x^2 + y^2)}{\omega_z^2} \right], \quad (2-14)$$

where P_0 is the total laser power, and ω_z is the spot size at the position z , which can be expressed as

$$\omega_z = \omega_0 \sqrt{1 + (z/z_0)^2}. \quad (2-15)$$

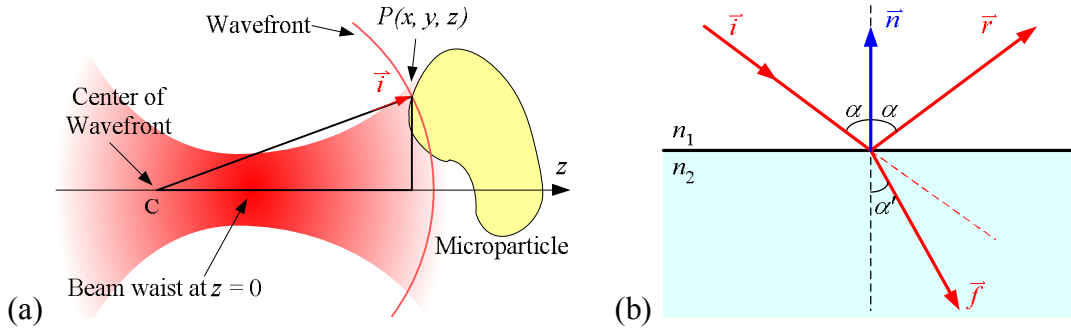


Figure 2.13. (a) Geometric sketch for the incident direction calculation at Point Q and (b) incident condition at the interface.

For a small area dS illuminated by the laser beam, which is centered at the point $P(x_b, y_b, z_t)$, the number of incident photons, N_t , can be expressed as

$$N_t = \frac{I(x, y, z)(-\vec{i} \cdot \vec{n})dt dS}{hc/\lambda}, \quad (2-16)$$

where dt is the time interval, h is the Planck constant, and c is the light speed in vacuum. The factor $(-\vec{i} \cdot \vec{n})$ indicates that the effective light intensity is the intensity component along the normal direction to the interface. The vectors \vec{n} , \vec{i} , \vec{r} , and \vec{f} represent the unit vectors along the interface normal direction, the incident direction, the reflected direction, and the refracted direction, respectively, as shown in Figure 2.13(b). The refractive indices of the incident medium and the refractive medium are n_1 and n_2 , respectively. The numerator of Eq.

(2-16) represents the total incident optical energy while the denominator is the energy of a single photon. The momentum change of each photon can be expressed as

$$\overline{dM} = N_t \frac{h}{\lambda} (n_1 R \cdot \vec{r} + n_2 T \cdot \vec{f} - n_1 \vec{i}), \quad (2-17)$$

where R and T are the Fresnel reflection and refraction coefficients, respectively. If the beam is not polarized, the Fresnel coefficients are

$$R = \frac{1}{2} \left[\frac{\tan^2(\theta - \theta')}{\tan^2(\theta + \theta')} + \frac{\sin^2(\theta - \theta')}{\sin^2(\theta + \theta')} \right], \quad T = 1 - R. \quad (2-18)$$

Here, θ is the incident angle and θ' is the refraction angle. Thus, the optical force exerted on the small region dS can be obtained as

$$\overline{dF} = \frac{\overline{dM}}{dt} = \frac{N_t \overline{dM}_0}{dt} = \frac{I(x, y, z)}{c} (n_1 \vec{i} - n_1 R \vec{r} - n_2 T \vec{f}) (-\vec{i} \cdot \vec{n}) dS. \quad (2-19)$$

The vector integral of all the force elements for each illuminated small surface region dS gives the total optical forces on each of the particles:

$$\vec{F} = \int_{all\ region} \overline{dF}. \quad (2-20)$$

In the next several sections, the trapping force of the dual fiber tweezers will be obtained by summing the optical force vectors obtained for each fiber. This technique will be applied to spherical, spheroidal particles for investigating their performance and trapping efficiency with the proposed dual fiber tweezers systems.

2.4.2. *Trapping force along the z direction*

Since the main difference between the SFOTs and the DFOTs is the z -axis trapping ability, the optical force obtained with the DFOTs along the z -axis is studied first. The z -axis optical force as a function of the bead displacement along the z axis is shown in Figure 2.14 when the total optical power is 8.05 mW. The origin of the displacement is at the beam intersection. The results obtained with different fiber inclination angles are compared here.

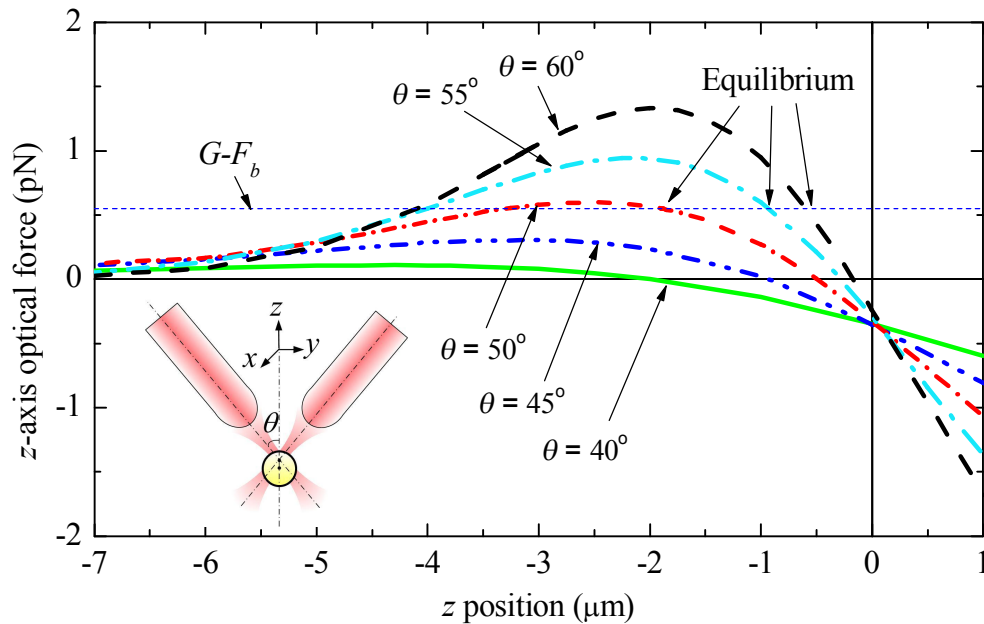


Figure 2.14. The simulation results of optical force versus bead displacement along z axis with different θ values. G is the gravity and F_b is the buoyancy of the trapped silica bead. The optical force should be larger than $G-F_b$ in order to trap the bead in the z direction. The total optical power emitted from both fibers is 8.05 mW. The bead size is 4.74 μm in diameter.

In order to lift up the bead, the optical force should be larger than the gravity minus buoyancy ($G-F_b$), which is illustrated as the horizontal dashed line in Figure 2.14. It can be seen that levitation can only be realized when $\theta \geq 50^\circ$. A larger θ provides a higher $+z$ optical force, and hence a stronger z -axis trap. In the case when $\theta \leq 45^\circ$, the DFOTs fail to lift up the bead along $+z$

direction. This indicates that the critical angle θ for levitation is between 45° and 50° , which matches the value observed in the experiments.

It is noted that the equilibrium position of the trapped bead is not at the beam intersection but somewhere below the intersection and that it varies with respect to the value of θ and the optical power. The equilibrium position can be obtained from Figure 2.14 as the right intersection (where a restoring force exists) of the optical force curve and the $G-F_b$ line. For example, for a given θ of 50° , the equilibrium position is $1.88 \mu\text{m}$ below the beam intersection when the optical power is 8.05 mW , while the value changes to $1.03 \mu\text{m}$ at a power of 15.3 mW . This is intuitive because a lower power renders a lower optical force at the same position. Therefore, if the power decreases, the equilibrium position of the trap will be even lower to the beam intersection so that enough optical force can be obtained to enable a lift-up of the bead. When the power becomes too low, the bead will eventually escape from the trap.

The simulation results also indicate that there is a tradeoff between the z -axis stability and flexibility of the trapping system. A larger θ is beneficial for obtaining better trapping stability. However, a larger θ also requires a larger horizontal span of the setup and brings the bead equilibrium closer to the optical axes, which makes it more difficult to pick up beads from lying on the substrate due to the physical size constraint of the fiber.

The influence of the bead size on the z -axis trapping ability is shown in Figure 2.15. The short dash-dot curve shows the results obtained with one of the bead sizes ($4.74 \mu\text{m}$) used in the experiments. It can be seen that larger particles are more difficult to lift up with the same DFOTs

setup. At an optical power of 8.05 mW, beads with sizes equal or larger than 6 μm cannot be lifted up, whereas smaller beads with sizes of 4.74 μm and 4 μm can. Actually, the beads with the sizes between 3.01 μm and 4.74 μm were lifted up in the experiment. The reason can be explained as that the gravity of the bead increases more quickly with the increasing bead size than the optical force does. Therefore, in order to trap larger particles, either the optical power or the inclination angle needs to be increased. The equilibrium z position is not strongly dependent on the bead sizes. Theoretically, smaller beads (in the micron size range) are easier to trap due to their smaller gravities. However, in the real experiment, beads smaller than 3 μm were difficult to trap due to the fiber misalignment along the x axis.

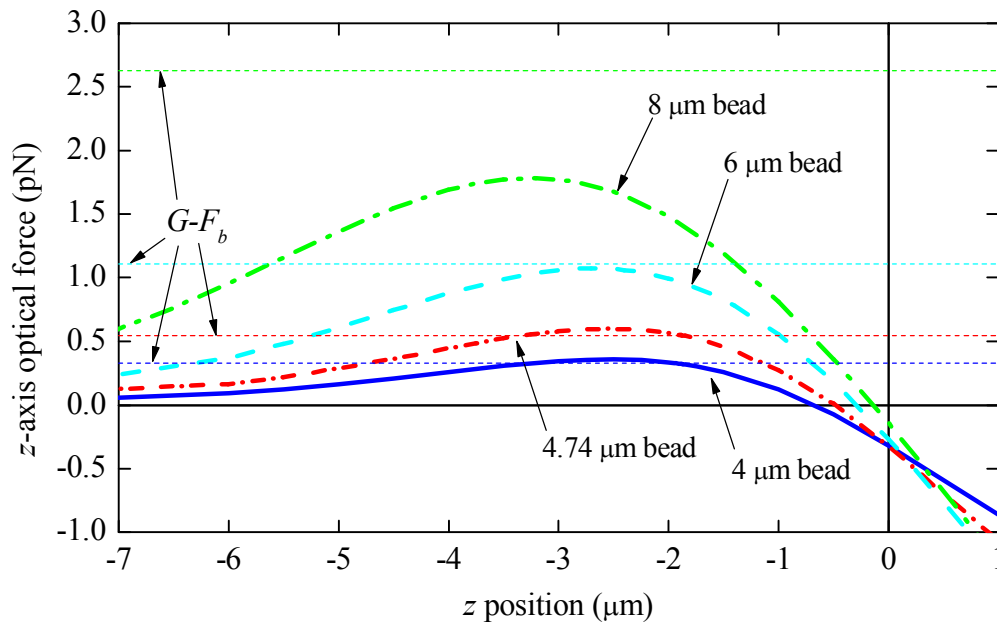


Figure 2.15. The simulation results of optical force versus bead displacement along z axis with different bead sizes. G is the gravity and F_b is the buoyancy of the trapped silica bead. For each bead sizes, $G-F_b$ is expressed with a horizontal dashed line with the same color as the optical force curve. The total optical power emitted from both fibers is 8.05 mW. The inclination angle θ is 50° .

2.4.3. *Trapping forces along the x and y directions*

The trapping forces versus the displacements along the x and y axes are shown in Figure 2.16. The bead size of $4.74 \mu\text{m}$ and the optical power of 15.3 mW are used in order to compare with the experimental results. The influence of inclination angles on the x - and y -axis trapping forces is investigated. It is noted that the z coordinate is fixed to be $-1.03 \mu\text{m}$, $-0.59 \mu\text{m}$, $-0.39 \mu\text{m}$, $-0.17 \mu\text{m}$, and $-0.10 \mu\text{m}$ for the curves with the inclination angle of 50° , 55° , 60° , 75° , and 90° , respectively. These values of the z coordinate correspond to the equilibrium positions of the bead located on the z axis, which are obtained by finding the intersections of the z -axis optical force curves with the horizontal $G-F_b$ lines. Here, only the cases when a 3D trapping is formed are studied, i.e., the inclination angles $\theta \geq 50^\circ$.

According to the x -axis optical forces obtained from the DFOTs shown (see Figure 2.16(a)), both the simulation and the experimental results exhibit the existence of a restoring force when the bead is displaced from the equilibrium. The slope of the x -axis optical force curves in the vicinity of the origin (i.e., the spring constant) can be obtained with curve-fitting. The spring constant obtained from the experiments ($2.68 \text{ pN}/\mu\text{m}$) and the simulations ($1.90 \text{ pN}/\mu\text{m}$) are in the same order of magnitude. If the drag force keeps increasing from 0, the displacement of the bead from the trap will increase until a maximum displacement is reached, which corresponds to the displacement at the peak or in the valley of the x -axis optical force curve obtained from the simulations. A larger displacement cannot be obtained experimentally as the bead will escape from the trap. The maximum displacement obtained in the simulations ($\pm 2.0 \mu\text{m}$) compares well

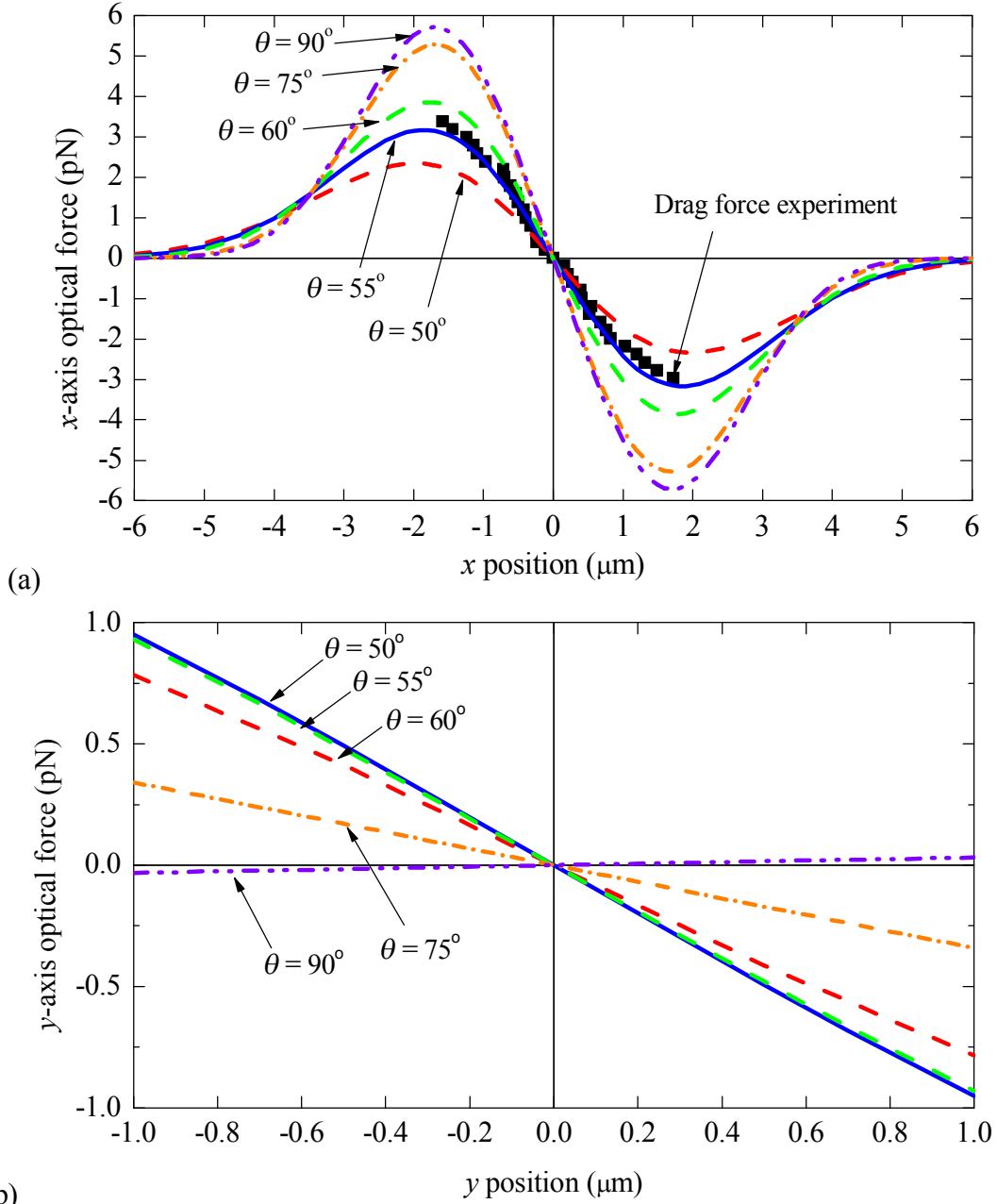


Figure 2.16. The dependence of optical forces on bead displacements along (a) the x axis and (b) the y axis for different fiber inclination angles. The total optical power emitted from both fibers is 15.3 mW. The bead size is 4.74 μm in diameter. The fiber separation along the y axis is 45 μm .

with that observed in the experiment ($-1.6 \mu\text{m}$ along $-x$ and $+1.7 \mu\text{m}$ along $+x$). The x -axis simulation results obtained with different fiber inclination angles (θ) implies that the larger the inclination angle θ , the larger the x -axis optical force (or the spring constant). This is because the

z -axis equilibrium position and the beam waist position change with respect to different inclination angles. For a larger θ , the bead is trapped to a position closer to the beam intersection, where the optical intensity is the highest. Furthermore, as the fiber separation is fixed, the beam waists are closer to the beam intersection for a larger inclination angle. Both factors contribute to the increase of the x -axis optical force when the fiber inclination angle increases.

The spring constant obtained from the drag force experiments is larger than that obtained from the simulations. The sources of errors include the error in the measurement of the fiber inclination angle θ , misalignment of the two fibers, and the beam profile being non-Gaussian and partially polarized. In the experiment, θ measurement error was $\pm 2^\circ$. According to the results shown in Figure 2.16(a), the x -axis optical force with $\theta = 55^\circ$ is 1.5 times larger than that with $\theta = 50^\circ$. The error in the measurement of θ may result in the error between the simulation and the experimental results. The alignment of the two fibers in the xy plane is realized under the microscope objective, which has a good accuracy ($\sim 1 \mu\text{m}$). However, it is difficult to achieve exactly the same height along the z axis for the two fibers. In this case, the z -axis misalignment may result in errors of the simulation results, which are obtained when assuming no misalignment occurs. The polarization is also a possible source of errors, since the light emitted from the lensed tip might still be partially polarized.

The optical forces along the y -axis versus the y -axis displacements with different inclination angles are shown in Figure 2.16 (b). It should be noted that these curves are obtained at fixed, non-zero z coordinates, i.e., the bead motion is considered to be parallel to the y axis. This is only valid for small (in submicrons) y displacements. Since the two optical beams are located in the yz

plane, the y -axis bead displacement is inevitably confined by the two optical beams. For example, at an inclination angle of 50° , the experimentally obtained y -axis displacement was within $-1 \mu\text{m}$ and $1 \mu\text{m}$ in order to maintain a 3D trap. In this sense, y -axis trapping has a less displacement allowance, and hence is less stable compared with the x -axis trapping. However, it is worth emphasizing that, since the experimental calibration with the power spectrum method was carried out only for small y displacements, Figure 2.16(b) does reflect the condition in the experiment. Therefore, the spring constants obtained from Figure 2.16(b) are valid in the vicinity of $y = 0$ and can be used to compare with the experimental results. According to the results shown in Figure 2.16(b), the y -axis optical force as well as the spring constant around the z axis first increases and then decreases as θ is increased from 50° to 90° . The maximum spring constant occurs when θ is around 60° . When $\theta = 90^\circ$, the DFOTs becomes a counter-propagating configuration, and the spring constant is positive, which means the equilibrium on the z axis is no longer stable. This result agrees with the previous work of Sidick *et al.* [97], in which the center position in the counter-propagating DFOTs was found to be unstable when the beam waists were set to be close to each other.

The x and y -axis spring constants of beads with different sizes ($3.01 \mu\text{m}$, $3.50 \mu\text{m}$, $3.93 \mu\text{m}$, and $4.74 \mu\text{m}$) at a power of 18.9 mW were obtained from simulations. The results are included in Table 2.1. The simulation results are consistent with the experimental results obtained from the power spectrum analysis, indicating that larger beads have larger spring constants. In addition to the fiber misalignments and errors in θ measurements discussed above, the influence of the unscattered light can also contribute to the differences between the experimental and the numerical results. Since the ray optics model can serve as a good approximation only when the

bead size is much (>10 times) larger than the wavelength. The fact that the bead sizes are not much larger than the wavelength may cause discrepancy between the experimental and simulation results, especially for small bead sizes ($3.01\ \mu\text{m}$ and $3.50\ \mu\text{m}$).

2.4.4. Robustness of the DFOTs to z-axis misalignment

In a practical system setup, fiber misalignment is inevitable for both inclined DFOTs ($\theta < 90^\circ$) and counter-propagating DFOTs ($\theta = 90^\circ$). Since the y -axis misalignment corresponds to the variation of the fiber separation, only the misalignments along the x and z directions are of interest. If an x -axis misalignment exists, inclined DFOTs and the counter-propagating DFOTs will exhibit similar robustness to such misalignment. The tolerances of the two configurations to z -axis misalignments are important to investigate since it can help determine whether a 3D trapping capability can be maintained. In Figure 2.17, the 2D force fields are obtained for both configurations when there exists a misalignment of $1\ \mu\text{m}$ along the z direction (the right fiber is higher than the left fiber). For counter-propagating DFOTs, the misalignment of $1\ \mu\text{m}$ is a practical value when the two fibers are embedded in the V-grooves of a substrate. [98] The misalignment may be caused by the environmental influence on the adhesive and by the uncontrollable adhesive thickness between the fiber and the inclined walls of the V-groove. In the inclined DFOTs, the heights of the fiber tips along the z axis are measured based on the distance between each optical beam (the auras in Figure 2.3) and the corresponding fiber tip along the y axis. The precision level of $1\ \mu\text{m}$ is readily achievable in the inclined DFOTs setup since the smallest feature size of the objective images is below $1\ \mu\text{m}$. In the simulations, each

fiber is considered to emit a power of 7.65 mW, and the fiber separation is 45 μm along the y axis for both the inclined and the counter-propagating DFOTs.

Figure 2.17(a) shows the results obtained from the inclined DFOTs when $\theta = 50^\circ$. The two beams still have an intersection despite of the existence of a z -axis misalignment. According to the force directions, it can be seen clearly that a 3D trap exists in the vicinity of the point (0, -1 μm). Moreover, the trap position moves to the right of the z axis instead of staying on the z axis when there is no misalignment. This is due to the asymmetry introduced by different beam waist positions with respect to the beam intersection. The beam waist of the left fiber is closer to the beam intersection, and hence it can induce larger optical forces applied to the bead, if the bead is moved on the z axis. In order to balance this asymmetry, the bead will be trapped closer to the beam emitted from the left fiber, which is to the right of the z axis. The dashed curve in Figure 2.17(a) defines the region where the bead will be trapped. If the bead is located above this curve, it will be trapped in three dimensions. The optical force is not strong enough to lift up the bead if it is below this curve. If the bead is to the right or the left of the curve, it will be trapped by a single optical beam and pushed downstream.

The results obtained from the counter-propagating DFOTs are shown in Figure 2.17(b). The force field is “twisted” counter-clockwise in the vicinity of the origin, which means that there is no effective trapping region where all the surrounding forces are pointing inside. Instead of being trapped at a stable position, the bead will circle around the origin, if the bead is close (i.e., < 2 μm) to the origin. If the bead is far (i.e., > 4 μm) from the origin, SFOTs become dominant and the bead will be pushed away and moved along the optical axis of one fiber.

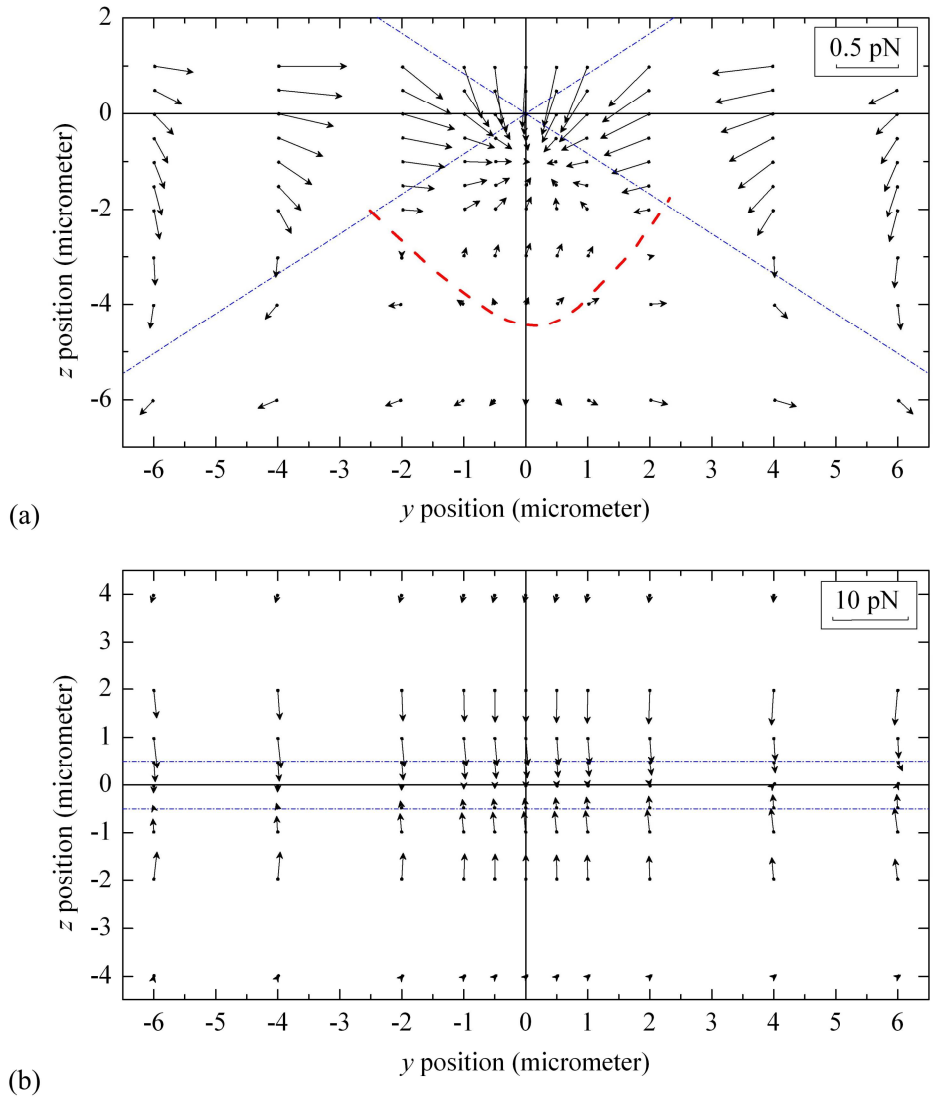


Figure 2.17. Simulation results of the forces applied on a 4.74- μm bead in the yz plane with a misalignment of 1 μm along the z axis for (a) the inclined DFOTs ($\theta = 50^\circ$) and (b) the counter propagation DFOTs ($\theta = 90^\circ$). The dash-dotted lines indicate the optical axes of the two fibers. It is noted that the forces are the net forces of optical forces, gravity, and buoyancy applied on the beads.

By comparing the force fields of the two systems with respect to z -axis misalignment, it can be seen that, with the same fiber separation, the inclined DFOTs are more robust to the misalignment along the z direction. Although z -axis fiber misalignment in the inclined DFOTs

influences the trapping efficiency as mentioned previously, its 3D trapping capability is retained. However, the counter-propagating DFOTs will lose the 3D trapping capability even with a 1- μm misalignment due to the twisted force field. When the z -axis misalignment increases, the twisting effect of the counter-propagating DFOTs becomes even worse and the trapping becomes more difficult. By contrast, simulation results show that the inclined DFOTs can still achieve a stable 3D trap with a z -axis misalignment of 8 μm .

When a much larger fiber separation or cleaved fibers instead of lensed fibers are used, the counter-propagating DFOTs will suffer less from the z -axis misalignment. In this sense, large ($> 100 \mu\text{m}$) fiber separations and cleaved fibers are preferable for the counter-propagating DFOTs to obtain stable trapping of particles. By contrast, for the inclined DFOTs, lensed fibers and smaller fiber separations are preferable to increase the trapping efficiency and to ensure the 3D trapping ability.

As for the limitations of the inclined DFOTs compared with the counter-propagation DFOTs, the inclined DFOTs have a longer fiber suspension length, and hence the stability of the trap is more susceptible to the movement of the fibers, which may be induced by the flow passing through the fibers. In addition, although the block containing two fibers (the board with two attached fibers in Figure 2.1(b)) provides the inclined DFOTs flexibility, the complexity of the system is inevitably increased by introducing another surface for attaching the block besides the substrate. Therefore, the counter-propagating DFOTs are simpler and can provide stable traps if fibers are properly aligned, whereas the inclined DFOTs are more flexible and more robust to the fiber misalignment.

2.5. Optical trapping of yeast cells with inclined DFOTs

2.5.1. 3D Cell trapping

Yeast cells have been successfully trapped by using the inclined DFOTs. The images of the 3D motion of a yeast cell manipulated by using the dual fiber tweezers are shown in Figure 2.18. The trapped cell (the cell in the center of the images) is levitated above the coverglass so that it is located at a higher level than the other cells. Other cells are out of focus and blurred. The dark circle identifies the reference cell in all the photographs, which stays still when the trapped cell is moved. Arrows and circles with crosses or dots are used to show the direction of the cell movement. The cell is first moved downward in the focal plane (Figure 2.18(A)-(C)), then to the

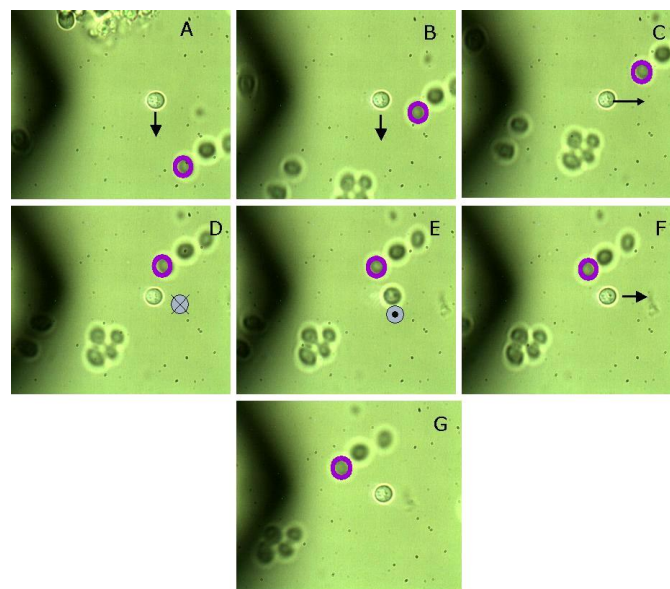


Figure 2.18. Images of 3D yeast cell manipulation by using inclined DFOTs, obtained with an Olympus 100*/1.25 oil-immersed objective.

right (Figure 2.18(C)-(D)). In Figure 2.18(E), as the optical trap is removed by switching the laser off, the cell escapes along the vertical direction toward the coverglass. Once the laser is turned on again, the cell is retrapped back to the focal plane (Figure 2.18(F)). Finally, it is again moved to the right within the trap (Figure 2.18(G)).

2.5.2. Spring constant calibration of yeast cell trapping

Since the cells are spheroids rather than spheres, the average lengths of the long and short axes are represented by the radius r in Eq. (2-1). As the drag force due to a low Reynolds number flow is not sensitive to the shape of the particles [99], it is reasonable to make such an approximation. Two cells in the optical trap are used for calibration of the effective spring constants. Here, only the drag force method (discussed in Section 2.3.2) was used to calibrate the trapping force on yeast cells. The power spectrum method is not suitable for cell measurement because it relies on the detection of the scattered light. Since the internal structures of cells are not uniform, the scattered light is unpredicted when cells perform the Brownian motion. In this sense, the advantages of power spectrum method, namely high measurement resolution and well characterized detection signals, do not exist any more. In the experiments, the distance between the two fibers is 27 μm and the inclination angle of each fiber is 45°. About 3 mW laser power is coupled into each optical fiber.

The first calibrated cell (Cell 1) is shown in Figure 2.19(a). The experimental results and fitted curve of the optical forces and the cell displacements (F - x) relationship are shown in Figure 2.19(b). The maximum displacement of the cell before escaping from the trap varies from 0.7

μm to $0.8 \mu\text{m}$. Based on the curve fitting, the effective spring constant of the optical trap for Cell 1 is obtained as $1.49 \text{ pN}/\mu\text{m}$. For comparison, another cell (Cell 2) was also manipulated and the experimental results are shown in Figure 2.20. In this case, the maximum displacement before the cell escapes from the trap was found to be larger, ranging from $1.3 \mu\text{m}$ to $1.5 \mu\text{m}$. The spring constant obtained from the fitted F-x curve is $0.70 \text{ pN}/\mu\text{m}$ for Cell 2, which indicates a difference in the spring constants between Cell 1 and Cell 2.

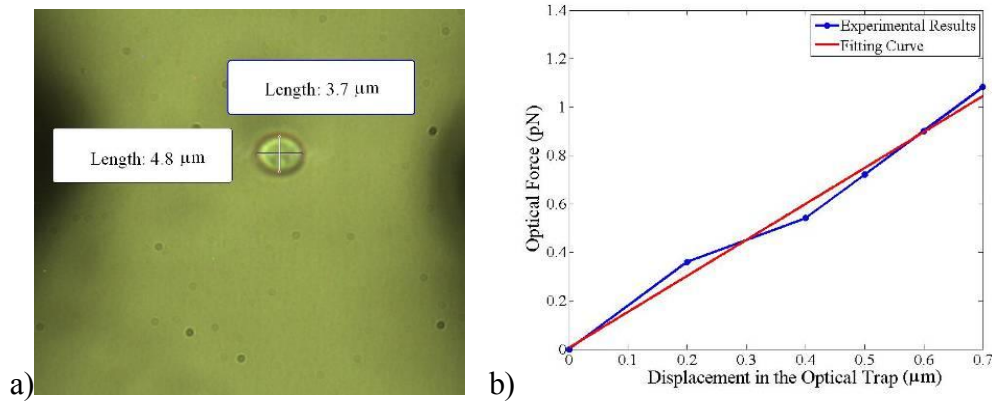


Figure 2.19. (a) Photograph of Cell 1 and (b) experimental results and fitted curve of the relationship between optical forces and cell displacements in the optical tap.

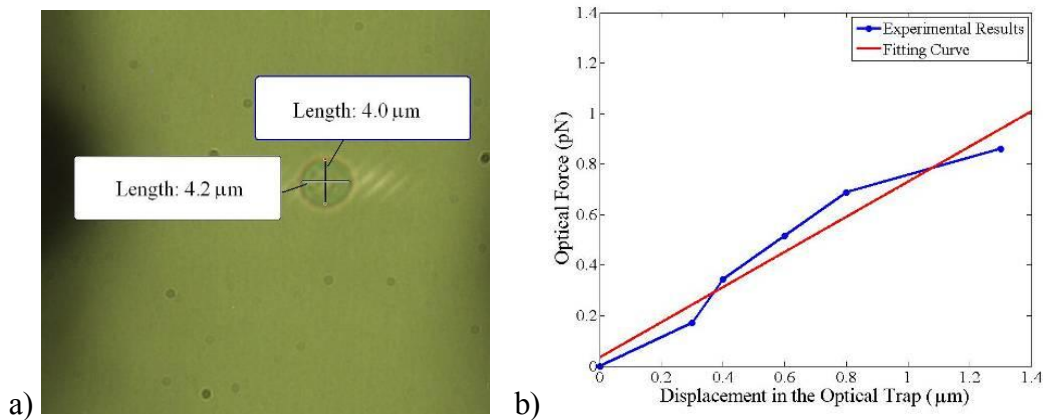


Figure 2.20. (a) Photograph of Cell 2 and (b) experimental results and fitted curve of the relationship between optical forces and cell displacements in the optical tap.

According to the cell-manipulation results, the dual fiber tweezers are capable of manipulating cells in three dimensions. Because fibers have better flexibility than microscope objectives, ideally, it is possible to manipulate cells at any location of the solution, not limited by the working distance of the objective. Furthermore, one can levitate cells from a surface, which helps overcome the limitation of the counter-propagating fiber tweezers. The calibration results (Figure 2.19(b) and Figure 2.20(b)) show that there is a linear relationship between the optical forces and cell displacements, which enables the use of the fiber tweezers system as a biological force sensor. However, the spring constant is different for different cells although the arrangement of fiber tweezers remains unchanged. It is possible to calibrate the spring constant for each cell before working with it, but this can be time-consuming. Dielectric beads can also be used as handles to manipulate cells. In this case, a constant spring constant can be obtained before working with cells, since the dielectric beads have identical size. However, using beads will introduce other issues such as interference with cells.

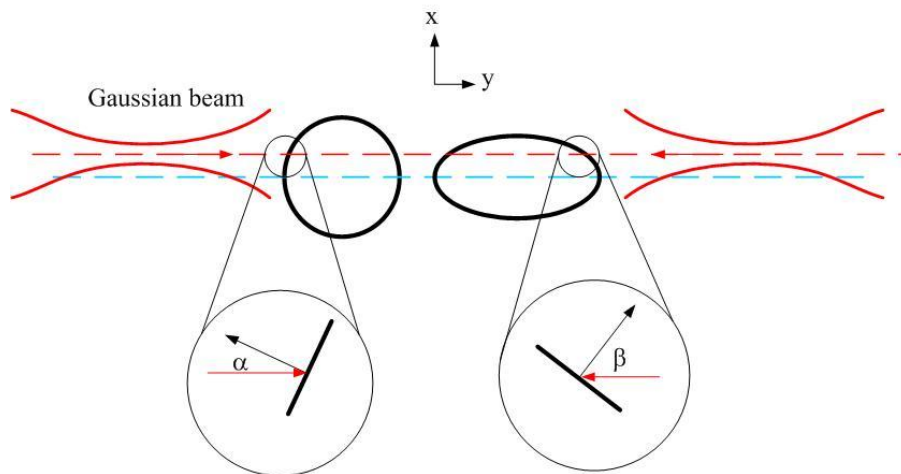


Figure 2.21. Schematic of round cell and prolate cells in optical traps.

According to the calibration results, an interesting observation is that the spring constants for the two cells differ by a factor of two. The cell with round shape has smaller spring constant, and thus it has higher sensitivity for force measurements. A possible reason can be described as follows. The prolate cell always aligns its long axis along the optical axis (y direction in Figure 2.21) with the cell center on the optical axis in equilibrium. When the displacements (distance between the two broken lines) along the x direction for the two cells are the same, the optical axis is closer to the x pole of the prolate cell. Therefore, the incident angle is also larger for the prolate cell ($\beta > \alpha$ in Figure 2.21). The larger incident angle leads to a larger gradient force (discussed in the next section), which results in a larger spring constant for the prolate cell.

2.5.3. *Simulation results on ellipsoidal particle trapping*

As can be seen in Figure 2.19 and Figure 2.20, the yeast cells used in the experiments are actually ellipsoidal rather than spherical. Therefore, a prolate spheroid particle is used as a trapped object in the simulations of the inclined DFOTs. The model used for carrying out the simulations has been discussed previously in Section 2.4. For a prolate spheroid,

$\frac{x^2 + y^2}{b^2} + \frac{z^2}{a^2} = 1$, the parametric equations are

$$\vec{r} = \begin{bmatrix} x \\ y \\ z \end{bmatrix} = \begin{bmatrix} b \sin \theta \cos \varphi \\ b \sin \theta \sin \varphi \\ a \cos \theta \end{bmatrix}, \quad (2-21)$$

for the polar angle $\theta \in [0, \pi]$ and the azimuthal angle $\varphi \in [0, 2\pi]$. Here, a is the polar radius, b is the equatorial radius, and $a > b$. Therefore, the normal vector can be obtained by

$$\vec{n} = \frac{\partial \vec{r}}{\partial \theta} \times \frac{\partial \vec{r}}{\partial \varphi} = \begin{bmatrix} ab \sin^2 \theta \cos \varphi \\ ab \sin^2 \theta \sin \varphi \\ b^2 \sin \theta \cos \theta \end{bmatrix}. \quad (2-22)$$

By normalizing \vec{n} , the normal vector \overline{nor} of the surface can be obtained. The surface area dS is

$$dS = \|\vec{n}\| d\theta d\varphi. \quad (2-23)$$

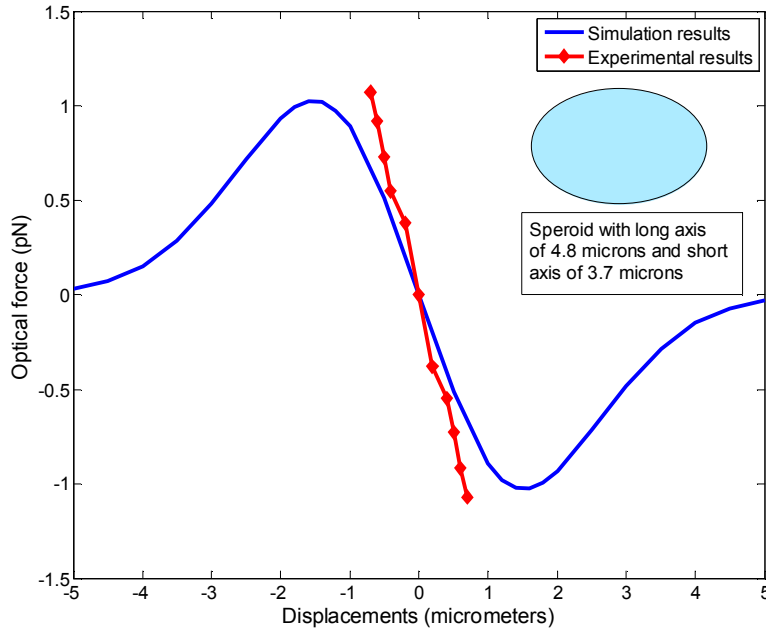


Figure 2.22. Simulation of the optical force versus the displacement for a spheroid particle with the same size as Cell 1 in Figure 2.19. Experimental results are also plotted for comparison.

The parameters used in the simulation are listed as the following. The inclination angle for the two fibers is $\pi/4$. Each of the Gaussian beams has a waist of $2 \mu\text{m}$ in diameter and a power of 3 mW, as measured in the experiments. The separation of the two laser beams along the y axis is $19 \mu\text{m}$. The refractive index of the water is 1.33, and the refractive index of the yeast cell is 1.5 [71]. It is noted that in the simulations the displacement of the particle is always along the x

direction (see Figure 2.2(b)), and that the polar axis a is along the y axis, similar to the situation in the experiment. The optical forces acting on two spheroids with the same sizes as the two cells calibrated in experiment are plotted as a function of the displacements in Figure 2.22 (Cell 1) and Figure 2.23 (Cell 2). Experimental results are also included in these figures for comparison. It can be seen that the prolate cell has a larger spring constant than the round cell.

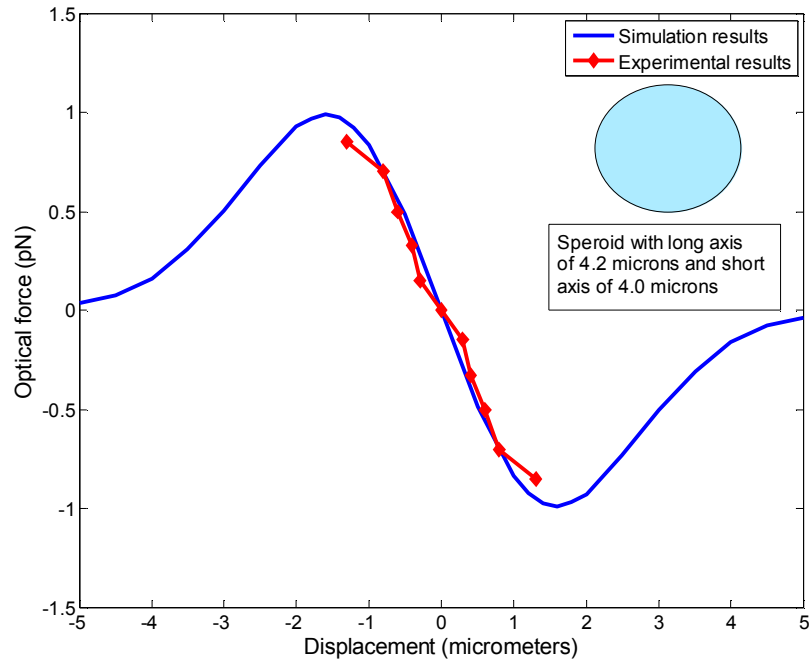


Figure 2.23. Simulation for the optical force versus the displacement for a spheroid particle with the same size as Cell 2 in Figure 2.20. Experimental results are also plotted for comparison

It can be seen that the simulation results coincide with experiments well for Cell 2, but more error exists for Cell 1. The errors might come from the calculation of the drag force for the spheroidal cell. To get the optical forces from the experimental results, a sphere is used to calculate the drag force by the water flow. The radius of the sphere is estimated by averaging the

polar radius and the equatorial radius. This estimation may introduce errors to the spring constants obtained from the experiments.

2.6. Summary

In this chapter, experimental study and numerical investigation of the inclined DFOTs system have been carried out in order to obtain a fundamental understanding of the system. 3D trapping ability of the inclined DFOTs has been demonstrated with both silica beads and yeast cells. For the first time, the trapping efficiency of particles with different sizes has been experimentally calibrated on the xy plane with two methods: drag force method and power spectrum analysis. The influence of the particle size and the fiber inclination angles over the trapping performance in three dimensions has been investigated with numerical simulations based on the ray optics model. Mapping of the optical forces on the yz plane has also been carried out. The simulation results indicate that the inclined DFOTs are more robust to the z -axis fiber misalignments compared with commonly used counter-propagating DFOTs, which makes the inclined DFOTs easier to set up. In this chapter, *an enhanced understanding of the inclined DFOTs system was achieved, which is an important contribution of this dissertation work.*

Chapter 3. Multiple traps created with inclined DFOTs

In this chapter, three optical traps, one 3D and two 2D, created with the inclined DFOTs system are studied both experimentally and numerically. This is the first time that multiple traps at different vertical levels with adjustable separations are realized with fiber optical tweezers. Moreover, multiple functionalities are realized with the multiple traps, including particle separation, particle grouping, and particle stacking, both in two dimensions and in three dimensions, rod alignment, rod rotation, and optical binding of beads and rods. The mechanisms of these functionalities are studied numerically by mapping the optical forces and optical torques. The multiple functionalities achieved with the inclined DFOTs system can address the problem of limited functionalities of the existing fiber optical tweezers.

The rest of this chapter is organized as follows. In Section 3.1, existing multiple optical traps, especially those created with optical fibers, are briefly introduced, with their limitations summarized and discussed. The experimental setup and working principles of the multiple traps are explained in Sections 3.2 and 3.3, respectively. Next, detailed experimental and numerical study of multiple functionalities achieved with the multiple traps are carried out for different particles, including silica beads in Section 3.4 and glass microrods in Section 3.5.

3.1. Review of existing multiple optical trapping systems

Although optical tweezers (OTs) were originally designed to manipulate a single particle at a time [88], multiple optical traps that can provide simultaneous manipulation of multiple particles are desirable in many applications. Multiple optical traps have been used to characterize the interactions of colloidal systems [100], to assemble particles into complex structures [101, 102], and to trap and orient delicate particles [103]. Various techniques have been employed to generate multiple optical traps, such as one or two objectives with multiple input beams [100, 104, 16], time-sharing approaches with a scanning laser beam [103], interference of multiple beams [34], fringes created with a phase-only rectangular ridge [105], diffractive optics [106], and, more commonly, computer-generated holograms [102, 15]. All of these methods make use of traditional objective-based OTs, which are bulky, expensive, and hard to integrate.

Particle manipulation methods that can provide multiple traps in parallel and be readily integrated in miniaturized systems for biological analysis and diagnostics [104, 20], e.g., lab-on-a-chip systems, are of great interest. In these integrated and scaled-down devices, the large objectives needed to enable optical traps have to be replaced by smaller units. In literature, an array of parabolic micromirrors has been used to create multiple traps with each trap formed at the focus of a micromirror [107]. Compared with these embedded micromirrors, optical traps built with optical fibers provide a more flexible solution towards compact, integrable multiple traps. Optical fibers are small in size and biocompatible [21], and therefore can be potentially integrated in a lab-on-a-chip system for biological applications. Multiple two-dimensional (2D) optical traps have been realized previously with a bundle of optical fibers [88], in which each individual fiber forms a separate trap. More recently, counter-propagating dual photonic crystal fiber traps have been demonstrated to confine multiple particles in the intensity minima or

maxima of the standing waves. [108] In another work, a Bessel beam emitted from a single optical fiber with an axicon-shaped fiber tip has been employed to trap multiple particles with a low refractive index. [109] For the abovementioned fiber-based multiple traps built with fiber bundles and standing waves, the separations between the traps cannot be adjusted. In addition to multiple optical traps, optical binding using fiber-based systems has also been exploited to confine particles of micrometers or sub-micrometers, such as the single optical fiber with an axicon-shaped fiber tip [110] and the counter-propagating dual fiber traps [108, 111]. The optical binding effects can be explained as that multiple particles are distributed in a self-organized way, due to the interaction between the particles and the optical field, to minimize the energy of the whole particle-light system. [111] The fiber-based optical binding introduced above can only confine particles in a chain-like one-dimensional structure with fixed particle separations.

In this chapter, multiple optical traps created with an inclined dual-fiber optical tweezers (DFOTs) system are investigated. Previously in Chapter 2, the performance of such a system for 3D trapping of single particles has been investigated both experimentally and numerically. Here, three optical traps are formed on different vertical planes, one 3D trap below the beam intersection and two 2D traps on the cover glass. The inclined DFOTs system can be controlled as a whole block containing two fibers, which enables controllable positions of the three traps with a single actuator. The trap separations are readily tunable by changing the vertical position of the block. Moreover, it is demonstrated experimentally that the multiple traps can perform multiple functions, which will be detailed in Sections 3.4.1 and 3.5.3.

3.2. Experimental setup

The experimental setup is similar with that described in Section 2.1, except a block is used here to facilitate the position control of the traps, as shown in Figure 3.1. The block contains a common board with both of the lensed fibers attached to, so that the whole system can be moved as a single module. The total optical power emitted from both fibers was fixed to be 15.3 mW. A coverglass with a water drop containing silica beads (Bangs Laboratories, Inc.) and glass rods (kindly donated by Prof. Wolfgang Losert at the University of Maryland) was placed on a two-dimensional stage. The rods are $3.5\ \mu\text{m}$ in diameter and $8\text{-}15\ \mu\text{m}$ in length. The silica beads have a diameter of $4.74\ \mu\text{m}$ and a density of $2.0\ \text{g}/\text{cm}^3$.

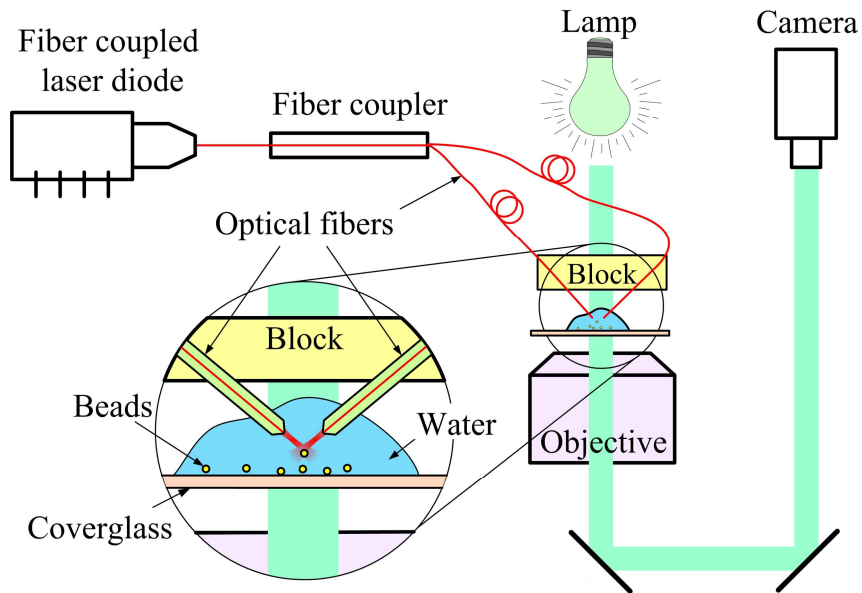


Figure 3.1. Experimental arrangement of the inclined DFOTs for creating multiple traps.

3.3. Principles of multiple traps created with inclined DFOTs

In the inclined DFOTs shown in Figure 3.2, there are one 3D trap formed at Bead 2 and two 2D traps at Beads 1 and 3. It is noted that, in this section, we use only spherical beads to explain the working principles of the multiple traps for convenience. The working principles with micro-rods will be specifically explained later in Section 3.5.2. Bead 2 is trapped by the 3D trap that we systematically studied in Chapter 2. The 2D traps at Bead 1 and Bead 3 are similar with each other due to symmetry, so here only the trapping of Bead 1 is discussed. The beam from Fiber 1 is much further away from Bead 1 than that from Fiber 2, so only the optical forces applied by the beam from Fiber 2 is considered. When the gradient force (F_g) and the scattering force (F_s) reach equilibrium with the normal force (N) applied by the substrate, Bead 1 is trapped on the substrate. By moving the two fibers as a block, the separations between the traps as well as the trap positions can be adjusted.

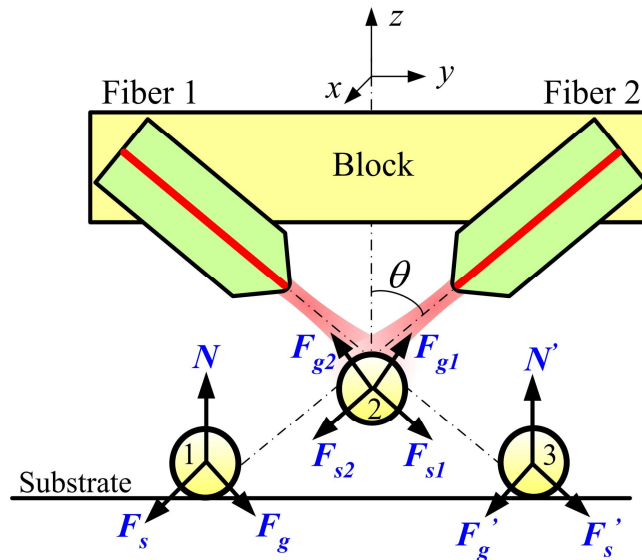


Figure 3.2. Principle of multiple traps created by using the inclined DFOTs.

3.4. Investigation of multiple traps and multiple functionalities with silica beads

In this section, experimental demonstration of multiple traps and multiple functions with silica beads is presented. Numerical simulations are performed to better understand the experimental results. Discussion and guidelines to improve the performance of the system are provided at the end of the section.

3.4.1. Experimental demonstration of multiple traps and multiple functionalities with silica beads

3.4.1.1. Demonstration of multiple traps and bead separation

The images captured consecutively from a video clip of the multiple traps are shown in Figure 3.3. There were five beads in the field-of-view, each labeled with a number to track their movements. The two shadows on both sides of the pictures are the fiber tips, which are out-of-focus and blurry. The beam intersection was initially close to the coverglass, which formed an aura as can be seen in the center of Figure 3.3(a). With the coverglass moved around, Beads 1, 2, and 3 were trapped, as shown in Figure 3.3(b). The three trapped beads were in contact with each other due to the position of the beam intersection. Beads 4 and 5 were free reference beads, which were lying on the coverglass and could be moved together with the coverglass. When the

fiber block was moved along $+z$ direction, the three trapped beads were separated: the separation between Beads 1 and 3 increased and Bead 2 was lifted up from the coverglass, as shown in Figure 3.3(b)–(d). At this moment, Bead 2 was trapped in three dimensions while Beads 1 and 3 were trapped in two dimensions on the coverglass. Then, the traps were fixed and the coverglass was moved in xy plane (see Figure 3.3(d)–(f)). During this process, all three traps remained stable. As the height of the fiber block was increased further, the two 2D traps became weaker and weaker. Beads 1 and 3 were found to remain trapped when the height of Bead 2 was up to 30 μm above the coverglass (the separation between Beads 1 and 3 were around 70 μm).

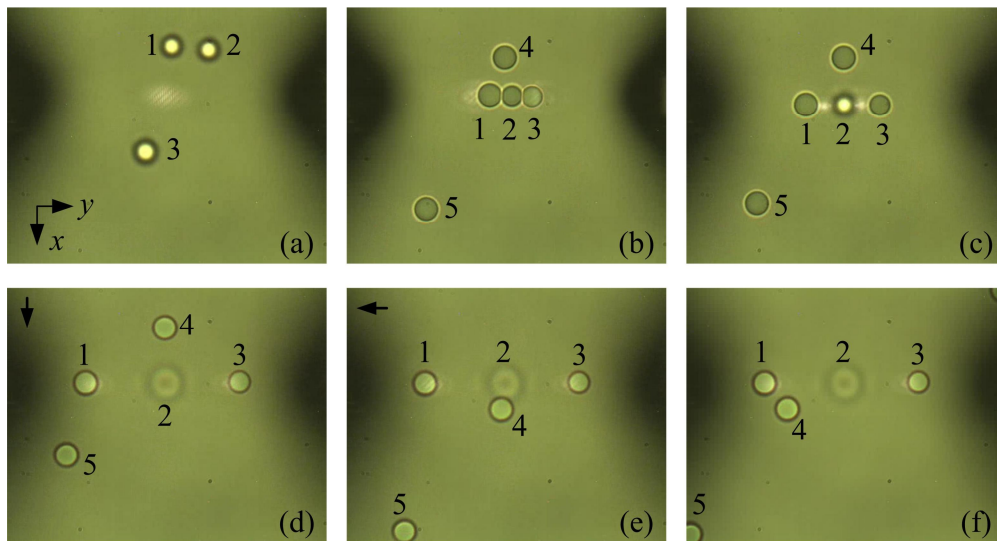


Figure 3.3. Images of beads manipulated in the multiple traps. (a) Three free beads on the coverglass. (b) Beads 1, 2, and 3 trapped in contact. (b)-(d) The fiber block was moved upward along $+z$ and trapped beads had been separated. (d)-(f) The coverglass was moved along $+x$ and then along $-y$. The arrows in (d) and (e) indicate the next movement direction of the coverglass. The xy coordinate system is shown at the lower left corner of (a). The bead size is 4.74 μm in diameter.

These experimental results demonstrate that the inclined DFOTs can be used to simultaneously manipulate multiple particles at different vertical levels as well as align particles in line. The positions and separations of the three traps can be controlled by moving the fiber block. When

the fiber block is lifted up, both the height of the 3D trap and the separation between the two 2D traps are increased, rendering the ability to separate particles that stick together. Moreover, the ability of particle separation can be used to study the interaction forces between the particles in colloidal systems.

The multiple traps created with the inclined DFOTs also bestow this setup multiple functionalities. In addition to particle separations, the capability of bead stacking, bead grouping, and trapping multiple beads in three dimensions, will be detailed in the following from Section 3.4.1.2 to Section 3.4.1.4.

3.4.1.2. Bead stacking

To better demonstrate particle stacking, four beads were trapped initially by the multiple traps, as shown in Figure 3.4(a). At this moment, Bead 2 was trapped in the 3D trap, and the rest of the beads were trapped by the two 2D traps, as illustrated in Figure 3.4(d). When the beam intersection was brought close to the coverglass by lowering down the fiber block, the separations between the four beads became smaller, as shown in Figure 3.4(b) and (e). As the fiber block was lowered down further, Beads 1, 2, and 3 became in contact with each other, and Bead 4 was stacked up above Bead 3, as shown in Figure 3.4(c) and Figure 3.4(f). Particle stacking has been realized both in two dimensions (in contact with the coverglass) and in three dimensions (without contacting the coverglass). The 3D particle stacking will be shown later in Section 3.4.1.4.

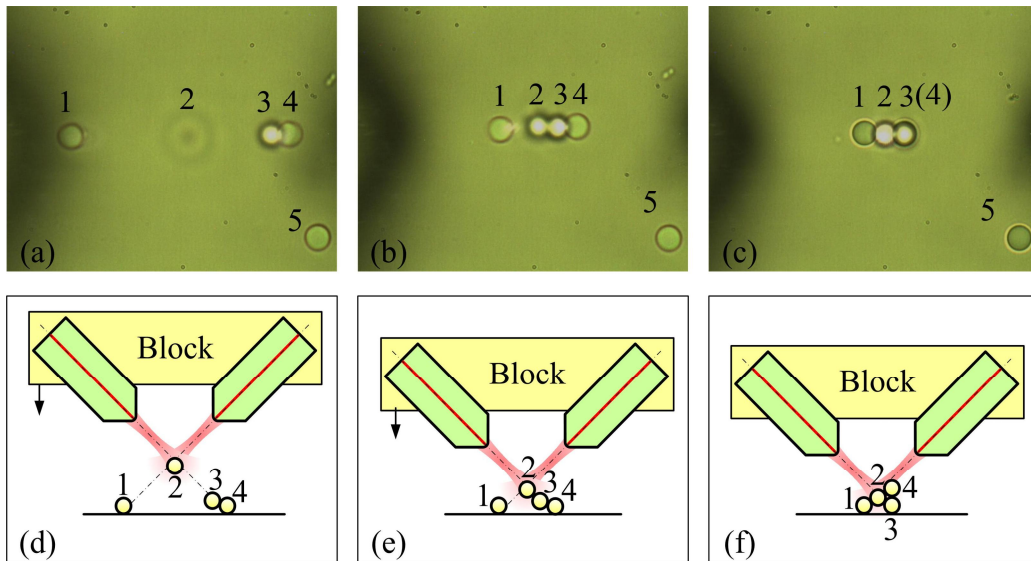


Figure 3.4. Experimental demonstration of particle stacking. With the fiber block lowered down toward the coverglass, the four beads were (a) first separated, (b) then brought into contact, and (c) finally stacked. (a)-(c): pictures captured from a video clip; (d)-(f): sketches illustrating pictures (a)-(c), respectively. The bead size is $4.74 \mu\text{m}$ in diameter.

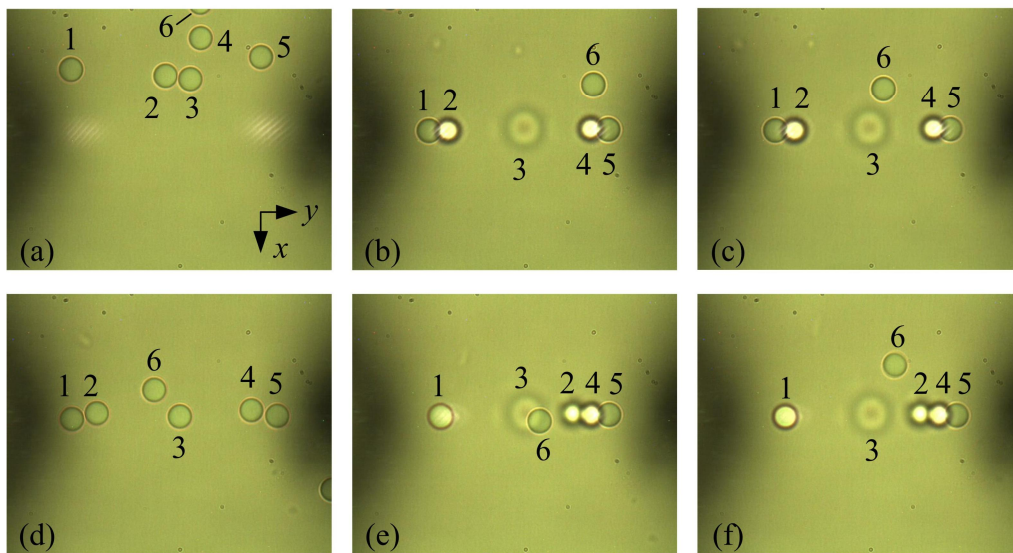


Figure 3.5. Experimental demonstration of particle grouping. (a) Six free beads were initially lying on the substrate. (b) Beads 1 to 5 were trapped and separated into three groups. Bead 6 was free and served as the reference of the coverglass movement. (c) The coverglass was move along $-y$. (d) The laser was switched off and all beads returned to the coverglass. (e) After the laser was turned on, Beads 1 to 5 were separated into three new groups, while Bead 6 remained free. (f) The coverglass was moved along $-x$. The bead size is $4.74 \mu\text{m}$ in diameter.

3.4.1.3. *Bead grouping*

For particle grouping, five beads (Beads 1 to 5) were first separated into three groups by the three traps created by the inclined DFOTs, as shown in Figure 3.5(b). Each 2D trap confined two beads in a group and the 3D trap trapped one bead above the other two groups. As the coverglass was moved along $-y$ direction (Figure 3.5(c)), Beads 1 to 5 remain trapped in the three groups. The laser was then switched off to allow all beads to return freely to the coverglass and to be regrouped. After regrouping, one bead (Bead 1) was trapped solely by one of the 2D traps, and three other beads (Beads 2, 4 and 5) were trapped in a group by the other 2D trap, with another bead (Bead 3) trapped by the 3D trap, as shown in Figure 3.5(e). When the coverglass was moved in $-x$ direction (Figure 3.5(f)), the five beads remained trapped in their groups, indicating that the traps and grouping were stable. It should be noted that there is an upper limit of the number of particles that can be grouped. The number of particles that can be trapped in each trap is limited by both the beam parameters (e.g., power, size, and wavelength) and the particle size. With the beam parameters and the particle size used in the experiment, the largest number of trapped particles in one 2D trap is found to be three. The largest number of particles that can be trapped by the 3D trap is also three, which will be shown in Section 2.6. Therefore, as many as 12 beads can be arranged into 4 groups, with three groups trapped and the rest one untrapped. The particles can be grouped in an arbitrary sequence, and hence can be used to group particles by their characteristics, such as sizes and materials.

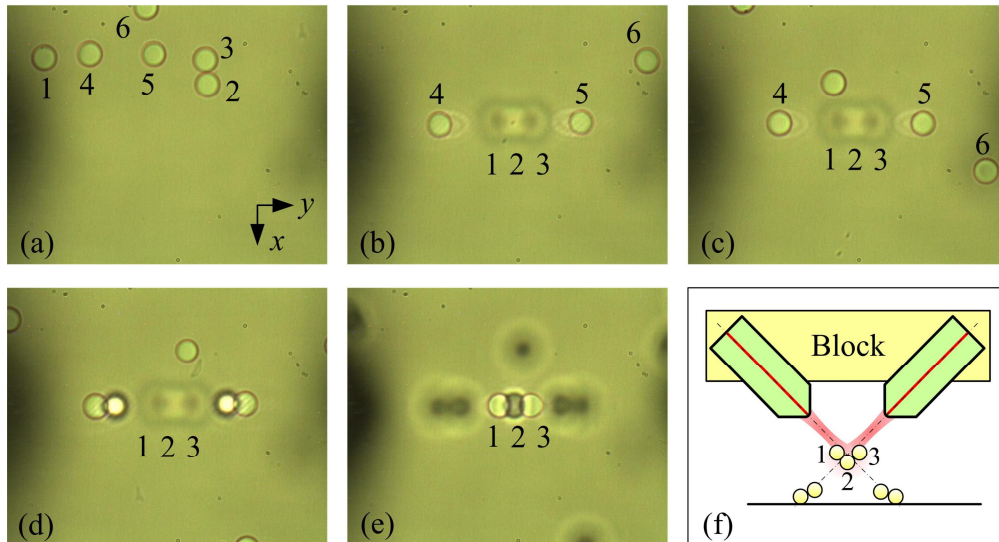


Figure 3.6. Experimental demonstration of multiple particles trapped in three dimensions. (a) Six free beads were lying on the coverglass. (b) Beads 1, 2, and 3 were trapped by the 3D trap, and Bead 4 and 5 were trapped by the 2D traps. Bead 6 was free and served as the reference of the coverglass movement. (c) The coverglass was moved along $+x$, with the trapped beads staying stable. (d)–(e) The objective lens was moved along $+z$ direction. Bead 2 was first brought into focus before Beads 1 and 3 (see the media). Beads 1 and 3 were in focus in (e). (f) The sketch illustrating the images (d) and (e).

3.4.1.4. Multiple beads trapping and stacking in three dimensions

In addition to 3D trapping of single particles discussed previously in Chapter 2, the 3D trap of the inclined DFOTs system was found to be able to trap and stack multiple particles in three dimensions. Six free beads stayed rest on the coverglass initially as shown in Figure 3.6(a). When the fiber block was lowered down and then lifted up, three beads (Beads 1, 2, and 3) were trapped by the 3D trap, as shown in Figure 3.6(b). As the coverglass was moved along the x direction, the trapping of the three beads remained stable, as shown in Figure 3.6(c). Each of the 2D traps was still able to trap two beads with three beads trapped by the 3D trap, as shown in Figure 3.6(d). As the objective was moved upwards along the z direction, Bead 2 was brought

into focus before Beads 1 and 3, which implies that Beads 1 and 3 were located higher along the z direction than Bead 2. Figure 3.6(e) shows that Bead 2 was out of focus when Beads 1 and 3 were in focus. All the bead groups/stacks are fully translatable across the coverglass. In the experiment, the largest number of silica beads that can be trapped simultaneously is nine, with three particles in each trap. Multiple particles trapping enables parallel manipulation of a group of particles of interest. Particle stacking can be used to create controllable artificial lattice structures with certain desirable properties that do not exist in nature [112].

3.4.2. Numerical study of multiple traps and multiple functionalities with silica beads

Based on the ray-optics model discussed in Chapter 2, numerical simulations are carried out to better understand the experimental results. The parameters used to obtain the simulation results are consistent with those used in the experiment.

The net force (F_n) of the optical force, gravity, and buoyancy experienced by a bead in the trapping area is mapped on the yz plane, as shown in Figure 3.7(a). Each arrow represents the net force applied on a bead that is centered at the starting point of the arrow. The arrow direction and length indicate the force direction and magnitude, respectively. The optical axes (dash-dotted lines) of the two optical beams exiting from the two fibers are plotted in Figure 3.7(a), which intersect at the origin of the xyz coordinate system. It should be noted that here, the optical forces are obtained under the assumption that only one bead exists in the optical field. However, in the real experimental situation that multiple beads are trapped, the distortion of the optical field by the upstream beads will influence the optical force applied on the downstream beads. This

influence is beneficial to the trapping of downstream beads, because the upstream beads focus the light as a lens and the intensity gradient of the light can be increased, resulting in tighter downstream traps.

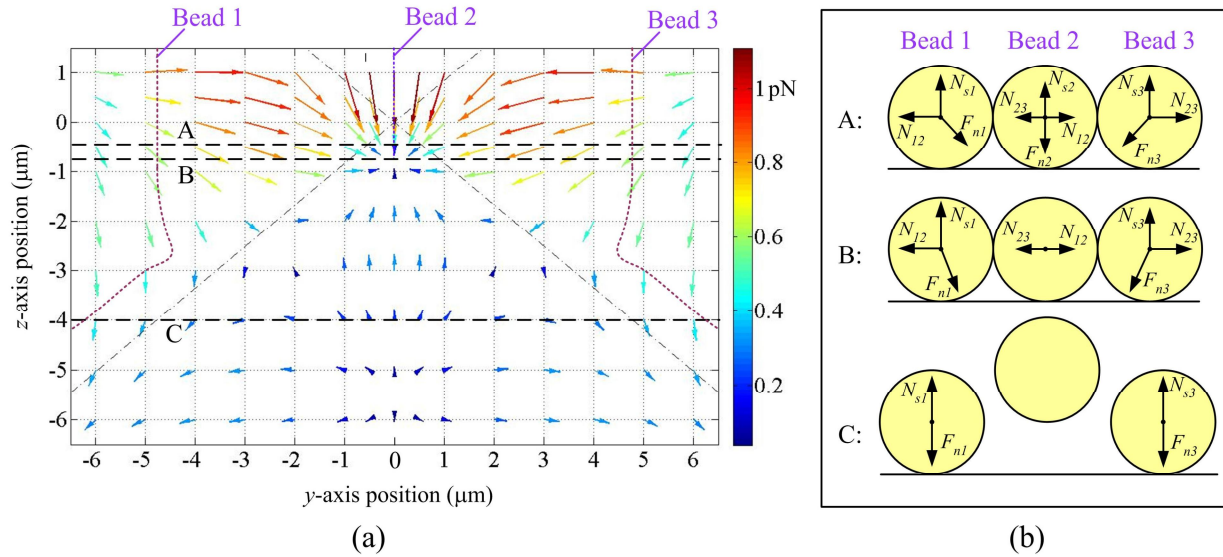


Figure 3.7. Simulation results to explain the principles of particle separation. (a) The yz plane force field of F_n (the net force of the optical force, gravity, and buoyancy, excluding the normal forces between the beads and between the beads and the coverglass); (b) free body diagrams of three beads (Beads 1, 2, and 3) at three different vertical levels shown in (a): Level A, B, and C. F_{ni} stands for F_n of Bead i . N_{si} and N_{ij} stand for the normal forces between the substrate (the coverglass) and Bead i and between Beads i and j , respectively.

Bead separation observed in the experiment can be explained according to the simulation results. Three beads corresponding to Beads 1, 2, and 3 in Figure 3.3 are considered lying on a coverglass and located near the beam intersection initially. When the coverglass is moved along $-z$ direction, the trajectories of the three trap positions (the dotted curves in Figure 3.7(a)) are obtained as the equilibrium positions of the bead centers corresponding to different vertical levels of the coverglass. The equilibrium of Bead 2 is always located on the z axis due to the symmetry of the system. The free body diagrams of the trapped beads centered at three different

vertical levels A, B, and C are shown in Figure 3.7(b). According to the simulations (data not shown), the 3D trap is located $0.87 \mu\text{m}$ below the beam intersection (i.e., at point $(0, 0, -0.87 \mu\text{m})$), where the net force (F_n) is zero. It is noted that this 3D trap position is the lowest equilibrium position of Bead 2. When the three beads are located above the 3D trap, for example, at $z = -0.5 \mu\text{m}$ (Level A in Figure 3.7(a)), i.e., the coverglass is $2.87 \mu\text{m}$ below the beam intersection, the y -components of F_{n1} and F_{n3} are pointing to the center bead (Bead 2). Therefore, the normal forces (N_{12} and N_{23}) are formed between the three beads. At the same time, the coverglass prevents the beads from being pushed down by the z -components of F_{n1} and F_{n3} . This corresponds to the experimental results shown in Figure 3.3(b). As the coverglass is moved along $-z$ direction, the net force (F_{n2}) applied to Bead 2 decreases and the normal forces (N_{12} and N_{23}) become smaller. At $z = -1.03 \mu\text{m}$ (Level B), F_{n2} reaches zero and the normal force (N_{s2}) disappears, while Beads 1 and 3 are still pushed against the coverglass by F_{n1} and F_{n3} . As the coverglass is lowered beyond Level B, Bead 2 is lifted up from the coverglass and Beads 1 and 3 are pushed towards each other by F_{n1} and F_{n3} , respectively. This explains the reason why the trajectories of Beads 1 and 3 curve slightly inside towards the z axis. In the experiment, this effect was observed as bead stacking, as shown in Figure 3.4. As the coverglass is lowered further, the y -components of F_{n1} and F_{n3} gradually change their directions and point away from the z axis, which results in the separation of Beads 1 and 3. For example, at $z = -4 \mu\text{m}$ (Level C), Beads 1 and 3 separate and eventually settle at the positions of $y = -6.2 \mu\text{m}$ and $6.2 \mu\text{m}$, respectively. These simulation results can be used to explain the experimental results shown in Figure 3.3(c)-(f). It is noted that the above discussion are based on the condition that the beads fall down from a position above the beam intersection. If, in another case, the beads are originally located below the beam intersection with Bead 2 centered on the z axis, Beads 1 and 3

will still be trapped in the 2D traps, but the trajectory of Bead 2 will depend on its original position, as discussed in Section 2.4.2. If the net force points up at its original position (for example, $z=-4$), Bead 2 will be lifted and trapped by the 3D trap. Otherwise, Bead 2 will be pushed downwards along the z axis. Due to the Brownian motion, Bead 2 will move away from the z axis randomly (either towards left or right), and eventually it will settle at one of the 2D traps.

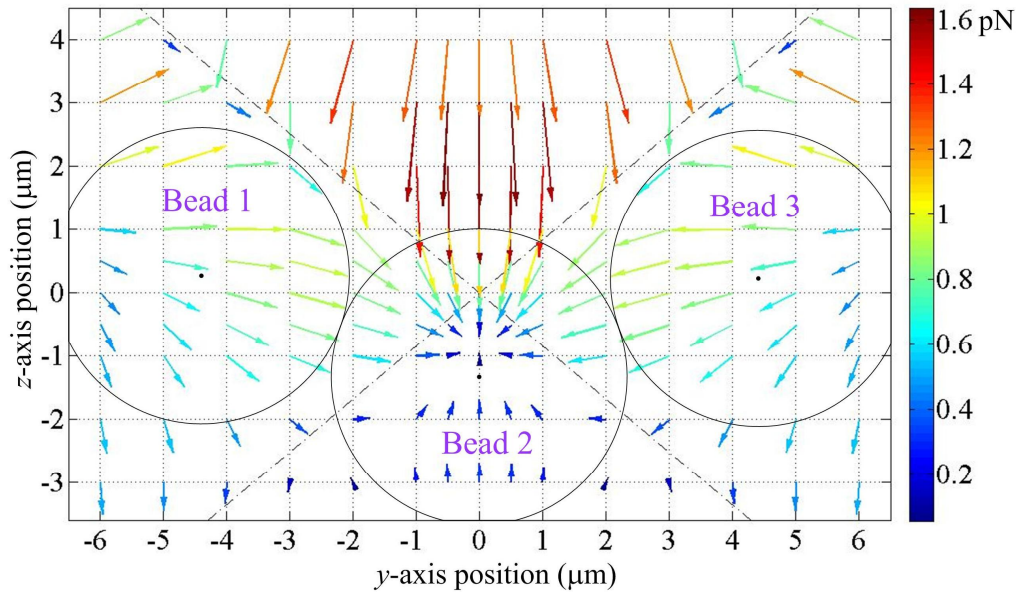


Figure 3.8. The yz plane force field of F_n (the net force of the optical force, gravity, and buoyancy, excluding the normal forces between the beads) in order to explain the principles of particle stacking in three dimensions. Beads 1, 2, and 3 are stacked in three dimensions.

Multiple beads 3D trapping can also be explained by the simulation results. Beads 1, 2, and 3 in Figure 3.8 correspond to the three 3D trapped beads shown in Figure 3.6. Beads 1 and 3 are pushed towards the beam intersection $(0, 0)$ by the optical forces, while the normal forces between the beads prevent Beads 1 and 3 from moving along the y and z axes. Bead 2 is pushed by the normal forces downward (along $-z$) from its original equilibrium $(0, 0, -0.87 \mu\text{m})$,

resulting in an upward optical force applied on Bead 2. Bead 2 reaches new equilibrium when the optical force balances the normal forces applied by Beads 1 and 3. In this case, all three beads are trapped stably in three dimensions.

The experimental results of 2D bead stacking shown in Figure 3.4 can also be explained. When the coverglass is close to the beam intersection, the outer beads (Beads 1, 3, and 4) are pushed inside by the optical forces. If there is a small perturbation of the z position of Bead 4 due to Brown motion, Bead 4 will “climb” over Bead 3, which explains the experimental results shown in Figure 3.4.

3.4.3. Discussion of multiple traps with silica beads

It has been demonstrated in both experiments and simulations that the inclined DFOTs have the ability to create multiple traps. In the current setup, manual 3D stages are used to fix the fibers on the common board. However, the stages can be removed if the board is replaced with a silicon wafer with etched V-grooves. In this case, the fibers are aligned automatically along the V-grooves and the block size can be significantly decreased. The positions of the traps can be controlled by controlling the position of the fiber block with a single actuator. The fiber block can also be rotated to change the orientation of the plane on which the three traps are aligned. Moreover, the separations between the three traps can be adjusted by simply tuning the height of the fiber block without bringing in another actuator. As the position of the fiber block is moved higher, both the height of the 3D trap and the separation between the two 2D traps can be increased. However, because the single actuator on the fiber block cannot provide enough

degrees of freedom, the three traps cannot be adjusted independently, like what the holographic OTs can achieve [15, 102]. The height of the 3D trap is coupled with the separation between the two 2D traps.

The ability of the inclined DFOTs for particle stacking implies that they can potentially be used for arranging trapped particles in a 3D particle matrix. As shown in Figure 3.6, seven trapped particles are arranged in four layers along the z direction. The created particle structures by particle stacking, also called “optical matter” [112], can be analogies to the lattices of natural crystals. Since the periods and crystalline structures can be designed, the resulting optical matter may serve as artificial materials with unique properties, which are not available in nature. Due to the limitation of the current setup, no more than four layers along the z axis can be achieved. However, along the x axis, multiple fiber blocks can be introduced to create multiple layers of the trapped particles. Due to the physical size of the optical fibers ($\sim 100\ \mu\text{m}$), there will be a minimum achievable separation between the adjacent layers. To further reduce the layer separation along the x direction, the optical fibers can be thinned with hydrofluoric acid (HF) etching.

Although the current single inclined DFOTs setup can only create three traps, it is possible to create a large number of traps by integrating multiple inclined DFOTs due to the flexibility and compact size offered by this setup. In addition to the potential to be integrated, the fact that neither the objective nor the substrate plays a role in forming the traps bestows the inclined DFOTs advantages over objective-based OTs. The working distance (the distance that the 3D trap can be moved up) of the inclined DFOTs is not constrained by the substrate whereas that of

the traps created with an objective is limited by the working distance of the objective, which is typically within 20 μm from the substrate for an oil immersion objective [16]. If imaging is not considered, the multiple traps created by the inclined DFOTs can work with any substrate, which is desirable for chip-based systems that use silicon or other lightproof substrates. It is worth noting that compared with the objective-based OTs, the trap quality of the inclined DFOTs is less susceptible to the location of the beam waist and the focus strength. This is due to the fact that the axial gradient force that is used to balance the scattering force for the objective based OTs is strongly influenced by the beam waist location and the strength of the focusing effect [114]. By contrast, the inclined DFOTs use the transverse gradient force from the other beam to balance the scattering force, and thus are more robust to the beam waist position and focus strength. In fact, it was found experimentally that when the beam intersection was around 17 μm downstream from the beam waists, the multiple traps were still retained. There is another advantage of the inclined DFOTs compared with objective based OTs, which is a higher allowable optical power. When used for manipulation of biological particles, because the beam spots at the traps are much larger for the inclined DFOTs, they can induce less damage to biological tissues than objective-based OTs at the same power. According to Reference [65], an optical power as high as 800 mW for each beam can be used without optical damage to the trapped cells in the optical stretcher. Due to the fact that the gradient forces need to overcome the scattering forces in order to achieve a 3D trap, the optical forces induced by the inclined DFOTs in the yz plane are smaller than those generated with objective based OTs (on the order of 1 pN per 10 mW [7]). However, one can increase the optical power to achieve a larger trapping force. It should also be noted that the x -axis optical forces of the inclined DFOTs, which are ~ 8 pN per 10 mW from each fiber (See Section 2.3.2), are at the same level as those of the objective based OTs.

3.5. Investigation of multiple traps and multiple functionalities with glass rods

In this section, the importance and motivation of optical manipulation and optical binding of cylindrical particles by using fiber based OTs are introduced, followed by a description of the working principles of rod manipulation by using the inclined DFOTs. Multiple functionalities as well as optical binding with glass microrods were experimentally demonstrated, with each functionality followed by a qualitative explanation. Numerical modeling of the optical force and torque fields was performed to obtain a quantitative analysis and to achieve a better understanding of the experimental results. At the end of this section, discussion is provided regarding the performance and potential applications of the multiple traps.

3.5.1. Motivation of optical manipulation of cylindrical particles

Compared with optical manipulation of multiple spherical particles as discussed in Section 3.4, optical manipulation of cylindrical particles in an optical trap is of particular interest due to its importance in various fronts, which to date have only been realized by using objective based OTs. For example, in biology, a large variety of cells, which can be optically trapped [115], are rod-shaped by nature [116]. Optical traps have been reported to fold red blood cells into rodlike shapes [50] and control the positions and orientations of Bacillariophyceae, a type of algae with long cylindrical shapes [117]. In a photonic force microscope [118], an optically trapped

cylindrical particle, instead of a regular spherical particle, has been used as a probe to achieve more accurate position detection with a better linearity. [119] Moreover, semiconductor nanowires have been manipulated and assembled into simple structures in an optical trap. [120] However, in literature, trapping of cylindrical particles have not been demonstrated with optical fiber based optical tweezers.

On the other hand, optical binding refers to the phenomenon that multiple particles trapped in optical tweezers can be distributed in a self-organized way. [110-113] As discussed earlier in Section 3.1, the current fiber-based optical binding, including the single optical fiber tweezers with an axicon-shaped fiber tip [110] and the counter-propagating dual fiber traps [108, 111], can only confine particles in a chain-like one-dimensional structure with fixed particle separations, and the observation of optical binding effects was limited to spherical particles. By contrast, we report in this section that two-dimensional (2D) structures can be achieved by optically binding spherical and cylindrical particles.

3.5.2. Working principles of multiple traps on glass rods

Compared to spherical particles that can be controlled in three degrees of freedom (positions), nonspherical particles including rods can be controlled in more degrees of freedom (orientations), and thus better controllability and more functionalities can be realized. To control these many degrees of freedom, an anisotropic optical intensity field is required to orient as well as trap the rods, which is enabled by the inclined DFOTs. First, at the two 2D traps of the inclined DFOTs, the beam shapes on the xy plane are elliptical due to the tilt of the incidence. As a result, the

elliptical shape of the spots enables the alignment of the rods along the long axis, which is the y axis in Figure 3.9. Second, the intensity distribution is not uniform in the elliptical spot: the intensity at the inner end (i.e., the left end at Location 3) of the spot is stronger than that at the outer end (i.e., the right end at Location 3) because of being closer to the beam waist. The non-uniform intensity distribution enables the rotation of the rods when they are off axis. Moreover, when the two 2D traps are close to each other, the strong intensity on the yz (vertical) plane tries to pull outside particles onto the plane, which enables the stacking of multiple rods. These functionalities have been demonstrated in experiments and investigated in simulations, as to be discussed in later parts of this paper

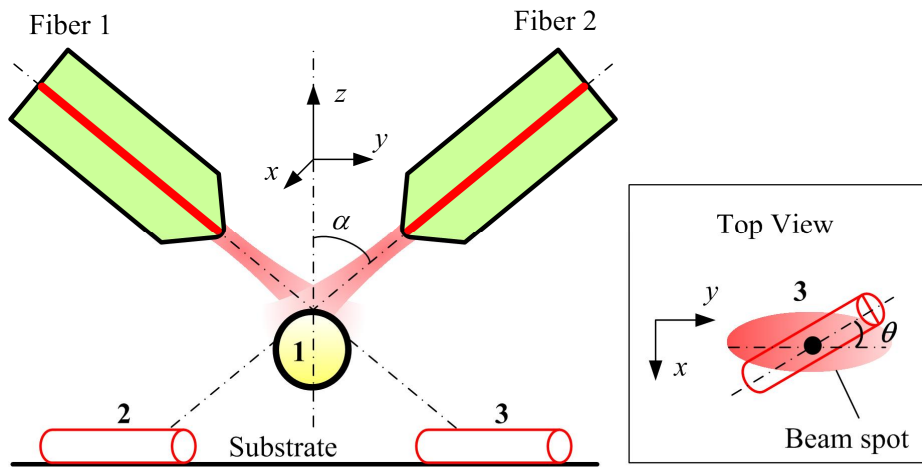


Figure 3.9. Diagram of multiple traps obtained from the inclined DFOTs. Inset is the top view of the rod trapped at Location 3.

3.5.3. *Experimental investigation of multiple functionalities with glass rods*

3.5.3.1. Trapping and alignment of glass rods

The multiple traps can be used to manipulate particles with other shapes in addition to the spherical shaped particles. By taking the advantage of the oval shaped spots produced by the inclined DFOTs, non-axisymmetrical particles can be manipulated to change not only their positions but also their orientations. As an example, micrometer-sized glass rods were successfully trapped and aligned. In experiment, two free glass rods were brought into the trapping area by moving the coverglass, as shown in Figure 3.10(a). Once they were moved close to the two 2D traps, the rods were trapped and aligned along the x axis, as shown in Figure 3.10(b). When the water was moved along the $+y$ axis, the trapped rods stayed stable in the 2D traps, while maintaining the same orientation, as shown in Figure 3.10(c). It is noted that the glass rods could not be trapped in three dimensions.

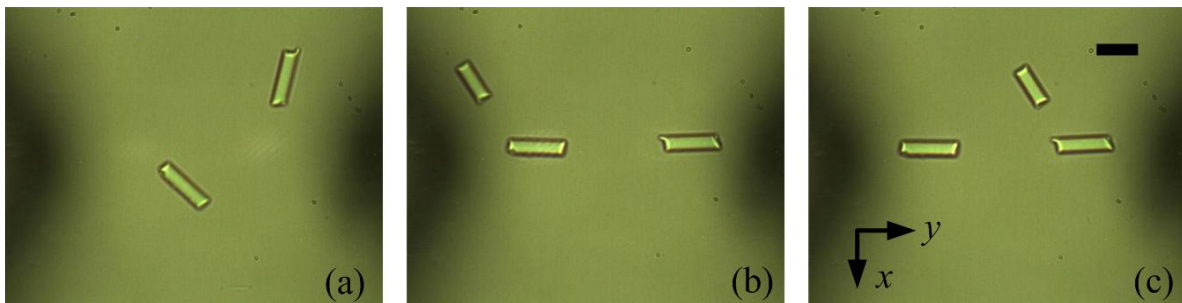


Figure 3.10. Experimental demonstration of trapping and alignment of glass rods. (a) Two free rods were initially lying on the substrate. (b) The two rods were trapped and aligned along the y axis. A third free rod (on the top left side) was moved into the view field serving as a reference. (c) The coverglass was moved along $+y$. The scale bar is $10\ \mu\text{m}$ in length. The rods are $\sim 3.5\ \mu\text{m}$ in diameter, and $8\sim 15\ \mu\text{m}$ in length.

Since the elliptical optical fields on the substrate exhibit directionality (with the long axis along the y axis), as can be seen from Figure 3.10, this directionality of the optical field enables control

of the orientations of glass rods. When a rod is trapped, both its ends will be trapped by the strongest intensity, resulting in its axis aligned long the long axis of the optical field (the y axis). This explains the results of rod alignment shown in Figure 3.10. The reason that glass rods cannot be trapped in three dimensions can be explained as follows. When the coverglass is lifted up so that a rod is moved close to the beam intersection, where the 3D trap for beads is located, considering the mirror symmetry of the system, the rod will be trapped along the y axis and centered at the 3D trap position. Due to the long length of the rod, each end of the rod will reach one optical axis of the two beams, where only one beam is dominant. Because the scattering force on the beam axis is always larger than the gradient force due to the weak focusing of the optical beams, the ends of the rod are pushed along $-z$ direction while the center of the rod is pulled along $+z$ direction (by the 3D trap). The 3D trap is not strong enough to balance the optical forces at the rod ends as well as the gravity of the rod, and hence no stable 3D trap of the rod can be achieved.

3.5.3.2. *Rotation of glass rods*

If the motion of the water is controlled to have a relatively fast speed, the trapped rods will escape from the traps. This phenomenon was found to be useful for rotating a rod in a controllable manner (clockwise or counter-clockwise). When the water was moved in $-x$ direction, the outer end of the rod escaped earlier than the inner end, resulting in a clockwise rotation of about 70° , as shown in Figure 3.11(a)-(b). When the rod was moved back to the trapping area by moving the coverglass in $+x$ direction, the end that first came into the trap was pushed outside (along $-y$), as shown in Figure 3.11(c)-(e). The rod was thus rotated clockwise by

180° in the entire process. If the process shown in Figure 3.11(a)-(e) is repeated, the rod can be continuously rotated. When the water was moved in the opposite direction (first $+x$, then $-x$), the rod was rotated counter-clockwise by 180° , as shown in Figure 3.11(e)-(h).

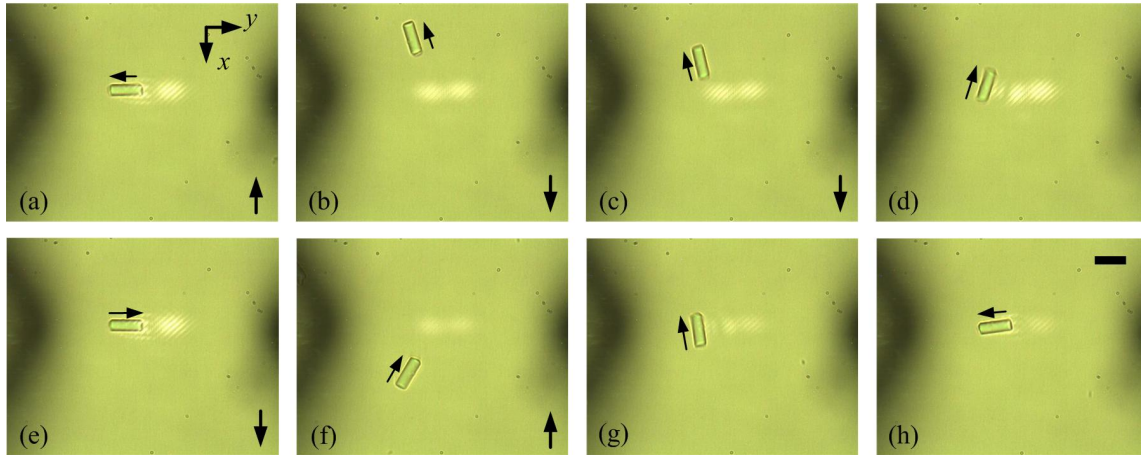


Figure 3.11. Experimental demonstration of rotating glass rods. The arrows at the lower right corner indicate the next movement of the coverglass, and the small arrow beside the rod shows the rod orientation. (a)-(b) The rod escaped from the trap when the water was moved fast in $-x$ direction. (b)-(e) The rod was re-trapped and eventually aligned along the x axis, when the water was moved in $+x$ direction. The rod was rotated clockwise by 180° in the above process. (e)-(h) The process of (a)-(e) was repeated with the opposite direction of water movement. The rod was rotated counter-clockwise by 180° . The scale bar is $10 \mu\text{m}$ in length. The rods are $\sim 3.5 \mu\text{m}$ in diameter, and $8\sim 15 \mu\text{m}$ in length.

The principle that can be used to explain the rods rotation is illustrated in Figure 3.12. Since the beams are inclined, the inner ends of the spots have stronger intensity than the outer ends. The outer end (End 1 in Figure 3.12(a)) of the trapped rod will escape earlier than the inner end (End 2) if the drag force from the water is large. After the rod escapes from the 2D trap, it is rotated clockwise, as shown in Figure 3.12(b) and Figure 3.12(b). If the water is moved backward to bring the rod into the trapping area, End 2 will get trapped first, as shown in Figure 3.12(c) and Figure 3.12(c). However, since the scattering force is dominant due to the weakly focused beams,

End 2 is pushed outwards so that End 1 will be brought into the trapping area. When the rod is finally settled down, it will be aligned along the y axis (Figure 3.12(d)) with an orientation opposite to that is formed at the beginning of the process (Figure 3.12(a)). Therefore, during the entire process shown in Figure 3.12, the rod is rotated clockwise by 180° , which was observed in the experiment. If the water is moved in the opposite direction in each step illustrated in Figure 3.12, the rod will then be rotated counter-clockwise by 180° during each cycle.

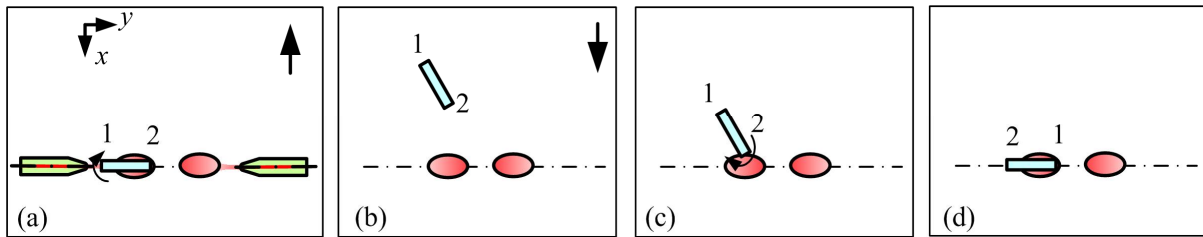


Figure 3.12. Working principle of rod rotation. The arrows at the top left corner indicate the next movement of the water. The two ovals illustrate the spots of the two beams.

3.5.3.3. Stacking of glass rods

Glass rods can also be stacked using the multiple traps. As shown in Figure 3.13, three glass rods can be stacked in three different ways: i) the two bottom rods aligned side by side and the third rod on top of the two bottom ones, as shown in Figure 3.13(a), ii) the two bottom rods aligned end to end and the third rod on top of the two bottom ones, as shown in Figure 3.13(b), and iii) the center rod sandwiched by the two outside rods and orientated vertically, as shown in Figure 3.13(c). Such stacking can potentially be used to synthesize micro- or nano-structures.

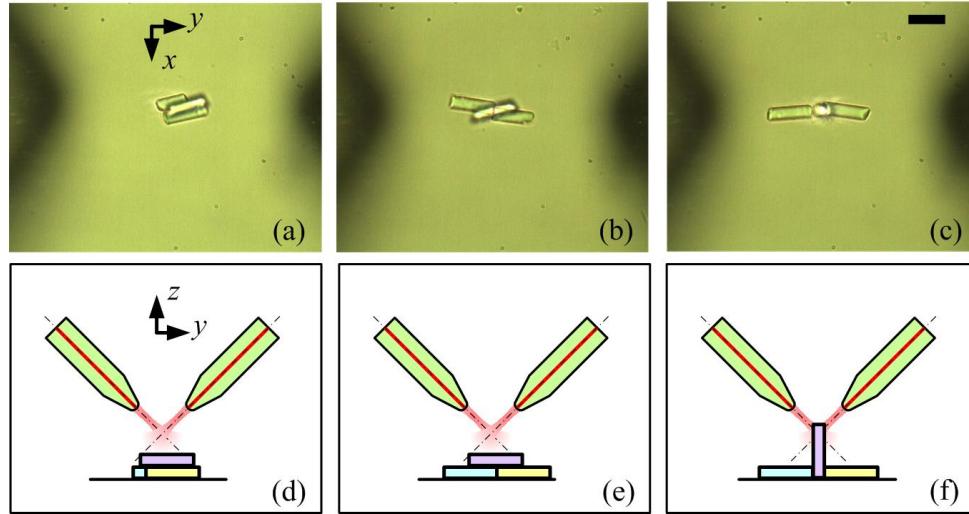


Figure 3.13. Experimental demonstration of glass rod stacking. (a)-(c) Images of glass rods stacked in different ways. The scale bar is $10\ \mu\text{m}$ in length. (d)-(f) Sketches of the stacked rods corresponding to (a)-(c), respectively. The rods are $3.5\ \mu\text{m}$ in diameter and $8\text{-}15\ \mu\text{m}$ in length.

The principle of rod stacking can be explained as follows. If the separation between the two 2D traps is small and two rods are trapped, the rods will contact with each other. Since both rods try to align their axes along the y axis, their ultimate positions in the traps will depend on their initial states. If two rods are brought into the traps along the x axis they will be trapped side by side, as shown in Figure 3.13(a). On the other hand, if they are brought into the traps along the y direction, they will push each other end to end, as shown in Figure 3.13(b) and (c). If there is a third rod in between, it will be squeezed by the two rods from both sides or from both ends, resulting in the stacking of the third rod. In most experiments, the third rods stayed parallel to and on top of the other two rods, as shown in Figure 3.13(a) and (b). However, in rare cases, when the third rod is squeezed, its one end will be trapped by the 3D trap, which is located above the substrate, resulting in the rods trapped in a vertical orientation, as shown in Figure 3.13(c).

3.5.3.4. Optical binding of silica beads and glass rods

The optical binding arises from the light redistribution induced by the trapped particles. [113] When multiple particles are trapped in an optical field, interactions between the particles are induced by the optical field. The particles trapped upstream can modify the optical fields and influence the behavior of the particles downstream. In this work, optical binding of both spherical beads and microrods can be realized with the inclined DFOTs. As shown in Figure 3.14, when Bead 1 was trapped in 3D, Bead 2 can be optically bound so that it can be manipulated in 3D. Compared to the free beads (Beads 3 and 4), Bead 2 was lifted up from the coverglass and it was remained at the bound position when the water was moved around. If no bead were trapped in the 3D trap, Bead 2 could only be trapped on the coverglass by the 2D trap. Similar optical binding effects can also be used to tilt glass rods. As shown in Figure 3.14, two glass rods (Rods 1 and 3) were tilted up due to the optical binding. The optically bound rods stayed stationary when the water was moved around. The up-tilting of the glass rods cannot be achieved without

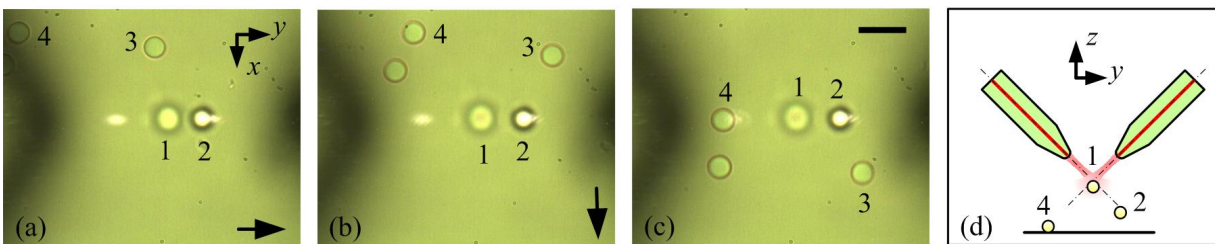


Figure 3.14. Experimental demonstration of optical binding of silica beads. The arrows at the lower right corner indicate the next movement of the coverglass. Bead 1 was trapped in 3D. Bead 2 was optically bound to Bead 1, so it was out of focus and not contacting the substrate. Beads 1 and 2 remained in the trapped and bound positions, respectively, when the water was moved in $+y$ ((a)-(b)) and $+x$ ((b)-(c)) directions. The scale bar is $10 \mu\text{m}$ in length. (d) A sketch of the three beads on the yz plane. The beads are $4.74 \mu\text{m}$ in diameter.

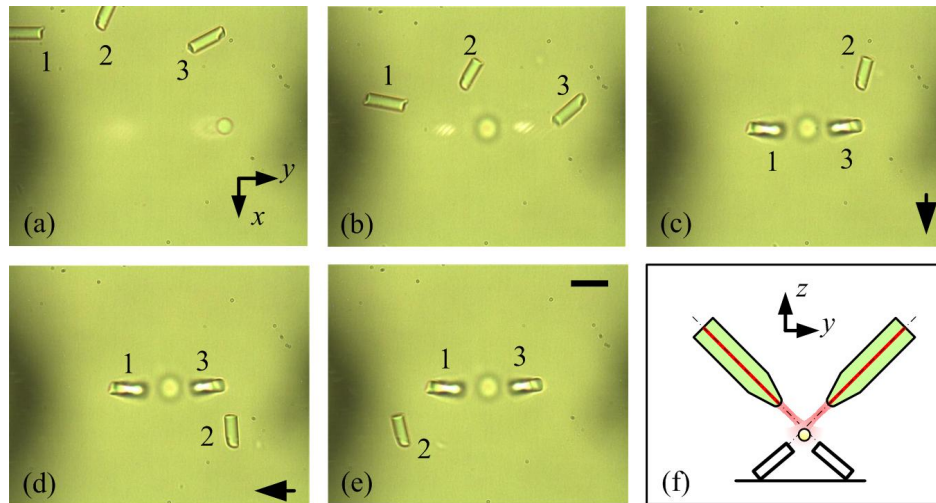


Figure 3.15. Experimental demonstration of optical binding of glass rods. (a) The three free rods lay on the coverglass, and the silica bead was trapped by the right 2D trap. (b) The bead was trapped by the 3D trap. It can be seen that the light beams were refocused by the bead. (c) Rod 1 and 3 were tilted up by the optical binding, while Rod 2 remained free. The optical binding helped Rods 1 and 3 remain stationary while the water was moved in $+x$ ((c)-(d)) and $-y$ ((d)-(e)) directions. The scale bar is $10\ \mu\text{m}$ in length. (f) Sketch shows the optical bound rods on the yz plane. The rods are $\sim 3.5\ \mu\text{m}$ in diameter, and $8\sim 15\ \mu\text{m}$ in length. The silica bead is $3.5\ \mu\text{m}$ in diameter.

the bead in the 3D trap. It is noted that the optical binding effects described here created a 2D structure, which is different from 1D chain-like structure created by previously published work.

In the experimental results of optical binding, the bead in the 3D trap served as a lens, which can be used to refocus both of the light beams. This focusing effect can be seen by comparing the spot sizes with (Figure 3.15(b)) and without (Figure 3.15(a)) the bead being trapped. A similar refocusing effect was studied and verified in an earlier work [113]. The refocusing increases the intensity gradient downstream, and hence the gradient force that is needed to overcome the scattering force is increased. The increase in the gradient force is necessary to keep the bead being trapped in 3D after the first trapped bead. It seems that the particles downstream are bound to the bead upstream, which explains why it is called optical binding. Owing to the optical

binding effect, the downstream beads and rods can be lifted up as shown in Figure 3.14 and Figure 3.15. Without the 3D trapped bead, only 2D trapping can be realized, which does not have the ability to lift up beads or glass rods.

The experiments discussed above demonstrate that the inclined DFOTs have the ability of trapping cylindrical particles and performing multiple functionalities. With two fibers assembled on a block, control of the positions as well as the separations of the traps can be realized easily. With a single actuator, in this case, a 3D translational stage, attached to the fiber block, optical alignment, rotation, stacking, and optical binding of microscopic glass rods can be achieved.

3.5.4. Numerical investigation of multiple functionalities with glass rod

Although the experimental results on rod manipulations have been explained qualitatively in the Section 3.5.3, to achieve an enhanced understanding of the experimental results, numerical simulations on the optical forces and torques are carried out based on a ray-optics model discussed previously in Section 2.4.1. Different from the case of a spherical particle, the incidence of a beam pencil on the sidewall of a cylindrical particle should be treated differently from that on the cylindrical endface. Five successive reflections of the beam pencil are calculated after each beam pencil enters the cylindrical particle. For a cylindrical particle, both optical forces and optical torques are calculated for a specific location and a specific orientation of the cylinder centroid.

The parameters (the optical power, wavelength, beam waist and location, fiber separation and inclination angle, and rods diameter and refractive index) are chosen to be the same as those used in the experiments. The rods used in the simulations are considered to have perfect flat ends and a length of 10 μm . The vertical distance between the beam intersection and the rod plane is 3.36 μm in the simulations. Note that some simulation parameters such as rod length, end face shape, and height of the beam intersection are difficult to determine due to the fact that these parameters were either constantly changed within a range or hard to measure in the experiments. The influence of these parameters will be discussed at the end of this section. Since all the rods in the experiments lied on the substrate except those in the optical binding experiment, the axes of the rods considered in our modeling always lie in the xy plane.

3.5.4.1. Optical force and torque fields of a single 2D trap applied on a y-oriented rod

As seen in Figure 3.10~Figure 3.15, the rods were always aligned along the y axis. In the simulations, it is considered that the rod is initially oriented along the y axis, and further it is assumed that only a single 2D trap (Trap 3 in Figure 3.9) takes effect. This is true when the two 2D traps are far ($>10 \mu\text{m}$) from each other. It is noted that the influence of the rod orientation and the forces when two 2D traps exist in the same area will be studied later in this paper.

The optical force field applied on a single y -oriented rod by a single 2D trap is obtained, as shown in Figure 3.16(a). It can be clearly seen from Figure 3.16 that a 2D trap of the rod exists near the beam axis, which is located on the yz plane and intersects the xy plane at $(0, 0)$. By plotting the optical force along the y axis (data not shown), the trap is found to be at $(0, 0.074$

μm). The fact that the trap is slightly shifted from the beam axis toward $+y$ direction is because the gradient force needs to have a $-y$ component to balance the scattering force, which always along the beam propagation direction and has a $+y$ component. The same reason can be used to explain why the trapping force is stronger in $-y$ direction than in $+y$ direction. When the rod is located in the $-y$ area, both the gradient force and the scattering force have $+y$ components and hence contribute to the trapping force. However, if the rod is located in the $+y$ area, the gradient force has a $-y$ component, but the scattering force still has a $+y$ component that pushes the rod away from the trap, resulting in weaker trapping forces.

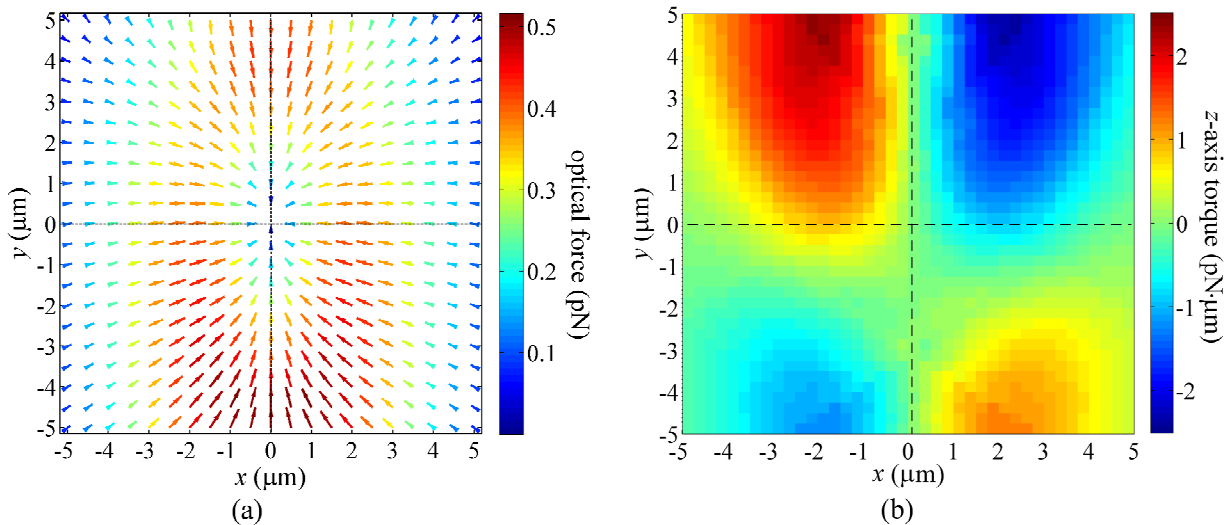


Figure 3.16. Simulation results of (a) the optical force field and (b) the z-axis optical torque field of a single 2D trap (Trap 3 in Figure 3.9). Each arrow in (a) stands for the optical force applied on a glass rod when the center of the rod is located at the start point of the arrow. The origin of the coordinate system is located at the intersection of the optical beam axis and the horizontal plane passing the rod center. The rod is $3.5 \mu\text{m}$ in diameter, $10 \mu\text{m}$ in length, and oriented along the y axis. The optical power is 7.65 mW .

The optical torque field applied on a single y -oriented rod is shown in Figure 3.16(b). As discussed in the previous section, the elliptical shape and the non-uniform intensity distribution

can cause torques on the rod. Depending on the position of the rod, it will be rotated clockwise (by the negative torques) or counter-clockwise (by the positive torques). Since the intensity field is symmetric about the y axis, there is no torque when the y -oriented rod is located on the y axis. On the other hand, the intensity field is not symmetric about the x axis (with stronger intensity in the $-y$ area). As a result, the optical torque is not zero on the x axis, unless the rod is far from the optical beam so that it does not feel the optical intensity.

3.5.4.2. Optical torque field of a single 2D trap applied on an arbitrarily oriented rod

In order to fully understand the principles of rod trapping and alignment, the relationship between the optical torque and the rod orientation is obtained and shown in Figure 3.17. Here, we consider a rod with an arbitrary orientation and located at three positions $(0, -1 \mu\text{m})$, $(0, 0.074 \mu\text{m})$, where the rod is stably trapped, and $(0, 1 \mu\text{m})$. It is noted that the angle θ (See Figure 3.9) increases when the rod is subject to a positive z -axis torque. There are four orientations, namely $\theta = 0, \pi/2, \pi$, and $3\pi/2$, with zero optical torques. The orientations of $\theta = \pi/2$ and $3\pi/2$ are not stable. If the rod rotates slightly away from, for example, $\theta = \pi/2$, due to the Brownian motion, the optical torque will drive the rod further way from $\pi/2$ until it reaches $\theta = 0$ or π , depending on the direction in which the rod initially deviates. However, at $\theta = 0$ or π , the restoring torque will pull the rod back when it rotates slightly away. In another word, $\theta = 0$ or π are potential wells while $\theta = \pi/2$ and $3\pi/2$ are potential hills. The stable orientations of $\theta = 0$ or π correspond to the conditions in which the rod axis is aligned with the y axis. Although only three positions ($y = -1 \mu\text{m}, 0.074 \mu\text{m}$, and $1 \mu\text{m}$) are shown in Figure 3.17, the stable orientations are always 0 and

π as long as the rod is located on the y axis and not too far away ($<10 \mu\text{m}$) from the beam axis (data not shown).

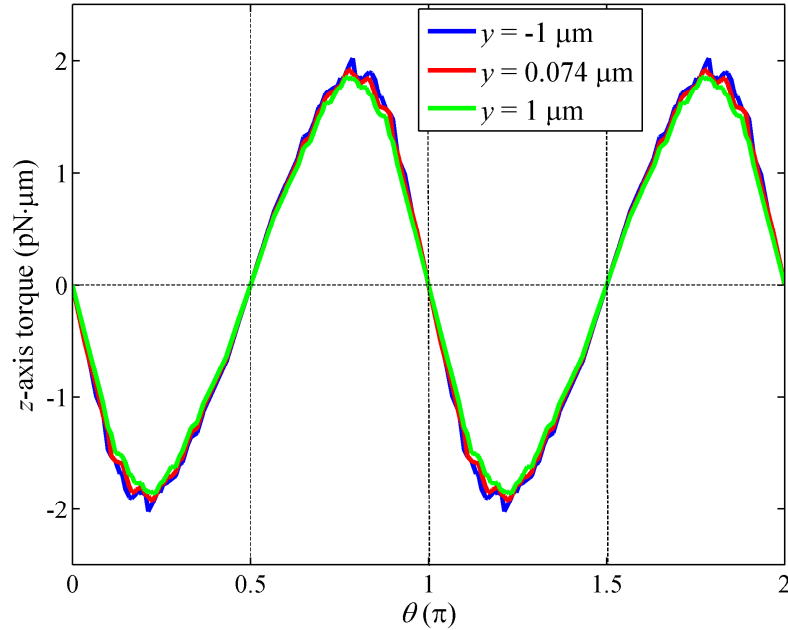


Figure 3.17. Simulation results of the dependence of the z -axis optical torque on the orientation of a rod. The torque is applied by a single 2D trap (Trap 3 in Figure 3.9). θ is the angle between the rod axis and the y axis, as shown in Figure 3.9. The rod is $3.5 \mu\text{m}$ in diameter, $10 \mu\text{m}$ in length at located on the y axis ($x=0$). The optical power is 7.65 mW .

3.5.4.3. Optical force and torque fields of two 2D traps applied on a y -oriented rod

When two 2D traps are close to each other, the force field will change from that with a single 2D trap. The optical force and torque fields on a y -oriented rod applied by two 2D traps are shown in Figure 3.18(a) and (b), respectively. Here, the vertical distance between the beam intersection and the rod plane (xy plane) is $3.36 \mu\text{m}$, and the corresponding separation between the two

intersections of the beam axes and the xy plane is $8\ \mu\text{m}$. It is noted that, different from Figure 3.16 and Figure 3.17, the origins of coordinate systems in Figure 3.18 is located right below the beam intersection, with equal distances from the two 2D traps. It can be seen from Figure 3.18 that the trap position is at the origin, which is in between the two 2D traps. Due to the symmetry of the system about both x and y axes, the optical torque is zero on both the x and y axes.

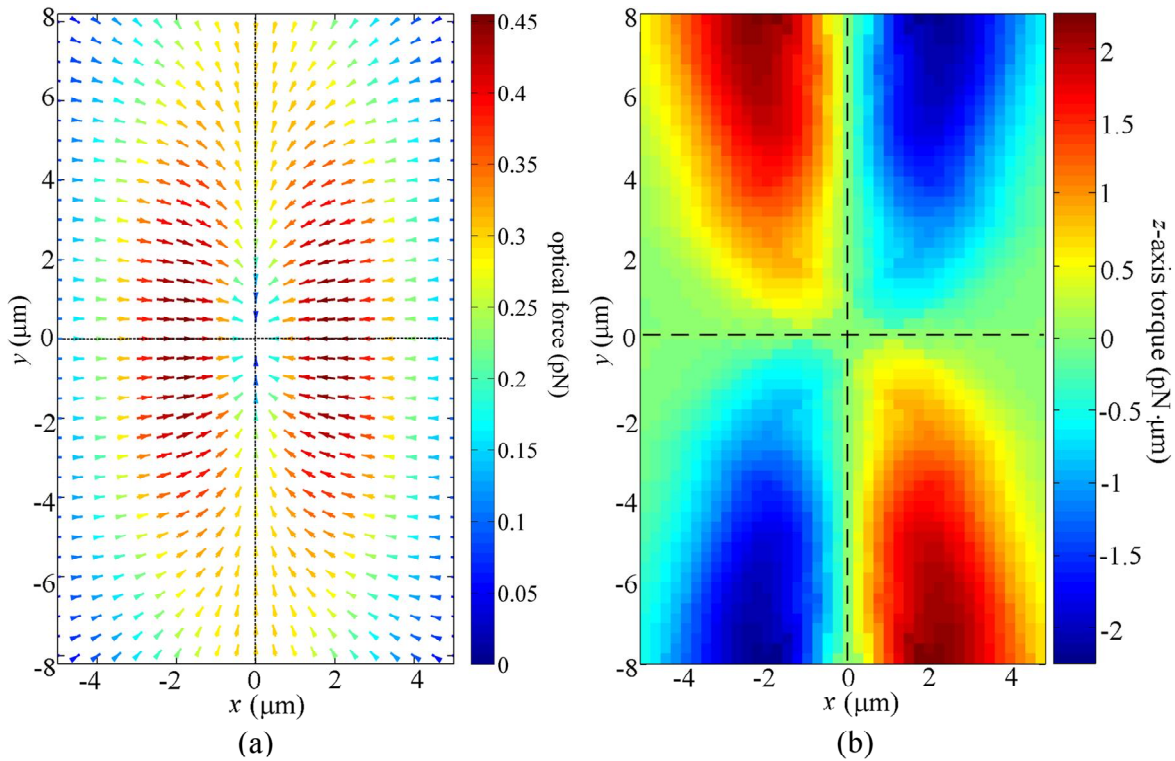


Figure 3.18. Simulation results of (a) the optical force field and (b) the z -axis optical torque field of two 2D traps (Traps 2 and 3 in Figure 3.9). Each arrow in (a) stands for the optical force applied on a glass rod when the center of the rod is located at the start point of the arrow. The origin of the coordinate system is located at the center of the line segment connecting the two traps. The intersections of the optical beams and the xy plane are at $(0, -4\ \mu\text{m})$ and $(0, 4\ \mu\text{m})$. The rod is $3.5\ \mu\text{m}$ in diameter, $10\ \mu\text{m}$ in length, and oriented along the y axis. The optical power is $7.65\ \text{mW}$ from each fiber.

3.5.4.4. *Explanation of optical trapping, alignment, rotation, and stacking of glass rods*

Combining the simulation results shown in Figure 3.16 and Figure 3.17, we can quantitatively explain the experimental results of the rod trapping and alignment. If a y -oriented rod is located off the y axis, it will be pushed toward the y axis (See Figure 3.16(a)), while being rotated under the optical torque with a direction depending on its initial position (See Figure 3.16(b)). Once the rod reaches the y axis, it will quickly settle down at the stable position of $(0, 0.074 \mu\text{m})$ (See Figure 3.16) as well as align itself along the y axis (See Figure 3.17). After it is trapped, although the Brownian motion or the moving water causes the rod to deviate from the stable position and orientation, the restoring force and torque retain the stable trapping and alignment of the rod, just as the experimental results shown in Figure 3.10.

If the water is moved along the $+x$ axis at a speed fast enough to drag the rod away from the trap, the rod will be rotated clock-wise by a negative torque (See Figure 3.16(b)). When the rod is brought back to the trapping area by the moving water, it will be further rotated clock-wise, and will align its axis again along the y axis. This process is the same as the one shown in Figure 3.11(a)-(e). It is noted that the rotation directions in Figure 3.16(b) and Figure 3.11 are opposite. This is because the simulation results shown in Figure 3.16(b) are obtained with Trap 3 (See Figure 3.9), while the experimental rotation results shown in Figure 3.11 were obtained with Trap 2.

If there are two rods in the optical field formed by two 2D traps, according to Figure 3.18, both rods are pushed toward the origin. The rods still try to align themselves along the y axis, and

hence they will tend to stay on either x or y axis, where the torque is zero (See Figure 3.18(b)). Depending on their initial positions, the two rods can be pushed against each other along the x axis (side by side) or along the y axis (end to end). This explains why the bottom two rods in the experiment were either side by side (See Figure 3.13(a)) or end to end (See Figure 3.18(b)). If there is a third rod existing in the optical field, it will also be pushed towards the origin. However, since there is not enough space left for it to stay on the xy plane, it will be stacked onto the first two rods by the force field with its axis aligned along the y axis (See Figure 3.18). When the third rod was sandwiched by the other two rods along the y axis, the third rod can be lifted up by the forces coming from both sides, and maintain this orientation by the support of the two rods on both sides, as shown in Figure 3.18(c)

3.5.5. Discussion of multiple traps with glass rods

There are some parameters used in the simulation that do not match exactly the ones in the experiments. The influence of these parameters is discussed here. The rods used in the experiments have different lengths ranging from 8 μm to 15 μm . In simulations, only a rod length of 10 μm is used. If a different rod length is used in the simulations, the results shown in Figure 3.16~Figure 3.18 would change slightly. For example, the stable trapping position will be displaced by a small amount ($<0.5 \mu\text{m}$), and the amplitude of the optical forces and torques will also change slightly. However, the important conclusions and the behaviors of the rods in the optical trap, such as alignment along the y axis and stable trapping positions located on the y axis, will not change. As a result, the understanding of the experimental results through the simulation results will still hold for slightly changed rod lengths. Another issue that was not considered in

the simulation is influence of the end face shape of the rods. As seen in the experimental results, most of the rods do not have a perfect flat end face. However, since the end faces have much smaller areas than the sidewall, the optical forces applied on the end faces are much smaller than those on the sidewalls. Therefore, the end face shapes will have little influence on the simulation results as long as the rod length is much larger than its radius. This issue of the influence of end face shapes has also been studied by previous work. [121] The height of the beam intersection with respect to the xy plane (the rod plane) is another parameter that constantly changed in the experiments. In our simulations, the value of $3.36 \mu\text{m}$ is used, while the height of the beam intersection ranged from 0 to $20 \mu\text{m}$ in the experiments. According to our experience in the experiments, the effects of two 2D traps (rods trapped in between the 2D traps as shown in Figure 3.18) are dominant if the beam intersection is close ($<3 \mu\text{m}$) to the xy plane. With a higher beam intersection, the distance between the two 2D traps is larger. In this case, the influence of the other beam on the rods trapped by one beam is smaller, resulting in more profound effects of a single 2D traps (rods trapped separately by one of the 2D traps as shown in Figure 3.16 and Figure 3.17). To facilitate different functionalities, proper beam intersection height might be chosen. A high beam intersection is preferable in the case of rod alignment, while a low beam intersection is necessary for rod stacking.

Furthermore, the trapped rods were not perfectly aligned along the y axis in the experiments (See Figure 3.11(h) and Figure 3.13) while a perfect alignment is predicted in the simulations. This is mainly because there always exists an error of the fiber alignment in the experiments. It is difficult, if not impossible, to align the two optical beams in exactly the same plane. This

alignment error can cause the force field shown in Figure 3.16 to be twisted (data not shown), resulting in an imperfect alignment of the rod along the y axis.

It has been demonstrated that the inclined DFOTs have the ability to control both the orientations and the positions of the microscopic glass rods. The inclined DFOTs system can be used as a system block in a microfluidic system. In the current setup, manual 3D stages are used to fix the fibers on the common board. However, the stages can be removed if the board is replaced with a silicon wafer with etched V-grooves. In this case, the fibers can be aligned well along the V-grooves and the block size can be significantly decreased. The position control of the trapped glass rods can be realized by controlling the position of the fiber block with a single actuator. The separations between the trapped glass rods can be adjusted by tuning the height of the fiber block. The orientations of the glass rods can be adjusted by rotating the fiber block about the z axis. However, because the single actuator on the fiber block cannot provide enough degrees of freedom, the trapped glass rods cannot be adjusted independently. They are both oriented along a line while lying on the substrate, unless they are tilted by the optical binding effects. Although multiple rods cannot be rotated independently, the ability to rotate the glass rods makes it feasible to control the orientation of the multiple rods simultaneously. Moreover, by controlling the motion of the fibers, the rods can be controlled to rotate by a fixed angle (e.g., 180° in an entire cycle and 90° in half a cycle)

The ability of aligning, positioning, stacking, and optically binding cylindrical particles, as well as spherical particles discussed in Section 3.4, makes it possible to create periodical structures with each node being one particle. These artificial lattice structures are also called “optical

matter,” [112] which are in analogy with the lattices of natural crystals. Since the periods and crystalline structures can be designed, the resulting optical matter may serve as artificial materials with unique properties, which are not available in nature. Along the x axis, multiple fiber blocks can be introduced to create multiple layers of the trapped particles. However, there will be a minimum achievable separation between the adjacent layers due to the physical size of the optical fibers. To further reduce the layer separation along the x direction, the optical fibers can be thinned with hydrofluoric acid (HF) etching. In this sense, it is possible to realize a large number of traps by integrating multiple inclined DFOTs thanks to the flexibility and compact size of this setup. Moreover, unlike the objective-based OTs that require thin, transparent substrates, the multiple traps created by the inclined DFOTs can work with any substrate, including silicon or other lightproof substrates.

3.6. Summary

In this chapter, a new phenomenon of multiple traps, one 3D and two 2D, has been discovered during the experiments carried out with the inclined DFOTs setup. The traps have been created at different vertical levels. The block, including the two inclined fibers and the common board, enables the system with multiple traps to be used as a module in a microfluidic system. The positions and separations of the traps can be readily controlled by a single actuator attached to the block, instead of one actuator for each trap. Investigations into the multiple traps revealed that the inclined DFOTs can perform multiple functionalities, which has been achieved for the first time with fiber optical tweezers. Beads separation, beads grouping, 2D and 3D beads stacking, rod alignment, rod rotation, and optical binding of beads and glass rods have been

demonstrated experimentally. These functionalities are studied carefully either by carrying out numerical simulations based on the models we developed. In summary, *the following original contributions have been achieved in this chapter: discovery of multiple traps with the inclined DFOTs system and realization of multiple functionalities with the inclined DFOTs system.*

Chapter 4. Trapping Efficiency Enhancement for Fiber Optical Tweezers

The most important disadvantage of fiber optical tweezers is that the gradient force is not as strong as that obtained by using a high NA objective [66, 75]. This is due to the weak focusing effect of the commonly used spherical lensed fibers. In order to improve the gradient force obtained from fiber optical tweezers, new methods need to be developed to obtain a smaller focus from an optical fiber-based device. Liu *et al.* [75] demonstrated single fiber 3D optical tweezers by reducing the fiber end diameter to confine the output optical beam size. However, the heating and drawing method they used may cause difficulty to control the shape of the abruptly broken fiber end. Furthermore, the smallest spot size is located right on the endface of the fiber, because of which physical contact with the trapped particles is inevitable. Most importantly, the power loss issues limit how small the focal size can be obtained, although the power loss was not reported in ref. [75]. The transmission scales as $(r/\lambda)^4$ for a small ($r < \lambda$) aperture with an infinitesimal thickness, with r being the aperture size and λ the wavelength. [122] The transmission is even smaller for an aperture with a depth. [122] Despite these limitations, the work reported in ref. [75] proves that as long as the beam emitted from an optical fiber can be focused small enough, fiber optical tweezers can also achieve a strong axial gradient force to overcome the scattering force, which currently can only be achieved by using objectives with a high NA. Therefore, the development of more controllable and effective methods to reduce the beam size would be a key solution to enable stronger fiber optical traps, and hence to significantly enhance the capabilities of fiber optical tweezers.

In this chapter, for the first time, the smallest focal size achievable with a high NA objective is experimentally realized by using an optical fiber with a planar surface plasmonic (SP) lens directly fabricated on the fiber endface. The fiber-based SP lens, therefore, provides a potential solution to significantly enhance the trapping capability of fiber optical tweezers as well as to bridge the optical signals and powers between the nanophotonic systems and the macroscale optical devices. Trapping of a live bacterium is successfully demonstrated in three dimensions with a power lower than any objective-based optical tweezers reported in literature. To the best of our knowledge, this is also the first time that bacteria have been successfully trapped in 3D by using fiber optical tweezers.

The rest of this chapter is organized as the following. In Section 4.1, the model and the designs to achieve superfocusing by using a fiber-based SP lens are described. The experimentally measured 3D intensity distribution from two fiber-based SP lenses are presented and discussed. The focusing effect is studied by the numerical simulations via the finite-difference time-domain (FDTD) method. The data obtained in the experiment and the simulation are compared and discussed. In Section 4.2, the trapping ability enhancement of the fiber optical tweezers are demonstrated by 3D trapping of a sub-micrometer-size bacterium with a low power. Parametric study of the optical trapping forces on Rayleigh particles are performed by using two analytical models. The 3D force fields of the SP fiber tweezers are mapped according to the experimentally measured intensity profiles.

4.1. Superfocusing with fiber-based surface plasmonic lenses

As mentioned earlier, in order to improve both axial and transverse gradient force of fiber optical tweezers, it is critical to obtain a tightly focused spot when the light is emitted from an optical fiber. However, it is not possible to design and fabricate a set of high NA, low aberration dielectric lenses on a fiber end face, as what has been done for microscope objectives [61]. Therefore, one has to seek new techniques to overcome this barrier. In this dissertation, “superfocusing” refers to achieving a focus with a size close to the diffraction limit that is not achievable using common focusing technologies. One way to achieve superfocusing is to use near-field optics, such as particle-lens [123], near-field ball lens [124], and near-field scanning probes [125]. However, the focus created with near-field optics is usually located at a distance of nanometers to sub-micrometers from the optical component surface [124]. To build a fiber optical trap, the focus must be far enough from the optical fiber to enable effective particle manipulation while avoiding any physical contact. Therefore, the optical trap (i.e., the focus) must be at least one micrometer away from the fiber end for fiber optical tweezers.

Recent development on surface plasmonic lenses provides a solution to solve this problem [126-131]. Surface plasmons (SP) propagate along the interface of a metal and a dielectric material as a combination of electromagnetic waves and surface charge density waves [129]. In general, light cannot pass through a subwavelength hole due to significant diffraction loss; transmission decreases significantly with a rate of $(r/\lambda)^4$ as the aperture radius r decreases [78]. However, SPs have been found to increase significantly (orders of magnitude) when light is transmitted through subwavelength apertures on a metal surface [132, 133]. SP components have been used

as waveguides and lenses [127, 130], and focusing with the SP lens has been achieved and investigated in one dimension [134], as shown in Figure 4.1. A modification to the dispersion relationship is proposed to be used in a 2D cylindrical SP lens. [135] Very recently, Fu *et al* [136, 137] experimentally achieved 2D superfocusing with the SP lens on a quartz substrate illuminated with a free-space laser beam, as shown in Figure 4.2. The smallest spot size defined by a full-width at half-maximum (FWHM) of 260 nm was achieved using a wavelength of 532 nm. However, the superfocusing achieved in ref. [137] is too close to the substrate (500 nm), which is not preferable for optical trapping. Moreover, an effective design model has not been provided for the two dimensional SP lens. Thus far, superfocusing with an optical fiber based on SP lens has not yet been reported. Since the optical fiber can serve as a perfect waveguide and it is compatible with MEMS systems, it is advantageous to develop a fiber-based SP lens rather than a SP lens on a substrate that requires illumination from a free-space optical beam.

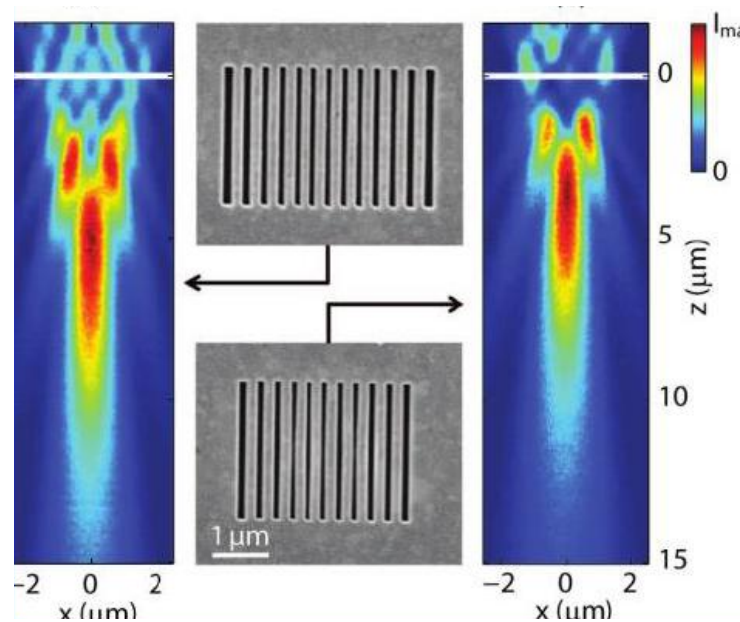


Figure 4.1. One-dimensional focusing using the SP lens on a fused silica substrate. [134]

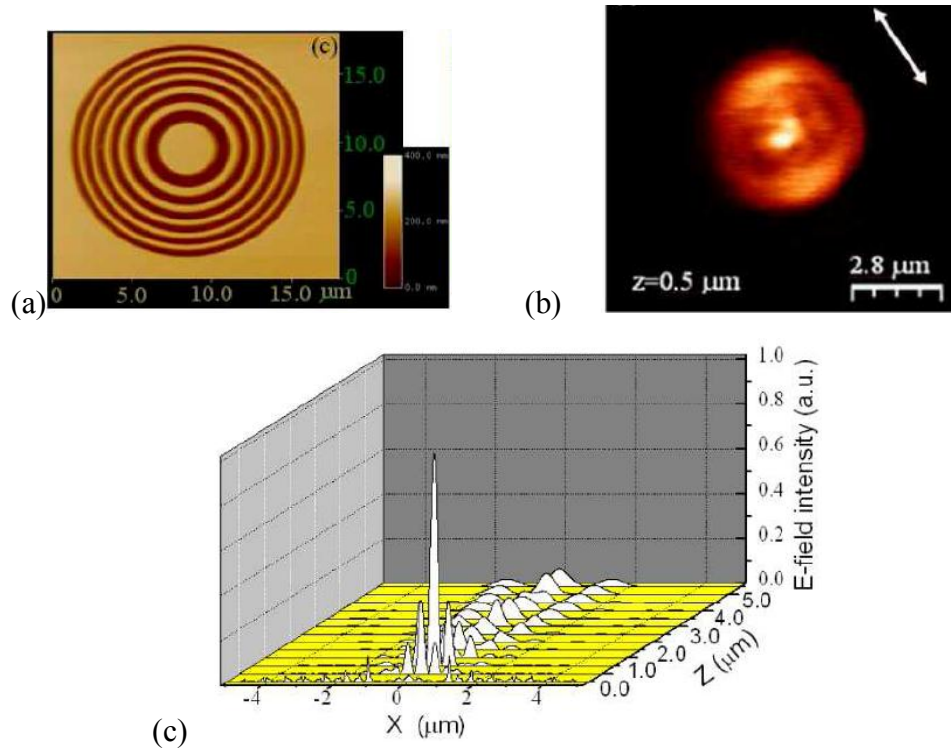


Figure 4.2. Two-dimensional focusing using the SP lens on a quartz substrate. [137] (a) Topography of the SP lens measured with atomic force microscopy (AFM). (b) Intensity distribution at the focus. (c) Intensity profile of the SP lens on the xz plane.

In this section, a model used for designing a 2D SP lens on a fiber end face is first introduced. Two sets of design parameters are then provided. Experimentally measured intensity distributions obtained from two SP fiber samples are presented, demonstrating the superfocusing effect achieved with fiber-based SP lenses. Simulation results obtained by using the FDTD method are compared with the experimental results, and good agreements are achieved in terms of the transverse spot sizes. The reasons for the differences in the experimental and simulation results are discussed. The significance and potential applications of the superfocusing with a fiber-based SP lens are discussed.

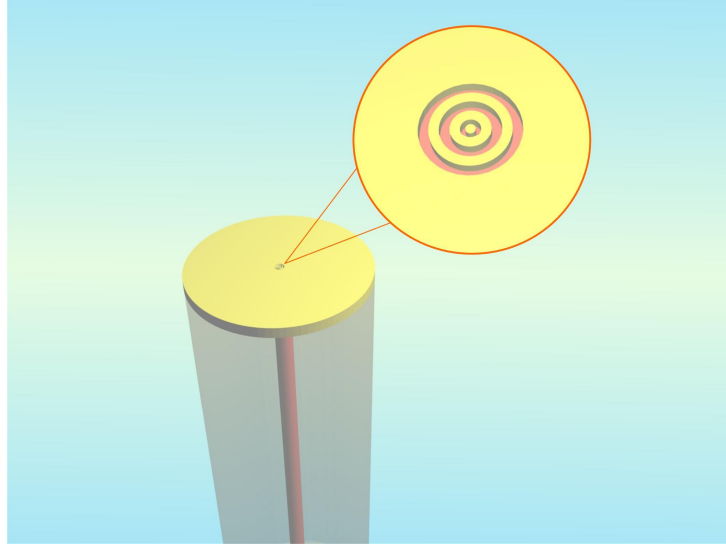


Figure 4.3. Illustration of SP lens fabricated on the endface of an optical fiber.

4.1.1. Modeling and design of fiber-based SP lenses

The SP lens on the endface of an optical fiber is composed of a set of concentric slits removed from a gold coating, as shown in Figure 4.3. The slit widths are less than the optical wavelength so that only the SP waves can propagate inside the slits. In Figure 4.4, the schematic of the principle of the fiber based SP lens is illustrated. The working principle is as follows. When a plane wave initially propagating in a fiber enters the SP lens, the SP waves are excited by the incident optical wave. The SP waves can propagate along the slits when the slits are smaller than the wavelength [122]. The propagation constants at different slits can be different, depending on the slit widths. Therefore, the phase delays associated with the SP wave propagation can be different even for the same propagation distance. The SP waves are then converted back to optical waves once they exit from the SP lens. The exit of each individual slit can be viewed as a source to generate an optical wave. The propagation of these optical waves in the medium is

determined by the initial phases of the sources, which can be tuned by adjusting the slit widths and the metal thickness. In this case, the planar SP lens can induce a curved wavefront as a regular spherical lens does. If the curved wavefront as shown in Figure 4.4 is achieved, a constructive interference (focus) will occur at the center of the wavefront; a focus close to or even smaller than the diffraction limit size can be achieved.

Next, details on how to design an SP lens are provided. Although there are multiple slits in the SP lens, the propagation of SP waves within adjacent slits can be considered to be uncoupled as long as the separation is much larger than the skin depth. The skin depth determines how deep the SP wave can penetrate into the metal. At the wavelength of 808 nm, the skin depth was measured to be around 13 nm. [138] In this work, the slits are designed with separations larger than 130 nm, so that the SP wave propagating through each slit can be analyzed individually as if there is no interference between the SP waves in the adjacent slits.

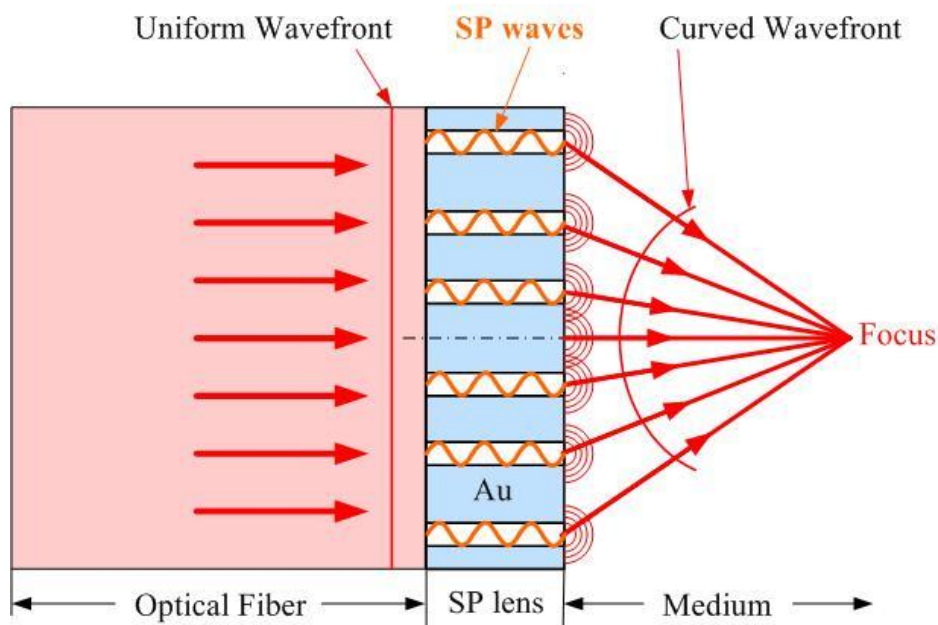


Figure 4.4. Schematic of the principle of a fiber based SP lens.

For a narrow slit surrounded by metallic walls, only the electric field with polarization perpendicular to the metallic walls can excite the SP wave. [122] Therefore, only the transverse magnetic (TM) mode is useful for SP generation. The dispersion relation is expressed as [139]

$$\tanh \left[\frac{w_i}{2} \sqrt{\beta_i^2 - k_0^2} \right] = - \frac{\varepsilon_d \sqrt{\beta_i^2 - k_0^2} \varepsilon_m}{\varepsilon_m \sqrt{\beta_i^2 - k_0^2} \varepsilon_d}, \quad (4-1)$$

where w_i is the width of the i -th slit, β_i the propagation constant of the SP wave, k_0 the wavenumber of the optical wave in vacuum, ε_d the permittivity of the dielectrics in the slit, and ε_m the permittivity of the metal. For a smaller slit width, the optical part of the SP wave will be confined tighter to the surface, and thus more of the mode will penetrate in the metal, resulting in a slower propagation speed. [134] For a fixed ε_d and ε_m , the smaller the slit width w_i , the larger the propagation constant β_i , and the larger the phase delay for a fixed metal thickness. Compared with the phase change at the entrance and the exit of the metal slits, the phase delay associated with the SP propagation and the optical wave propagation is dominant [139]. Therefore in this work, only such phase delay is considered. In order to achieve constructive interference at the designed focal length, f , the phase delays from different slits should differ by integer times 2π ,

$$2\pi \frac{\sqrt{r_i^2 + f^2} - \sqrt{r_{i-1}^2 + f^2}}{\lambda} + (\beta_i - \beta_{i-1})d = 2\pi N, \quad (4-2)$$

where r_i is the i -th slit radius, λ is the wavelength in the medium outside the SP lens, d is the thickness of the gold layer, and N is any integer. The first term of Eq. (4-2) stands for the phase delay of the metal propagation from the exit side of the SP lens to the focus, and the second stands for the phase delay of the SP wave propagation inside the i -th slit.

Based on Eq. (4-2), the basic principle of designing the slits of an SP lens can be summarized as the following: the phase delay of optical wave propagation in the medium (determined by r_i) should be compensated by the phase delay of the SP wave propagation in the slits (determined by w_i and d) so that constructive interference can be obtained at the focus. The desired wavefront in the medium is a spherical surface centered at the focal position. Generally this curved wavefront, and hence the focusing effect, is achieved by using a curved surface of a lens. In the case of the objective lens, it is achieved by a set of carefully designed and fabricated lenses to compensate aberrations. [61] However, fabricating a spherical lens with well controlled profile on a fiber end face is difficult. Fresnel zone plates with a set of concentric rings have also been used to achieve focusing effect [140]. However, due to its large size ($\sim 10 \mu\text{m}$ in diameter for the smallest ring [140]), the Fresnel lens is hard to be implemented on fibers. More importantly, the size of the focus achieved by using both the curved lens and the Fresnel lens is limited by the diffraction limit. By contrast, the SP lens described here can achieve a focus that can potentially overcome the diffraction limit [137].

Two designs of fiber-based SP lenses are obtained following Eqs. (4-1) and (4-2): one with 4 slits and the other with 3 slits. The design parameters of these lenses are listed in Table 4.1 and Table 4.2. The parameters used to obtain the designs are the following: the wavelength $\lambda_0=808$ nm, the medium permittivity $n_d=1.33^2$, the gold layer thickness $d=100$ nm, the refractive index of gold at 808 nm $n_m=-27.0+1.9i$ [141], the focal length $f=20 \mu\text{m}$. It should be noted that the beam waist at the fiber endface is $2.8 \mu\text{m}$ for the fiber used in this work (SM800, Fibercore Ltd.). Therefore, the radius of the outer slits should be smaller than $2.8 \mu\text{m}$ for obtaining enough illumination from the laser beam. The design described in ref. [137] is not feasible to be used on

the optical fiber due to the large radius of the outer slits ($\sim 7 \mu\text{m}$). Another issue that needs to be considered in the design is that the separations between the adjacent slits should be larger than 200 nm to prevent the sidewalls from collapsing during the fabrication process.

Table 4.1. Design parameters of 4-slit SP lens.

Slit #	Radius (nm)	Width (nm)
1	300	60
2	828	72
3	1074	85
4	1393	120

Table 4.2. Design parameters of 3-slit SP lens.

Slit #	Radius (nm)	Width (nm)
1	200	53
2	776	76
3	1072	120

4.1.2. Development and experimental study of fiber-based SP lenses

A 100-nm-thick gold (Au 99.999%, ACI Alloys) layer was deposited on the cleaved fiber end face by E-beam evaporation (BJD-1800, Temescal). A 3-nm-thick titanium coating was used as the adhesion layer. Titanium is chosen because of its resistance to corrosion [142]. During the early stage of the SP lens development, chromium was also used as the adhesion layer. However, due to the heat associated with the optical absorption, vapor bubbles were generated on the SP

lens when it was tested in water. Using titanium as the adhesion layer can decrease the possibility of the bubble generation. The sidewall of the gold coated fiber was then coated with 5 nm of gold without adhesion layer. This gold layer is necessary to dissipate the charge accumulated in focus ion beam milling (FIB) process. The fiber was mounted on an aluminum metal strip ($1/4'' \times 1/2'' \times 1/16''$) by a piece of carbon double-sided tape, and a layer of copper single-sided tape was applied on the top to immobilize the fiber. In this way of mounting, the fiber endface was grounded with the metal strip to avoid any charging problem associated with the FIB fabrication. FIB milling was used to remove the gold in the designed slits. The FIB fabrication was carried out using a Zeiss NVision 40 FIB workstation by our collaborators (Dr. Xu and Dr. Zhitenev) at the National Institute of Standards and Technology (NIST).

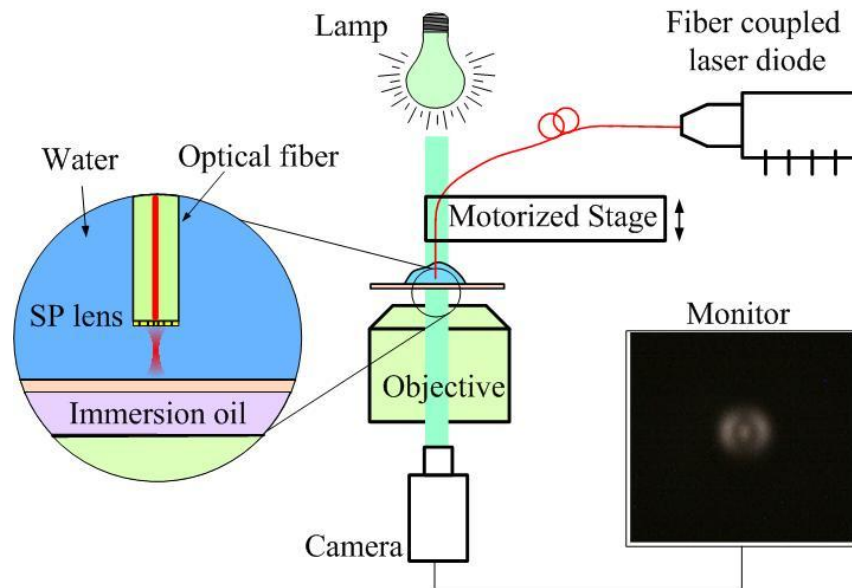


Figure 4.5. Schematic of the experimental arrangement for SP lens testing.

The experimental setup for testing the fiber-based SP lens is shown in Figure 4.5. The fiber was mounted vertically on the microscope platform, with the SP lens facing the objective lens (Plan CN, 100 \times , 1.25 NA, Olympus). The fiber end with the SP lens was submerged in a water drop

(~5 mm thick) on a coverglass. A motorized stage (VP-5ZA, Newport) with a resolution of 100 nm was used to move the fiber along the vertical direction. A laser beam of 808 nm (the same light source used in Section 2.3) was coupled into the fiber. The output beam at the focal plane of the objective lens was imaged onto a camera, which can also be viewed by using a monitor. Two cameras were used for the measurements: one being the Motic camera (Moticam 1000, Motic) with an 8-bit dynamic range and a (nominal) resolution of 50 nm per pixel calibrated using the objective lens and the other being the DS camera (DS-Qi1, Nikon) with a 12-bit dynamic range and a (nominal) resolution of 60 nm per pixel calibrated using the objective lens. Each pixel of the camera served as an individual optical powermeter, and the recorded grayscale value was considered to be proportional to the intensity of the corresponding position at the object plane. By sweeping the SP lens in the vertical direction, 3D intensity distribution can be reconstructed from the images captured. Note that the illumination lamp was turned off during the measurements.

4.1.3. Experimental results of fiber-based SP lenses

Two fiber-based SP lenses were successfully fabricated and tested. Strong focusing effect was observed from both SP lenses with the focal sizes close to the diffraction limit. The results are described and discussed next.

4.1.3.1. Experimental results obtained from the 4-slit fiber-based SP lens (SP1)

The sample SP1 is a four-slit SP lens following the design parameters shown in Table 4.1. The scanning electron microscope (SEM) image of the SP lens on the fiber endface is shown in Figure 4.6.



Figure 4.6. SEM image of the sample SP1 on a fiber endface.

SP1 was measured by using the DS camera with a dynamic range of 12 bits (0~4096). The experimentally measured intensity distribution on the xz and yz plane is shown in Figure 4.7, providing the z axis is the optical axis of the fiber. The bar on the right of the plot shows the grayscale of the data, which is proportional to the intensity. The endface of the SP lens is located at the $z=0$ plane. A strong focus is clearly seen at $z=3.2\pm 0.1 \mu\text{m}$.

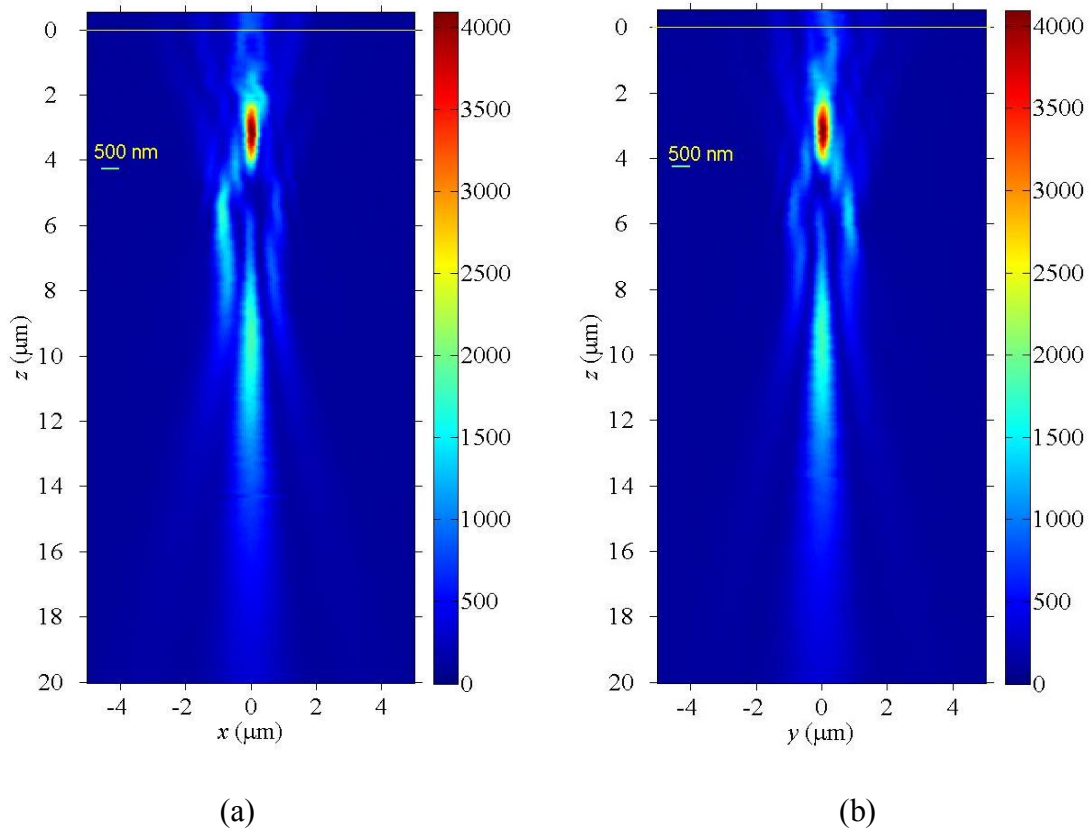


Figure 4.7. Experimentally measured intensity distribution from SP1 on two orthogonal planes: (a) xz plane and (b) yz plane. The origin of the coordinate system is located at the center of the SP lens surface. The optical beam is propagating downwards.

To further investigate the focal size, the intensity profiles near the focus along three orthogonal directions are obtained, as shown in Figure 4.8 (a)-(c). The spot sizes defined by the FWHM are found to be 440 ± 60 nm along the x direction, 500 ± 60 nm along the y direction, and 1.758 ± 0.1 μm along the z direction. The focal sizes in the x and y directions are slightly different by 60 nm. This asymmetry of the intensity pattern can also be seen in the xy -plane image at the focal plane shown in Figure 4.8 (d). The slight difference is believed to come from the asymmetry of the polarization of the input wave in the single mode fiber, where the guided wave is linearly polarized. [143]

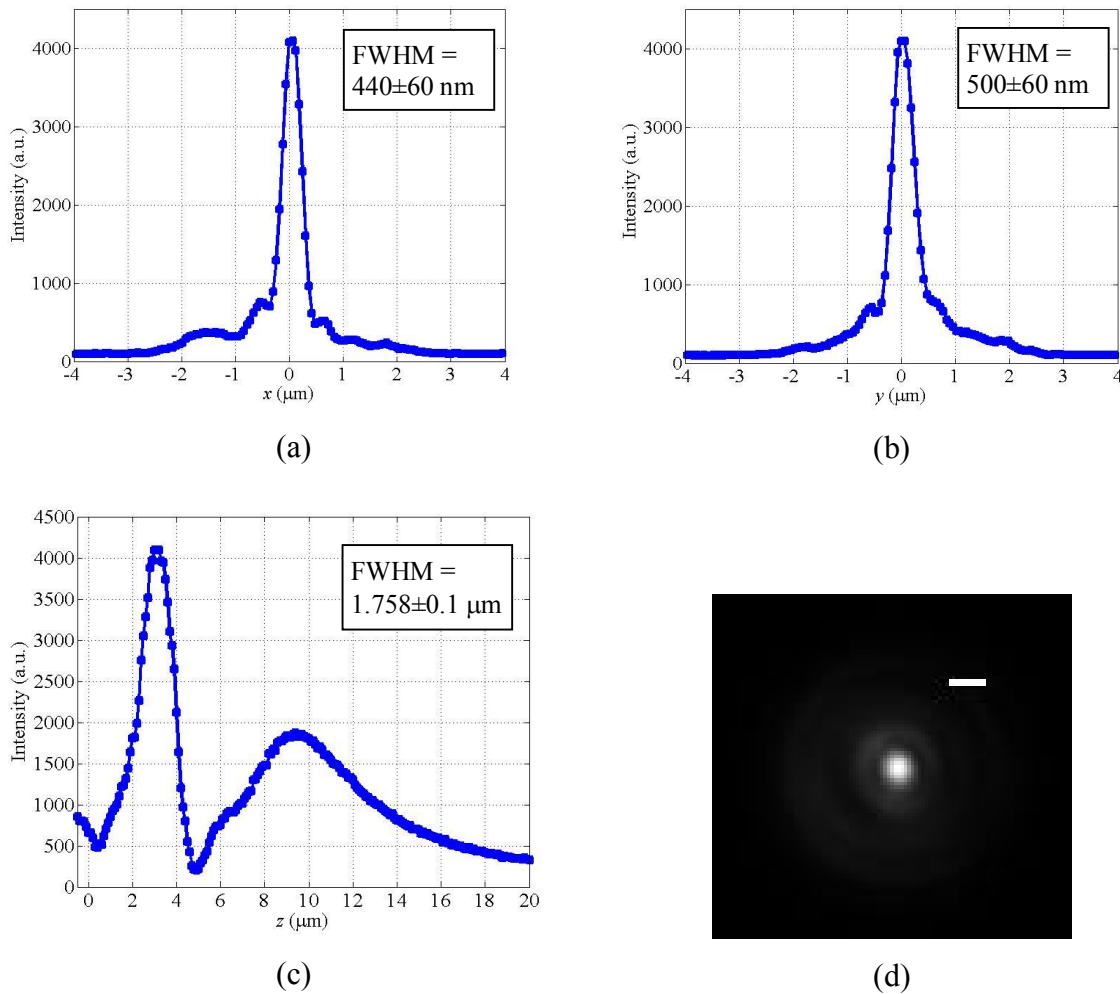


Figure 4.8. Experimentally measured intensity profile of SP1 at the strongest intensity position ($z = 3.2 \pm 0.1 \mu\text{m}$) along (a) x axis, (b) y axis, and (c) z axis. (d) The image of the focus at $z = 3.2 \mu\text{m}$. The scale bar at the upper right corner of (d) denotes 600 nm (10 pixels).

4.1.3.2. Experimental results obtained from the 3-slit fiber-based SP lens (SP2)

SP2 is a 3-slit SP lens following the design parameters shown in Table 4.2. The scanning electron microscope (SEM) image of the SP lens on the fiber endface is shown in Figure 4.9.

Compared with SP1 shown in Figure 4.6, the slits of SP2 are much smoother. Moreover, the interference effects between the slits are much smaller due to the larger slit separations.

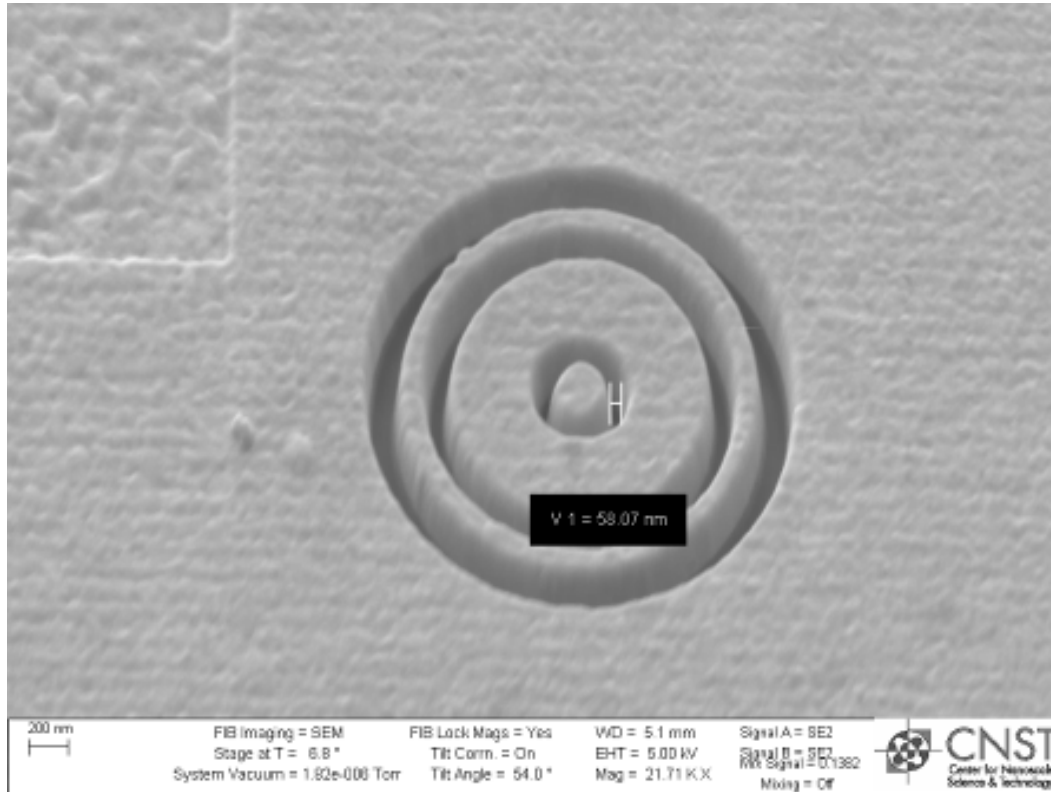


Figure 4.9. SEM image of the sample SP2 on a fiber endface.

The intensity profile of SP2 was measured with the 8-bit Motic camera with a dynamic range of 0~256. The experimentally obtained intensity distribution is shown in Figure 4.10. SP2 also exhibited a small focus at $z = 1.1 \mu\text{m}$. It can be seen that the intensity patterns on the xz and yz planes are mirror symmetrical. Further quantitative evaluation of the focus can be obtained from the intensity profile along three orthogonal directions across the focus, as shown in Figure 4.11 (a)-(c). The focal spot size (FWHM) is found to be $352 \pm 50 \text{ nm}$ along the x direction and 533 ± 50 along the y direction. The focal depth (FWHM) along the z direction is obtained to be 743 ± 100

nm. An obvious difference between the x and y direction spot sizes is observed, which can be confirmed by the image of the focus shown in Figure 4.11 (d).

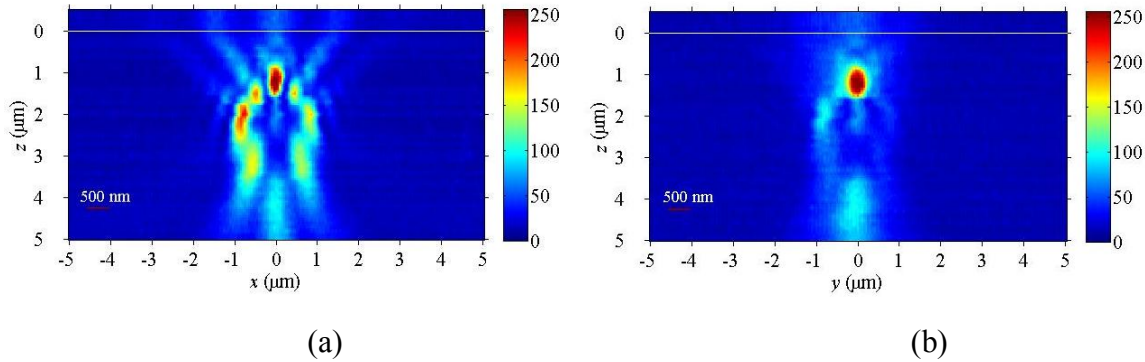


Figure 4.10. Experimentally measured intensity distribution from SP1 on two orthogonal planes: (a) xz plane and (b) yz plane. The origin of the coordinate system is located at the center of the SP lens surface. The optical beam is propagating downwards.

4.1.3.3. Discussion of the superfocusing results obtained with the SP lenses

Overestimation of the focal spot size

The spot sizes obtained from the measurements are influenced by two main issues: the resolution power of the objective lens and the pixel size of the camera. These two issues cause overestimation of the focal spot size of the fiber-based SP lens. The real spot size is expected to be smaller than the measured values. Detailed explanation is provided as follows.

The experimentally measured intensity is actually the intensity passing through the objective. It is not surprising that the resolution of the measured intensity distribution is limited by that of the objective. For each point at the object plane, the image will be enlarged due to the point spread

function [144], which limits how small a resolved area at the object plane can be. If two points are closer than this limit, their images will be smeared and cannot be distinguished at the image plane. [61] This will cause the fine intensity changes filtered out by the objective lens before the intensity is measured. In another word, the focus measured in the experiment is the smeared version of the real focus, resulting in an overestimation of the spot size.

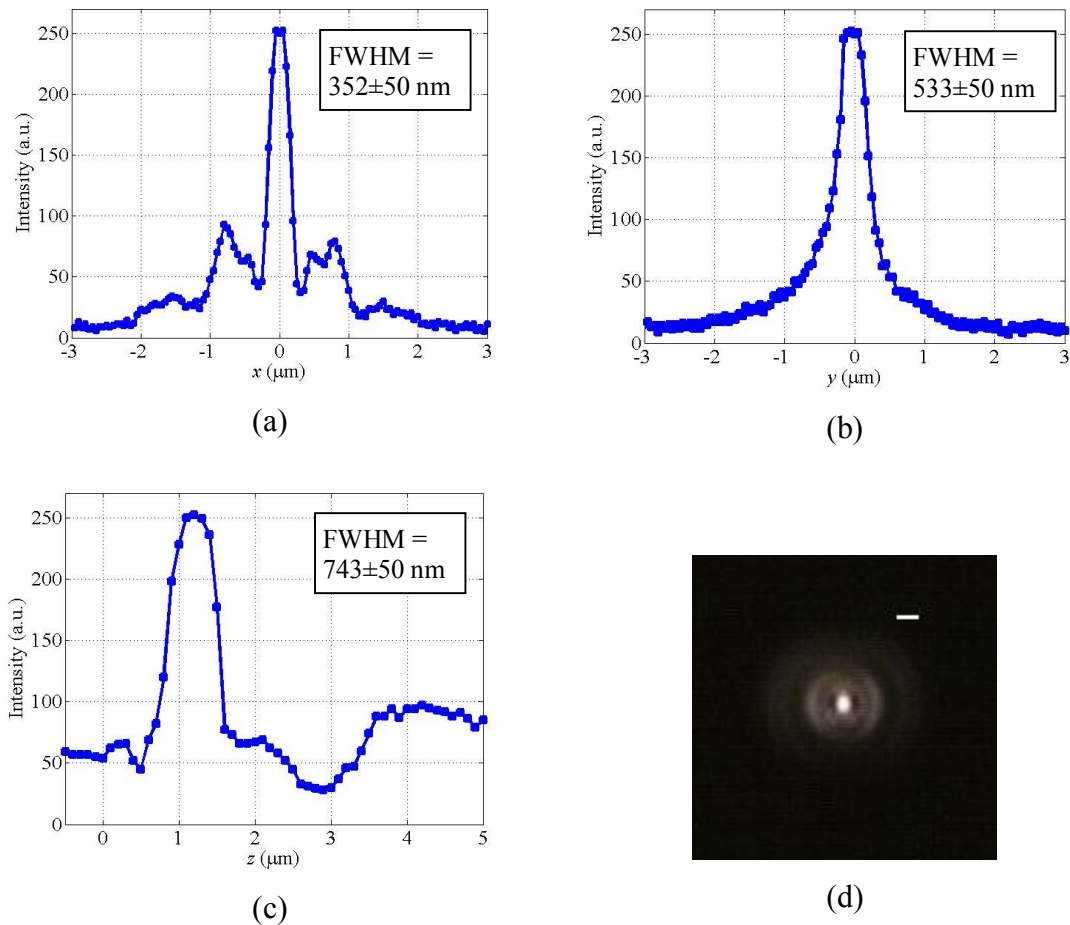


Figure 4.11. Experimentally measured intensity profile at the strongest intensity position ($z = 1.1 \pm 0.1 \mu\text{m}$) along (a) x axis, (b) y axis, and (c) z axis. (d) The image of the focus at $z = 1.1 \mu\text{m}$. The scale bar at the upper right corner of (d) denotes 500 nm (10 pixels).

The pixel size of the camera also introduces a positive error to the measured spot size. The intensity (grayscale) obtained for each pixel was the averaged value over the whole pixel area.

This does not influence the edge of the focus, but the highest intensity is underestimated. As an example, according to Figure 4.8 (b), it seems that the highest intensity is 4095 (a.u.) located at $y=0$ and $y=0.06 \mu\text{m}$. However, because of the averaging effect, the real highest intensity might be 6000 located at $y=0.03 \mu\text{m}$. Because the spot size was measured as the FWHM, this underestimation of the maximum intensity directly results in an overestimation of the spot size. If the maximum intensity of 6000 is used, the y -axis spot size in Figure 4.8 (b) would be ~ 340 nm instead of 500 nm. Similar overestimations can also rise from the sweeping step of the z axis.

Comparison with the spot size achievable with objective lenses

According the measured spot sizes of SP1 and SP2, the focusing effects of the SP fibers are much stronger than that obtained with the lensed fiber used in Chapter 2 and Chapter 3. The spot sizes achieved on the fiber endfaces are even comparable to those created with high NA objective lenses.

The Abbe's diffraction limit for the focal spot size is $\lambda/2n$, with λ being the vacuum wavelength and n the medium refractive index. [145, 146] For the wavelength of 808 nm and the medium of water, this limit is calculated to be 304 nm. However, the smallest spot size that can be achieved with an objective is larger than the Abbe's diffraction limit. The FWHM of the smallest spot obtained from an objective lens with a numerical aperture of NA is given by [147]

$$D_{obj} = FWHM = \frac{0.61\lambda}{NA}. \quad (4-3)$$

The smallest spot size (FWHM) for an objective is 394 nm with $NA = 1.25$ and 352 nm with $NA = 1.4$. The highest NA of commercially available objective lenses is 1.4. It should be noted that

the value calculated with Eq. (4-3) is the optimal spot size obtained in an ideal case. Due to some practical issues, this limit may not be achievable with a high NA objective lens. First of all, the effective NA is lower than the designed value. [144] Secondly, if the free-space optical path is not properly adjusted, or if the back focal plane is not filled with the optical power, the spot size will be larger. [147] Moreover, high NA objectives usually use oil immersion, which is a must for NA=1.4. The mismatch of the refractive index between the immersion oil and the water introduces additional aberrations, which will result in a smeared focus, and thus an increased spot size. [16] It is noted that although some imaging techniques such as confocal microscopy can an imaging resolution smaller than the diffraction limit, they cannot focus the optical power into an area below the diffraction limit, which is necessary to increase the trapping efficiency of fiber optical tweezers, the reason we intend to investigate superfocusing in the first place.

The x -direction spot size of SP2, which is 350 nm, is comparable to the smallest spot size achieved with an objective lens with the highest NA. Considering the overestimation of the spot sizes, the real spot size achieved with this fiber-based SP lens is expected to be even smaller. Furthermore, the fiber as a perfect waveguide is less susceptible to the noise introduced by the environmental factors, and a fundamental Gaussian beam is almost always guaranteed at the entrance of the SP lens. Unlike the objective lenses with which the smallest spot size is always difficult to achieve, the fiber-based SP lens can readily achieve a small focus close to the diffraction limit size.

Even though the spot size was underestimated, focuses close or equal to the smallest focal size of objectives have been achieved by using fiber-based SP lenses. It will be demonstrated in Section

4.2.1 that this focus can be used to achieve a stronger trap than objective-based optical tweezers, which indicates that the real focus should be smaller than the focal size of the objective.

Dependence of focal lengths on the aperture size

The measured focal lengths are 3.2 μm and 1.1 μm for SP1 and SP2, respectively, which are significantly bigger than the designed focal length of 20 μm . This level of mismatch has also been reported and discussed in ref. [134]. The major cause of this mismatch is believed to be the aperture size. The aperture size plays the most important role in limiting the effective focal length and elongating the focal depth [148]. The smaller the lens aperture, the stronger diffraction effect at the lens edge, and the larger the difference between the real focal length and the designed value. This can also be observed from the results obtained in this dissertation: the 4-slit SP1 has a focal length of 3.2 μm while the 3-slit SP2 has a focal length of 1.1 μm . As discussed previously, the spot size of the fiber limits the aperture of the SP lens. Therefore, the real focal length is always smaller than the designed value. The diffraction effect also makes the focus longer in the longitudinal direction compared with the transverse directions. [148] This effect has also been observed from the results obtained by using the fiber-based SP lenses.

In addition to the aperture effects, other issues can also cause the focal length to vary from the designed value. One reason is the resonance of the SP wave in the slits. Each slit can be viewed as an optical resonator. The SP wave propagating inside may travel multiple trips before exiting the slit. This effect is not considered in the design model. The resonance effect can change the phase delay and hence cause focus shift. Power differences between the optical waves emitted

from the slits also introduce differences to the designed parameters. Since the power distribution in different slits is not considered in designing the SP lens, the output optical powers from different slits are expected to be non-uniform. The Gaussian distribution of the light propagating in the optical fibers, the different attenuation of the SP wave when passing through the slits with different widths, and the varying radius of slits all contribute to the power difference between the optical waves from different slits. It is known that the visibility of the interference pattern reaches maximum when the incident waves have equal amplitudes. [61] Difference in the intensity of incident waves can smear the focus and also cause the focus shift.

Comparisons with the results in ref. [137]

Compared with the superfocusing achieved by the SP lens on a glass substrate [137] as shown in Figure 4.2, the intensity distribution of the fiber-based SP lens (see Figure 4.8 and Figure 4.11) is much sharper and cleaner on the focal plane, which means more power is focused at one spot instead of being distributed over a large area. The SP lenses developed in this dissertation work only consist of 3 or 4 rings and have radii of less than $1.5 \mu\text{m}$ in radius, compared with a much larger ($\sim 6 \mu\text{m}$), 6-ring SP lens in ref. [137]. Moreover, the fiber-based SP lenses have the longer focal lengths of $1.1 \mu\text{m}$ and $3.2 \mu\text{m}$, while the focal length achieved in ref. [137] is $0.5 \mu\text{m}$. Most importantly, the superfocusing achieved in this dissertation work is with a fiber-based SP lens, which can fully take the advantages of a large variety of mature technology associated with optical fibers.

4.1.4. Modeling of fiber-based SP lens: FDTD simulations

As discussed in Section 4.1.3.3, there are some issues that are not considered in the design model. However, these issues can be considered in numerical simulations using finite-difference methods. [134] In this section, a commercial software, FDTD Solutions, is used to model the optical wave emitted from the SP lenses, which is useful for achieving a better understanding of the superfocusing mechanism of the fiber-based SP lens.

4.1.4.1. Basic principles of FDTD methods

FDTD method is one kind of space-grid time-domain techniques that is widely used in solving electromagnetic (EM) problems. [149] In the FDTD method, the space of interest is divided into a number of small volumes. Within each small volume, the Maxwell's curl equations can be approximated with finite differences, enabling the solution of Maxwell's equations in a spatial stepping procedure. In this case, the spatial distribution of the EM wave at time $t + \Delta t$ can be obtained by using the previous distribution at time t . This time-stepping continues as the numerical wave analogs propagate in the space lattice. The marching-in-time procedure can be used to effectively simulate how the EM wave propagates in the space with time going forward. Since no assumption is necessary for performing FDTD simulations, providing the calculations converge, FDTD is believed to be able to solve a large variety of EM wave interaction problems, from radar-guided devices to nanoscale optical resonators. [149]

The basic idea of FDTD is to replace the derivatives in the Maxwell's equations with corresponding finite differences. Maxwell's curl equations in a linear, isotropic and nondispersive material are written as [149]:

$$\left\{ \begin{array}{l} \frac{\partial \mathbf{H}}{\partial t} = -\frac{1}{\mu} \nabla \times \mathbf{E} - \frac{1}{\mu} (\mathbf{M}_{\text{source}} + \sigma^* \mathbf{H}), \\ \frac{\partial \mathbf{E}}{\partial t} = -\frac{1}{\varepsilon} \nabla \times \mathbf{H} - \frac{1}{\varepsilon} (\mathbf{J}_{\text{source}} + \sigma \mathbf{E}). \end{array} \right. \quad (4-4)$$

$$\left\{ \begin{array}{l} \frac{\partial \mathbf{H}}{\partial t} = -\frac{1}{\mu} \nabla \times \mathbf{E} - \frac{1}{\mu} (\mathbf{M}_{\text{source}} + \sigma^* \mathbf{H}), \\ \frac{\partial \mathbf{E}}{\partial t} = -\frac{1}{\varepsilon} \nabla \times \mathbf{H} - \frac{1}{\varepsilon} (\mathbf{J}_{\text{source}} + \sigma \mathbf{E}). \end{array} \right. \quad (4-5)$$

where the vectors \mathbf{E} and \mathbf{H} are the electric field and the magnetic field, ε and μ denote the permittivity and permeability in the medium, t is the time, and $\mathbf{J}_{\text{source}}$ and $\mathbf{M}_{\text{source}}$ are the electric current density and equivalent magnetic current density, which are independent sources of E- and H-field, respectively. The symbol ∇ denotes the vector differential operator,

$\nabla = \mathbf{i} \frac{\partial}{\partial x} + \mathbf{j} \frac{\partial}{\partial y} + \mathbf{k} \frac{\partial}{\partial z}$ in a Cartesian coordinate system, where \mathbf{i} , \mathbf{j} , and \mathbf{k} are the unit vectors

along the x , y and z directions, respectively. The vector components of Eq. (4-4) and (4-5) can be written separately:

$$\left\{ \begin{array}{l} \frac{\partial H_x}{\partial t} = \frac{1}{\mu} \left[\frac{\partial E_y}{\partial z} - \frac{\partial E_z}{\partial y} - (M_{\text{source}x} + \sigma^* H_x) \right], \\ \frac{\partial H_y}{\partial t} = \frac{1}{\mu} \left[\frac{\partial E_z}{\partial x} - \frac{\partial E_x}{\partial z} - (M_{\text{source}y} + \sigma^* H_y) \right], \\ \frac{\partial H_z}{\partial t} = \frac{1}{\mu} \left[\frac{\partial E_x}{\partial y} - \frac{\partial E_y}{\partial x} - (M_{\text{source}z} + \sigma^* H_z) \right], \end{array} \right. \quad (4-6)$$

$$\left\{ \begin{array}{l} \frac{\partial H_x}{\partial t} = \frac{1}{\mu} \left[\frac{\partial E_y}{\partial z} - \frac{\partial E_z}{\partial y} - (M_{\text{source}x} + \sigma^* H_x) \right], \\ \frac{\partial H_y}{\partial t} = \frac{1}{\mu} \left[\frac{\partial E_z}{\partial x} - \frac{\partial E_x}{\partial z} - (M_{\text{source}y} + \sigma^* H_y) \right], \\ \frac{\partial H_z}{\partial t} = \frac{1}{\mu} \left[\frac{\partial E_x}{\partial y} - \frac{\partial E_y}{\partial x} - (M_{\text{source}z} + \sigma^* H_z) \right], \end{array} \right. \quad (4-7)$$

$$\left\{ \begin{array}{l} \frac{\partial H_x}{\partial t} = \frac{1}{\mu} \left[\frac{\partial E_y}{\partial z} - \frac{\partial E_z}{\partial y} - (M_{\text{source}x} + \sigma^* H_x) \right], \\ \frac{\partial H_y}{\partial t} = \frac{1}{\mu} \left[\frac{\partial E_z}{\partial x} - \frac{\partial E_x}{\partial z} - (M_{\text{source}y} + \sigma^* H_y) \right], \\ \frac{\partial H_z}{\partial t} = \frac{1}{\mu} \left[\frac{\partial E_x}{\partial y} - \frac{\partial E_y}{\partial x} - (M_{\text{source}z} + \sigma^* H_z) \right], \end{array} \right. \quad (4-8)$$

$$\left\{ \begin{array}{l} \frac{\partial E_x}{\partial t} = \frac{1}{\varepsilon} \left[\frac{\partial H_z}{\partial y} - \frac{\partial H_y}{\partial z} - (J_{\text{source}x} + \sigma E_x) \right], \\ \frac{\partial E_y}{\partial t} = \frac{1}{\varepsilon} \left[\frac{\partial H_x}{\partial z} - \frac{\partial H_z}{\partial x} - (J_{\text{source}y} + \sigma E_y) \right], \\ \frac{\partial E_z}{\partial t} = \frac{1}{\varepsilon} \left[\frac{\partial H_y}{\partial x} - \frac{\partial H_x}{\partial y} - (J_{\text{source}z} + \sigma E_z) \right]. \end{array} \right. \quad (4-9)$$

$$\left\{ \begin{array}{l} \frac{\partial E_x}{\partial t} = \frac{1}{\varepsilon} \left[\frac{\partial H_z}{\partial y} - \frac{\partial H_y}{\partial z} - (J_{\text{source}x} + \sigma E_x) \right], \\ \frac{\partial E_y}{\partial t} = \frac{1}{\varepsilon} \left[\frac{\partial H_x}{\partial z} - \frac{\partial H_z}{\partial x} - (J_{\text{source}y} + \sigma E_y) \right], \\ \frac{\partial E_z}{\partial t} = \frac{1}{\varepsilon} \left[\frac{\partial H_y}{\partial x} - \frac{\partial H_x}{\partial y} - (J_{\text{source}z} + \sigma E_z) \right]. \end{array} \right. \quad (4-10)$$

$$\left\{ \begin{array}{l} \frac{\partial E_x}{\partial t} = \frac{1}{\varepsilon} \left[\frac{\partial H_z}{\partial y} - \frac{\partial H_y}{\partial z} - (J_{\text{source}x} + \sigma E_x) \right], \\ \frac{\partial E_y}{\partial t} = \frac{1}{\varepsilon} \left[\frac{\partial H_x}{\partial z} - \frac{\partial H_z}{\partial x} - (J_{\text{source}y} + \sigma E_y) \right], \\ \frac{\partial E_z}{\partial t} = \frac{1}{\varepsilon} \left[\frac{\partial H_y}{\partial x} - \frac{\partial H_x}{\partial y} - (J_{\text{source}z} + \sigma E_z) \right]. \end{array} \right. \quad (4-11)$$

It can be seen that the differentiation of all the components are carried out along the two orthogonal directions. For example, E_z and H_z are differentiated along x and y directions, but not z direction. Yee [150] presented a special lattice and a set of finite-difference equations to solve the Maxwell's equation. The famous Yee's lattice is shown in Figure 4.21. Each grid (i, j, k) is surrounded by the six components of the EM field. Three electric field components are located at the centers of three adjacent edges. Three magnetic field components are located at the centers of the three adjacent surfaces. Each component is along the corresponding axis.

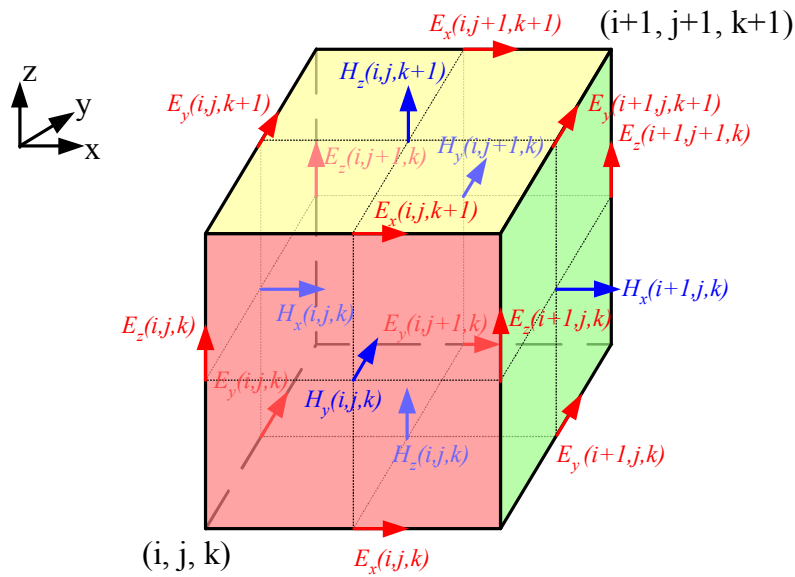


Figure 4.12. Components of the electric and magnetic fields in a cubic cell of the Yee's lattice.

Applying the central differences

$$\frac{df}{dx} = \frac{f(x + \frac{1}{2}\Delta x) - f(x - \frac{1}{2}\Delta x)}{\Delta x} \quad (4-12)$$

to Eq. (4-4)~ (4-11), the final equations used for the FDTD method can be obtained in terms of the components in the Yee's lattice shown in Figure 4.21. Here only the final results by applying Eq. (4-12) to Eq. (4-4) are given in Eq. (4-13), and other results can be found in ref. [149].

$$\begin{aligned}
H_x \Big|_{i-1/2, j+1/2, k+1}^{n+1} = & \left(\frac{1 - \frac{\sigma_{i-1/2, j+1, k+1}^* \Delta t}{2\mu_{i-1/2, j+1, k+1}}}{1 + \frac{\sigma_{i-1/2, j+1, k+1}^* \Delta t}{2\mu_{i-1/2, j+1, k+1}}} \right) H_x \Big|_{i-1/2, j+1/2, k+1}^{n+1} \\
& + \left(\frac{\frac{\Delta t}{\mu_{i-1/2, j+1, k+1}}}{1 + \frac{\sigma_{i-1/2, j+1, k+1}^* \Delta t}{2\mu_{i-1/2, j+1, k+1}}} \right) \cdot \left(\frac{E_y \Big|_{i-1/2, j+1, k+3/2}^{n+1/2} - E_y \Big|_{i-1/2, j+1, k+1/2}^{n+1/2}}{\Delta z} \right. \\
& \left. - \frac{E_z \Big|_{i-1/2, j+3/2, k+1}^{n+1/2} - E_z \Big|_{i-1/2, j+1/2, k+1}^{n+1/2}}{\Delta y} - M_{sourcex} \Big|_{i-1/2, j+1, k+1}^{n+1/2} \right)
\end{aligned} \tag{4-13}$$

Here, Δx , Δy , and Δz are the lengths of the lattice cube along the x , y , and z axes, respectively, and Δt is the time step. Each field component has one superscript for the number of the time step and three subscripts for the numbers of the spatial steps along three axes. A semi-implicit approximation is usually used to estimate the field components at time $n\Delta t$: [149]

$$H_x \Big|_{i-1/2, j+1/2, k+1}^n = \frac{H_x \Big|_{i-1/2, j+1/2, k+1}^{n-1/2} + H_x \Big|_{i-1/2, j+1/2, k+1}^{n+1/2}}{2} \tag{4-14}$$

According to Eq. (4-13) and Eq. (4-14), the field components at any time can be directly obtained from the field components of previous times. Therefore, the FDTD method is a marching-in-time procedure with the help of Yee's lattice to simulate the EM wave propagation by solving Maxwell's equations.

4.1.4.2. FDTD simulations carried out with FDTD Solutions

FDTD Solutions (Lumerical, Inc) is a powerful FDTD simulation software that provides a computer aid designing (CAD) interface and high calculation efficiency. The procedure of carrying out the FDTD simulations with FDTD Solutions is shown in Figure 4.13.

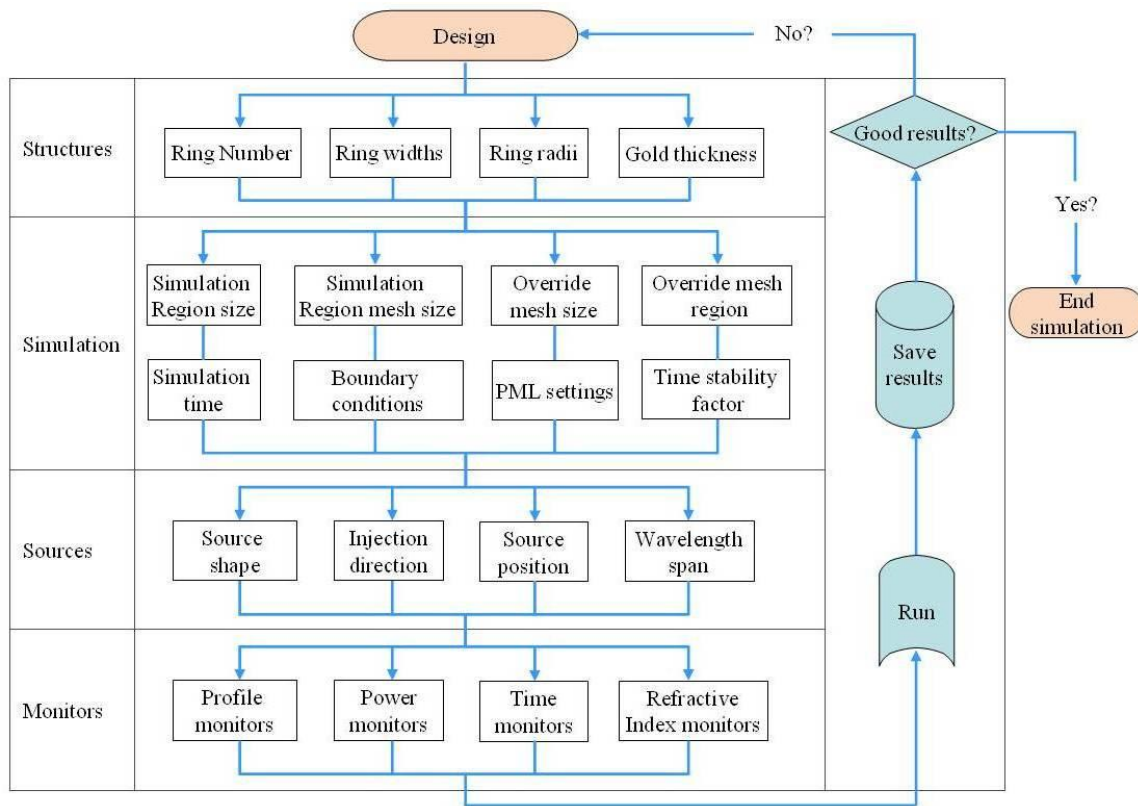


Figure 4.13. Procedure of FDTD simulations.

The setup of a model and the input of the parameters can be realized by four modules in the software: Structures, Simulation, Sources, and Monitors. The model of the fiber-based SP lens is drawn with the CAD interface in the Structures module. The number of the slits (rings), the radius and width of each slit, and the gold layer thickness can be adjusted. Other parameters such

as the refractive indices of the medium, the fiber, and the metal can also be modified. There are different dispersion models for determining the permittivity of dispersive materials. If the models used are inappropriate, the simulation results can be unstable (divergent). Appropriate models thus should be chosen by comparing the values provided by the models and those available in the databases.

The settings of the simulation region are then specified in the Simulation module. The simulation region size determines the space in which the simulation should be performed. The simulation region mesh size is actually the size of Yee's lattice cube, which controls the grid size of the whole simulation region. If there are regions with fine structures or sharp changes of the material properties, the override mesh can be used to create a finer grid within that region. Since FDTD Solutions use EM pulse to simulate the EM behavior, the simulation time determines the total number of time steps to be calculated, which should be set long enough so that the majority of the optical power leaves the simulation region. Long simulation time requires more computational resources (more memory usage and longer calculation time). Boundary conditions (BCs) are also very important for the simulations to work properly and efficiently. The symmetric and antisymmetric BCs can make the simulation region two-fold or four-fold smaller. The perfectly matched layer (PML) is a type of BCs that can absorb all the incident EM waves. When the simulation region is in an open space, the PML is used outside the whole simulation region to avoid the EM wave reflecting back to the region. The stability of the simulation depends largely on the settings of the PML, such as the number of PML layers, PML types, and the relative position of the PML type. In addition, the time stability factor also helps achieve a

convergent simulation. These settings have to be properly adjusted via a trial-and-error procedure.

The Sources module defines the properties of the incident wave. The parameters of the sources can be input here, including the source shape, wavelength span, source inject position and direction, and source polarization. Generally these parameters do not affect the convergence of the simulation. Modifications are necessary only when different beam parameters are tested.

The monitors elaborate the data to be recorded after the simulation. This module determines what data should be kept for viewing while removing other unnecessary data from the simulation. Large sizes and large number of monitors can significantly increase the required memory during the simulation as well as the file size. Different types of monitors are available for evaluating the simulation results.

After the settings of all the modules are finished, the simulation can be started by running with the built-in FDTD codes. The running time ranges from 2 hours to 12 hours, depending on the settings. The simulation results can be checked from the data saved in the Monitors module.

4.1.4.3. FDTD simulation results of SP1

FDTD simulations are carried out to obtain the intensity distribution of the designed fiber-based SP lenses. The incident beam is set to have a flat wavefront and a Gaussian intensity profile with the beam waist of 2.8 μm , which is consistent with the wave in an SM800 single model fiber.

The polarization is considered to be along the x axis and the wavelength is 808 nm. The beam is incident from a glass medium with a refractive index of 1.458, which is the value of the fiber core refractive index. The beam waist is set to be at the interface between the glass and the gold layer. The gold layer is 100 nm thick according to the experimentally measured value described in Section 4.1.2. The parameters of the SP lenses used in the simulations are the same as those listed in Table 4.1.

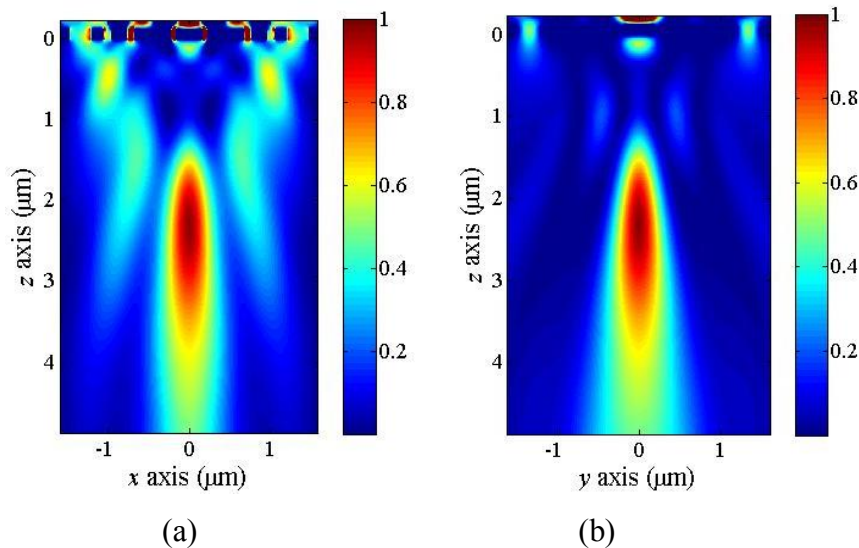


Figure 4.14. Intensity distribution obtained from the simulations of SP1 on two orthogonal planes: (a) xz plane and (b) yz plane. The origin of the coordinate system is located at the center of the SP lens surface. The optical beam is propagating downwards.

The intensity distributions along the two orthogonal planes are shown in Figure 4.14. According to the simulation results, the focus (the strongest intensity) is located at $z = 2.29 \mu\text{m}$ on the optical axis. The intensity profiles at the strongest intensity position along different directions are obtained in the simulations, as shown in Figure 4.15. The focal size (i.e., FWHM size) obtained

from the simulation is 544 nm along the x direction, 520 nm along the y axis, and $3.42 \mu\text{m}$ along the z axis.

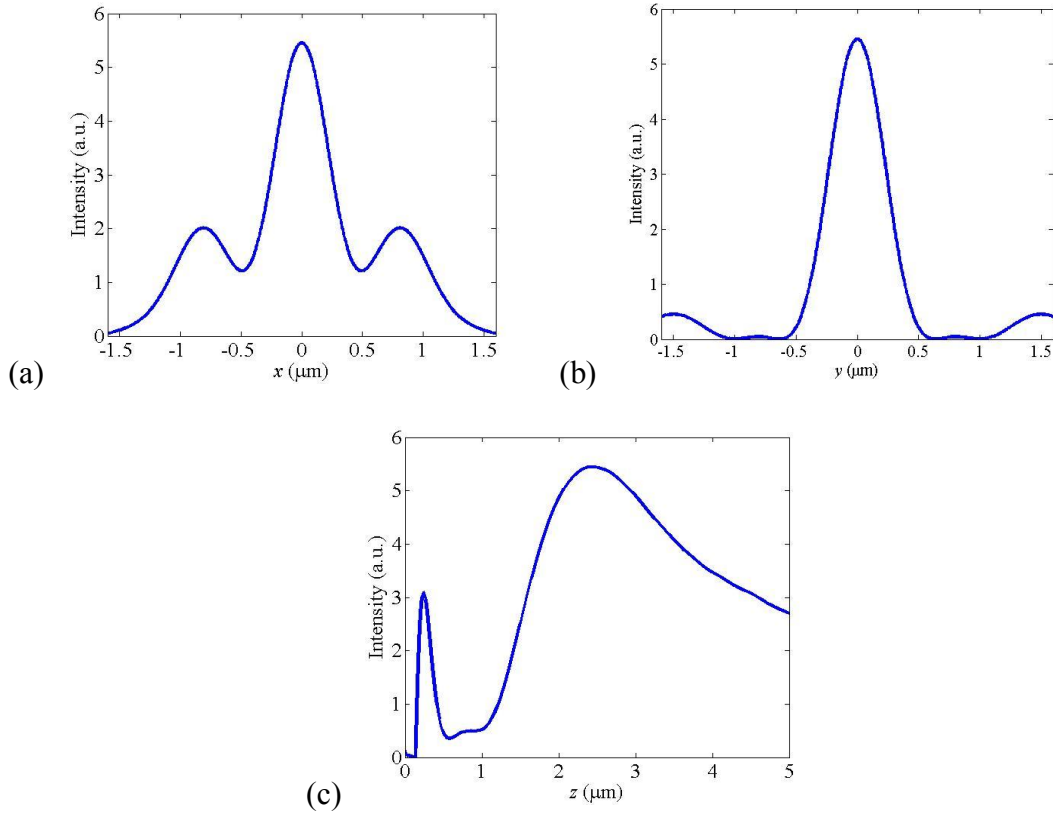


Figure 4.15. Intensity profile at the strongest intensity position ($z = 2.42 \mu\text{m}$) along (a) x axis, (b) y axis, and (c) z axis.

4.1.4.4. FDTD simulation results of SP2

The intensity distribution of SP2 is also obtained by using FDTD Solutions. The design parameters shown in Table 4.2 are used in the simulations. The intensity distributions along the xz and yz planes are shown in Figure 4.16. It is found that the focus is located at $z=1.47 \mu\text{m}$ on

the optical axis. The 3D intensity profile at the focus is shown in Figure 4.17. The focal size is obtained to be 404 nm along the x axis, 364 nm along the y axis and 3.20 μm along the z axis.

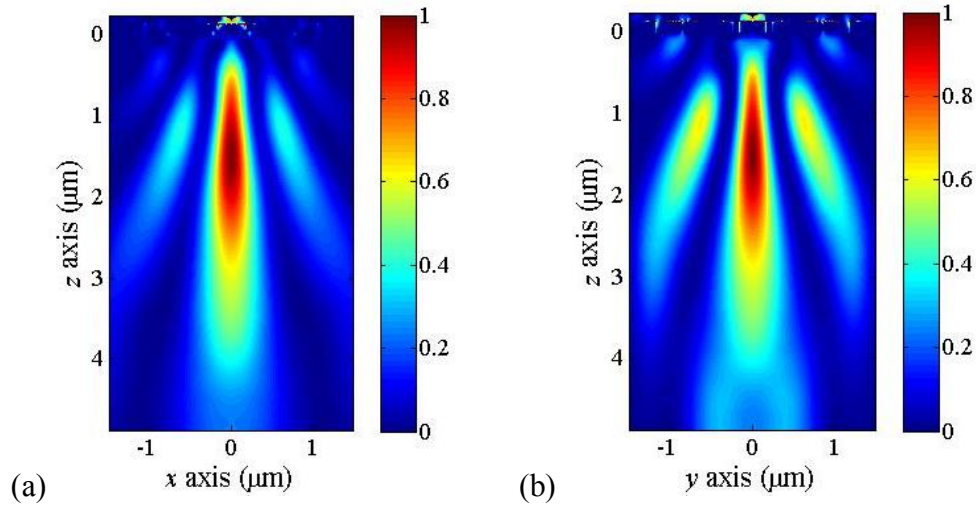


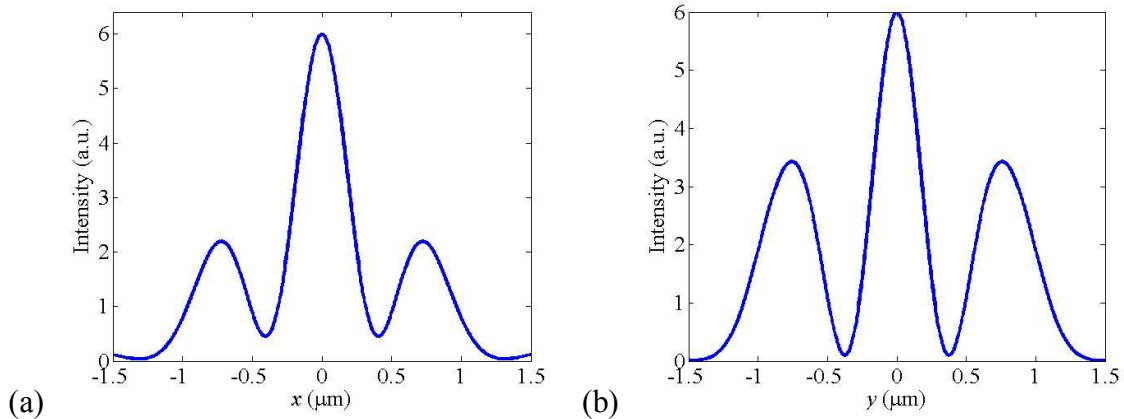
Figure 4.16. Intensity distribution of SP2 obtained from the simulations on two orthogonal planes: (a) xz plane and (b) yz plane. The origin of the coordinate system is located at the center of the SP lens surface. The optical beam is propagating downwards.

4.1.4.5. Discussion of the simulation results of the SP lenses

Symmetry of the intensity distributions

The simulation results of both SP lenses exhibit non-rotational symmetry: differences between the intensity distributions of xz and yz planes and differences in the spot sizes along the two transverse directions. Although the fiber-based SP lens is rotationally symmetric, the linear polarization of the incident optical beam induces a difference in the intensity distributions along the two orthogonal transverse directions. This non-rotational symmetry has also been seen in the

experimental data of the spot sizes and the intensity distributions obtained from SP2. However, many other issues in the experiment (e.g., lens misalignment, blocked slits, and etc.) can result in the difference between the x and y directions, which may influence the intensity distributions and spot sizes even more than the effect of the linear polarization. This explains why the difference between the intensity distributions on the xz and yz planes is apparent for SP2, but not obvious for SP1. For SP2, the intensity distributions are symmetric on both the xz and yz planes, which indicates that there is no serious misalignment of the SP lens exists. The intensity patterns on the xz and yz planes are different from each other due to the linear polarization. However, in the case of SP1, the misalignment between the SP lens and the fiber does exist, which can be seen from the asymmetry of the intensity distributions on both the xz and yz planes. The effect of the misalignment dominates that of the linear polarization, resulting in the intensity patterns on both the xz and yz planes are similar to each other.



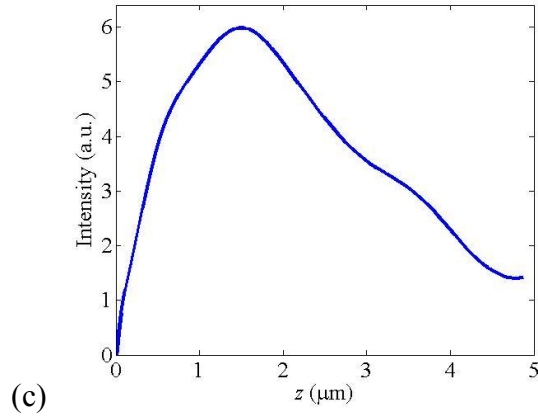


Figure 4.17. Intensity profile at the strongest intensity position ($z = 1.47 \mu\text{m}$) along (a) x axis, (b) y axis, and (c) z axis.

Spot size

Comparison of the spot sizes obtained from the simulation results and those measured in the experiment are summarized in Table 4.3. It should be noted that the x and y directions defined in the experiments are not the same as those defined in the simulation, because the polarization directions in the experiment are unknown.

Table 4.3. Spot sizes (FWHMs) of SP1 and SP2.

	SP1		SP2	
	Simulation	Experiment	Simulation	Experiment
x axis (nm)	520	440	364	352
y axis (nm)	544	500	404	533
z axis (μm)	3.42	1.758	3.20	0.743

It can be seen from Table 4.3 that the experimental obtained spot sizes agree well with those obtained in simulation. The maximum discrepancy (~ 130 nm in diameter) is found to be in the

transverse spot sizes (FWHMs) obtained with SP2 along the y direction. Considering the camera pixel size of ~ 60 nm, this discrepancy is reasonable. However, the discrepancy in the z direction focal depth is much larger. The reason is still unclear and further investigation is needed.

Focal length

In the simulation, the focal lengths are obtained to be $2.29 \mu\text{m}$ and $1.47 \mu\text{m}$ for SP1 and SP2, respectively. As discussed in Section 4.1.3.3, the smaller the aperture, the shorter the focal length. This has been observed in the experimental data, and now confirmed in the simulation results. In the experiments, the focal lengths were measured to be $3.2 \mu\text{m}$ and $1.1 \mu\text{m}$ for SP1 and SP2, respectively, which are comparable to the values obtained in the simulations.

4.1.5. Discussion of the differences between the experimental and simulation results

It is believed that the difference is mainly due to the errors associated with the SP lens fabrication. First, it is hard to obtain a precision of 10 nm in fabricating nanoscale slits with the FIB milling. The widths of the fabricated slits may vary for different samples even with the same metal thickness and the same settings in the FIB software. Second, the method used to determine the dimensions of the fabricated slits can also introduce random errors on a level of 10 nm. Currently the dimensions (widths and radii) are determined by counting the pixel numbers of the SEM images. However, the edges of the slits on the SEM images are not sharp due to the slanted sidewalls. Due to the high aspect ratio (1.5~2) of the slits, it is difficult to determine the slit dimensions from the SEM images. In addition, the exact thickness of the gold layer is also

difficult to determine. In the experiment, when the gold layer was evaporated, the fibers were mounted opposite to the target, and a wafer was mounted close to the fiber ends for calibration of the evaporated gold layer thickness. It was difficult to place the wafer at the same vertical position, and this might cause the difference in the coating thickness on the wafer and the fiber ends. The measurement of the gold layer thickness can also give different results (± 30 nm at the largest) at different positions of the wafer. All the abovementioned issues can result in differences between the fabricated devices and the designed ones.

In addition to the fabrication errors, there are many other factors that are not considered in the simulations, which can also result in the discrepancy of the simulation results and experimental results. First, the nanoscale slits fabricated with FIB have slanted sidewalls, while in the simulations the slits are considered to have straight sidewalls. Second, the dose used in the FIB fabrication was always more than enough to make sure all the gold inside the slits were totally removed. In this case, undercutting of the glass endface of the fibers was inevitable. Third, the Ga ions used in the FIB may be implanted into the glass substrate, which can change the refractive index and thus distort the incident beam. All these issues are difficult to quantify, but can certainly contribute to the discrepancy in the results.

4.1.6. Significance of the superfocusing achieved with fiber-based SP lenses

To the best of our knowledge, the results presented in this dissertation are the first demonstration of superfocusing with fiber-based devices. The optical fiber is an excellent waveguide with low cost and low loss, and is widely used in fiber communication industry. The fiber-based SP lens

can play an important role in bridging the nanoscale devices and macroscale light sources and detectors.

Compared with free-space optical components, optical fibers are much less susceptible to the noise introduced by the environment (temperature change, air flow, ambient light, and so on). A fundamental Gaussian beam can be readily available at the entrance of the SP lens. Once the SP lens is fabricated on the fiber endface, no additional alignments between the optical beam and the SP lens are needed. Therefore, the performance of the fiber-based SP lens is much more robust than that involving free-space optics, which reduces the efforts to build up and maintain the system.

Compared with the focuses achieved with the objectives, those of fiber-based SP lenses can potentially overcome the diffraction limit. [137] The focusing task that often requires bulky and expensive objectives can now be accomplished by using a much smaller and cheaper system. The small and cost-effective configuration makes the fiber-based SP lens highly competitive especially in microscale systems. The fiber-based SP lens can find applications in nanoscale fluorescence detection, nanoscale lithography, and power supply of nanoscale photonics, in addition to the optical trapping, which will be discussed in the next section.

4.2. Optical trapping ability enhancement with fiber-based SP lenses

It has been demonstrated in Section 4.1 that the fiber-based SP lens can be used to create a focus size comparable to that obtained with a high NA objective. Here, the small focus from an SP

fiber is used to perform fiber-based optical trapping with an enhanced trapping efficiency. The rest of this section is arranged as the following. In Section 4.2.1, experimental study of trapping of a sub-micrometer-size bacterium in three dimensions is presented. The optical trapping of particles with sizes smaller than the wavelength is investigated using two models in Section 4.2.2. The methods to enhance trapping forces are explored through a parametric study. In Section 4.2.3, mapping of the 3D optical forces is carried out for both SP1 and SP2 using the experimentally measured intensity distribution. The significance of the SP fiber optical tweezers is briefly discussed in Section 4.2.4.

4.2.1. Experimental demonstration of enhanced trapping ability achieved with fiber-based SP lenses

4.2.1.1. Experimental results of bacteria trapping with SP fiber tweezers

To experimentally demonstrate the enhanced trapping ability by using fiber-based SP lenses, a bacterium was successfully trapped in three dimensions with SP2.

The laser source used here is the same one that has been described in Section 2.3. A couple drops of tap water were added onto the coverglass on the microscope stage. The illumination light of the microscope was turned on with the maximal intensity. Bacteria could be seen after 20 minutes of illumination. The bacterium trapped in the experiment is a cylindrical particle with a diameter of $\sim 0.5 \mu\text{m}$ and lengths of $\sim 2 \mu\text{m}$. The successive images captured from a video clip are

shown in Figure 4.18. The bright spot is the focus created with SP2. A free bacterium was trapped when the laser was turned on, as shown in Figure 4.18 (a)-(c). After being trapped, the bacterium tried to swim away but did not succeed due to the strong optical trap. When the fiber was lifted up, the bacterium was moved together with the trap so that it was gradually out of focus, as shown in Figure 4.18 (d)-(f). When the focal plane was brought up to the bacterium, it

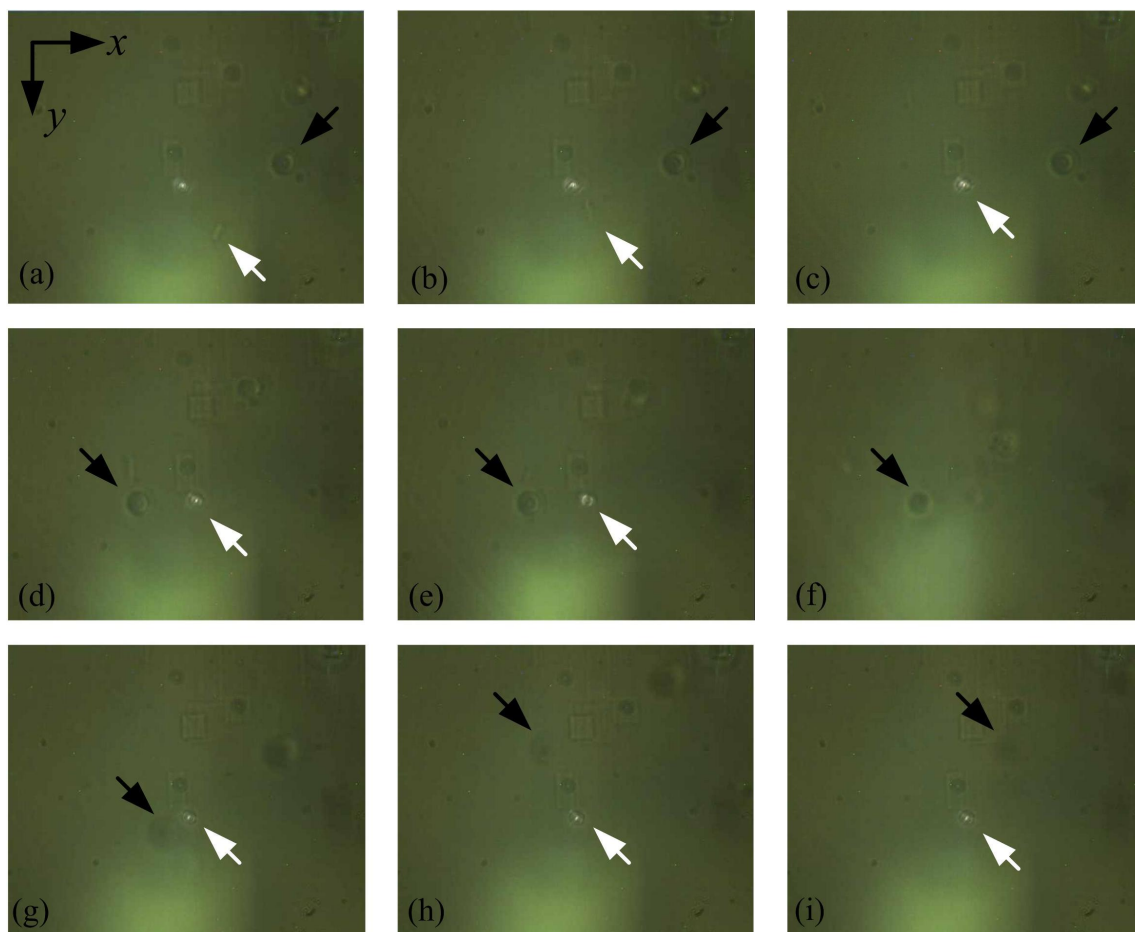


Figure 4.18. Images showing 3D trapping of a bacterium with SP2. The white arrows point to the bacterium, and the black arrows show the location of a reference silica bead. (a-c) A free bacterium was trapped by the focus created with SP2. (d-f) The bacterium was lifted up in the vertical direction while the focal plane is on the coverglass. (g) The focal plane was brought to the plane where the bacterium is located. In (g-h), the water is moved in the x direction, and in (h-i), the water is moved in the y direction with the bacterium remaining trapped. The optical power measured outside the SP lens was 0.91 mW.

can be seen from Figure 4.18 (g) that the bacterium remained trapped. The water was then moved in the x and y directions and the bacterium still stayed stable in the trap, as shown in Figure 4.18 (h) and (i). The optical power emitted from the fiber-based SP lens was 0.91 mW, which was measured with a free-space powermeter (PM144, Thorlabs). The moving speed of the water was more than 10 $\mu\text{m/s}$ in both transverse directions and the bacterium remained trapped, which indicates that a strong 3D optical trap was enabled with a power of power of 0.91 mW.

The transmission efficiency of the system is $\sim 5.5\%$, which is the ratio of the power transmitted through the SP lens to that of the light source. The power loss includes the losses at the FC/PC connectors, the splicing losses, and the losses due to the absorption and reflection at the metal layer of the SP lens. It is noted that the absorption of the optical power can create thermal flow near the SP lens, which has the same direction as the scattering force, and thus, it prevents the bacteria from being trapped in three dimensions. After a bacterium was trapped in the 3D trap, the power at the focus was decreased to $\sim 0.8 \mu\text{W}$ for 20 seconds, and the bacteria remained trapped.

The bacteria are believed to be either *E. coli* or *Legionella*. *E. coli* are 0.2~0.8 μm in diameter and a couple of micrometers in length [151, 152], while *Legionella* are 0.3~0.9 μm in diameter and 2~20 μm in length [153]. The bacteria size observed in the experiment is within the range of both types. Both of these two types of bacteria are rod-shaped and can be found in tap water [152, 153]. For these reasons, it is believed that the bacteria trapped here are one of these two types of bacteria. Ashkin and Dziedzic [48] have also trapped these bacteria with objective-based optical

tweezers in his experiment since he found these bacteria can be easily obtained in the water kept around for a couple of days.

4.2.1.2. Discussion of the trapping force enhancement demonstrated by using the SP lensed fiber tweezers

It should be noted that trapping bacteria is challenging even with conventional objective-based tweezers. [154] This is due to the fact that the bacteria have a low refractive index, small dimensions (sub-micrometers in diameter), and fast motility. The refractive index of bacteria is 1.38 over the visible range of frequencies [154, 155], which is smaller than that of the polystyrene beads (1.58~1.60 [156]) and that of the silica beads (1.45) used in this work. Considering the water has a refractive index of 1.33, the bacteria are much more difficult to trap than the polystyrene or silica beads with the same sizes, and this has been verified by other researchers [155]. The bacteria observed in the experiment are $\sim 0.5 \mu\text{m}$ in diameter and a couple of micrometers in length. Trapping of particles smaller than $1 \mu\text{m}$ requires highly focused laser beams and, to the best of our knowledge, has not been realized with fiber optical tweezers. Moreover, living bacteria have ability to swim by rotating their flagella as propellers [157]. When they are trapped by optical tweezers, they will struggle to escape [48], which makes it even more difficult to trap them compared with nanoscale dielectric beads.

Compared with the bacteria trapping achieved by using objective-based tweezers, the fiber tweezers based on the SP lens can achieve a stable 3D trap with a lower power. Generally in order to achieve a stable 3D trap of bacteria with objective-based optical tweezers, the required

optical powers are tens of milliWatts (18 mW in ref. [158], 50 mW in ref [159]) or even 100 mW [160]. The lowest optical power reported is a couple of milliWatts (6 mW in ref. [158], 3~6 mW in ref. [48]). It should be noted that with these low power levels, 3D traps were not very stable. [158] If the power is decreased further, the bacteria can only be trapped in two dimensions. [48] In this dissertation work, the 3D trapping of bacteria was achieved by using SP lensed fiber tweezers with a power of 0.91 mW at the focus. At this power level, it was found that the water can be moved at a speed of $\sim 20 \mu\text{m/s}$ without losing the bacteria from the 3D trap, which indicates that the trap was very stable. Since a lower power is required for realizing a stable trap with SP lensed fiber tweezers, it is believed that the fiber tweezers with a SP lens enables a stronger trap than that of conventional objective-based tweezers. This is also the first work to demonstrate trapping of sub-micrometer sized particles with fiber optical tweezers

The experimental results of 3D bacteria trapping with a low power have demonstrated that using the SP lens can indeed significantly improve the trapping ability of fiber optical tweezers. The trapping efficiency of the fiber optical tweezers can be comparable and even stronger than objective-based tweezers.

4.2.2. Modeling of enhanced trapping efficiency with fiber-based SP lenses

In this section, two models used to obtain the trapping forces in the Rayleigh regime are introduced and discussed, with the detailed derivations of one model presented. Based on these models, parametric studies of Rayleigh trapping forces are carried out. This is the first attempt to

compare the two models in parametric studies. The comparison helps one to select a valid model to analyze the Rayleigh trapping forces.

4.2.2.1. Models for obtaining trapping forces on Rayleigh particles

The optical trapping theory is available in two extreme cases: Mie particles ($a \gg \lambda$) and Rayleigh particles ($a \ll \lambda$). [7] For Mie particles, ray-optics approximation is valid, and optical forces can be calculated by the photon momentum change due to reflection and refraction, as described in Section 2.4.1. By contrast, Rayleigh particles can be considered as induced dipoles in the time-harmonic electromagnetic fields, and the optical forces are essentially the forces that the electromagnetic fields apply to the induced dipoles.

In principle, the optical forces can be obtained by integrating the Maxwell's tensor on a closed boundary surface that encloses the particles [161]. However, the scattered optical field should be known in advance in order to calculate the Maxwell's tensor at each spatial point, which significantly increases the complexity and difficulty. [162] A simple expression of the optical forces that only depend on the incident fields and the particle material properties is desirable. There are currently two different analytical solutions [7] for the optical forces on Rayleigh particles: those of Harada and Asakura (HA model) [163] and Chaumet and Nieto-Vesperinas (CN model) [164]. Details of these models are introduced as follows.

HA model

The time averaged trapping force on Rayleigh particles can be separated into two parts: the scattering force and the gradient force. The scattering force is given by [7, 163]

$$F_{scatt} = \frac{I\sigma n_m}{c}, \quad (4-15)$$

where I is the intensity of the incident light, n_m is the refractive index of the surrounding medium, c is the speed of light in vacuum, and σ is the effective scattering cross section of the sphere. For a sphere with a refractive index of n_s and a radius of a , σ can be expressed as

$$\sigma = \frac{128\pi^5 a^6}{3\lambda_m^4} \left(\frac{n_r^2 - 1}{n_r^2 + 2} \right)^2, \quad (4-16)$$

where λ_m is the wavelength in the medium and n_r is the relative refractive index (n_s/n_m). The scattering force is always along the propagation direction of the light. On the other hand, the vector gradient force is given by

$$\mathbf{F}_{grad} = \frac{2\pi\alpha_0}{cn_m} \nabla I, \quad (4-17)$$

where the polarizability α_0 is [163]

$$\alpha_0 = n_m^2 a^3 \frac{n_r^2 - 1}{n_r^2 + 2}. \quad (4-18)$$

Note that Eq. (4-17) was cited in ref. [7], but in a wrong form. It can be seen that the gradient force is along the direction of the intensity gradient. The derivations of Eqs.

(4-15) and (4-17) are given in details in ref [163]. The derivation is briefly summarized as follows. The scattering force is derived from the momentum change of the EM field, which results from the EM waves scattered or radiated from the induced dipole on the particle. The gradient force is derived from the Lorentz force applied by the incident EM field onto the induced dipole.

For the HA model to hold, the size of a particle should be electrically much smaller than the wavelength. The validity size of particles will be discussed later in this section.

ii) CN Model

The time-averaged force on a sphere in the Rayleigh regime of the Gaussian unit system, can be expressed as [7, 164]

$$\langle F_l \rangle = \frac{1}{2} \text{Re} \left[\alpha \sum_{j=1}^3 E_j \frac{\partial E_j^*}{\partial x_l} \right], \quad (4-19)$$

where $l=1, 2,$ and $3,$ correspond to the three coordinate axes, E_j is the complex amplitude of the incident electric field (trapping optical field), E_j^* is the complex conjugate of $E_j,$ and α is a generalized polarizability given by [164, 165]

$$\alpha = \alpha_0 / \left(1 - \frac{2}{3} i k_m^3 \alpha_0 \right), \quad (4-20)$$

Here, α_0 is the static polarizability of the sphere, given by Eq. (4-18), k_m is the wave number of the trapping laser in the medium, and i is an imaginary number equal to $\sqrt{-1}.$ The generalized polarizability has an additional damping term (imaginary part), which corresponds to the scattering force. [164]

Eq. (4-19) describes the net optical forces along the three axes without distinguishing the scattering forces and gradient forces from each other. Therefore, the forces applied on a Raleigh particle by an arbitrary optical field can be obtained. Moreover, this result presents a much

simpler form compared with HA model, and it can be applied to analyze optical trapping forces on larger particles. [164]

Derivation of optical forces in CN model

Here, detailed derivations of Eq. (4-19) as well as the associated assumptions are provided. Although Eq. (4-19) can be found in ref [164], the derivations are not given explicitly, nor are they straightforward, as can be seen from the following. The knowledge of the derivation process is essential to understand the physical principles involved in the CN model, which can help explain the differences between the results obtained from the two models, as can be seen later in Section 4.2.2.3 and 4.2.2.6. It is also important to know what assumptions are involved in order to determine the validity size range of Eq. (4-19) for the trapping force calculation, which will also be discussed later in this section. Moreover, it was found that the conventions used in the derivation process of the CN mode are different from those used for the HA model. Proper modifications are necessary to make for the CN model in order to get comparable results, and these modifications will be discussed in Section 4.2.2.2.

The model used to derive Eq. (4-19) is described as follows. When a polarizable Rayleigh particle is placed in an EM field, a dipole is induced due to the time-harmonic EM field. The induced dipole is subject to the EM force, which is of interest due to the interactions with the EM field. Note that the EM forces and the optical forces refer to the same forces: forces applied by the optical (EM) fields. Using the phasor representation, the time-harmonic EM fields can be written as

$$\mathbf{E}(\mathbf{x}, t) = \text{Re}(\tilde{\mathbf{E}}(\mathbf{x}) \cdot e^{i\omega t}) \text{ and } \mathbf{B}(\mathbf{x}, t) = \text{Re}(\tilde{\mathbf{B}}(\mathbf{x}) \cdot e^{i\omega t}). \quad (4-21)$$

For simplicity, $\mathbf{E}(\mathbf{x})$ and $\mathbf{B}(\mathbf{x})$ are used instead of $\tilde{\mathbf{E}}(\mathbf{x})$ and $\tilde{\mathbf{B}}(\mathbf{x})$ in the following derivations to denote the field phasors. Following the convention, the bold letters and the underlined letters denote vectors. The induced dipole momentum on a particle is

$$\mathbf{p}(\mathbf{x}) = \alpha \mathbf{E}(\mathbf{x}). \quad (4-22)$$

Note that the dipole is also time-harmonic and it always has the same direction (but not the same phase due to the imaginary part of α) as the electrical field. The EM field varies in such a high frequency (this is especially true in the optical frequency range) that only the time averaged forces can be observed. The goal is therefore to find the time averaged EM forces applied on the induced dipole.

A dipole can be viewed as a pair of electrical charges with equal magnitudes and opposite signs:

$$\mathbf{p} = q \cdot d\mathbf{r}, \quad (4-23)$$

where q is the charge magnitude and $d\mathbf{r}$ is the vector separation between the two charges, as shown in Figure 4.19. Here \mathbf{x} is omitted because the dependence of both \mathbf{p} and \mathbf{r} on \mathbf{x} is taken for granted.

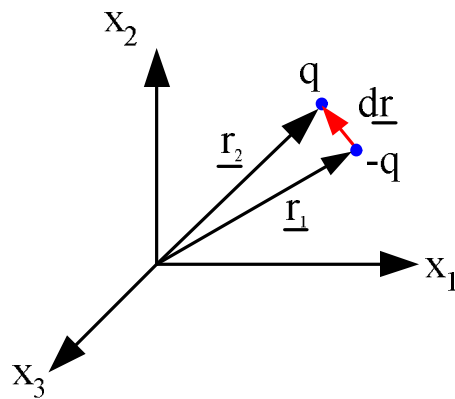


Figure 4.19. An electric dipole.

In the Gaussian unit system, the EM force applied on a dipole takes the form of a Lorentz force [166]

$$\mathbf{F} = \left[(\mathbf{p} \cdot \nabla) \mathbf{E} + \frac{1}{c} \frac{d}{dt} (\mathbf{p}) \times \mathbf{B} \right]. \quad (4-24)$$

The first term is the gradient force, which is related to the gradient of the electrical field. The second term is the scattering force, which comes from the changes of the dipole momentum either by rotating the dipole or by varying the strength of the dipole.

A time averaged Lorentz force can be written as

$$\langle \mathbf{F} \rangle = \text{Re} \left(\langle (\mathbf{p} \cdot \nabla) \mathbf{E} \rangle + \frac{1}{c} \langle \frac{d}{dt} \mathbf{p} \times \mathbf{B} \rangle \right). \quad (4-25)$$

Here $\langle \rangle$ denotes the time average. Time average of scalar products is to take one-half of the real part of the product of one complex quantity with the complex conjugate of the other [161].

Therefore, it can be obtained that

$$\langle \mathbf{F} \rangle = \frac{1}{2} \text{Re} \left[(\mathbf{p} \cdot \nabla) \mathbf{E}^* + \frac{1}{c} \frac{d}{dt} \mathbf{p} \times \mathbf{B}^* \right]. \quad (4-26)$$

Introducing the Levi-Civita tensor, [167]

$$\varepsilon_{ijk} = \begin{cases} +1 & \text{if } (i, j, k) \text{ is } (1, 2, 3), (2, 3, 1) \text{ or } (3, 1, 2), \\ -1 & \text{if } (i, j, k) \text{ is } (1, 2, 3), (2, 3, 1) \text{ or } (3, 1, 2), \\ 0 & \text{otherwise: } i=j \text{ or } j=k \text{ or } k=i, \end{cases} \quad (4-27)$$

and the Kronecker delta [167]

$$\delta_{ij} = \begin{cases} 1; & \text{if } i = j, \\ 0; & \text{if } i \neq j. \end{cases} \quad (4-28)$$

The vector cross product can be expressed with the Levi-Civita tensor as

$$\mathbf{p} \times \mathbf{B} = \sum_{i,j,k=1}^3 \varepsilon_{ijk} \mathbf{e}_i p_j B_k . \quad (4-29)$$

where \mathbf{e}_i is the unit vector along the x_i axis, and p_j and B_k are the components of \mathbf{p} and \mathbf{B} along x_j and x_k axis, respectively. According to Eqs. (4-26) and (4-29), the component of $\langle \mathbf{F} \rangle$ along the x_i axis ($i = 1, 2, 3$) as

$$\langle F_i \rangle = \frac{1}{2} \text{Re} \left[\sum_{j=1}^3 p_j \frac{\partial E_i^*}{\partial x_j} + \frac{1}{c} \sum_{j,k=1}^3 \varepsilon_{ijk} \frac{dp_j}{dt} B_k^* \right] . \quad (4-30)$$

With three variables, \mathbf{p} , \mathbf{B} , and \mathbf{E} , in the formulation, the number of variables is to be reduced next. According to Eq. (4-22), \mathbf{p} can be replaced by \mathbf{E} and \mathbf{B} is related to \mathbf{E} through the Maxwell's Equation

$$\mathbf{B} = \frac{c}{i\omega} \nabla \times \mathbf{E} . \quad (4-31)$$

Using the Levi-Civita tensor, it is found that

$$B_k = \frac{c}{i\omega} \sum_{l,m=1}^3 \varepsilon_{kml} \frac{\partial E_m}{\partial x_l} . \quad (4-32)$$

By substituting Eqs. (4-22) and (4-32) into Eq. (4-30), it yields

$$\begin{aligned} \langle F_i \rangle &= \frac{1}{2} \text{Re} \left\{ \sum_{j=1}^3 (\alpha E_j) \frac{\partial E_i^*}{\partial x_j} + \frac{1}{c} \sum_{j,k=1}^3 \left[\varepsilon_{ijk} \frac{d(\alpha E_j)}{dt} \cdot \frac{ic}{\omega} \sum_{l,m=1}^3 (\varepsilon_{kml} \frac{\partial E_m^*}{\partial x_l}) \right] \right\} \\ &= \frac{1}{2} \text{Re} \left[\alpha \sum_{j=1}^3 E_j \frac{\partial E_i^*}{\partial x_j} + \frac{\alpha}{c} \sum_{j,k,l,m=1}^3 (\varepsilon_{ijk} \varepsilon_{kml} \frac{dE_j}{dt} \cdot \frac{ic}{\omega} \frac{\partial E_m^*}{\partial x_l}) \right] \\ &= \frac{1}{2} \text{Re} \left[\alpha \sum_{j=1}^3 E_j \frac{\partial E_i^*}{\partial x_j} + \alpha \sum_{j,k,l,m=1}^3 (\varepsilon_{ijk} \varepsilon_{kml} E_j \frac{\partial E_m^*}{\partial x_l}) \right] . \end{aligned} \quad (4-33)$$

Note that $\frac{dE_j}{dt} = -i\omega E_j$. Further simplification of Eq. (4-33) requires the relationship between

the Levi-Civita tensor and the Kroneck delta [167]

$$\sum_{k=1}^3 (\varepsilon_{kij} \varepsilon_{kml}) = \delta_{im} \delta_{jl} - \delta_{il} \delta_{jm} = \begin{cases} 1; & \text{if } i = m \text{ and } j = l \text{ and } i \neq j, \\ -1; & \text{if } i = l \text{ and } j = m \text{ and } i \neq j, \\ 0; & \text{otherwise.} \end{cases} \quad (4-34)$$

By applying Eq. (4-34), the second term on the right-hand side of Eq. (4-33) can be transformed to

$$\begin{aligned} & \sum_{j,k,l,m=1}^3 (\varepsilon_{ijk} \varepsilon_{kml} E_j \frac{\partial E_m^*}{\partial x_l}) \\ &= \sum_{j,l,m=1}^3 \left[\sum_{k=1}^3 (\varepsilon_{kij} \varepsilon_{kml}) \right] E_j \frac{\partial E_m^*}{\partial x_l} \\ &= \sum_{j,l,m=1}^3 (\delta_{im} \delta_{jl} - \delta_{il} \delta_{jm}) E_j \frac{\partial E_m^*}{\partial x_l} \\ &= \sum_{\substack{j=1 \\ j \neq i}}^3 E_j \frac{\partial E_j^*}{\partial x_i} - \sum_{\substack{j=1 \\ j \neq i}}^3 E_j \frac{\partial E_i^*}{\partial x_j} \\ &= \left(\sum_{j=1}^3 E_j \frac{\partial E_j^*}{\partial x_i} - E_i \frac{\partial E_i^*}{\partial x_i} \right) - \left(\sum_{j=1}^3 E_j \frac{\partial E_i^*}{\partial x_j} - E_i \frac{\partial E_i^*}{\partial x_i} \right) \\ &= \sum_{j=1}^3 E_j \frac{\partial E_j^*}{\partial x_i} - \sum_{j=1}^3 E_j \frac{\partial E_i^*}{\partial x_j}. \end{aligned} \quad (4-35)$$

By substituting Eq. (4-35) into Eq. (4-33), the final expression of the EM force can be obtained as

$$\langle F_i \rangle = \frac{1}{2} \text{Re} \left[\alpha \sum_{j=1}^3 E_j \frac{\partial E_j^*}{\partial x_i} \right] \quad (4-36)$$

This is the same result as Eq. (4-19), which was first presented in ref. [164]. According to the derivation discussed above, the only assumption is that the particle is electrically small (compared with the wavelength) and can be polarized by the external electrical field following Eqs. (4-18) and (4-20). It can be seen from Eq. (4-36) that the optical forces on trapped particles depend on the polarizability, the electrical field, and the gradient of the electrical field. Eq. (4-20) cannot be further written in terms of the intensity because of the imaginary part of α . Although it

is not mentioned in ref. [164], it is worth noting that Eq. (4-19) provides a result using the Gaussian units, which can be seen from the above derivations. The modifications will be made to the CN model in Section 4.2.2.2 to obtain comparable results from both the CN model and the HA model.

Particle size range for the HA and CN models

The two models are valid for similar particle size ranges. The reason is that both models are derived starting from the Lorentz force on dipoles (Eq. (4-24)) with no further assumption added. An immediate conclusion that one can draw is that the models work for particles that can be viewed as single electrical dipoles ($a \ll \lambda$). However, they can be applied to particles larger than this size range. Simulation results have shown that the HA model is valid for particle diameters up to $\sim 2w_0$ (w_0 = the beam waist) in the transverse force calculation and $\sim 0.4\lambda$ in the axial force calculation. [163] As mentioned above, the CN model should be valid for the same particle size range. It should also be noted that the validity size range in the transverse direction is found to be up to $\sim w_0$ in diameter in ref. [7], which was cited incorrectly from ref. [163], although ref. [7] has been cited for much more times than ref. [163].

4.2.2.2. Modifications to the CN model following the conventions used in the HA model

There are different conventions to express the electromagnetic waves due to historical reasons, among which one typical example is the electromagnetic unit systems [161]. The expressions of the same physical principle under different conventions can be distinct. There are two differences

in the conventions used in the HA model and CN model, namely the unit systems and the plane wave expressions. In this dissertation, the conventions used in the HA model will be adopted. The CN model will be modified in order to obtain results comparable with those obtained with the HA model. The conventions used in the CN mode were not explicitly pointed out in the published literature, and here, these differences in the conventions are found out by comparing the derivation of the two models.

Expression of the CN model under the SI unit system

The electric field in Gaussian units can be transferred to those in SI units by multiplying a factor of $\sqrt{4\pi\epsilon_0}$ [161]. In order to compare with the HA model, which is in SI units, the optical forces obtained with the CN model in SI units can be expressed as

$$\langle F_i \rangle = 2\pi\epsilon_0 \operatorname{Re} \left[\alpha \sum_{j=1}^3 E_j \frac{\partial E_j^*}{\partial x_i} \right] \quad (4-37)$$

Modification of the generalized polarizability

The expression of a plane wave propagating along +z direction also have two different conventions: $\exp[i(k_m z - \omega t)]$ and $\exp[i(\omega t - k_m z)]$. These two expressions have the same real parts but opposite imaginary parts. Equations involving the imaginary parts of EM waves will have different results following different conventions. Errors may occur when the results following two conventions are combined [168]. Unlike the simple translation between the unit systems, the errors resulting from this type of conventions are difficult to check and correct. The

generalized polarization Eq. (4-20), which is used by the CN model, uses the convention of $\exp[i(k_m z - \omega t)]$, while the HA model uses $\exp[i(\omega t - k_m z)]$.

Next, following the derivation of Eq. (4-20) in ref [165], the modified expression will be provided when the EM wave of $\exp[i(\omega t - k_m z)]$ is used. The “radiation reaction” electric field \mathbf{E}_{rad} , which comes from the radiation of the induced dipole \mathbf{P} , can be written as

$$\mathbf{E}_{rad} = -\frac{2}{3} i k_m^3 \mathbf{P}_j. \quad (4-38)$$

Note Eq. (4-48) is different from the similar equation in ref. [165] by a factor of -1, which comes from the different expression conventions of the EM wave. The induced dipole is determined by both \mathbf{E}_{rad} and the incident wave, \mathbf{E}_{ext} by

$$\mathbf{P}_j = \alpha \mathbf{E}_{ext} = \alpha_0 (\mathbf{E}_{ext} + \mathbf{E}_{rad}), \quad (4-39)$$

Here α is the generalized polarizability and α_0 is the conventional polarizability defined by Eq. (4-18). By substituting Eq. (4-38) into Eq. (4-39), the modified generalized polarizability for plane waves expressed as $\exp[i(\omega t - k_m z)]$ can be obtained as

$$\alpha = \alpha_0 / (1 + \frac{2}{3} i k_m^3 \alpha_0), \quad (4-40)$$

The modified polarizability definition enables the results obtained with the CA and HA models to be comparable with each other.

4.2.2.3. Summary and comparisons of the HA and CN models

The HA model separates the gradient force from the scattering force, and only the intensity information is required from the incident optical fields. The optical forces in the HA model are derived from two different physical principles: the gradient force from the Lorentz force applied on the induced dipole, and the scattering force from the changes of the EM momentum by an effective scattering area. The CN model encapsulates both the gradient force and the scattering force into one simple expression and only the electrical fields are required for the calculation of the forces. The force in the CN model originates only from the Lorentz force, as can be seen in the abovementioned derivation process.

It first appears that the CN model misses the scattered fields, which is considered by the HA model. Actually the information of the scattered fields is considered in the CN model because it uses a different definition of the polarizability. The CN model uses a generalized polarizability in Eq. (4-20), which is essentially adding an imaginary modification to the polarizability used by the HA model (Eq. (4-18)). This correction of the imaginary part is equivalent to the scattering force considered in the HA model. [164] However, the transverse gradient forces in both models are obtained from the same principle: the Lorentz force, but different definitions of the polarizability are used. This surely will cause difference in the transverse forces, as can be seen later in Section 4.2.2.6. Fortunately, this difference is not noticeable unless the particle size is getting close to the beam waist. Therefore, the CN model is essentially the same as the HA mode in the transverse directions, although they have distinct expressions. For large particles, the CN model deviates from the HA mode even in the transverse directions due to different polarization definitions. All these differences will be discussed along with some simulation results in Sections 4.2.2.6 and 4.2.3.

The complexity of the two models depends on what information is available. When multiple known optical fields are overlapped, it might be complicated to calculate the intensity resulting from the interference effects. The CN model should be used in this case without the necessity for finding the intensity distribution. On the other hand, if the intensity of an irregularly shaped optical field is measured, the HA model should be used, since the CN model cannot be used without the knowledge of the electrical fields.

4.2.2.4. Stability of optical trapping versus particle sizes in the Rayleigh regime

Due to the complexity of the generalized polarizability (Eq. (4-20)), the dependence of optical forces on the particle size is not straightforward for the CN model. However, the HA model provides a clear knowledge of this dependence. According to the HA model, the scattering force is proportional to a^6 , while the gradient force is proportional to a^3 , under the assumption of a fixed intensity distribution. It seems that smaller particles are easier to trap because the scattering force decreases much faster with decreasing particle sizes than the gradient force while the gradient force contributes positively to a 3D trap. However, this is not true in the experiment. Dielectric particles under 300 nm are difficult to trap. [169] The major reason is that the Brownian force (thermal random force) remains the same with decreasing particle sizes. [170] When the particle size shrinks to hundreds of nanometers, the optical force cannot overcome the Brownian force to achieve a stable trap, although the gradient force dominates the scattering force. In addition to the Brownian force, the difficulty of imaging under a microscope also makes it harder to trap small particles.

4.2.2.5. Electric fields of fundamental (TEM₀₀) Gaussian beams

Zerth-order Gaussian beams are generally used to characterize the laser beams focused by an objective lens (TEM₀₀ mode). A zerth-order x -polarized TEM₀₀ beam that propagates along $+z$ direction can be expressed as [163]

$$\begin{aligned} \mathbf{E}(\mathbf{r}) &= \hat{x}E(x, y, z) \\ &= \hat{x}E_0 \frac{ik_m w_0^2}{ik_m w_0^2 + 2z} \exp\left(-\frac{(k_m w_0)^2 (x^2 + y^2)}{(k_m w_0^2)^2 + (2z)^2} - i\frac{2k_m z (x^2 + y^2)}{(k_m w_0^2)^2 + (2z)^2} - ik_m z\right), \end{aligned} \quad (4-41)$$

where w_0 is the beam waist, E_0 is the electric field at the center of the waist, and the origin of the coordinate system is at the center of the beam waist. It is intuitive to normalize the coordinates by the focal sizes along the Cartesian directions, because the characteristics of a Gaussian beam are determined by the beam waist in the transverse directions and by the focal depth (kw_0^2) along the longitudinal direction. By introducing normalized coordinates [171]

$$\xi = \frac{x}{w_0}, \quad \eta = \frac{y}{w_0}, \quad \text{and} \quad \zeta = \frac{z}{k_m w_0^2}. \quad (4-42)$$

Eq. (4-41) becomes

$$\begin{aligned} \mathbf{E}(\mathbf{r}) &= \hat{x}E_x(\mathbf{r}) = \hat{x}E(\xi, \eta, \zeta) \\ &= \hat{x}E_0 \frac{i}{i + 2\zeta} \exp\left(-\frac{\rho^2}{1 + (2\zeta)^2} - i\frac{2\zeta\rho^2}{1 + (2\zeta)^2} - i(kw_0)^2 \zeta\right) \\ &= \hat{x}E_0 \frac{i}{i + 2\zeta} \exp\left(-\rho^2 \frac{i}{i + 2\zeta}\right) \exp\left(-i\frac{\zeta}{s^2}\right) \\ &= \hat{x}E_0 iQ \exp(-i\rho^2 Q) \exp\left(-i\frac{\zeta}{s^2}\right), \end{aligned} \quad (4-43)$$

where $\rho = \sqrt{\xi^2 + \eta^2}$ and $Q = \frac{1}{i + 2\zeta}$. The nondimensional parameter s , which can describe the focusing strength, is given by [171]

$$s = \frac{1}{kw_0} = \frac{1}{2\pi} \left(\frac{\lambda}{w_0} \right). \quad (4-44)$$

The intensity at an arbitrary position can be expressed in terms of the magnitude of the electric field at the same place [163]

$$I(\mathbf{r}) = \frac{n_m \varepsilon_0 c}{2} |E(\mathbf{r})|^2, \quad (4-45)$$

with ε_0 being the vacuum permittivity (8.85×10^{-12} F/m).

The components of the gradient of the electric field are also given as the following

$$\frac{\partial E_x}{\partial x} = -2iQ \frac{\xi}{w_0} E_x, \quad (4-46)$$

$$\frac{\partial E_x}{\partial y} = -2iQ \frac{\eta}{w_0} E_x, \quad (4-47)$$

$$\frac{\partial E_x}{\partial z} = \frac{E_x}{k_m w_0^2} \left(-\frac{i}{s^2} - 2Q + 2i\rho^2 Q^2 \right). \quad (4-48)$$

It should be noted that there is an error associated with the expression in Eq. (4-43) for large s values (tightly focused laser beams). The expression of zeroth-order Gaussian beams is valid for moderately focused beams where the paraxial approximation holds. [172] However, when the beam waist shrinks close to the diffraction limit, the paraxial approximation fails, and the Maxwell's equations are not precisely satisfied by the zeroth-order expression. For example, if the waist decreases to $0.32 \mu\text{m}$ (\sim diffraction limit), s is about 0.3, and the associated error with the TEM₀₀ mode is 15.3%. [171] Despite the existence of this error, the use of Eq. (4-43) still

provides reasonable predictions and analyses for trapping forces using highly focused laser beams, and good agreements between the simulation and experimental results have been observed previously [155, 173]. Therefore, the zeroth-order TEM₀₀ mode (Eq. (4-43)) will be used in this dissertation work to model the focused beam exiting from the objectives.

4.2.2.6. Parametric study of Rayleigh particle trapping

Matlab codes based on both the CN model and the HA model are developed. To compare the results obtained by using the two different models, examples given in published literature are revisited. The first example is the force mapping along the x axis (transverse direction) and the z axis (longitudinal direction) on a Rayleigh particle. The parameters used in the simulations are the same as those given in ref. [163]: the vacuum wavelength $\lambda_0=0.5145 \mu\text{m}$, waist $w_0=5 \mu\text{m}$, power $P=100 \text{ mW}$, bead refractive index $n_s=1.592$, bead radius $a=10 \text{ nm}$, and medium refractive index $n_m=1.332$.

As shown in Figure 4.20, the results obtained here with the HA model match perfectly with those provided in ref. [163], both in the x direction and the z direction, which verifies the correctness of codes developed for the HA model. Furthermore, the results obtained with the CN model match very well with the HA model results in the x axis, while discrepancy is observed for the z axis results from the two models. This can be explained by tracing the differences between the two models. As discussed in Section 4.2.2.3, the transverse forces of both models are based on the Lorentz force but with different definitions of polarization. Such difference is not noticeable for

small particles ($a \ll \lambda$), and thus, a good match is observed in Figure 4.20 (a). However, the two models use different principles to determine the longitudinal (scattering) forces, and this contributes to the differences observed in Figure 4.20 (b). This difference can be explained by the errors associated with the estimation of the effective scattering cross section (Eq. (4-16)) in the HA model and the generalized polarization (Eq. (4-40)) in the CN model. Although the CN results and the HA results are different by a factor of ~ 1.4 according to Figure 4.20 (b), the shape of the longitudinal force curves and the position of maximum forces are the same for both models.

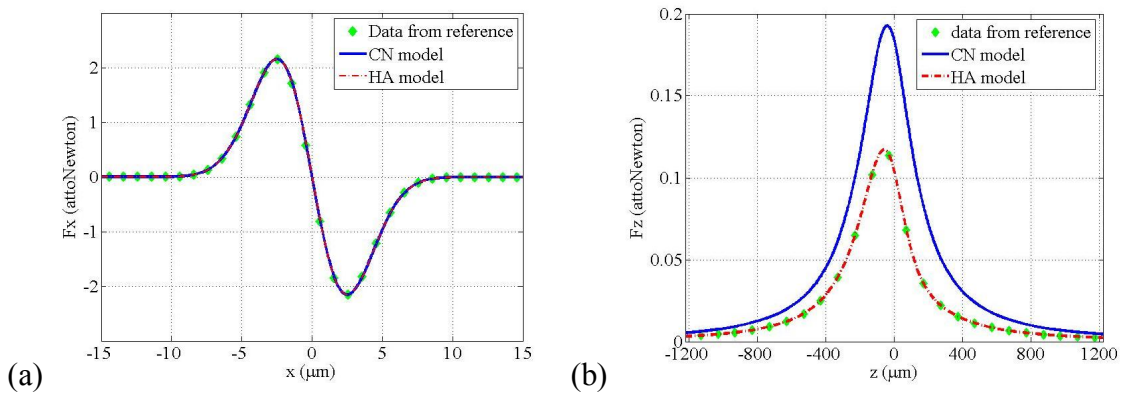


Figure 4.20. Comparison of results obtained with both HA and CN models. (a) The x -axis transverse force versus the x position for the bead coordinates of $y=0$ and $z=0$. (b) The z -axis longitudinal force versus the z position along the optical axis ($x=0$ and $y=0$). The diamond data points are the results provided in ref. [163].

It is noted that the length scales along the x and the z directions are different. Due to the weakly focused laser beam, the waist of the beam is $5 \mu\text{m}$ while the focus depth is around $400 \mu\text{m}$. Therefore, the different scales (with two orders of magnitude difference) of the transverse and longitudinal directions are used so that the trends of the forces can be seen. The stronger the focusing, the less the scale difference of these two directions, which can be seen from Eq. (4-42).

Next, the parametric study will be performed to find out the influence of some important parameters to the trapping forces, including the particle size, the beam waist, and the particle refractive index. It is taken for granted that the optical force is proportional to the optical power along every direction, so the dependence of the trapping forces on the power is not considered.

i) Particle size

Another example from the published literature is revisited here, which is used to carry out the parametric study. The parameters used for the simulation are obtained from the ref. [155] as the following: the beam waist $w_0=0.44 \mu\text{m}$, the vacuum wavelength $\lambda_0=1064 \text{ nm}$, the power $P=1\text{ W}$, the refractive index $n_s=1.38$ (for biological particles), the medium refractive index $n_m=1.33$. The particle radius a changes from $0.03w_0$ ($\sim 13 \text{ nm}$) to w_0 (440 nm). The escape force, defined as the maximum transverse force, is used to characterize the strength of an optical trap. For a TEM_{00} mode beam, the escape force can be obtained at the transverse plane at $z=0$. The results of the escape force obtained using both the CN and HA models are plotted in Figure 4.21.

The data (diamond points in Figure 4.21) from ref. [155] are calculated with the generalized Lorentz Mie theory (GLMT). The GLMT provides a general and complete solution for the scattering field around the trapped particles, and the optical forces can be obtained in an arbitrary particle size regime. [155] However, it is much more difficult to implement the GLMT compared with the Rayleigh regime trapping models used in this dissertation. Moreover, the GLMT is a numerical method similar with the FDTD. However, unlike the Rayleigh models, the GLMT

cannot provide an analytical insight into the understanding of the trapping principles. Here, the data calculated with the GLMT is only used to verify the simulation codes for the HA and CN models and provide comparison with the results obtained from these models.

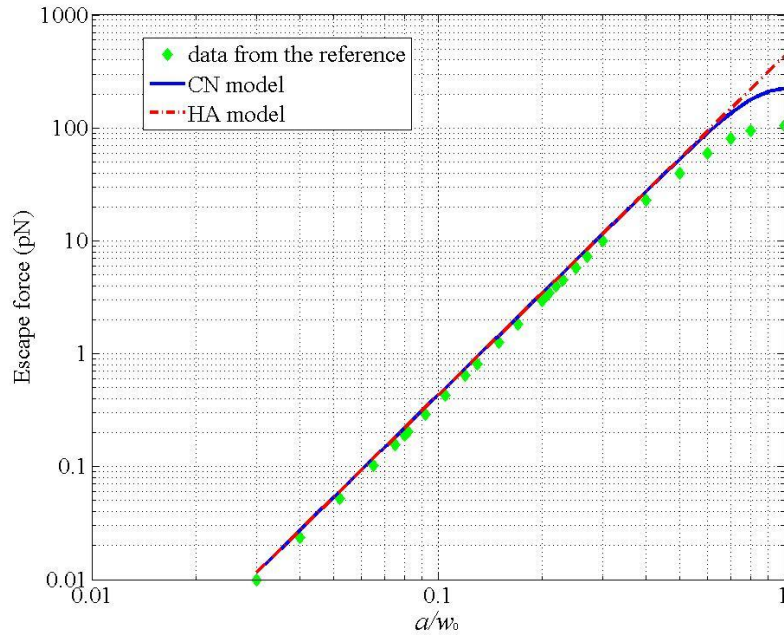


Figure 4.21. Dependence of the x -axis escape force on the particle size. The escape force is determined by the maximum x -axis force with the particle coordinates of $y=0$ and $z=0$. The diamond data points are the results provided in ref. [155].

It can be seen that the results obtained from both HA and CN models match well with those from the reference for the particle size range of $a < 0.4w_0$, but discrepancy starts to increase for larger particles beyond this range. It is not surprising because the Rayleigh models are valid in the Rayleigh regime where $a \ll \lambda$. The HA results and CN results match with each other perfectly for $a < 0.6w_0$, as can be observed in Figure 4.20. For large particles, the difference due to the

polarizabilities used in these two models start to show up in the results, which has been discussed in Section 4.2.2.3. These results again have proved the validity of the simulation codes.

As can be seen in Figure 4.21, the relationship between the escape force and the particle size is linear in the logarithmic scale. This can be explained by using Eqs. (4-17) and Eq. (4-18) of the HA model. The transverse force is proportional to the polarizability and hence to the cubic of the particle radius. Therefore, the curve of transverse force versus the particle size in the logarithmic scale should have a slope of 3, which can be verified in Figure 4.21.

With the same set of parameters, the influence of the particle radius to the z -axis trapping force is also studied, as shown in Figure 4.22. This has not been studied in ref. [155], so no results from the GLMT can be used for comparison. Because the beam is propagating in the $+z$ direction, a stable 3D trap is possible only when negative restoring forces exist for $+z$ displacements. This is always difficult compared with $-z$ displacements, because the scattering force is always along $+z$ direction, preventing the bead from being pulled back to the focus. It is noted that the forces shown in Figure 4.22 are the minimum forces along the z direction with $+z$ displacements. Therefore, a 3D trapping can only be achieved for those particle sizes that enable negative restoring forces. As can be seen in Figure 4.22, the results obtained with the HA and CN models agrees well with each other for $a < 100$ nm. The errors between the HA and CN model can be seen for large particle sizes again, which is due to the different principles used in their force derivations. However, based on both models, the maximum bead size that can be trapped in three dimensions can be determined.

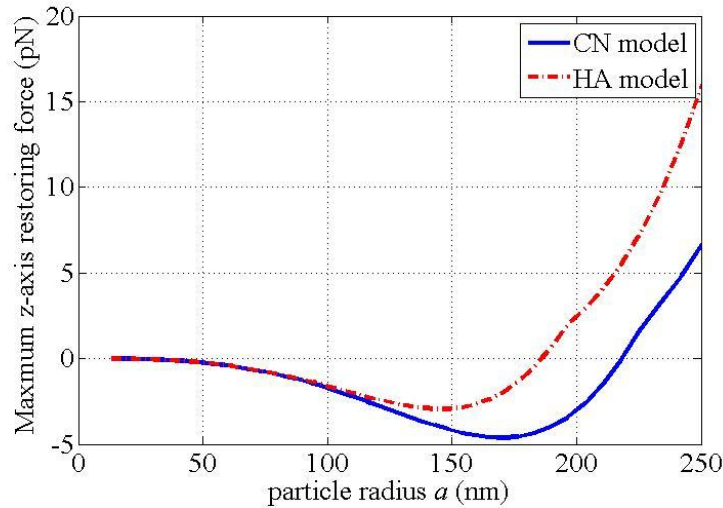


Figure 4.22. Dependence of the z -axis restoring force on the particle size. Here the forces indicate the maximum restoring forces (or minimum scattering forces). The optical wave is propagating along $+z$ direction. A 3D trap is possible only when there exists a negative restoring force.

ii) Beam spot size

The beam spot size is one of the most important parameters of the optical tweezers. For specific particles of interest, it is not possible to change the bead size and refractive index. In this case, beam spot size is the most important parameters that can be tailored to improve the performance of the optical tweezers. The dependence of x -axis escape force on the beam waist is shown in Figure 4.23. The particle is assumed to be a sphere with $n_s = 1.38$. The results of three different particle sizes are shown: $a=50$ nm, 100 nm, and 150 nm. The laser has a wavelength of 808 nm and a power of 1 W. As can be seen in Figure 4.23, results obtained with the CN model and HA model match well with each other for all three particle sizes. The results demonstrate that decreasing beam waist can increase the magnitude of the optical force. Especially in the small beam waist region, even a small decrease in the beam waist (for example, from 0.2 μm to 0.18 μm) can significantly improve the optical force (from 68 pN to 92 pN for $a=100$ nm). The

smaller the particles, the weaker the trapping force at the same power, which confirms the results shown in Figure 4.21.

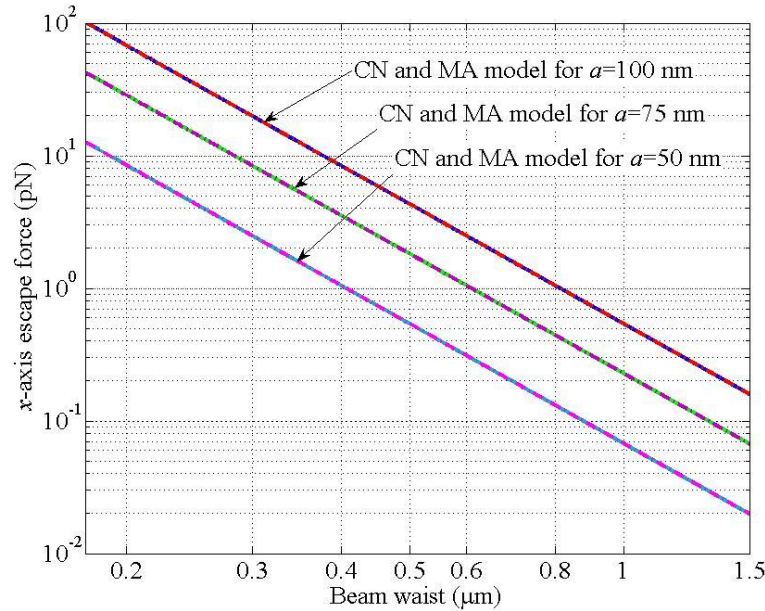


Figure 4.23. Dependence of the x-axis escape force on the beam waist. The optical power is 1 W. The particle is a sphere with a refractive index of $n_s=1.38$. The results of three particle sizes are obtained, $a=50$ nm, 100 nm, and 150 nm.

The z -axis restoring forces as a function of the beam waist are also obtained with the same parameters, as shown in Figure 4.24. The CN model and the HA model agree with each other, with the forces obtained from the CN model stronger than the HA model. It is clearly seen that only small focus sizes can enable 3D trapping of biological particles with a radius within the range of 50~100 nm. Smaller particles are more difficult to be trapped in 3D, due to the weaker optical forces. The optical force obtained in Figure 4.24 is based on an optical power of 1 W. In the real case, this level of power will easily kill biological particles [160]. If the allowed power is smaller to avoid optical damages, the optical force is proportionally smaller, which makes smaller focus sizes more valuable for 3D trapping. As the beam waist ($\sim 0.2 \mu\text{m}$) gets close to the

particle size, the discrepancy between the HA and CN increases. This is because the particle size should be smaller than the beam waist in order to get valid results from both models.

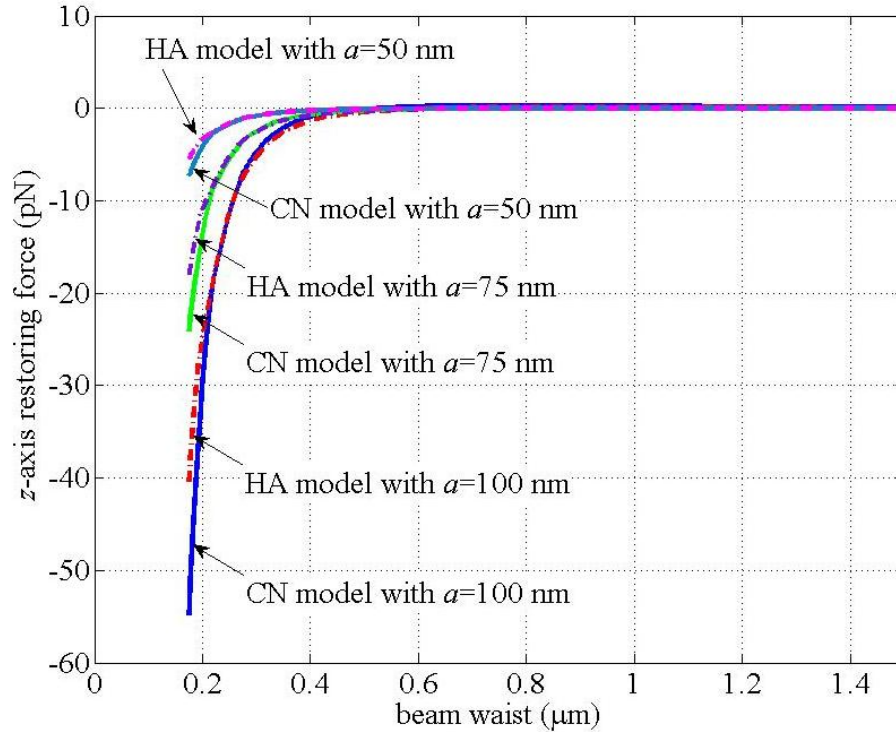


Figure 4.24. Dependence of the z -axis restoring force on the beam waist. The negative z -axis force is a restoring force that enables a 3D trap. The optical power is 1 W. The particle is a sphere with a refractive index of $n_s=1.38$ and a radius of $a=50$ nm, 75 nm, or 100 nm.

It is noted that for large beam waists ($w_0 > 0.4 \mu\text{m}$), the results in Figure 4.24 show the restoring force to be close to 0. This does not mean the particle will stay at an equilibrium position. For large beam waists, the z -axis optical force is always positive due to the weak focusing, which will push the particle downstream. Therefore, for large beam waists, there are no negative restoring forces (no 3D trap enabled) and the particle is pushed away from the waist.

iii) Particle refractive index

The dependence of x -axis escape force on the particle refractive index is shown in Figure 4.25. The particle is assumed to be a sphere with a refractive index of 1.38 and a size $a=50$ nm, 100 nm, and 150 nm. The laser has a wavelength of $\lambda_0=808$ nm and a beam waist of $0.44 \mu\text{m}$. The laser power is $P=1$ W. The CN model and HA model agree well with each other. The results demonstrate that the higher refractive index of the particle, the larger the optical force. The dependence of the optical force on the refractive index is close to a linear relationship. Therefore, particles with a higher refractive index are always easier to be trapped. The smaller the particle, the smaller the trapping force, and the better the HA and CN models match with each other.

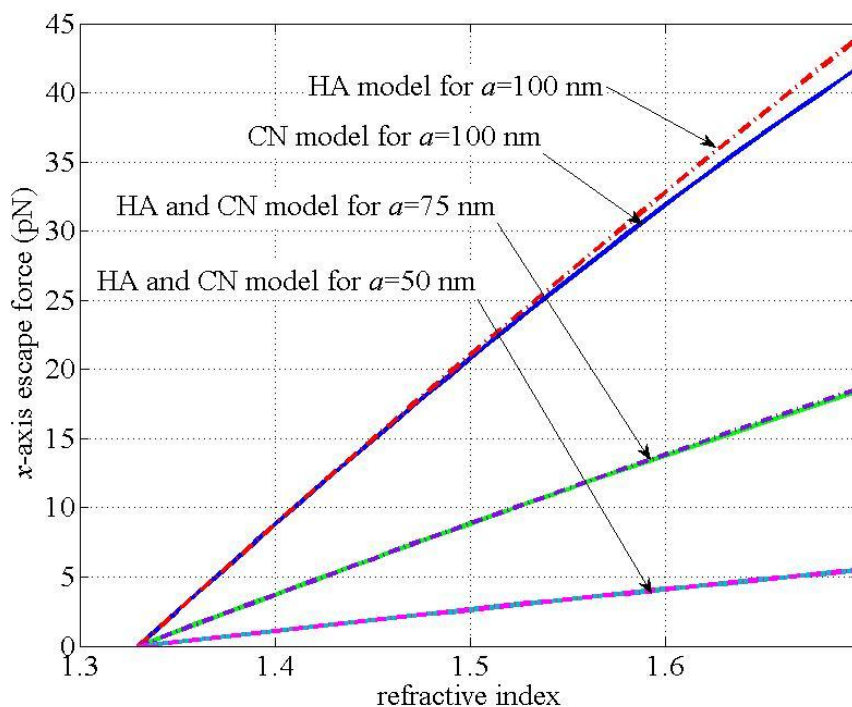


Figure 4.25. Dependence of the x -axis escape force on the refractive index. The optical power is 1 W and the beam waist is $0.44 \mu\text{m}$. The particle is a sphere with a radius of $a=50$, 75, or 100 nm.

According to the results shown in this section, the CN model and HA model matches well in the transverse directions. In the longitudinal directions, the forces from the CN mode are larger in +z direction. This difference is believed to be due to the different principles associated with the two modes. However, the two models still show the same tendency of the optical forces in the longitudinal direction.

4.2.3. 3D Trapping force fields of the SP fiber optical tweezers

Since the electric fields cannot be experimentally measured for the SP fiber, CN model cannot be used to calculate the optical forces of the SP lensed fiber optical tweezers. Therefore, only the HA model will be used to calculate the optical forces from the SP fiber based on the experimentally measured intensity profiles.

The following method is used to determine the optical power. Since the measured intensity is pixelated, each data point is assumed to be the averaged intensity value over the whole area of the pixel. Therefore, the optical power is estimated as the pixel area times the sum of the grayscale values of all the pixels around the focus, while the grayscale values are directly used as the intensities.

The parameters used here for mapping the optical forces are as the following: the optical power $P = 1$ W, the vacuum wavelength $\lambda_0 = 808$ nm, the bead radius $a = 100$ nm, the bead refractive index $n_s = 1.38$, and the medium refractive index $n_m = 1.33$.

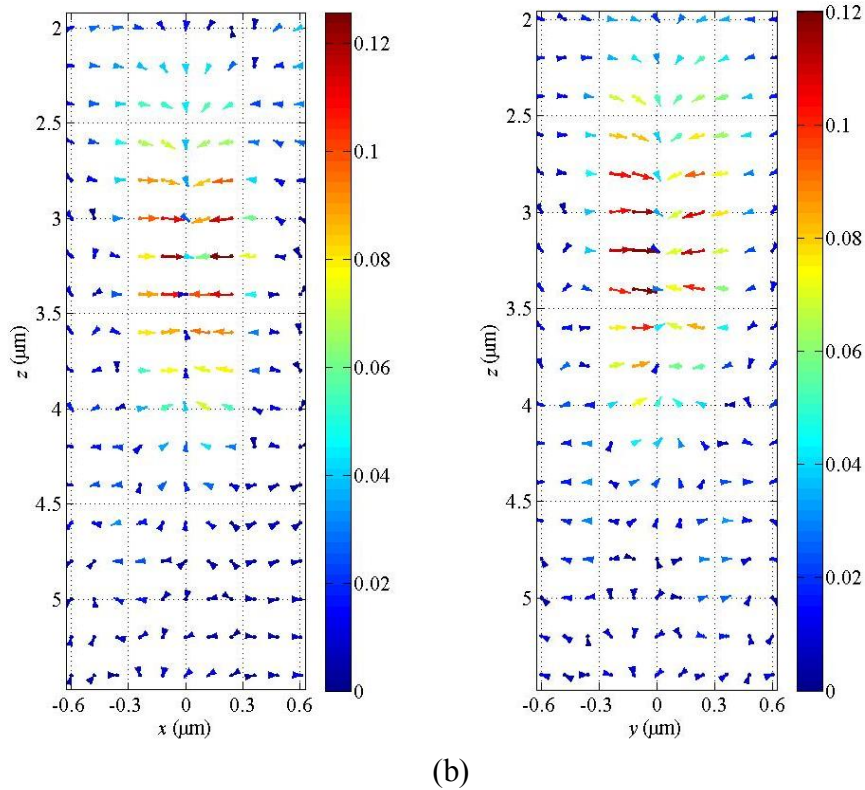


Figure 4.26. Force mapping in the (a) xz and (b) yz planes of SP1. The optical power is 1 W and the wavelength is $0.808 \mu\text{m}$. The particle is a sphere with a radius of $a=100 \text{ nm}$ and a refractive index of 1.38.

4.2.3.1. 3D force mapping of SP1

The force maps in both the xz and yz planes for SP1 are shown in Figure 4.26. A stable 3D trap is clearly seen at $z=3.4 \mu\text{m}$ on the z axis. To further evaluate the position of the trap and the force levels, the optical forces along three dimensions are plotted in Figure 4.27. The restoring forces exist along the three directions at $x=0$, $y=0$, and $z=3.4 \mu\text{m}$, where the 3D trap is located. The maximum x -axis trapping force is 3.65 pN at $x=0.24 \mu\text{m}$, $y=0$, and $z=3.2 \mu\text{m}$. The maximum y -

axis trapping force is 3.57 pN at $x=0$, $y=-0.18 \mu\text{m}$, and $z=3.2 \mu\text{m}$. The maximum z -axis restoring force is 1.13 pN at $x=0$, $y=0$, and $z=4 \mu\text{m}$.

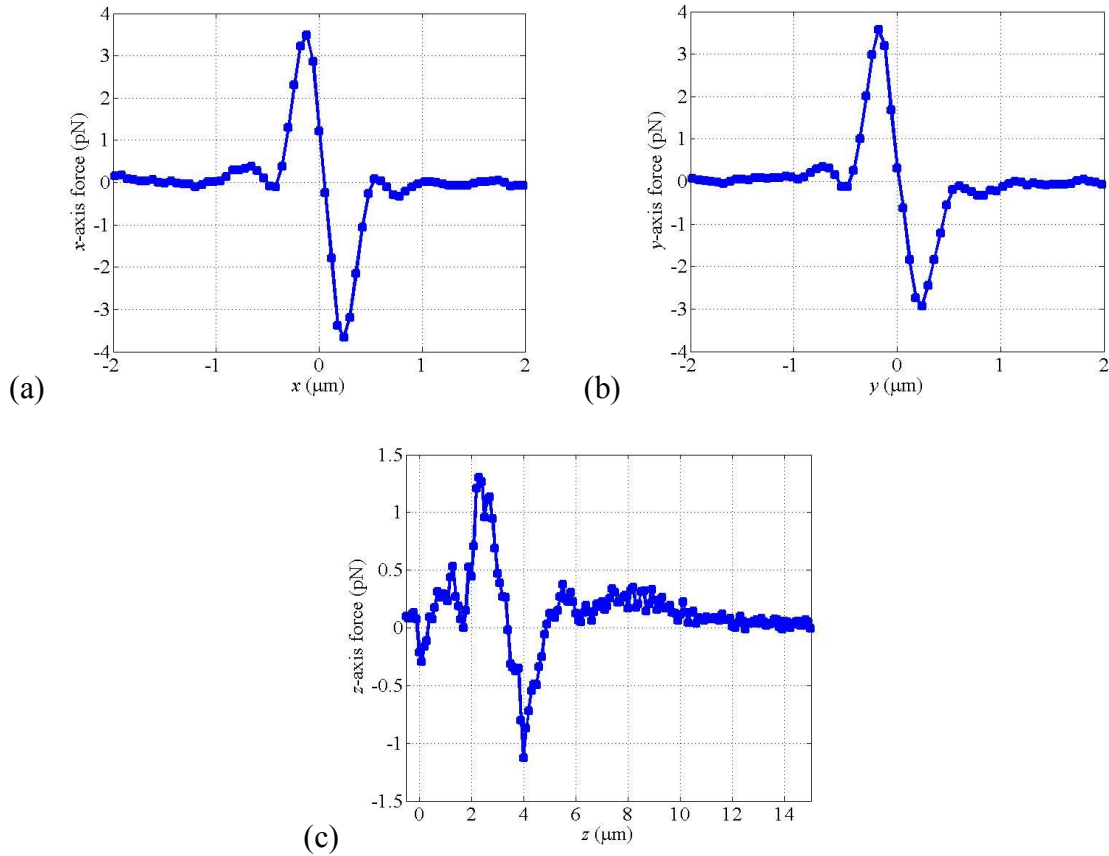


Figure 4.27. Optical forces along three orthogonal directions for SP1. (a) x -axis optical force versus the x displacement for $y=0$ and $z=3.2 \mu\text{m}$. (b) y -axis optical force versus the y displacement for $x=0$ and $z=3.2 \mu\text{m}$. (c) z -axis optical force versus the z displacement for $x=0$ and $y=0$. The forces are calculated according to the intensity profile measured in the experiment. The optical power is 1 W and the wavelength is $0.808 \mu\text{m}$. The particle is a sphere with a radius of $a=100 \text{ nm}$ and a refractive index of 1.38.

4.2.3.2. 3D force mapping of SP2

The trapping forces for SP2 are mapped in three dimensions, and the results in the xz and yz planes are shown in Figure 4.28. A stable 3D trap is located at the position of $z=1.3\sim 1.4\ \mu\text{m}$ on the optical axis. The optical force along three dimensions are plotted across the focus point at $z=1.1\ \mu\text{m}$, as shown in Figure 4.29. The maximum x -axis trapping force is 2.60 pN at $x=-0.15\ \mu\text{m}$, $y=0$, and $z=1.1\ \mu\text{m}$. The maximum y -axis trapping force is 1.91 pN at $x=0$, $y=-0.2\ \mu\text{m}$, and $z=1.1\ \mu\text{m}$. The maximum z -axis restoring force is 1.67 pN at $x=0$, $y=0$, and $z=1.5\ \mu\text{m}$.

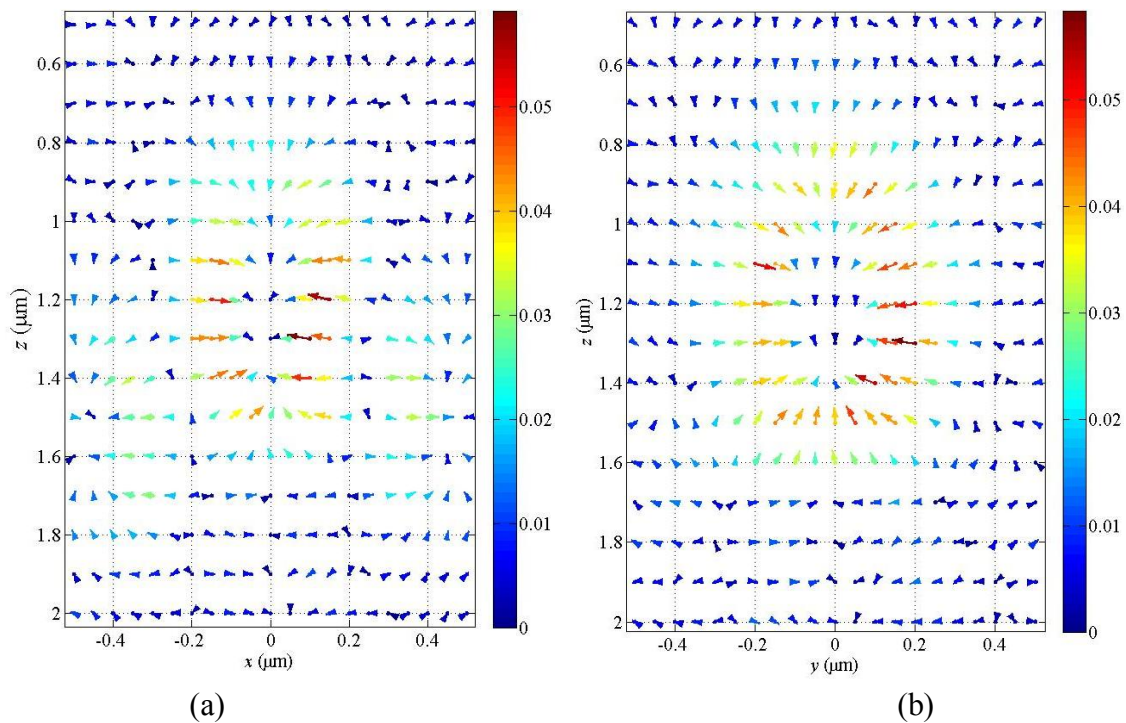


Figure 4.28. Force mapping in the (a) xz and (b) yz planes of the SP 2. The optical power is 1 W and the wavelength is $0.808\ \mu\text{m}$. The particle is a sphere with a radius of $a=100\ \text{nm}$ and a refractive index of 1.38.

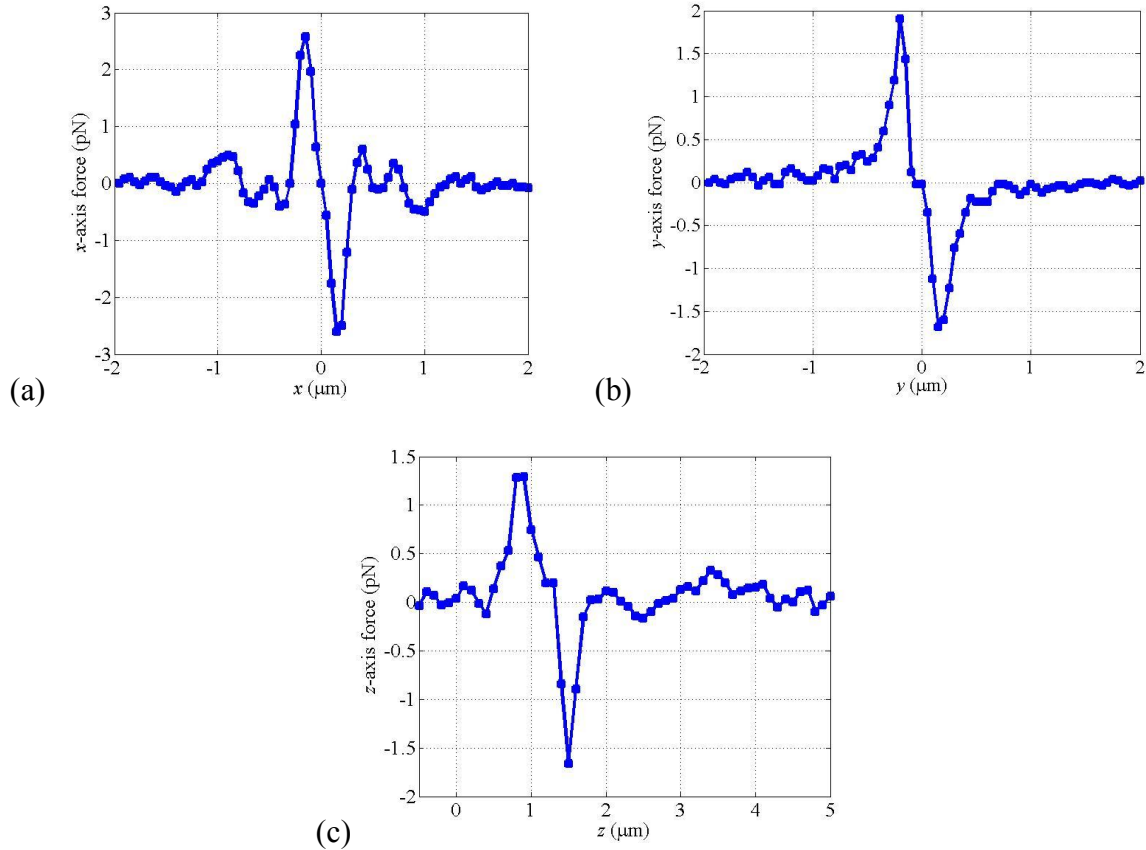


Figure 4.29. Optical forces along three orthogonal directions for SP2. (a) x -axis optical force versus the x displacement for $y=0$ and $z=1.1 \mu\text{m}$. (b) y -axis optical force versus the y displacement for $x=0$ and $z=1.1 \mu\text{m}$. (c) z -axis optical force versus the z displacement for $x=0$ and $y=0$. The forces are calculated according to the intensity profile measured in the experiment. The optical power is 1 W and the wavelength is $0.808 \mu\text{m}$. The particle is a sphere with a radius of $a=100 \text{ nm}$ and a refractive index of 1.38.

4.2.3.3. Discussion of the calculated trapping force fields

Comparison of the optical forces between the two SP fibers

The maximum trapping forces for SP1 and SP2 are summarized in Table 4.4. Both samples have the maximum trapping forces of a couple of piconewtons. For both SP fibers, the x -axis force is

larger than the y-axis force. This is because the x-axis focus is smaller than the y-axis focus (See Table 4.3). However, the z-axis restoring force of SP2 is larger. This is due to the large intensity gradient of the SP2 along the z direction, which can be seen by comparing Figure 4.8 (c) with Figure 4.11 (c).

Table 4.4. Maximum forces of SP1 and SP2.

	SP1	SP2
x-axis force (pN)	3.65	2.60
y-axis force (pN)	3.57	1.91
z-axis negative restoring force (pN)	-1.13	-1.67

Underestimation of the optical forces

It is noted that the optical force from the simulations are underestimated. The major reason is the overestimation of the optical power. As mentioned in Section 4.2.3, the sum of the grayscale over the whole image was used to estimate the power. However, due to the dark reading, the camera does not have a “0” grayscale output even when there is no intensity incident onto the CCD chip. For example, all pixels in the black areas in Figure 4.15 (d) and Figure 4.17 (d) have a dark reading. For the 12-bit DS camera with the saturation grayscale of 4096, the dark reading is ~100. For the 8-bit Motic camera with the saturation grayscale of 256, the dark reading is ~10. These dark readings are all summed up to estimate the power, resulting in overestimation of the power. Since we calculate the trapping forces at a unit power (1 W), the overestimation of the optical power directly results in the underestimation of the trapping forces. The real trapping forces are expected to be larger than the values listed in Table 4.3. It can also be seen that the

Motic camera suffers more from the dark reading than the DS camera. In another word, the power overestimation is more serious for SP2 than for SP1. This explains why the x -direction focus of SP2 is smaller but the x -direction trapping force of SP2 is weaker.

In addition to the overestimation of the optical powers, the errors related with the intensity measurements (discussed in Section 4.1.3.3) can also cause the optical forces to be underestimated. Because the intensity is averaged over each pixel area, the sharp changes of the intensity are not recorded, resulting in a smaller intensity gradient in the measurements. The large measurement step ($0.1 \mu\text{m}$) may also cause the loss of the information of the real intensity maximum and thus underestimate the intensity gradient.

The overestimation of the optical powers can be alleviated by two methods. One is to use a confocal microscope with a photon counter to measure the intensity at the object plane point by point, as used in ref. [134]. Photon counters have very small dark readings and thus can reduce the overestimation due to the dark reading. However, the diffraction limit of the objective in the confocal microscope still limits the resolution of the intensity measurement. The underestimation of the spot size due to the objective resolution still exists, resulting in underestimations of the trapping forces. The other way to reduce the overestimation of the optical powers is to use scanning near-field microscopy (SNOM) to measure the intensity distribution of the SP lenses, as used in ref. [137]. However, the probe of the SNOM may significantly distort the original electric fields so that the measured fields are distinct from the real ones [174]. In addition to the problems discussed above, both the two solutions, namely, the confocal microscopy and the SNOM, are based on the scanning methods that measure the intensity serially. It will take a much

longer time to carry out the scanning measurements. The optical fiber may drift during the long-time measurement process, causing the measurement to fail. Compared with the scanning methods, the method used in this dissertation is a parallel measurement, and the drift of the fiber position does not influence the measurement as much.

Trapping force enhancement compared with lensed fibers

Although the trapping forces are underestimated, the calculated forces of the SP lenses are still larger than those of the lensed fibers used in Chapter 2 and Chapter 3. The lensed fiber with a tapered lens has a beam waist of 1.35 μm . According to the results shown in Figure 4.23 and Figure 4.24, the transverse escape force on the same particle ($a=100\text{ nm}$, $n_s=1.38$) with the same power (1 W) is 0.22 pN and no 3D trap exists due to the weak focusing. The comparison of the trapping forces along the three directions are shown in Table 4.5. The fiber-based SP lens improves the transverse trapping forces by one order of magnitude compared with the commercial lensed fibers, and a 3D trap can be enabled by the former but not by the latter.

Table 4.5. Comparisons of optical forces obtained using the fiber-based SP lens and the tapered fiber lens.

	SP2	Tapered fiber lens
x -axis escape force (pN)	2.60	0.22
y -axis escape force (pN)	1.91	0.22
z -axis negative restoring force (pN)	-1.67 (3D trap enabled)	not exist (no 3D trap enabled)

Trapping force compared with objective-based optical tweezers.

As previously discussed, the smallest beam waist from an objective is determined on the NA. Following Eq. (4-3), the smallest beam spot size (FWHM) for an objective is 394 nm with NA = 1.25 and 352 nm with NA = 1.4. If the beam is described by a TEM₀₀ mode, the corresponding beam waist, which is different from FWHM, is 335 nm with NA = 1.25 and 299 nm with NA = 1.4. The corresponding optical forces are, according to Figure 4.23, ~12 pN and ~20 pN, respectively.

However, these forces calculated for the objective-based optical tweezers only provide an upper limit of the achievable forces. They are not achievable even when every component in the optical path is perfectly aligned. As discussed in Section 4.1.3.3, the smallest spot size obtained with Eq. (4-3) is generally not achievable due to the lower effective NA and aberration, which are inevitable for high NA objectives. Considering the trapping forces for the SP lensed fiber tweezers are underestimated, the trapping ability of the SP lensed fiber tweezers is expected to be comparable or even stronger compared with their counterpart based on objective lenses. This has been confirmed with the previously described 3D bacterium trapping with SP lensed fiber tweezers at a lower power.

4.2.4. Significance of the enhanced trapping ability with the SP fiber optical tweezers

The trapping strength of fiber optical tweezers has been improved to be close to or even stronger than that of objective-based tweezers. This indicates that it is possible to replace the conventional

optical tweezers systems based on microscope objectives with the fiber trapping systems that are compact in size and less expensive, while keeping their strength.

Currently one of the biggest barriers of optical tweezers is their accessibility due to the high price. [60] The less expensive SP lensed fiber optical tweezers will greatly improve the accessibility of optical tweezers both as a research tool and a diagnostic instrument. New ideas and more applications will show up once the optical tweezers with the same strength become readily available for a vast number of researchers. Furthermore, the much smaller while equally strong version of the optical tweezers has great potential to be used to perform high-resolution sensing as well as high-strength manipulation in microfluidic chips.

4.3. Summary

In this chapter, superfocusing with a planar surface plasmonic lens on the fiber endface has been experimentally demonstrated. This is the first time that superfocusing is realized by using a fiber-based SP lens. The numerical simulation with the FDTD method has been carried out, which can help understand the superfocusing effect, and the obtained focus sizes are similar to those measured in the experiments. By taking the advantage of the superfocusing of the fiber-based SP lenses, optical trapping of a sub-micrometer-size bacterium in three dimensions has been successfully demonstrated. The power used in the 3D trapping is smaller than any power used by objective-based optical tweezers reported in the published literature, which indicates the SP fiber optical tweezers have stronger trapping efficiency. The optical trapping of a Rayleigh particle is investigated through parametric studies. It is shown that decreasing the focal spot size can

significantly increase the trapping forces. Moreover, the 3D trapping forces are mapped for the two SP fibers based on the experimentally measured intensity distributions. In this chapter, the following contributions are achieved: *i) superfocusing on a fiber endface with a planar SP lens successfully achieved and ii) trapping ability enhancement by SP lensed fiber optical tweezers successfully demonstrated.*

Chapter 5. Summary and Future Work

5.1. Summary and contributions of the dissertation work

Thanks to their ability of probing single molecules with high precision, optical tweezers (OTs) have been used to facilitate new scientific findings as well as benchmark single-molecule studies [7]. In the coming decade, more great discoveries in biology and physics are expected to be made with the help of OTs. [60] One of the next level applications using OTs is expected to be medical diagnostics [60], where parallel manipulation, sorting, and diagnosis of large number of biological particles with OTs will make the current clinical procedures quicker and cheaper.

Most of current OTs are based on objective lenses, which are bulky, expensive, and hard to integrate. The high price and bulkiness have become issues that limit the applications of OTs. [60] Moreover, objective-based OTs have other limitations coming from the objective lens and the free-space optics, which include being susceptible to environmental perturbations, having limited ($\sim 100 \mu\text{m}$) working distance, and having restrictions on the substrate.

OTs based on optical fibers have great potential to solve the abovementioned limitations. Fiber-based OTs are compact in size, less expensive, and readily integrable. No free-space optics and objective lenses are needed to generate optical traps. However, fiber-based OTs have much weaker trapping efficiency compared with objective-based OTs, which greatly limits their applications. In addition to the weak trapping efficiency, other problems of the existing fiber-

based OTs include difficulty to achieve 3D traps (for single fiber tweezers), cumbersome system configurations (for counter-propagation fiber OTs), and limited functionalities (for all the existing fiber OTs).

This doctoral research attempts to provide solutions to overcome the limitations of current fiber-based OTs, with the objective of achieving fundamental understanding and improving the performance of fiber-based OTs. Based on the research work described in the previous chapters, the contributions of this dissertation work are summarized as follows.

Contribution 1: An enhanced understanding of the inclined dual-fiber optical tweezers (DFOTs) system has been developed. The 3D trapping ability of inclined dual fiber optical tweezers (DFOTs) system has been carefully investigated through thorough experimental study and modeling. Experimental calibrations have been carried out via two methods, namely, the drag force method and the power spectrum analysis method, to evaluate the force-displacement relationship. *This is the first time that such a system has been experimentally calibrated. The calibration results enable the inclined DFOTs to be used as force sensors.* Furthermore, a theoretical model based on ray optics has been developed and parametric studies based on the model have been carried out to enhance the understanding of the inclined DFOTs. Through the parametric studies, the influence of the system parameters on the 3D trapping performance has been thoroughly studied, which can help achieve a better system design of the inclined DFOTs. In addition, modeling of the system has helped reveal a new finding that the inclined DFOTs are more robust to the fiber misalignments compared with the commonly used counter-propagation DFOTs. *This is the first time that the inclined DFOTs have been systematically investigated.*

Contribution 2: Multiple traps created with the inclined DFOTs system have been discovered and investigated for the first time. During the experimental study of the inclined DFOTs system, a new phenomenon has been discovered; multiple traps can be created with the inclined DFOTs system. Three traps, two 2D and one 3D, located at different vertical levels with controllable separations, have been successfully created. Furthermore, the force field of the inclined DFOTs system has been studied in numerical simulations to fully understand the multiple traps. The fiber-based multiple trapping system can be used as a building block that is readily integrable in microfluidic systems. Different from multiple traps created with other fiber-based OTs, only one actuator is required to adjust both the positions and the separations of the traps. *This is the first time that a controllable multi-trap fiber optical tweezers system has been achieved.*

Contribution 3: Multiple functionalities have been realized with the inclined DFOTs system for the first time. The discovery of multiple traps enables the inclined DFOTs system to perform complex functionalities that cannot be realized by using other fiber-based OTs. *Multiple functions have been experimentally demonstrated for the first time with fiber-based OTs, including particle separation, particle stacking, particle grouping, parallel manipulation, rod alignment, rod rotation, rod stacking, and optical binding between beads and rods.* The ability of performing versatile functionalities will help the inclined DFOTs system find new applications in many fronts including medical diagnosis and biological/physical research.

Contribution 4: A novel fiber based surface plamonic (SP) lens has been developed and far-field superfocusing effect has been demonstrated for the first time with the fiber based SP lens. A planar SP lens with nanometer-scale concentric ring patterns has been designed on the endface of an optical fiber. *With the help of SP wave propagation through nanometer scale structures, far-field superfocusing has been realized for the first time with a fiber based SP lens.* Focii with sizes close to the diffraction limit have been experimentally obtained with fiber-based SP lenses. The focus size of the fiber-based SP lens has reached that of the smallest achievable focus of a high NA (1.4) objective. The fiber based SP lens can serve as a useful tool to bridge macroscale sources/detectors and nanoscale devices. In addition to optical trapping, the superfocusing achieved with fiber-based SP lenses can open up many other applications, including coupling power into nanophotonic devices, superresolution fluorescence detection, and subwavelength imaging.

Contribution 5: Trapping efficiency enhanced with fiber-based SP lens has been successfully demonstrated. The fiber-based SP lens greatly enhances the trapping efficiency of fiber OTs. *For the first time, 3D trapping of a submicron-size bacterium has been successfully demonstrated in experiment by using fiber OTs built with the fiber-based SP lens.* The power used for such 3D trapping has been found to be lower than that used in any reported objective-based OTs. Furthermore, optical trapping of Rayleigh particles has been studied numerically based on two popular electromagnetic models: HA model and CN model. *For the first time, investigation has been carried out to compare the two models in a parametric study to find out their applicability in terms of particle sizes.* Based on the HA model, the 3D force fields of SP lensed fiber OTs have been mapped by using experimentally measured intensity distributions of

the fiber-based SP lenses. *Despite of the underestimation of the trapping forces, the trapping efficiency has been enhanced by an order of magnitude compared with that of the OTs built with lensed fibers.*

5.2. Future work

The ultimate goal of developing fiber OTs with performance comparable with objective-based OTs is far from being realized. However, this dissertation work has provided a framework that can lead to many exciting directions towards the goal. To further improve the fiber OTs, the suggested future work is summarized as follows.

i) Suggestions to overcome the limitations of the current inclined DFOTs setup

The current setup of the inclined DFOTs still uses two manual stages to perform the fiber alignments. However, the positions of the manual stages drift with time, resulting in misalignments of the fibers. This is the main reason why 3D trapping of silica beads smaller than 3 μm is difficult to achieve with the current setup. A possible solution is to fix the fibers in V-grooves etched in a silicon wafer with epoxy. The challenge is that the epoxy thicknesses may be different for the two fibers, introducing fiber misalignments.

The conical tips of the lensed fibers used in this dissertation work have large cone angles, which prevent two lensed fibers from being brought close to each other. In this case, the focuses of the optical beams are not located at the beam intersection in the

inclined DFOTs setup. If a sharper fiber tip with a smaller opening angle is used, the beams may intersect at the focuses so that the trapping efficiency of the inclined DFOTs can be stronger.

ii) Suggestions to overcome the limitations of current SP lensed fiber OTs

One of the limitations of the SP lens is the short focal length. It is difficult to trap particles lying on the substrate due to the physical size of the regular fiber. One possible solution is to increase the number of slits or slit radii because a larger aperture of the SP lens will result in a longer focal length. However, there are two constraints that limit the aperture size: the fiber-guided beam size ($2.8\ \mu\text{m}$ in radius) and the minimum separation between the adjacent slits. With the current design parameters (the gold thickness, the radius, and the width of the smallest slit), the slit width increases faster than the slit radius when the radius is larger than $\sim 1.3\ \mu\text{m}$, resulting in overlap between the adjacent slits for a slit radius larger than $\sim 1.5\ \mu\text{m}$.

The misalignments and the blocking of the fabricated slits in the fiber-based SP lens have been the issues that limit the success rate of the SP lens fabrication. To address the misalignments, a marker can be milled on the fiber endface prior to the gold evaporation, and the marker should be still visible under the FIB with the gold coating. The mechanism of the blocking of the patterns during the FIB fabrication is still not clear so far, which need to be further investigated in future work.

The design model give in this dissertation is for a planar waveguide (metal-insulator-metal structure) with an infinite thickness. The dispersion of the SP wave in a cylindrical structure is different from that in a planar one, which has not been studied yet. The dispersion relationship in a cylindrical structure will enhance the understanding of the SP wave propagation in the fiber-based SP lens.

The better measurement of the intensity distributions of the SP lenses is necessary, in which the dark readings of the photodetectors should be removed. Single-photon counting detectors (such as PCD100, Newport) with very low dark readings are suggested to carry out the intensity measurements. Photon counting detectors measure the intensity at a single point at one time, so a measurement setup should be designed to enable the scanning of the probe with a small step size. The small aperture of the probe should also be designed so that the fine features of the intensity can be resolved. The SNOM probe is an option to be used as the scanning probe, but it will distort the electric field, which can cause the measured data unfaithful.

iii) Experimental calibration of SP fiber tweezers

The experimental calibration data using SP fiber tweezers would be a tangible proof that the fiber OTs can have equal or stronger trapping efficiency compared with objective-based OTs. However, due to the immature fabrication process, such calibration has not been achieved yet. Refinement and modification of both the SP lens design and the fabrication are suggested in future work.

iv) Intensity and phase modulation in inclined DFOTs

By taking the advantage of the high performance intensity and phase modulation devices that are widely used in fiber optic communication industry, the dynamic trapping position control can be achieved. This can enable the study of the dynamics of small particles in an ultra fast time scale.

v) Inclined DFOTs built with SP lenses

If SP lenses are used, the inclined DFOTs can retain the flexibility and functionality while having significantly increased the trapping strength. Longer focal lengths should be realized with the fiber-based SP lens so that enough space between the focus and the fiber end can be obtained for the inclined DFOTs setup.

vi) Integration of inclined DFOTs

The setup of inclined DFOTs has the potential to be miniaturized and used as a module in integrated microscale systems. It is envisioned that an integrated system that can separate and sort cells, and probe the properties of the selected ones, will be developed in the future. This integrated system can open up many new applications in medical diagnosis. One of the issues to be addressed is to find a way to image and monitor the traps, which can totally remove the microscope and objective from the system.

APPENDIX A: MATLAB CODES

A.1. Matlab codes for trapping force calculation with ray optics

```
% To test the error that different distances along the optical axis gives
different signs of the spring coefficient.

format long;

clear all;
n1=1.33; %input('the refractive index of water=');
n2=1.45; %input('the refractive index of the bead (beads)=');
c=3e8;
wavelength=0.808;%input('wavelength (um)')

W=15.3e-3;%input('laser power=(W)'); %at 90 mA
r0=1.35;%input('radius of waist (um)')
Sr=2.37;%input('bead/half of long axis of cell=');

alpha = 50/180*pi; % inclination angle of fiber relative to the normal to
the coverslip surface
% this angle definition has been checked to be correct
z0=n1*pi*r0*r0/wavelength;
D=45;
L0=D/2/sin(alpha)-14; % beam waist position
to_real = [1 0 0; 0 cos(alpha) -sin(alpha); 0 sin(alpha), cos(alpha)];
%transformation matrix from calculation coordinate (x'y'z') to real system
(xyz)

from_real = [1 0 0; 0 cos(alpha) sin(alpha); 0 -sin(alpha) cos(alpha)];
%transformation matrix from real coordinate xyz to calculation coordinate
x'y'z'

beamcenter_real = [0 0 0]; %when (0,0,0) is at the waist center
beamcenter_cal = [0 0 0]; %when (0,0,0) is at the waist center in calculation
coordinate sys x'y'z'
beaminter_cal = [0 0 -L0]; % beam intersection coordinates in calculation
coordinate system
beaminter_real = (to_real * beaminter_cal)';

z_origin = -1.0342; % the z position where Fz=0; for 70 mA, this value is -
1.88

pos=[-6 -5 -4 -3.5 -3 -2.5 -2.2 -2 -1.8 -1.5 -1 -0.5 0];
pos_num=length(pos);

forcex = 1 : pos_num;
forcey = 1 : pos_num;
forcez = 1 : pos_num;
```

```

for i= 1:pos_num % different bead position
%i=5; %5:-1 or 7:1
beadcen_relato_beaminter_real = [pos(i) 0 z_origin];

beadcen_relato_beaminter_cal = (from_real *...
beadcen_relato_beaminter_real)';
beadcenter_real = beadcen_relato_beaminter_real + beaminter_real;
beadcenter_cal = beadcen_relato_beaminter_cal + beaminter_cal;

lA=20; %lr is division of spherical angle, or, how many pieces are in
pi/2 (half a longitude)
la=20; %la is division of circle angle, or, how many pieces are in 2*pi
(a whole latitude)
dA=pi/lA;
da=2*pi/la;
F=[0 0 0];

%start force calculation
for j=1:lA % cut the half sphere along latitude
%j=3;
dr1 = Sr*sin(dA*(j-0.5));
dz1 = Sr*cos(dA*(j-0.5)); % z coordinate relative to bead center in
real coord

for k=1:la
dS = Sr*dr1; % *da*dA will be multiplied at last
dx1 = dr1*cos(da*(k-0.5)); dy1 = dr1*sin(da*(k-0.5)); % x y
coordinates relative to bead center
dpoint_real = [dx1 dy1 dz1]; %coordinate of calculated point
on bead surface relative to bead center, or, normal
vector of bead surface in real coord
point_real = dpoint_real + beadcen_relato_beaminter_real +
beaminter_real; %coordinate of calculated point relative to
waist center (in calculation coordinate system)
normal_real = dpoint_real/norm(dpoint_real);

point_cal = (from_real * point_real)'; % calculated point
coord in calculation coord sys relative to beam center
normal_cal = (from_real * normal_real)';
in_cal = inci_dir(point_cal,beamcenter_cal,z0,-1);
judge = dot(normal_cal,in_cal); % if this area illuminated?

dF=[0 0 0];
if(judge < 0) % Yes, illuminated
% all the calculation should be within calculation
coord sys
rr=sqrt((point_cal(1))^2+(point_cal(2))^2); % distance
from calculated point to optical axis
Ir=intens(r0,W,point_cal(3),wavelength,rr);

[reflect,refract,dF,R,T]=ref(in_cal,normal_cal,n1,n2,Ir);
F=F-dF*dS*judge; %negative sign comes from judge being
negative;

```

```

in_cal=refract; % next incident direction
Ir=Ir*T;
for l=1:5

    rpoint_cal=ptsphere(point_cal,in_cal,beadcenter_cal,Sr); %
    rpoint is the next incident point while point is the
    current one
    rpoint_relato_beadcen = rpoint_cal - beadcenter_cal;
    normal_cal = -...
        rpoint_relato_beadcen/norm(rpoint_relato_beadcen);

    [reflect,refract,dF,R,T]=ref(in_cal,normal_cal,n2,...
        n1,Ir);
    judge_temp=dot(normal_cal,in_cal);
    if judge_temp>0
        disp('wrong when calculation multiple reflection
            inside bead, judge>0 !');
    end

    F=F-dF*dS*judge; %negative sign comes from judge being
        negative; use the same "judge" and "dS" as the
        first incidence
    Ir=Ir*R;
    in_cal=reflect;
    point_cal=rpoint_cal;
end
end % end for if
end % end for k
end %end for j
F_real=(to_real*F)';
forcex(i)=F_real(1)*da*dA;
forcey(i)=F_real(2)*da*dA;
forcez(i)=F_real(3)*da*dA;
end % end for i

plot(pos, forcex*1e12, '-rs');

```

A.2. Matlab codes for investigation of trapping robustness to the fiber misalignments

```

% To test the error that different distances along the optical axis
% gives different signs of the spring coefficient.

```

```
format long;
```

```

clear all;
n1=1.33;%input('the refractive index of water=');
%http://www.answers.com/refractive%20index
n2=1.45; %input('the refractive index of the bead (beads)=');
c=3e8;
wavelength=0.808;%input('wavelength (um)')

```

```

W_left=7.65e-3;%input('laser power=(W)');
W_right=7.65e-3;
r0=1.35;%input('radius of waist (um)')
Sr=2.37;%input('bead/half of long axis of cell=');

alpha = 50/180*pi; % inclination angle of fiber relative to the
%normal to the coverslip surface
% this angle definition has been checked to be correct
z0=n1*pi*r0*r0/wavelength;
D=45;
L0=D/2/sin(alpha)-14; % beam waist position (line distance from the
%bead center (beam intersection) to the waist when the bead is located
%on optical axis);

%real is respect to the spheroid (xyz); calculation is respect to the
%beam axis (x'y'z')
to_real_left = [1 0 0; 0 cos(alpha) -sin(alpha); 0 sin(alpha), cos(alpha)];
from_real_right = to_real_left;
%transformation matrix from calculation coordinate (x'y'z') to real
%system (xyz)
%this is to_real for fiber 1 (left), from_real for fiber 2 (right)
%[x y z]=(to_real*[x' y' z']')'

from_real_left = [1 0 0; 0 cos(alpha) sin(alpha); 0 -sin(alpha) cos(alpha)];
to_real_right = from_real_left;
%transformation matrix from real coordinate xyz to calculation
%coordinate x'y'z'
%this is from_real for fiber 1 (left), from_real for fiber 2 (right).

z_misalign = 1;
delta_L0 = z_misalign/sin(2*alpha)*sin(alpha);

beamcenter_real_left = [0 0 0]; %when (0,0,0) is at the waist center
beamcenter_cal_left = [0 0 0]; %when (0,0,0) is at the waist center in
%calculation coordinate sys x'y'z'
beamcenter_real_right = [0 0 0];
beamcenter_cal_right = [0 0 0];
beaminter_cal_left = [0 0 -L0+delta_L0]; % beam intersection
%coordinates in calculation coordinate system
beaminter_cal_right = [0 0 -L0-delta_L0];
beaminter_real_left = (to_real_left * beaminter_cal_left)';
beaminter_real_right = (to_real_right * beaminter_cal_right)';

pos=[-6 -4 -3 -2 -1.5 -1 -0.5 0 0.5 1];
pos_num=length(pos);

forcex = 1 : pos_num;
forcey = 1 : pos_num;
forcez = 1 : pos_num;

for i= 1:pos_num % different bead position
%i=5; %5:-1 or 7:1

```

```

beadcen_relato_beaminter_real = [0 0 pos(i)];
    %both the left and the right use the
    same %beadcen_relato_beaminter_real

%left
beadcen_relato_beaminter_cal_left = (from_real_left ...
* beadcen_relato_beaminter_real)';
beadcenter_real_left = beadcen_relato_beaminter_real ...
+ beaminter_real_left;
beadcenter_cal_left = beadcen_relato_beaminter_cal_left ...
+ beaminter_cal_left;

%right
beadcen_relato_beaminter_cal_right = (from_real_right ...
* beadcen_relato_beaminter_real)';
beadcenter_real_right = beadcen_relato_beaminter_real ...
+ beaminter_real_right;
beadcenter_cal_right = beadcen_relato_beaminter_cal_right...
+ beaminter_cal_right;

lA=20; %lr is division of spherical angle, or,
    % how many pieces are in pi/2 (half a longitude)
la=20; %la is division of circle angle, or,
%how many pieces are in 2*pi (a whole latitude)
dA=pi/lA;
da=2*pi/la;
F_left=[0 0 0];
F_right=[0 0 0];

%start force calculation at specific bead position
for j=1:lA
    % cut the half sphere along latitude
    %j=3;
    dr1 = Sr*sin(dA*(j-0.5));
    dz1 = Sr*cos(dA*(j-0.5));
    % z coordinate relative to bead center in real coord

    for k=1:la
        dS = Sr*dr1; % *da*dA will be multiplied at last
        dx1 = dr1*cos(da*(k-0.5)); dy1 = dr1*sin(da*(k-0.5));
        % x y coordinates relative to bead center
        %both the left and the right use the same dpoint_real
        %andnormal_real
        dpoint_real = [dx1 dy1 dz1];
        %coordinate of calculated point on bead surface relative to
        % bead center, or, normal vector of bead surface in real
        % coordinate
        normal_real = dpoint_real/norm(dpoint_real);

        %left
        point_real_left = dpoint_real + beadcen_relato_beaminter_real +
        beaminter_real_left; %coordinate of calculated point relative to
        waist center
        %(in calculation coordinate system)
        point_cal_left = (from_real_left * point_real_left)';
        % calculated point coord in calculation coord sys relative to

```

```

beam center
normal_cal_left = (from_real_left * normal_real)';
in_cal_left = ...
inci_dir(point_cal_left,beamcenter_cal_left,z0,-1);
judge_left = dot(normal_cal_left,in_cal_left);
% if this area illuminated?
%right
point_real_right = dpoint_real + beadcen_relato_beaminter_real +
beaminter_real_right;
%coordinate of calculated point relative to waist center
%(in calculation coordinate system)
point_cal_right = (from_real_right *
point_real_right)'; %calculated point coord in calculation coord
sys relative %to beam center
normal_cal_right = (from_real_right * normal_real)';
in_cal_right = inci_dir(point_cal_right, ...
beamcenter_cal_right, z0,-1);
judge_right = dot(normal_cal_right,in_cal_right);
% if this area illuminated?

%left
dF_left=[0 0 0];
if(judge_left < 0) % Yes, illuminated
    % all the calculation should be within calculation
    %coord sys

    rr_left=sqrt((point_cal_left(1))^2+(point_cal_left(2))...
^2); % distance from calculated point to optical axis

    Ir_left=intens(r0,W_left,point_cal_left(3),wavelength,...
rr_left);

    [reflect_left,refract_left,dF_left,R_left,T_left]= ...
ref(in_cal_left,normal_cal_left,n1,n2,Ir_left);
F_left=F_left-dF_left*dS*judge_left; %negative sign
    %comes from judge being negative;

    in_cal_left=refract_left; % next incident direction
    Ir_left = Ir_left*T_left;
    for l=1:5

        rpoint_cal_left=ptsphere(point_cal_left,in_cal_ ...
left,beadcenter_cal_left,Sr); %rpoint is the
next %incident point while point is the current one
rpoint_relato_beadcen_left = rpoint_cal_left - ...
beadcenter_cal_left;
normal_cal_left = -rpoint_relato_beadcen_left ...
/norm(rpoint_relato_beadcen_left);

        [reflect_left,refract_left,dF_left,R_left,T_left]...
=ref(in_cal_left,normal_cal_left,n2,n1,Ir_left);
judge_temp_left=dot(normal_cal_left,in_cal_left);
if judge_temp_left>0
    disp('wrong when calculation multiple ... reflection
inside bead, judge>0 !');
end
end

```

```

        F_left=F_left-dF_left*dS*judge_left;
        %negative sign comes from judge being negative;
        % use the same "judge" and "dS" as the first
        % incidence
        Ir_left=Ir_left*R_left;
        in_cal_left=reflect_left;
        point_cal_left=rpoint_cal_left;
    end
end % end for if

%right
dF_right=[0 0 0];
if(judge_right < 0) % Yes, illuminated
    % all the calculation should be within calculation ...
    % coord sys

    rr_right=sqrt((point_cal_right(1))^2+(point_cal_...
        right(2))^2); % distance from calculated point to ...
    % optical axis

    Ir_right=intens(r0,W_right,point_cal_right(3),...
        wavelength,rr_right);
        [reflect_right,refract_right,dF_right,R_right, ...
        T_right]=ref(in_cal_right,normal_cal_right,n1,n2, ...
        Ir_right);
    F_right=F_right-dF_right*dS*judge_right; %negative ...
    % sign comes from judge being negative;

    in_cal_right=refract_right; % next incident direction
    Ir_right = Ir_right*T_right;
    for l=1:5

        rpoint_cal_right=ptsphere(point_cal_right,in_cal_...
            right,beadcenter_cal_right,Sr); %rpoint is the ...
            % next incident point while point is the current one
            rpoint_relato_beadcen_right = rpoint_cal_right ...
            - beadcenter_cal_right;
            normal_cal_right = -rpoint_relato_beadcen_right ...
            /norm(rpoint_relato_beadcen_right);
            [reflect_right,refract_right,dF_right,R_right,...
            T_right]=ref(in_cal_right,normal_cal_right,n2,n1,...
            Ir_right);
            judge_temp_right=dot(normal_cal_right,in_cal_right);
            if judge_temp_right>0
                disp('wrong when calculation multiple...
                    reflection inside bead, judge>0 !');
            end
            %
            dS=Sr*sqrt(Sr^2-rpoint_relato_beadcen(3)^2);
            F_right=F_right-dF_right*dS*judge_right; %negative sign
            % comes from judge being negative; use the same "judge" and
            % "dS" as the first incidence
            Ir_right=Ir_right*R_right;
            in_cal_right=reflect_right;
            point_cal_right=rpoint_cal_right;
        end
    end
end

```

```

        end % end for if
    end % end for k
    end %end for j
    F_real=(to_real_left*F_left)'+(to_real_right*F_right)';
    forcex(i)=F_real(1)*da*dA;
    forcey(i)=F_real(2)*da*dA;
    forcez(i)=F_real(3)*da*dA;
end % end for i

plot(pos, forcez*1e12, '-rs');

```

A.3. Matlab codes for power spectrum analysis

```

% function psfitting_real_lin3(filename)
function psfitting_real_lin4

format long eng;
% this code is to use Lorentzian to fit the experimental power spectrum
% data; it loads data from a file containing the experimental data
% obtained from a labview program.

% It considers Phydro (aliased Lorentzian with corrected drag force).

%The blocked point will be evenly distributed along linear frequency
%scale.

%before using this program, make sure:
%1. data points separation along f axis is 0.2; otherwise, change 0.2
%in the code.
%2. spectrum scale (y-axis data) has a unit of dB.

%parameters can be changed below

Tmsr = 50; %total time of sampling
fstep = 1/Tmsr; %step on frequency
fsampling = 10e3; % sampling frequency

startHz=1;
endHz=2000;

R=2.37;
% R=1.965; %radius of bead with a unit of um

height = 45; %height of bead center above the glass with a unit of um

f3db=257e3; % f3dB of electronics

mu = 0.89e-3; %unit: Pa.s; mu=nv*rho; dynamic viscosity of water at
%25oC. data from http://www.thermexcel.com/english/tables/eau_atm.htm
rho = 0.997e3; %unit: kg/m^3
nu = 0.893e6; % kinematic viscosity of water; unit: um^2/s. This

```

```

%is what we will use here
gama0 = 6*pi*mu*R*1e-6; %friction coefficient of the bead in SI unit

% data1=loaddata(filename); %data is a n*m matrix, while n is data
%number.

load '060403';
% load '301 aver x'; % ps y axis is in linear scale; see change in
% line 22

[n,m]=size(data1);
powerspec=data1(:,2); % power spectrum in dB scale
linearpower=10.^(powerspec./10);
% power spectrum in linear scale(arb. unit)
% linearpower = powerspec;

frequency=(fstep*(1:n))';
%for unknown reason, the values of data(n,1) is always
%ingeter for a large n, such as 1e5; before using this program,
%make sure to change 0.2 to the exact separation of data points.

%blocking start
m=100; %data number of each blocking

% determine the start and of frequencies for the Lorentzian fitting

%total blocks required
startno=startHz/fstep;
endno=endHz/fstep;
nprime2=fix((endno+1-startno)/m);
%number of data points used for fitting
newf=1:nprime2;
newpowerspec=1:nprime2;

%blocking
for i=1:nprime2
    startn = startno + m*(i-1);
    endn = startno + m*i -1;
    newf(i)=mean(frequency(startn:endn));
    newpowerspec(i)=mean(linearpower(startn:endn));
end

plot(newf,newpowerspec,'rd');
hold on;

%calculate the values of fc and D by curve fitting

fv = nu/(pi*R^2); %unit Hz
fm = 0.9*fv; % it is different from the value give in the paper
%(2004 apl), because our bead has a density of 2.0g/cm^3

start_point = [2e-6 14]; %start values for D and fc, respectively
model = @Pexpected;

```

```

opts1 = optimset ('MaxFunEvals',1e5);
opts2 = optimset('maxiter',1e5);
options = optimset(opts1,opts2);
[estimates, fval, exitflag] = fminsearch(model, start_point,options);

% this is the Phydro provided by the paper
function [sse Paliased] = Pexpected(params)
    D = params(1);
    fc = params(2);
    Paliased = D./(fc^2+newf.^2);
    ErrorVector = (Paliased - newpowerspec)./Paliased;
    sse = sum(ErrorVector .^ 2);
end

D=estimates(1);
fc=estimates(2);

%calculate the errors of fc
xmin = startHz/fc; %x1
xmax = endHz/fc; %x2
u = 2*xmax/(1+xmax^2) - 2*xmin/(1+xmin^2) + 2*atan((xmax-xmin)/(1+xmax*xmin));
v = 4/(xmax-xmin)*(atan((xmax-xmin)/(1+xmax*xmin)))^2;
Sfc = sqrt(pi/(u-v));
sigma_fc = fc*Sfc/sqrt(pi*fc*Tmsr); %error of fc

[sse, FittedCurve] = model(estimates);
plot(newf,FittedCurve, '-b');

hold off;

k = 2*pi*gama0*fc;
sigma_k = 2*pi*gama0*sigma_fc;
disp(['The fitting range is from' blanks(1) num2str(startHz) 'Hz to' ...
blanks(1) num2str(endHz) '. The number of data points after blocking ...
is' blanks(1) num2str(nprime2) '.']);
disp(['Linear axis equidistance blocking, m =' blanks(2) num2str(m) ...
'(' num2str(m*fstep) blanks(1) 'Hz).']);
disp(['The error of curve fitting sub(((Pfit-Pexp)/Pfit)^2) is' ...
blanks(1) num2str(fval) '. The exitflag is' blanks(1) num2str(exitflag)]);
disp(blanks(3));
disp(['The fitted D is D =' blanks(2) num2str(D)]);
disp(['The fitted fc is fc =' blanks(2) num2str(fc) blanks(1) '+-' ...
blanks(1) num2str(sigma_fc) blanks(1) 'Hz.']);
disp(['The fitted k is k =' blanks(2) num2str(k*1e6) blanks(1) '+-' ...
blanks(1) num2str(sigma_k*1e6) blanks(1) 'pN/micron.']);

end

```

A.4. Matlab codes for x-axis Rayleigh trapping force simulation with the CN model

```
function CNtrap00x
```

```

format long;
% to calculate the trapping force according to CN model

%parameter to change
w0=0.44e-6; % beam waist
lambda=0.808e-6; % wavelength in vacuum
n = 1.33; % refractive index of medium
ns = 1.38; % 1.578 for ps; 1.45 for silica; 1.38 for biological particles
a=1e-7;

nlist = 1.33:0.01:1.7; % bead radius;
epsilon0 = 8.85e-12;
c=3e8;
nl=length(nlist);
escn=[];

for j=1:nl

    ns=nlist(j);

    km = 2*pi.*n./lambda; % k in medium
    s = 1./(km.*w0);
    nr=ns./n; % relative refractive index
    sigma = 128*pi^5*a^6/3/(lambda/n)^4 * ((nr^2-1)/(nr^2+2))^2; %scattering
    crosssection
    alpha0 = n^2 * a^3 * (nr^2-1)/(nr^2+2); %polarizability
    alpha = alpha0/(1+2/3*1i*km^3*alpha0);

    x = (-1.5:0.001:1.5)*1e-6; % x positions
    y = 0;
    zpos = 0e-6;

    dx=0.001e-6;
    dz=0.01e-6;

    Exx=[];
    dExx=[];
    dExy=[];
    dExz=[];

    z=0;

    xi = x./w0; % greek letter Xi: nomalized x
    eta = y./w0; % greek letter Eta: nomalized y
    zita = z./(km*w0^2); % greek letter zeta: nomalized z

    Q = 1./(2.*zita+1i);
    rho = sqrt(xi.^2 + eta.^2);
    psi = 1i.*Q.*exp(-1i.*rho.^2.*Q);

    Ex = psi.*exp(-1i.*zita./s.^2);
    dExdx = Ex .* (-2i.*Q.*xi)./w0;

```

```

dExdy = Ex .* (-2i.*Q.*eta)./w0;
dExdz = Ex ./ (km.*w0.^2) .* (-1i./s^2 + 2i.*rho.^2.*Q.^2);

Exx=[Exx;Ex];
dExx=[dExx;dExdx];
dExy=[dExy;dExdy];
dExz=[dExz;dExdz];

Fxt = alpha .* (Exx.*conj(dExx));
Fyt = alpha .* (Exx.*conj(dExy));

Fx = 1/2*real(Fxt);

P_HA = pi*w0^2*n*epsilon0*c/4; % power under SI units
P_CN = 1/16*n*c*w0^2; % power under gaussian units
FFx = Fx./P_CN;

Fmax_temp=max(FFx);
esccn=[esccn,Fmax_temp];

end

plot(nlist,esccn*1e12,'-b','LineWidth',3);

```

A.5. Matlab codes for Rayleigh trapping force simulation with the HA model

```

function HAtrap00x

format long;
% to calculate the trapping force according to CN model

%parameter to change

% w0=0.44e-6; % beam waist
lambda=0.808e-6; % wavelength in vacuum
n = 1.33; % refractive index of medium
ns = 1.38;
% 1.578 for ps; 1.45 for silica; 1.38 for biological particles
a=1e-7;

startw=175e-9;
endw=1.5e-6;

wlist=[startw:1e-9:endw]; % bead radius;

epsilon0 = 8.85e-12;
c=3e8;

wl=length(wlist);

```

```

escha=[];

for j=1:w1

    w0=wlist(j);
    %% end input parameters

    km = 2*pi*n/lambda; % k in medium
    s = 1/(km*w0);
    nr=ns/n; % relative refractive index
    sigma = 128*pi^5*a^6/3/(lambda/n)^4 * ((nr^2-1)/(nr^2+2))^2;
    %scattering crosssection
    alpha0 = n^2 * a^3 * (nr^2-1)/(nr^2+2); %polarizability
    alpha = alpha0/(1+2/3*1i*km^3*alpha0);

    x = (-1.5:0.001:1.5)*1e-6; % x positions
    y = 0;
    zpos = 0e-6;

    zt =(-0.005:0.001:0.005)*1e-6 + zpos;

    dx = 0.001e-6;
    dz = 0.001e-6;

    ##### temporary codes start
    lz=length(zt);
    I= [];
    Ext=[];

for i=1:lz
    z=zt(i);
    %## temporary codes end
    xi = x./w0; % greek letter Xi: nomalized x
    eta = y./w0; % greek letter Eta: nomalized y
    zita = z./(km*w0^2); % greek letter zeta: nomalized z

    Q = 1./(2.*zita+1i);
    rho = sqrt(xi.^2 + eta.^2);
    P = 1./(km.*w0.^2).*(-2./(2.*zita +1i) + 1i*2.*rho.^2./ ...
    (2.*zita +1i).^2 - 1i.*km.^2.*w0.^2);
    psi = 1i.*Q.*exp(-1i.*rho.^2.*Q);

    ##### start to calculate the electric field

    Ex = psi.*exp(-1i.*zita./s.^2);

    Ix = epsilon0*n*c/2 * (Ex.*conj(Ex));

    I=[I;Ix]; % I when E0 = 1

```

```

Ext=[Ext;Ex];
end
#####HA model

[Igradx,Igradz] = gradient(I,dx,dz);
Fgradx = 2*pi*alpha0/c/n.*Igradx; % 11*201, from -0.5 to +0.5
Fgradz = 2*pi*alpha0/c/n.*Igradz;

P_HA = pi*w0^2*n*epsilon0*c/4; %P when E0=1
Fgradx = Fgradx/P_HA; %force x
Fgradz = Fgradz/P_HA;

Fscat = I.*sigma.*n./c; % always along +z direction
Fscat = Fscat./P_HA;
Fztotal = Fscat + Fgradz; %force z

escha=[escha,max(Fgradx(6,:))];
end

plot((wlist)*1e6,escha.*1e12,'-r');

```

A.6. Matlab codes for Rayleigh trapping force calculation for SP2 based on the measured intensity distribution

```

function HAtrap00xzsp1

format long;

%parameter to change
load('xz for force field.mat'); % to load the measured intensity
Inten = interestedData;
P=135373*(5e-8)^2; % power measured experimentally 2584760
lambda=0.808e-6; % wavelength in vacuum
n = 1.33; % refractive index of medium
ns = 1.38; % 1.578 for ps; 1.45 for silica; 1.38 for biological particles
nr=ns/n; % relative refractive index

a=1e-7;

epsilon0 = 8.85e-12;
c=3e8;

km = 2*pi*n/lambda; % k in medium

sigma = 128*pi^5*a^6/3/(lambda/n)^4 * ((nr^2-1)/(nr^2+2))^2; %scattering
crosssection
alpha0 = n^2 * a^3 * (nr^2-1)/(nr^2+2); %polarizability
alpha = alpha0/(1+2/3*1i*km^3*alpha0);

```

```

x = (-5:0.05:5)*1e-6;    % x positions
z = (-0.5:0.1:5)*1e-6;

dx = 0.05e-6;
dz = 0.1e-6;

[Igradx,Igradz] = gradient(Inten,dx,dz);
Fgradx = 2*pi*alpha0/c/n.*Igradx; % x force
Fgradz = 2*pi*alpha0/c/n.*Igradz; % z force
Fgradx = Fgradx./P;    %force x
Fgradz = Fgradz./P;

Fscat = Inten.*sigma.*n./c; % always along +z direction
Fscat = Fscat./P;

Fx = Fgradx;
Fz = Fscat + Fgradz; %force z

dispdx=1;
dispdz=1;
dispxin=91:dispdx:111;
dispzin=11:dispdz:26;

dispx = x(dispxin);
dispz = z(dispzin);
dispFx = Fx(dispzin,dispxin);
dispFz = Fz(dispzin,dispxin);

% get start pts and end pts for arrow3 command
startp = [];
endp = [];

scale = min(dispdx*dx,dispdz*dz)/max(max(max(dispFx)),max(max(dispFz)));
stpt=zeros(length(dispz),2);
endpt=zeros(length(dispz),2);

for i=1:length(dispz)
    stpt(:,1) = ones(length(dispz),1)*dispz(i); % x coordinate of
start pts
    stpt(:,2) = dispz'; % z coordinate of
start pts
    endpt = stpt + [dispFx(:,i),dispFz(:,i)].*scale;

    startp=[startp;stpt];
    endp=[endp;endpt];
end

figure(2);
arrow3(startp*1e6,endp*1e6,'|2',0.7,1,0.4);

axis equal;
axis tight;
set(gca,'YDir','reverse')

```

```
colorbar;
```

```
ARROW3 UPDATE
```

```
figure(4);  
maxFx=Fx(17,:);  
plot(x*1e6,maxFx*1e12);
```

```
figure(5);
```

```
axFz2=Fz(:,100);  
plot(z*1e6,axFz2*1e12,'-b');
```

APPENDIX B: PUBLICATIONS

Journal Publications

- **Yuxiang Liu** and Miao Yu, “Optical manipulation and binding of microrods with multiple traps enabled in an inclined dual-fiber system”, *Biomicrofluidics*, Vol. 4, Art. No. 043010 (2010).
- **Yuxiang Liu** and Miao Yu, “Investigation of inclined dual-fiber optical tweezers for 3D manipulation and force sensing,” *Optics Express*, Vol. 17, No. 16, pp. 13624-13638 (2009). (Selected for publication in *the Virtual Journal for Biomedical Optics*, Editor: Gregory W. Faris, Vol. 4, Iss. 10, Oct. 2, 2009).
- **Yuxiang Liu** and Miao Yu, “Multiple traps created with an inclined dual-fiber system,” *Optics Express*, Vol. 17, pp. 21680-21690 (2009) (Selected for publication in *the Virtual Journal for Biomedical Optics*, Editor: Gregory W. Faris, Vol. 4, Iss. 13, Dec. 2, 2009).
- X. M. Zhang, **Yuxiang Liu**, H. Bae, C. Pang, and M. Yu, “Phase modulation with micromachined resonant mirrors for low-coherence fiber-tip pressure sensors,” *Optics Express*, Vol. 17, pp. 23965-23974 (2009).
- **Yuxiang Liu**, Hua Xu, Felix Stief, Nikolai Zhitenev, and Miao Yu, “Far-field superfocusing with an optical fiber based surface plasmonic lens made of nanoscale concentric annular slits”, *Applied Physics Letters* (in revision).
- **Yuxiang Liu** and Miao Yu, “Fiber optic network for simultaneous strain and pressure measurements”, *Applied Optics* (to be submitted).

Conference Proceedings

- **Yuxiang Liu** and Miao Yu, “Inclined dual-fiber optical tweezers: modeling and experiments,” in Optics + Photonics: Nanoscience + Engineering (San Diego, CA, August 20, 2009), *Proc. of SPIE*, Vol. 7400, Article No. 740027 (2009).
- **Yuxiang Liu** and Miao Yu, “3D Optical Force Field of Inclined Fiber Optical Tweezers,” in Conference on Lasers and Electro-Optics (CLEO) (Baltimore, MD, June 2 2009), OSA Technical Digest (CD) (Optical Society of America), Paper No. JTuD60 (2009).
- **Yuxiang Liu**, Alexander Lacher, Gang Wang, Ashish Purekar, and Miao Yu, “Wireless fiber optic sensor system for strain and pressure measurements on a rotor blade,” in Optics East (Boston, MA, September 9, 2007), *Proc. of SPIE*, Vol. 6770, Article No. 67700Y (2007).
- **Yuxiang Liu** and Miao Yu, “Fiber Optical Tweezers for Cell Manipulation and Force

Sensing,” in Conference on Lasers and Electro-Optics (CLEO) (Baltimore, MD, May 6, 2007), Paper No. CMAA6 (2007).

- **Yuxiang Liu** and Miao Yu, “Three-dimensional fiber optical trap for cell manipulation and force measurement,” in Smart Structures and Materials & Nondestructive Evaluation and Health Monitoring (San Diego, CA, March 18, 2007), *Proc. of SPIE*, Vol. 6528, Article No. 65280Z (2007).
- Zhong Chen, **Yuxiang Liu**, He Li, and Miao Yu, “Real-time demodulation scheme based on phase-shifting interferometry with error compensations for miniature Fabry-Perot acoustic sensors”, in Smart Structures and Materials 2006 (San Diego, CA, February 26, 2006), *Proc. of SPIE*, Vol. 6167, Article No. 61670N (2006).
- **Yuxiang Liu**, Anding Zhu, and Wenhao Huang, “Theoretical calculation of light-induced forces and torques on complex microrotors, ” in Photonics Asia 2004 (Beijing, China, November 8, 2004), *Proc. of SPIE*, Vol. 5641, pp. 255-263 (2004).

REFERENCES

1. A. Ashkin, "History of optical trapping and manipulation of small-neutral particle, atoms, and molecules," *IEEE Journal of Selected Topics in Quantum Electronics*, Vol. 6, No. 6, pp. 841-859, 2000.
2. G. M. Whitesides, "The 'right' size in nanobiotechnology," *Nature Biotechnology*, Vol. 21, No. 10, pp. 1161-1165, 2003.
3. S. Hormeno and J. R. Arias-Gonzalez, "Exploring mechanochemical processes in the cell with optical tweezers," *Biology of the Cell*, Vol. 98, No. 12, pp. 679-695, 2006.
4. K. J. Van Vliet, G. Bao, S. Suresh, "The biomechanics toolbox: experimental approaches for living cells and biomolecules," *Acta Materialia*, Vol. 51, pp. 5881-5905, 2003.
5. A. Ashkin and J. M. Dziedzic, "Internal cell manipulation using infrared laser traps," *Proceedings of National Academy of Sciences of the United States of America*, Vol. 86, pp. 7914-7918, 1989.
6. L. Sacconi, I. M. Tolic-Nørrelykke, C. Stringari, R. Antolini and F. S. Pavone, "Optical micromanipulations inside yeast cells," *Applied Optics*, Vol. 44, No. 11, pp. 2001-2027, 2005.
7. K. C. Neuman and S. M. Block, "Optical trapping," *Review of Scientific Instruments*, Vol. 75, No. 9, pp. 2787-2809, 2004.
8. E. A. Abbondanzieri, W. J. Greenleaf, J. W. Shaevitz, R. Landick and S. M. Block, "Direct observation of base-pair stepping by RNA polymerase," *Nature*, Vol. 438, pp. 460-465, 2005.
9. D. G. Grier, "Optical tweezers in colloid and interface science," *Current Opinion in Colloid & Interface Science*, Vol. 2, pp. 264-270, 1997.
10. J. C. Crocker and D. G. Grier, "When like charges attract: the effects of geometrical confinement on long-range colloidal interactions," *Physical Review Letters*, Vol. 77, No. 9, pp. 1897-1900, 1996.
11. D. McGloin, "Optical tweezers: 20 years on," *Philosophical Transactions of the Royal Society A-Mathematical Physical and Engineering Sciences*, Vol. 364, pp. 3521-3537, 2006.
12. A. Ashkin, "Optical trapping and manipulation of neutral particles using lasers," *Proceedings of National Academy of Sciences of the United States of America*, Vol. 94, pp. 4853-4860, 1997.
13. D. G. Grier, "A revolution in optical manipulation," *Nature*, Vol. 424, pp. 810-816, 2003.
14. S. C. Chapin, V. Germain and E. R. Dufresne, "Automated trapping, assembly, and sorting with holographic optical tweezers," *Optical Express*, Vol. 14, No. 26, pp. 13095-13100, 2006.
15. E. R. Dufresne, G. C. Spalding, M. T. Dearing, S. A. Sheets and D. G. Grier, "Computer-generated holographic optical tweezer arrays," *Review of Scientific Instruments*, Vol. 72, No. 3, pp. 1810-1816, 2001.
16. W. Grange, S. Husale, H. Guntherodt and M. Hegner, "Optical tweezers system measuring the change in light momentum flux," *Review of Scientific Instruments*, Vol. 73, No. 6, pp. 2308-2316, 2002.

17. M. Capitanio, G. Romano, R. Ballerini, M. Giuntini, F. S. Pavone, D. Dunlap and L. Finzi, "Calibration of optical tweezers with differential interference contrast signals," *Review of Scientific Instruments*, Vol. 73, No. 4, pp. 1687-1696, 2002.
18. K. C. Vermeulen, G. J. L. Wuite, G. J. M. Stienen and C. F. Schmidt, "Optical trap stiffness in the presence and absence of spherical aberrations," *Applied Optics*, Vol. 45, No. 8, pp. 1812-1819, 2006.
19. R. Daw and J. Finkelstein, "Lab on a chip," *Nature*, Vol. 442, No. 7101, pp. 442, 2006.
20. H. Craighead, "Future lab-on-a-chip technologies for interrogating individual molecules," *Nature*, Vol. 42, No. 7101, pp. 387-393, 2006.
21. Y. K. Song, J. Stein, W. R. Patterson, C. W. Bull, K. M. Davitt, M. D. Serruya, J. Zhang, A. V. Nurmikko and J. P. Donoghue, "A microscale photovoltaic neurostimulator for fiber optic delivery of functional electrical stimulation," *Journal of Neural Engineering*, Vol. 4, pp. 213-218, 2007.
22. S. J. Walker and D.J. Nagel, "Optics & MEMS," a Naval Research Laboratory Report, Washington, DC, USA, 1999.
23. "Optical tweezers an introduction,"
<http://www.stanford.edu/group/blocklab/Optical%20Tweezers%20Introduction.htm>
Last accessed on Oct. 31, 2007.
24. M. M. Burns, J. Fournier and J. A. Golovchenko, "Optical binding," *Physical Review Letters*, Vol. 63, No. 12, pp. 1233-1235, 1989.
25. N. W. Charon, S. F. Goldstein, S. M. Block, K. Curci, J. D. Ruby, J. A. Kreiling and R. J. Limberger "Morphology and dynamics of protruding spirochete periplasmic flagella," *Journal of Bacteriology*, Vol. 174, pp. 832-840, 1992.
26. N. Arneborga, H. Siegumfeldt, G. H. Andersen, P. Nissen, V. R. Daria, P. J. Rodrigo and J. Glückstad, "Interactive optical trapping shows that confinement is a determinant of growth in a mixed yeast culture," *FEMS Microbiology Letters*, Vol. 245, pp. 155-159, 2005.
27. F. V. Ignatovich and L. Novotny, "Experimental study of nanoparticle detection by optical gradient forces," *Review of Scientific Instruments*, Vol. 74, No. 12, pp. 5231-5235, 2003.
28. T. M. Grzegorzcyk, B. A. Kemp and J. A. Kong, "Passive guiding and sorting of small particles with optical binding forces," *Optics Letters*, Vol. 31, No. 22, pp. 2278-3380, 2006.
29. Olympus CKX41 brochure, available at
http://www.olympusamerica.com/files/seg_clinical_ckx31-ckx41_bro.pdf
Last accessed on Oct. 31, 2007.
30. A. Ashkin, "Acceleration and trapping of particles by radiation pressure," *Physical Review Letters*, Vol. 24, No. 4, pp. 156-159, 1970.
31. A. Ashkin, J. M. Dziedzic, J. E. Bjorkholm and S. Chu, "Observation of a single-beam gradient force optical trap for dielectric particles," *Optics Letters*, Vol. 11, No. 5, pp. 288-290, 1986.
32. S. Chu, J. E. Bjorkholm, A. Cable and A. Ashkin, "Experimental observation of optically trapped atoms," *Physical Review Letters*, Vol. 57, pp. 314-317, 1985.
33. P. Kraikivski, B. Pouligny and R. Dimova, "Implementing both short- and long-working-distance optical trappings into a commercial microscope," *Review of Scientific Instruments*, Vol. 77, Art. No. 113703, 2006.
34. M. P. MacDonald, L. Paterson, W. Sibbett and K. Dholakia, "Trapping and manipulation of low-index particles in a two-dimensional interferometric optical trap," *Optics Letters*, Vol. 26, No. 12, pp. 863-865, 2001.

35. J. E. Reiner, A. M. Crawford, R. B. Kishore, L. S. Goldner, K. Helmersen and M. K. Gilson, "Optically trapped aqueous droplets for single molecule studies," *Applied Physics Letters*, Vol. 89, Art. No. 013904, 2006
36. K. T. Gahagan and G. A. Swartzlander, "Simultaneous trapping of low-index and high-index microparticles observed with an optical-vortex trap," *Journal of Optical Society of America B*, Vol. 16, No. 4, pp. 533-537, 1999.
37. N. A. Ivanova and B. A. Bezuglyi, "Optical thermocapillary bubble trap," *Technical Physics Letters*, Vol. 32, No. 10, pp. 854-856, 2006.
38. P. J. Rodrigo, V. R. Daria and J. Glückstad, "Real-time interactive optical micromanipulation of a mixture of high- and low-index particles," *Optics Express*, Vol. 12, No. 7, pp. 1417-1425, 2004.
39. D. McGloin and K. Dholakia, "Bessel beams: diffraction in a new light," *Contemporary Physics*, Vol. 46, No. 1, pp. 15-28, 2005.
40. J. Arlt, V. Garcés-Chavez, W. Sibbett, K. Dholakia, "Optical micromanipulation using a Bessel light beam," *Optics Communications*, Vol. 197, pp. 239-245, 2001.
41. J. E. Curtis and D. G. Grier, "Structure of optical vortices," *Physical Review Letters*, Vol. 90, No. 13, 2003.
42. A. Jesacher, S. Fürhapter, S. Bernet and M. Ritsch-Marte, "Size selective trapping with optical 'cogwheel' tweezers," *Optical Express*, Vol. 12, No. 17, pp. 4129-4135, 2004.
43. R. C. Gauthier, "Optical levitation and trapping of a micro-optic inclined end-surface cylindrical spinner," *Applied Optics*, Vol. 40, No. 12, pp. 1961-1973, 2001.
44. H. Ukita and M. Kanehira, "A shuttlecock optical rotator – its design, fabrication and evaluation for a microfluidic mixer," *IEEE Journal on Selected Topics in Quantum Electronics*, Vol. 8, No. 1, pp. 111-117, 2002.
45. E. Higurashi, R. Sawada and T. Ito, "Optically induced rotation of a trapped micro-object about an axis perpendicular to the laser beam axis," *Applied Physics Letters*, Vol. 72, No. 23, pp. 2951-2953, 1998.
46. P. Galajda and P. Ormos, "Complex micromachines produced and driven by light," *Applied Physics Letters*, Vol. 78, No. 2, 2001.
47. A. Ashkin, J. M. Dziedzic, J. E. Bjorkholm and Steven Chu, "Observation of a sing-beam gradient force optical trap for dielectric particles," *Optics Letters*, Vol. 11, No. 5, pp. 288-290, 1986.
48. A. Ashkin and J. M. Dziedzic, "Optical trapping and manipulation of viruses and bacteria," *Science*, Vol. 235, No. 4795, pp. 1517-1520, 1987.
49. A. Ashkin, J. M. Dziedzic and T. Yamane, "Optical trapping and manipulation of single cells using infrared laser beams," *Nature*, Vol. 330, pp. 769-771, 1987.
50. J. A. Dharmadhikari, S. Roy, A. K. Dharmadhikari, S. Sharma and D. Mathur, "Torque-generating Malaria-infected red blood cells in an optical trap," *Optics Express*, Vol. 12, No. 6, pp. 1179-1184, 2004.
51. S. Bayouth, T. A. Nieminen, N. R. Heckenberg and H. Rubinsztein-Dunlop, "Orientation of biological cells using plane-polarized Gaussian beam optical tweezers," *Journal of Modern Optics*, Vol. 50, No. 10, pp. 1581-1590, 2003.
52. K. Im, S. Ju, S. Han, H. Park and B. Kim, "Trapping efficiency of a femtosecond laser and damage thresholds for biological cells," *Journal of Korean Physical Society*, Vol. 48, No. 5, pp. 968-973, 2006.

53. M. Dao, C. T. Lim, and S. Suresh, "Mechanics of the human red blood cell deformed by optical tweezers," *Journal of the mechanics and Physics of Solids*, Vol. 51, pp. 2259-2280, 2003.
54. D. R. Murdock, S. A. Ermilov, A. A. Spector, A. S. Popel, W. E. Brownell, B. Anvari, "Effects of chlorpromazine on mechanical properties of the outer hair cell plasma membrane," *Biophysical Journal*, Vol. 89, pp. 4090-4095, 2005.
55. I. M. Tolic-Norrelykke, E.-L. Munteanu, G. Thon, L. Oddershede, K. Berg-Sorensen, "Anomalous diffusion in living yeast cells," *Physical Review Letters*, Vol. 93, pp. 078102-1-078102-4, 2004.
56. M. Balland, A. Richert, F. Gallet, "The dissipative contribution of myosin II in the cytoskeleton dynamics of myoblasts," *European Biophysics Journal*, Vol. 34, pp. 255-261, 2005.
57. I. Titushkin, M. Cho, "Distinct membrane mechanical properties of human mesenchymal stem cells determined using optical tweezers," *Biophysical Journal*, Vol. 90, pp. 2582-2591, 2006.
58. T. Nishizaka, Q. Shi, M. P. Sheetz, "Position-dependent linkages of fibronectin-integrin-cytoskeleton," *Proceedings of the National Academy of Science of the United States of America*, Vol. 97, pp. 692-697, 2005.
59. A. Ranaweera, "Investigations with optical tweezers: construction, identification, and control," Ph.D. Dissertation, Department of Mechanical Engineering, University of California, Santa Barbara, 2004.
60. J. N. A. Matthews, "Commercial optical traps emerge from biophysics labs," *Physics Today*, Vol. 62, pp. 26-28, 2009.
61. M. Born and E. Wolf, *Principles of Optics, 7th (expanded) Edition*, Cambridge University Press, 1999.
62. E. Papagiakoumou, D. Pietreanu, M. I. Makropoulou, E. Kovacs and A. A. Serafetinides, "Evaluation of trapping efficiency of optical tweezers by dielectrophoresis," *Journal of Biomedical Optics*, Vol. 11, Art. No. 014035, 2006.
63. Nikon Instruments Information Center, "Oil immersion objectives", <http://www.nikoninstruments.com/infocenter.php?n=Oil%20Immersion>
Last accessed on Oct. 31, 2007.
64. M. A. Green and M. Keever, "Optical properties of intrinsic silicon at 300 K," *Progress in Photovoltaics*, Vol. 3, No. 3, pp. 189-192, 1995.
65. J. Guck, R. Ananthkrishnan, H. Mahmood, T. J. Moon, C. C. Cunningham and J. Käs, "The optical stretcher: a novel laser tool to micromanipulate cells," *Biophysical Journal*, Vol. 81, pp. 767-784, 2001.
66. R. S. Taylor and C. Hnatovsky, "Particle trapping in 3-D using a single fiber probe with an annular light distribution," *Optics Express*, Vol. 11, No. 21, pp. 2775-2782, 2003.
67. K. Taguchi, H. Ueno, T. Hiramatsu and M. Ikeda, "Optical trapping of dielectric particle and biological cell using optical fibre," *Electronics Letters*, Vol. 33, No. 5, pp. 413-414, 1997.
68. K. Taguchi, K. Atsuta, T. Nakata and M. Ikeda, "Experimental and theoretical study of the single-beam optical fiber trap," *Proceeding of SPIE Conference on Electronics and Structures for MEMS*, Vol. 3891, pp. 238-245, Queensland, Australia, 1999.
69. K. Taguchi, K. Atsuta, T. Nakata and M. Ikeda, "Single laser beam fiber optic trap," *Optical and Quantum Electronics*, Vol. 33, pp. 99-106, 2001.

70. Z. Hu, J. Wang and J. Liang, "Manipulation and arrangement of biological and dielectric particles by a lensed fiber probe," *Optics Express*, Vol. 12, No. 17, pp. 4123-4128, 2005.
71. Z. Hu, J. Wang and j. Liang, "Theoretical and experimental investigation of the optical trapping force in single lensed fibre trapping," *Journal of Optics A: Pure and Applied Optics*, Vol. 8, pp. 891-896, 2006.
72. K. S. Abedin, C. Kerbage, A. Fernandez-Nieves and D. A. Weitz, "Optical manipulation and rotation of liquid crystal drops using high-index fiber-optics tweezers," *Applied Physics Letters*, Vol. 91, Art. No. 091119, 2007.
73. T. Numata, A. Takayanagi, Y. Otani and N. Umeda, "Manipulation of metal nanoparticles using fiber-optic laser tweezers with a microspherical focusing lens," *Japanese Journal of Applied Physics*, Vol. 45, No. 1A, pp. 359-363, 2006.
74. S. Cabrini, C. Liberale, D. Cojoc, A. Carpentiero, M. Prasciolu, S. Mora, V. Degiorgio, F. De Angelis and E. Di Fabrizio, "Axicon lens on optical fiber forming optical tweezers, made by focused ion beam milling," *Microelectronic Engineering*, Vol. 83, pp. 804-807, 2006.
75. Z. Liu, C. Guo, J. Yang and L. Yuan, "Tapered fiber optical tweezers for microscopic particle trapping: fabrication and application," *Optics Express*, Vol. 14, No. 25, pp. 12510-12516, 2006.
76. L. Yuan, Z. Liu, J. Yang, and C. Guan, "Twin-core fiber optical tweezers," *Optics Express*, Vol. 16, No. 7, pp. 4551-4558, 2008.
77. Y. Huang, Y. Lu, J. Chen, Y. Hsu, Y. Huang, S. Huang, and W. Cheng, "Broadband emission from Cr-doped fibers fabricated by drawing tower," *Optics Express*, Vol. 14, pp. 8492-8497, 2006.
78. A. Degiron, H. J. Lezec, N. Yamamoto and T. W. Ebbesen, "Optical transmission properties of a single subwavelength aperture in a real metal," *Optical Communications*, Vol. 239, pp. 61-66, 2004.
79. A. Constable, J. Kim, J. Mervis, F. Zarinetchi and M. Prentiss, "Demonstration of a fiber-optical light-force trap," *Optics Letters*, Vol. 18, No. 21, pp. 1867-1869, 1993.
80. E. R. Lyons and G. J. Sonek, "Confinement and bistability in a tapered hemispherically lensed optical fiber trap," *Applied Physical Letters*, Vol. 66, No. 13, pp. 1584-1586, 1995.
81. J. Guck, S. Schinkinger, B. Lincoln, F. Wottawah, S. Ebert, M. Romeyke, D. Lenz, H. M. Erickson, R. Ananthakrishnan, D. Mitchell, J. Kas, S. Ulvick and C. Bilby, "Optical Deformability as an Inherent Cell Marker for Testing Malignant Transformation and Metastatic Competence," *Biophysical Journal*, Vol. 88, pp. 3689-3698, 2005.
82. C. Jensen-McMullin, H. P. Lee, "Demonstration of trapping, motion control, sensing and fluorescence detection of polystyrene beads in a multi-fiber optical trap," *Optics Express*, Vol. 13, No. 7, pp. 2634-2642, 2005.
83. R. C. Gauthier, M. Friesen, T. Gerrard, W. Hassouneh, P. Koziorowski, D. Moore, K. Oprea and S. Uttamalingam, "Self-centering of a ball lens by laser trapping: fiber-ball-fiber coupling analysis," *Applied Optics*, Vol. 42, No. 9, pp. 1610-1619, 2003.
84. K. Taguchi, K. Atsuta, T. Nakata and M. Ideda, "Levitation of a microscopic object using plural optical fibers," *Optics Communications*, Vol. 176, pp. 43-47, 2000.
85. K. Taguchi, M. Tanaka and M. Ikeda, "Dual-beam trapping method for an object with large relative refractive index," *Japanese Journal of Applied Physics*, Vol. 39, No. 1A, pp. L1302-L1304, 2000.

86. K. Taguchi, M. Tanaka and M. Ikeda, "Investigation on the radius of a hemispherical microlens of an optical fiber end for three-dimensional trapping," *Optical and Quantum Electronics*, Vol 34, pp. 993-999, 2002.
87. K. Taguchi and K. Ogawa, "Optically vibrated manipulation technique of a microsphere in a liquid using plural optical fibers," *Journal of Physics: Conference Series*, Vol. 61, pp. 1132-1136, 2006.
88. J. M. Tam, I. Biran and D. R. Walt, "An imaging fiber-based optical tweezers array for microparticle array assembly," *Applied Physics Letters*, Vol. 84, No. 21, pp. 4289-4291, 2004.
89. S. D. Collins, R. J. Baskin and D. G. Howitt, "Microinstrument gradient-force optical trap," *Applied Optics*, Vol. 38, No. 28, pp. 6068-6074, 1999.
90. C. Liberale, P. Minzioni, F. Bragheri, F. De Angelis, E. Di Fabrizio, and I. Cristiani, "Miniaturized all-fiber probe for three-dimensional optical trapping and manipulation," *Nature Photonics*, Vol. 1, pp. 723-727, 2007.
91. H. Lamb, *Hydrodynamics, Sixth Edition*, Dover Publications, 1945, Chap. XI, pp. 616.
92. F. Cardarelli, *Materials Handbook, A Concise Desktop Reference, Second Edition*, Springer, 2008, Chap. 10, pp. 672-675.
93. A. Ashkin, "Forces of a single-beam gradient laser trap on a dielectric sphere in the ray optics regime," *Biophysical Journal*, Vol. 61, pp. 569-582, 1992.
94. K. Berg-Sørensen and H. Flyvbjerg, "Power spectrum analysis for optical tweezers," *Review of Scientific Instruments*, Vol. 75, pp. 594-612, 2004.
95. K. Svoboda, and S. M. Block, "Biological applications of optical forces," *Annual Review of Biophysics and Biomolecular Structure*, Vol. 23, pp. 247-285, 1994.
96. R. C. Gauthier, "Optical trapping: a tool to assist optical machining," *Optics & Laser Technology*, Vol. 29, pp. 389-399, 1997.
97. E. Sidick, S. D. Collins, and A. Knoesen, "Trapping forces in a multiple-beam fiber-optic trap," *Applied Optics*, Vol. 36, pp. 6423-6433, 1997.
98. A. Priyadarshi, L. H. Fen, S. G. Mhaisalkar, V. Kripesh, and A. K. Asundi, "Fiber misalignment in silicon V-groove based optical modules," *Optical Fiber Technology*, Vol. 12, pp. 170-184, 2006.
99. Z. Yan, *Low Reynolds Number Flow Theory*, Beijing University Press, Beijing, 2002.
100. J. C. Crocker, and D. G. Grier, "Microscopic measurement of the pair interaction potential of charge-stabilized colloid," *Physics Review Letters*, Vol. 73, pp. 352-355, 1994.
101. M. P. MacDonald, L. Paterson, K. Volke-Sepulveda, J. Arlt, W. Sibbett and K. Dholakia, "Creation and manipulation of three-dimensional optically trapped structures," *Science*, Vol. 296, pp. 1101-1103, 2002.
102. Y. Roichman, and D. G. Grier, "Holographic assembly of quasicrystalline photonic heterostructures," *Optics Express*, Vol. 13, pp. 5434-5439, 2005.
103. K. Visscher, G. J. Brakenhoff, and J. J. Krol, "Micromanipulation by 'multiple' optical traps created by a single fast scanning trap integrated with the bilateral confocal scanning laser microscope," *Cytometry*, Vol. 14, pp. 105-114, 1993.
104. G. Boer, R. Johann, J. Rohner, F. Merenda, G. Delacrétaz, Ph. Renaud, and R.-P. Salathé, "Combining multiple optical trapping with microflow manipulation for the rapid bioanalytics on microparticles in a chip," *Review of Scientific Instruments*, Vol. 78, No. 11, Art. No. 116101, 2007.

105. K. J. Moh, W. M. Lee, W. C. Cheong, and X.-C. Yuan, "Multiple optical line traps using a single phase-only rectangular ridge," *Applied Physics B*, Vol. 80, No. 8, pp. 973–976, 2005.
106. E. R. Dufresne, and D. G. Grier, "Optical tweezer arrays and optical substrates created with diffractive optics," *Review of Scientific Instruments*, Vol. 69, No. 5, pp. 1974–1977, 1998.
107. F. Merenda, J. Rohner, J. M. Fournier, and R. P. Salathé, "Miniaturized high-NA focusing-mirror multiple optical tweezers," *Optics Express*, Vol. 15, No. 10, pp. 6075–6086, 2007.
108. D. M. Gherardi, A. E. Carruthers, T. Čižmár, E. M. Wright, and K. Dholakia, "A dual beam photonic crystal fiber trap for microscopic particles," *Applied Physics Letters*, Vol. 93, No. 4, Art. No. 041110, 2008.
109. K. S. Mohanty, C. Liberale, S. K. Mohanty, and V. Degiorgio, "In depth fiber optic trapping of low-index microscopic objects," *Applied Physics Letters*, Vol. 92, No. 15, Art. No. 151113, 2008.
110. S. K. Mohanty, K. S. Mohanty, and M. W. Berns, "Organization of microscale objects using a microfabricated optical fiber," *Optics Letters*, Vol. 33, No. 18, pp. 2155–2157, 2008.
111. W. Singer, M. Frick, S. Bernet, and M. Ritsch-Marte, "Self-organized array of regularly spaced microbeads in a fiber-optical trap," *Journal of Optical Society of America B*, Vol. 20, No. 7, pp. 1568–1574, 2003.
112. M. M. Burns, J.-M. Fournier, and J. A. Golovchenko, "Optical matter: crystallization and binding in intense optical fields," *Science*, Vol. 249, No. 4970, pp. 749–754, 1990.
113. N. K. Metzger, E. M. Wright, W. Sibbett, and K. Dholakia, "Visualization of optical binding of microparticles using a femtosecond fiber optical trap," *Optics Express*, Vol. 14, No. 8, pp. 3677–3687, 2006.
114. W. H. Wright, G. J. Sonek and M. W. Berns, "Parametric study of the forces on microspheres held by optical tweezers", *Applied Optics*, Vol. 33, No. 9, pp. 1735–1748, 1994.
115. H. Zhang and K. Liu, "Optical tweezers for single cells," *Journal of the Royal Society Interface*, Vol. 5, No. 24, pp. 671–690, 2008.
116. B. Alberts, A. Johnson, J. Lewis, M. Raff, K. Roberts, and P. Walter, *Molecular Biology of the Cell, Fifth Edition*, Garland Science, New York, 2008, Chapt. 1, pp. 14.
117. M. Ichikawa, K. Kubo, K. Yoshikawa, and Y. Kimura, "Tilt control in optical tweezers," *Journal of Biomedical Optics*, Vol. 13, No. 1, Art. No. 010503, 2008.
118. E. Florin, A. Pralle, J. K. Heinrich Hörber, and E. H. K. Stelzer, "Photonic force microscope based on optical tweezers and two-photon excitation for biological applications," *Journal of Structural Biology*, Vol. 119, No. 2, pp. 202–211, 1997.
119. H. Kress, E. H. K. Stelzer, and A. Rohrbach, "Tilt angle dependent three-dimensional-position detection of a trapped cylindrical particle in a focused laser beam," *Applied Physics Letters*, Vol. 84, pp. 4271–4273, 2004.
120. P. J. Pauzauskie, A. Radenovic, E. Trepagnier, H. Shroff, P. Yang, and J. Liphardt, "Optical trapping and integration of semiconductor nanowire assemblies in water," *Nature Materials*, Vol. 5, pp. 97–101, 2006.
121. R. C. Gauthier, "Theoretical investigation of the optical trapping force and torque on cylindrical micro-objects," *Journal of Optical Society of America B*, Vol. 14, No. 12, pp. 3323–3333, 1997.
122. C. Genet and T. W. Ebbese, "Light in tiny holes," *Nature*, Vol. 445, pp. 39–46, 2007.

123. R. Piparia and E. W. Rothe and R. J. Baird, "Nanobumps on silicon created with polystyrene spheres and 248 or 308 nm laser pulses," *Applied Physics Letters*, Vol. 89, Art. No. 223113, 2006.
124. W. Guo, Z. B. Wang, L. Li, D. J. Whitehead, B. S. Luk'yanchuk and Z. Liu, "Near-field laser parallel nanofabrication of arbitrary-shaped patterns," *Applied Physics Letters*, Vol. 90, Art. No. 243101, 2007.
125. G. Wysocki, J. Heitz, and D. Bäerle, "Near-field optical nanopatterning of crystalline silicon," *Applied Physics Letters*, Vol. 84, pp. 2025-2027, 2006.
126. Leilei Yin, Vitali K. Vlasko-Vlasov, John Pearson, Jon M. Hiller, Jiong Hua, Ulrich Welp, Dennis E. Brown, and Clyde W. Kimball, "Subwavelength focusing and guiding of surface plasmons," *Nano Letters*, Vol. 5, pp 1399 – 1402, 2005.
127. H. Yuan, B. Xu, B. Lukiyanchuk, T. Chong, "Principle and design approach of flat nano-metallic surface plasmonic lens," *Applied Physics A*, Vol. 89, pp 397-401, 2007.
128. H. J. Lezec, A. Degiron, E. Devaux, R. A. Linke, L. Martin-Moreno, F. J. Garcia-Vidal, T. W. Ebbesen, "Beaming light from a subwavelength aperture," *Science*, Vol. 297, pp. 820-822, 2002.
129. W. L. Barnes, A. Dereux and T. W. Ebbesen, "Surface plasmon subwavelength optics," *Nature*, Vol. 424, pp. 824-830, 2003.
130. E. Ozbay, "Plasmonics: merging photonics and electronics at nanoscale dimensions," *Science*, Vol. 311, pp. 189-193, 2006.
131. Z. Sun and H. K. Kim, "Refractive transmission of light and beam shaping with metallic nano-optic lenses," *Applied Physics Letters*, Vol. 85, No. 4, pp. 642-644, 2004.
132. W. L. Barnes, W. A. Murray, J. Dintinger, E. Devaux and T. W. Ebbesen, "Surface Plasmon polaritons and their role in the enhanced transmission of light through periodic arrays of subwavelength holes in a metal film," *Physical Review Letters*, Vol. 92, No. 10, Art. No. 107401, 2004.
133. S. S. Akarca-Biyikli, I. Bulu and E. Ozbay, "Enhanced transmission of microwave radiation in one-dimensional metallic gratings with subwavelength aperture," *Applied Physics Letters*, Vol. 85, No. 7, 2004.
134. L. Verslegers, P. B. Catrysse, Z. Yu, J. S. White, E. S. Barnard, M. L. Brongersma, and S. Fan, "Planar lenses based on nanoscale slit arrays in a metallic film," *Nano Letters*, Vol. 9, No. 1, pp. 235-238, 2009.
135. P. B. Catrysse and S. Fan, "Understanding the dispersion of coaxial plasmonic structures through a connection with the planar metal-insulator-metal geometry," *Applied Physics Letters*, Vol. 94, Art. No. 231111, 2009.
136. Y. Fu, R. G. Mote, Q. Wang, and W. Zhou, "Experimental study of plasmonic structures with variant periods for sub-wavelength focusing: analyses of characterization errors," *Journal of Modern Optics*, Vol. 56, No. 14, pp. 1550-1556, 2009.
137. Y. Fu, Y. Liu, X. Zhou, Z. Xu, and F. Fang, "Experimental investigation of superfocusing of plasmonic lens with chirped circular nanoslits," *Optics Express*, Vol. 18, No. 4, pp. 3438-3443, 2010.
138. V. V. Temnov, G. Armelles, U. Woggon, D. Guzatov, A. Cebollada, A. Garcia-Martin, J. Garcia-Martin, T. Thomay, A. Leitenstorfer, and R. Bratschitsch, "Active magneto-plasmonics in hybrid metal-ferromagnet structures", *Nature Photonics*, Vol. 4, pp. 107-111, 2010.

139. H. Shi, C. Wang, C. Du, X. Luo, X. dong, H. Gao, "Beam manipulating by metallic nano-slits with variant widths," *Optics Express*, Vol. 13, No. 18, pp. 6815-6820, 2005.
140. E. Schonbrun, C. Rinzler, and K. B. Crozier, "Microfabricated water immersion zone plate optical tweezers," *Applied Physics Letters*, Vol. 92, Art. No. 071112, 2008.
141. E. D. Palik, *Handbook of optical constants of solids*, Academic Press Limited, 1998, Page 294.
142. "Titanium", WIKIPEDIA, The free Encyclopedia, <http://en.wikipedia.org/wiki/Titanium>. Last accessed on May. 7, 2010.
143. K. Okamoto, *Fundamentals of Optical waveguides, Second Edition*, Elsevier, Inc., 2006, Chapt. 3, Page 82.
144. C. D. Meinhart and S. T. Wereley, "The theory of diffraction-limited resolution in microparticle image velocimetry," *Measurement Science and Technology*, Vol. 14, pp. 1047-1053, 2003.
145. E. Abbe, "Beiträge zur Theorie des Mikroskops und der mikroskopischen Wahrnehmung," *Arch. Mikrosk. Anat. Entwicklungsmech.*, Vol. 9, pp. 413-468, 1873.
146. V. P. Kalosha and I. Golub, "Toward the subdiffraction focusing limit of optical superresolution," *Optics Letters*, Vol. 32, No. 24, pp. 3540-3542, 2007.
147. J. B. Pawley, *Handbook of Biological Confocal Microscopy, Second Edition*, Springer Science+Business Media, Inc, 1995, Chapt. 9, Page 142.
148. P. Ruffieux, T. Scharf, and H. P. Herzig, "On the chromatic aberration of microlenses," *Measurement Science and Technology*, Vol. 14, pp. 1047-1053, 2003.
149. A. Taflove and S. C. Hagness, *Computational Electrodynamics: The Finite-Difference Time-Domain Method, Second Edition*, Artech House, Inc., 2000.
150. K. S. Yee, "Numerical solution of initial boundary value problems involving Maxwell's equations in isotropic media," *IEEE Transactions on Antennas and Propagation*, Vol. AP-14, No. 3, pp. 302-307, 1966.
151. H. C. Berg, *Ecoli in Motion*, Springer-Verlag New York, Inc, 2003, Chapt. 1, Page 1.
152. "Water Health Series: Filtration Facts," United States Environmental Protect Agency (EPA). Available at http://www.epa.gov/safewater/faq/pdfs/fs_healthseries_filtration.pdf. Last access on April 22, 2010.
153. "Legionella: Drinking Water Health Advisory," United States Environmental Protect Agency (EPA). Available at <http://www.epa.gov/waterscience/criteria/humanhealth/microbial/legionellaha.pdf>. Last access on April 22, 2010.
154. M. Righini, P. Ghenuche, S. Cherukulappurath, V. Myroshnychenko, F. J. García de Abajo, and R. Quidant, "Nano-optical trapping of Rayleigh particles and *Escherichia coli* bacteria with resonant optical antennas," *Nano Letters*, Vol. 9, No. 10, pp. 3387-3391, 2009.
155. Y. K. Nahmias, and D. J. Odde, "Analysis of radiation forces in laser-trapping and laser-guided direct writing applications," *IEEE Journal of Quantum Electronics*, Vol. 38, No. 2, pp. 131-141, 2002.
156. X. Ma, J. Q. Lu, R. S. Brock, K. M. Jacobs, P. Yang, and X. Hu, "Determination of complex refractive index of polystyrene microspheres from 370 to 1610 nm," *Physics in Medicine and Biology*, Vol. 48, pp. 4165-4172, 2003.

157. D. E. Metzler, *Biochemistry, Volume 2, Second Edition: The Chemical Reactions of Living Cells*, Academic Press, 2003, Chapt. 19, Page 1089.
158. M. B. Rasmussen, L. B. Oddershede, and H. Siegmundfeldt, "Optical tweezers cause physiological damage to *Escherichia coli* and *Listeria* bacteria," *Applied and Environmental Microbiology*, Vol. 74, No. 8, pp. 2441-2446, 2008.
159. M. Ericsson, D. Hanstorp, P. Hagberg, J. Enger, and T. Nyström, "Sorting our bacterial viability with optical tweezers," *Journal of Bacteriology*, Vol. 182, No. 19, pp. 5551-5555, 2000.
160. K. C. Neuman, E. H. Chadd, G. F. Liou, K. Bergman, and S. M. Block, "Characterization of photodamage to *Escherichia coli* in optical traps," *Biophysical Journal*, Vol. 77, pp. 2856-2863, 1999.
161. J. D. Jackson, *Classical Electrodynamics, 3rd ed.*, John Wiley & Sons, Inc, 1998.
162. J. P. Barton, D. R. Alexander, and S. A. Schaub, "Theoretical determination of net radiation force and torque for a spherical particle illuminated by a focused laser beam," *Journal of Applied Physics*, Vol. 66, No. 10, pp. 4594-4602, 1989.
163. Y. Harada and T. Asakura, "Radiation forces on a dielectric sphere in the Rayleigh scattering regime," *Optics Communications*, Vol. 124, pp. 529-541, 1996.
164. P. C. Chaumet and M. Nieto-Vesperinas, "Time-averaged total force on a dipolar sphere in an electromagnetic field," *Optics Letters*, Vol. 25, pp. 1065-1067, 2000.
165. B. T. Draine, "The discrete-dipole approximation and its application to interstellar graphite grains," *The Astrophysical Journal*, Vol. 333, pp. 848-872, 1988.
166. J. P. Gordon, "Radiation forces and momenta in Dielectric media," *Physical Review A*, Vol. 8, No. 1, pp. 14-21, 1973.
167. "Levi-Civita symbol", WIKIPEDIA, The free Encyclopedia, http://en.wikipedia.org/wiki/Levi-Civita_tensors. Last accessed on April 20, 2010.
168. B. H. J. Mckellar, M. A. Box, C. F. Bohren, "Erratum: sum rules for optical scattering amplitudes," *Journal of Optical Society of America: Optics, Image Science, and Vision*, Vol. 1, No. 12, pp. 1206, 1984.
169. P. M. Hansen, V. K. Bhatia, N. Harrit, and L. Oddershede, "Expanding the optical trapping range of gold nanoparticles," *Nano Letters*, Vol. 5, No. 10, pp. 1937-1942, 2005.
170. P. Török, F. Kao, *Optical Imaging and Microscopy, Techniques and Advanced Systems, Second Edition*, Springer, 2007, Chapt. 17, Page 471-472.
171. J. P. Barton and D. R. Alexander, "Fifth-order corrected electromagnetic field components for a fundamental Gaussian beam," *Journal of Applied Physics*, Vol. 66, No. 7, pp. 2800-2802, 1989.
172. H. Kogelnik, and T. Li, "Laser beams and resonators," *Applied Optics*, Vol. 5, No. 10, pp. 1550-1567, 1966.
173. P. Wu, R. Huang, C. Tischer, A. Jonas, and E. Florin, "Direct measurement of the nonconservative force field generated by optical tweezers," *Physical Review Letters*, Vol. 103, Art. No. 108101, 2009.
174. S. M. Orbons, D. Freeman, B. Luther-Davies, B. C. Gibson, S. T. Huntington, D. N. Jamieson, A. Roberts, "Optical properties of silver composite metamaterials," *Physica B*, Vol. 394, pp. 176-179, 2007.